

ISI

**bilimi ve tekniği
dergisi**

**Journal of Thermal Science
and Technology**

**2022 Cilt/Volume 42 Sayı/Number 1
ISSN 1300-3615**

Türk Isı Bilimi ve Tekniği Derneği tarafından yılda iki kez
Nisan ve Ekim aylarında yayınlanır.

*A publication of the Turkish Society for Thermal Sciences and
Technology, published twice a year, in April and October.*

TIBTD Adına Yayın Sahibi Sorumlu Yayımcı/Publisher:
Prof. Dr. Nuri Yücel, Gazi Üniversitesi

Sorumlu Yazı İşleri Müdürü-Editör/Editor-in-Chief:
Prof. Dr. Selin ARADAĞ ÇELEBİOĞLU
TED Üniversitesi Makine Mühendisliği Bölümü,
submit@tibtd.org.tr

Yayın Türü: Yaygın, süreli

Editörler Kurulu/Editorial Board:

Prof. Dr. Murat KÖKSAL, Hacettepe Üniversitesi
Doç. Dr. Özgür EKİCİ, Hacettepe Üniversitesi
Doç. Dr. Barbaros ÇETİN, İhsan Doğramacı Bilkent
Üniversitesi
Doç. Dr. Özgür BAYER, Orta Doğu Teknik Üniversitesi

Dil Editörleri (Language Editors):

Prof. Dr. Zafer DURSUNKAYA, Orta Doğu Teknik
Üniversitesi (İngilizce/English)
Prof. Dr. Haşmet TÜRKÖĞLU, Çankaya Üniversitesi
(Türkçe/ Turkish)

Teknik Danışman/Technical Advisor

Doç. Dr. Ülkü Ece AYLI, Çankaya Üniversitesi

Baskı/Printed at: KALKAN Matbaacılık San. Tic. Ltd.
Büyük Sanayi 1. Cadde, Alibey İş Hanı No: 99/32 İskitler,
ANKARA 312 342 16 56

TIBTD

Türk Isı Bilimi ve Tekniği Derneği: Dernek ve bu dergi,
Türkiye'de ısı bilimi ve tekniğini geliştirmek amacıyla 1976
yılında Prof. Dr. Yalçın A. GÖĞÜŞ tarafından kurulmuştur.

Turkish Society of Thermal Sciences and Technology: The
association and the journal was founded by Prof. Dr. Yalçın A.
GÖĞÜŞ in 1976 to improve thermal sciences and technology
in Turkey.

Adresi/Address: TIBTD, Mühendislik Fakültesi, Zemin Kat
No.22 Gazi Üniversitesi, 06570 ANKARA
http://www.tibtd.org.tr, ibtd@tibtd.org.tr
Üyelik aidatları için: İş Bankası Maltepe Şubesi Hesap No:
42120867567, IBAN: TR08 0006 4000 0014 2120 8675 67

Yönetim Kurulu/Executive Board:

Prof. Dr. Nuri YÜCEL (Bşk), Prof. Dr. İlhami HORUZ (Bşk.
Yrd.), Doç. Dr. Mustafa Zeki YILMAZOĞLU (Genel Sek.),
Dr. Duygu UYSAL (Muhasip Üye), Prof. Dr. Oğuz TURGUT,
Prof. Dr. Selin ARADAĞ ÇELEBİOĞLU, Doç. Dr. Ece AYLI

İÇİNDEKİLER / CONTENTS

Sayfa / Page

Dik kanal içerisindeki taşınım ile ısı transferinin yarı silindirik akış engelleri kullanılarak iyileştirilmesinin sayısal olarak incelenmesi <i>Numerical investigation of enhancing mixed convection heat transfer by using semi-cylindrical obstacles in a vertical channel</i> Sedat ÖZDEMİR, Mustafa KILIÇ, Tamer ÇALIŞIR ve Şenol BAŞKAYA	1
The determination of the heat extraction ratio in the solar pond <i>Güneş havuzlarında ısı çekme oranının belirlenmesi</i> Hacı SOĞUKPINAR and İsmail BOZKURT	17
Modüler Helyum reaktörünün kaza durumunun zamana bağlı ısı akışı analizi <i>Transient thermal hydraulic analysis of modular Helium reactor under accident condition</i> Ömür AKBAYIR	25
Numerical analysis of microwave cancer therapy using single and double slot antennas for breast and liver tissues <i>Meme ve karaciğer dokularında tek ve çift yuvalı anten kullanılarak yapılan mikrodalga kanser tedavisinin nümerik analizi</i> Aykut EREN, Zeynep AYTAÇ, Oğuz TURGUT and Burak TIĞLI	37
Determination of indoor design temperature, thermal characteristics and insulation thickness under hot climate conditions <i>Sıcak iklim şartları altında iç dizayn sıcaklığı, termal özellikler ve yalıtım kalınlığının belirlenmesi</i> Meral ÖZEL	49
Analysis and optimization of activated carbon coated heat sinks <i>Aktif karbon kaplamalı soğutucuların analiz ve optimizasyonu</i> Alperen GÜNAY	65
Experimental investigation of the effects of water adding into the intake air on the engine performance and exhaust emissions in a spark-ignition engine <i>Bir benzin motorunda emme havasına su eklenmesinin motor performansına ve egzoz emisyonlarına etkilerinin deneysel olarak incelenmesi</i> Derya SOYSAL, Zehra ŞAHİN and Orhan DURGUN	75
An accelerated nodal discontinuous Galerkin method for thermal convection on unstructured meshes: Formulation and validation <i>Isı Taşınımı için yapısal olmayan ağlarda bir hızlandırılmış süreksiz Galerkin metodu: Formülasyonu ve doğrulaması</i> Ali KARAKUS	91
Exergy analysis of Graphene-based nanofluids in a compact heat exchanger <i>Kompakt bir ısı değiştiricisinde Grafen bazlı nano akışkanların ekserji analizi</i> Ferhat KILINÇ and Cihan Zeki UYGUN	101
Implementation, verification and assessment of vortex capturing capabilities of k-kL turbulence model <i>k-kL türbülans modelinin uygulaması, doğrulaması ve girdap yakalama yeteneklerinin değerlendirilmesi</i> Erdem DİKBAŞ and Özgür Uğraş BARAN	113
Design fire curve selection of small scale pool fires in a scaled metro station <i>Ölçeklendirilmiş bir metro istasyonunda küçük ölçekli sıvı havuz yangınlarının yangın tasarım eğrisi seçimi</i> Umut Barış YILMAZ, Oğuz TURGUT, Nuri YÜCEL and Muhammed İler BERBEROĞLU	123
Fast and predictive heat pipe design and analysis toolbox: H-PAT <i>Hızlı ve öngörülü ısı borusu tasarım ve analiz aracı: H-PAT</i> Samet SAYGAN, Yiğit AKKUŞ, Zafer DURSUNKAYA and Barbaros ÇETİN	141

Amaç/Objective

Isı bilimi ve tekniğinin geliştirilmesini teşvik etmek, ısı bilimi ve tekniği alanında özgün, teorik, sayısal ve deneysel çalışmaların yayınlanmasına olanak sağlamaktır.

To contribute to the improvement of thermal sciences and technology and publication of original, theoretical, numerical and experimental studies in thermal sciences and technology.

İçerik/Content

Isı bilimi ve tekniği alanındaki özgün ve derleme makaleler.
Original and review articles in thermal sciences and technology.

Değerlendirme/Evaluation

Dergi hakemli bir dergi olup, her bir makale konusunda uzman en az iki hakem tarafından değerlendirilir.

Each article published in this journal is evaluated by at least two referees.

Science Citation Index Expanded (SCIE), Engineering Index (EI), EBSCO ve Mühendislik ve Temel Bilimler Veri Tabanı (TÜBİTAK-ULAKBİM) tarafından taranmaktadır.

Indexed by Science Citation Index Expanded (SCIE), Engineering Index (EI), EBSCO and Engineering and Natural Sciences Data Base (TÜBİTAK-ULAKBİM).



DİK KANAL İÇERİSİNDEKİ KARIŞIK TAŞINIM İLE ISI TRANSFERİNİN YARI SİLİNDİRİK AKIŞ ENGELLERİ KULLANILARAK İYİLEŞTİRİLMESİNİN SAYISAL OLARAK İNCELENMESİ

Sedat ÖZDEMİR*, Mustafa KILIÇ**, Tamer ÇALIŞIR* ve Şenol BAŞKAYA*

*Gazi Üniversitesi Mühendislik Fakültesi Makina Mühendisliği Bölümü, 06570 Maltepe, Ankara

ozdemirsedat@gmail.com, ORCID: 0000-0002-6790-4608

tamercalisir@gazi.edu.tr, ORCID: 0000-0002-0721-0444

baskaya@gazi.edu.tr, ORCID: 0000-0001-9676-4387

** Adana Alparslan Türkeş Bilim ve Teknoloji Üniversitesi Makina Mühendisliği Bölümü 01250 Sarıçam, Adana
mkilic@atu.edu.tr, ORCID: 0000-0002-8006-149X

(Geliş Tarihi: 03.06.2021, Kabul Tarihi: 26.11.2021)

Özet: Bu çalışmada; dik ve içinde ısı akısına sahip yarı silindirik engeller bulunan bir kanaldaki karışık konveksiyonun ısı transferine ve akış özelliklerine etkisi sayısal olarak incelenmiştir. Yarı silindirik engellerin birbirlerine olan uzaklıkları, konumları ve sayıları değiştirilerek ısı transferine ve akış özelliklerine etkisi belirlenmeye çalışılmıştır. Çalışmada, tek yarı silindirik engelin, alt alta bulunan iki yarı silindirik engelin ve karşılıklı bulunan iki yarı silindirik engelin karışık konveksiyonla olan akış ve ısı transferine etkileri irdelenmiştir. Sonuç olarak; engel çapının kanal genişliğine oranının (BR) artırılmasının ısı transferini arttırdığı görülmüştür. $BR=0,15$ den $0,75$ değerine değiştirildiğinde; Ri sayısının artışına bağlı olarak ($Ri = 50-200$) ortalama Nu sayısındaki artışın %58,3 olduğu belirlenmiştir. Engellerin birbirine olan uzaklıklarını temsil eden L/D oranı arttığında; Nusselt sayısının genel olarak arttığı görülmüştür. $L/D = 0,25-1,5$ aralığında arttırıldığında; ortalama Nu sayısında %25,2'lik bir artış olduğu, en yüksek Nu sayısının $L/D = 1$ ve $Ri = 300$ olduğu durumda meydana geldiği tespit edilmiştir. Karşılıklı bulunan iki yarı silindirik engelin olması durumunda ise; BR oran arttıkça, Ri sayısının artmasına bağlı olarak Nusselt sayısının arttığı tespit edilmiştir. $BR = 0,15-0,30$ aralığında arttırıldığında; düşük Ri sayılarında ($Ri=50$) ortalama Nu sayısındaki artış %36,3 olarak belirlenmiş, yüksek Ri sayılarında ($Ri = 200$) ise ortalama Nu sayısındaki artışın %23,1 olarak meydana geldiği tespit edilmiştir. Ayrıca; sayısal çalışmanın sonuçları literatürde bulunan deneysel çalışmalarla da karşılaştırılarak; sıcaklık dağılımını ve akış özelliklerini iyi şekilde temsil edebildiği görülmüştür.

Anahtar Kelimeler: Kanal akışı, Karışık taşınım, Akış engelleri, Hesaplamalı akışkanlar dinamiği (HAD)

NUMERICAL INVESTIGATION OF ENHANCING MIXED CONVECTION HEAT TRANSFER BY USING SEMI-CYLINDRICAL OBSTACLES IN A VERTICAL CHANNEL

Abstract: In this study; effects of mixed convection on heat transfer and flow properties was investigated numerically for a vertical channel which has semi-cylindrical obstacles with heat flux. Effects of distance, location and number of these semi-cylindrical obstacles on heat transfer and flow properties have been examined. The effect of one semi-cylindrical obstacle, two semi-cylindrical obstacles located one under the other and two semi-cylindrical obstacles on opposite sides were investigated in the study. As a result; it is obtained that increasing the ratio of the obstacle diameter to the channel width (BR) causes an increase on heat transfer. Increasing BR ratio from 0.15 to 0.75, depending on the increase of Ri number from 50 to 200 causes an increase of 58.3% on average Nu number. Increasing L/D ratio, which represents the distance between obstacles, causes generally an increase in the average Nu number. Increasing L/D ratio from 0.25 to 1.5 results in an increase of 25.2% on the average Nu number. The highest Nu number can be obtained for $L/D = 1$ and $Ri = 300$. For the case of two semi-cylindrical obstacles on opposite sides; it was seen that increasing the BR ratio causes an increase in the average Nu number depending on the increase in the Ri number. Increasing BR ratio from 0.15 to 0.30 yields an increase of 36.3% for a low Ri number ($Ri=50$) and an increase of 23.1% for a high Ri number ($Ri = 200$) in the average Nu number. Moreover; it has been shown that numerical results can well represent the temperature distribution and flow properties by comparison of these results with experimental results in the literature.

Keywords: Channel flow, Mixed convection, Flow obstacle, Computational Fluid Dynamics (CFD)

SEMBOLLER

BR	Engel çapının kanal genişliğine oranı $[D/W]$
C_p	Özgül Isı $[J/kgK]$
D	Silindirik engelin çapı $[m]$
D/W	Engel çapının kanal genişliğine oranı
g	Yer çekimi ivmesi $[m/s^2]$
Gr	Grashof Sayısı $[=g\beta(T_s-T_{bulik})L_c^3/\gamma^2]$
H	Kanal uzunluğu $[m]$
k	Isı iletim katsayısı $[W/mK]$
L	Engellerin birbirine olan uzaklıkları $[m]$
L/D	Engellerin birbirine uzaklığının kanal çapına oranı $[L/D]$
Nu	Nusselt Sayısı $[=Q.D_h/\Delta T.k]$
P	Basınç $[Pa]$
Pr	Prandtl Sayısı $[=\mu.C_p/k]$
q	Isı akısı $[W/m^2]$
$Q_{ışınım}$	Işınım ile olan ısı transferi
Re	Reynolds Sayısı $[=V.\rho.D_h/\mu]$
Ri	Richardson Sayısı $[=Gr/Re^2]$
T	Sıcaklık $[^\circ C]$
T_o	Kanal girişindeki su sıcaklığı $[^\circ C]$
T_w	Yarı silindirik engelin ortalama sıcaklığı $[^\circ C]$
u, v	Hız bileşenleri $[m/s]$
u_o	Akışkan hızı $[m/s]$
W	Kanal genişliği $[m]$
α	Isıl yayılım katsayısı $[m^2/s]$
ρ	Akışkan yoğunluğu $[kg/m^3]$
μ	Dinamik Viskozite $[Pa.s]$
ν	Kinematik Viskozite $[m^2/s]$

GİRİŞ

Son dönemlerde artan enerji maliyetleri ve endüstrileşen dünyadaki rekabet mühendislik uygulamalarında insanları daha çok verim elde etme yoluna itmiştir. Akış uygulamalarında da daha fazla verim elde etmek için farklı parametrelerin, ısı transferine ve akış karakteristiklerine etkisinin belirlenmesi önemli bir rol oynamaktadır. Özellikle kanal içi akış uygulamalarında, doğal taşınım ve karışık taşınım son zamanlarda çok büyük bir ilgi çekmektedir. Bunun nedeni ise doğal ve karışık taşınımın sessiz ve daha güvenilir işletme olanakları sunuyor olmasıdır. Çoğu elektronik ekipmanlar, bloklanmış akışlardaki düzgün olmayan yüzeylerin ısıtılması ve çıkıntılı yüzeylerdeki akış uygulamaları doğal ve karışık konveksiyon uygulamalarına örnek olarak gösterilebilir. Kanal içi akışlarda ısı transferi ve akış karakteristikleri kanalın ve engelin geometrisi, akışkan ve engel arasındaki sıcaklık farkı ve akışkanın hızı gibi birçok parametreye bağlıdır. Kanal içi akışlarda genellikle akış bir engel veya blokla sınırlandırılmakta, bu yüzeylerden olan akış ve ısı transferi karakteristikleri detaylı bir şekilde incelenmektedir.

Bu çalışmanın amacı; engellerle sınırlandırılan kanal içi akışlarda farklı parametrelerin ısı transferine ve akış karakteristiklerine etkilerini incelemek, yeni yaklaşımlar yaparak akış uygulamalarında kullanılacak ekipmanların verimlerini arttırmak, maliyetlerini düşürmek, daha güvenli ve çevreye duyarlı ürünler yapabilmektir. Bu parametrelerin başında; akışkan tipi, akışın kısıtlandığı engelin geometrisi ve boyutları gelmektedir. Literatürde zorlanmış taşınım ve doğal taşınım ile ilgili çalışmalar yapılmış olsa da, karışık taşınım ile ısı transferinin arttırılmasına yönelik çalışmalar ve karışık taşınım farklı parametrelerin etkisinin incelendiği çalışmalar oldukça sınırlıdır.

Bu kapsamda; literatürdeki çalışmalar incelendiğinde; Adache ve Uehara (2001) çalışmalarında, ana akış yönünde periyodik olarak sıralanmış oyuklardaki basınç düşümü ve ısı transferi arasındaki ilişkiyi 2 boyutlu olarak varsayılan çeşitli kanal konfigürasyonlarıyla tam gelişmiş akış ve sıcaklık bölgelerinde incelemişlerdir. Kararlı akıştan titreşimli bölgeye geçişte ısı transferinin ve basınç düşümünün arttığını gözlemlemişlerdir. Auletta vd. (2001) dik ve simetrik olarak ısıtılmış aşağı yönlü akışın olduğu kanalda adyabatik genişlemenin etkilerini deneysel olarak inceleyen bir çalışma yapmışlardır. Sonuç olarak; kanalın uzama ve genişleme oranlarına bağlı olarak ısı transfer miktarının %10-20 oranında değiştiğini tespit etmişlerdir. Barboy vd. (2012) çalışmalarında; duvar geometrisinin, akışkan akışına ve kanaldaki ısı transferine etkilerini sabit ısı akısı bulunan dalgalı duvarın enerji kaybı ile birlikte incelemiştir. Duvardaki dalgalılık, dalga genişliği ve periyodu ile karakterize edilen değişkenlerin ısı transferini belirgin şekilde etkilediğini gözlemlemişlerdir.

Barletta ve Zanchini (1999), çalışmalarında dik bir kanaldaki referans akışkan sıcaklığı seçiminin tam gelişmiş bir akışta, karışık ısı taşınım problemi içinde çözüme etkisini sayısal olarak incelemişlerdir. Referans sıcaklığın seçiminin, hız profilleri ile basınç ve hidrostatik basınç arasındaki farkın eksenel değişikliği üzerindeki etkisi ile belirlenebileceğini ortaya koymuşlardır. Boutina ve Bessaih (2011), çalışmalarında eğimli bir kanalda ve laminar olarak incelenen bir akıştaki eş iki ısı kaynağının karışık taşınım yoluyla soğutulmasını incelemiştir. Kanalın eğiminin, ısı kaynaklarının boyutlarının ve aralarındaki mesafenin değiştirilmesinin ısı transferine önemli etkileri olduğunu belirlemişlerdir.

Du vd. (1998) çalışmalarında birbirinden ayrı ısıtıcıların bulunduğu üstü ve altı açık dik bir kanaldaki karışık ısı transferini sayısal olarak incelemişlerdir. Akışın kararlı ve laminar olduğu varsayılırken çözümler iki boyutlu olarak yapılmıştır. Giriş ve çıkışların uzunluk oranları ve kanaldaki ısıtıcıların pozisyonlarının ısı transferine ve akışa olan etkileri

incelenmiştir. Forooghi ve Hooman (2013), çalışmalarında iki dalgalı plaka arasında, kaldırma kuvvetlerinin etkisinde türbülanslı bir akıştaki ısı transferini nümerik olarak incelemişleridir. Kaldırma kuvvetinin etkisiyle oluşan akışlarda ısı transferinin belli bir noktaya kadar azalırken belli bir noktadan sonra bu durumun değiştiğini, kaldırma kuvveti etkisine ters akışlarda ise durumun farklı geliştiğini tespit etmişlerdir. Buradaki akışlarda ısı transferi ve Grashof sayısının sürekli olarak arttığını ortaya koymuşlardır. Hamouche ve Bessaih (2009), çalışmalarında yatay bir kanalda ve laminar bir akışta iki elektronik parçanın temsili olarak konulan çıkıntılı iki ısı kaynağının hava ile soğutulmasındaki karışık ısı taşınımını sayısal olarak ele almışlardır. Yapılan çözümlerde; elektronik parçaların birbirlerine olan uzaklıklarının, genişliklerinin ve yüksekliklerinin değiştiğinde ısı transferinin artırılabilirdiği belirlenmiştir.

Herman ve Kang (2002), çalışmalarında oyuklu bir kanal içinde eğimli kanatçıklar kullanılarak karasız sıcaklık alanları ile yalın kanatçiksız oluklu kanalları karşılaştırmışlardır. Kararlı akıştan titreşimli akışa geçişin çoğunlukla $Re = 450$ civarında oluştuğunu gözlemlemişlerdir. Ayrıca; oyuklu kanatçıklı bir kanalda, yalın oyuklu kanala göre ısı transferinin 1,5-3,5 kat daha fazla olduğu, basınç düşümünün ise 3-5 kat arası daha fazla olduğu belirlenmiştir. Jang ve Yan (2004), çalışmalarında dik ve dalgalı bir yüzeydeki karışık ısı taşınımını ve kütle transferini sayısal olarak inceleyen bir çalışma yapmışlardır. Dalgalı yüzey üniform duvar sıcaklığı ve sabit duvar konsantrasyonu ile korunurken bu çevre şartlarından daha yüksek bir değerdir.

Lakkis ve Moukalled (2008), çalışmalarında izotermal olarak ısıtılmış bir kanalın konveks yüzeylerindeki laminar doğal konveksiyonu incelemişlerdir. Sonuç olarak; eğriliğin en küçük derecesindeki hesaplarda bütün Grashof değerlerinde kanalın çıkış bölümünde resirkülasyon alanları gözlemlemişlerdir. Eğrilik derecesi arttıkça Grashof değerleri ve resirkülasyon oluşumunda bir artış tespit etmişlerdir. Asimetrik dalgalı kanaldaki ve laminar akıştaki ısı transferinin artırılmasını sayısal olarak inceleyen bir çalışma Mills vd. (2016) tarafından yapılmıştır. Duvarın dalga periyodu ve genişliğinin basınç ve ısı transferi üzerindeki etkileri, kararlı ve kararsız akışlarda incelenmiştir. Sonuç olarak; akım oranlarının düşük olduğu kararlı rejimlerde ısı transferinin zenginliği duvarın dalgalılık büyüklüğüne bağlı iken, akım oranı arttığında ve kararsız rejime geçişte daha çok basınç düşümüne bağlı olduğu belirlenmiştir. Bu durumun, düz kanallarla karşılaştırıldığında Reynolds sayısının %50 daha az olduğu durumlarda bile daha fazla ısı transferi sağladığını tespit etmişlerdir. Moukalled vd. (2000) eğimli yüzeylerin ısıtıldığı ve duvarların adyabatik olarak sınırlandırıldığı dik bir kanaldaki

karışık ısı taşınımını sayısal olarak inceleyen bir çalışma yapmışlardır. Konveks yüzeyin ısıtıldığı kanalda kesit alanı artarken, akış hızının azaldığı ve buna bağlı olarak kaldırma kuvvetinin arttığı, ısıtılan yüzeylerin yakınlarda düşük Richardson sayıları görülürken karşı dik duvarda yüksek Ri sayıları olduğunu belirlemişlerdir.

Oztop (2005) çalışmasında eğrisel olarak şekillendirilmiş borudaki akışı ve ısı transferini sayısal olarak inceleyen bir çalışma yapmıştır. Akış geometrisinin ısı transferini ve akış karakteristiğini önemli ölçüde etkilediği tespit etmiştir. Rao ve Narasimham (2007) çalışmalarında yatay ve dik bir kanalda, tabaka üzerinde birbirine yatay olarak sıralanmış ısı üretimi olan parçalardan oluşan duvarın ortaya çıkardığı bileşik karışık konveksiyonu sayısal olarak irdelemişlerdir. Akışkandan iletim yoluyla tabakaya geçen ısı transferinin %41-%47 oranında arttığını tespit etmişlerdir. Singh vd. (2016) çalışmalarında bir ısı değiştiricide kıvrımlı iki plaka arasındaki ısı transferini deneysel olarak incelemişlerdir. Elde ettikleri sonuçlardan, Nusselt sayısı ve Reynolds sayısı arasında yeni korelasyonlar oluşturmuşlardır. Tanda (2004) çalışmasında tekrar edilen engellerin kullanıldığı bir ısı değiştiricide türbülans ile birlikte ısı transferinin iyileştirilmesini deneysel olarak incelemiştir. Çalışmasında yerel ısı transferi katsayıları türbülanslı akış rejimi için farklı engel şekilleri ve engelsiz durumlar açısından karşılaştırmıştır.

Kılıç ve Başkaya (2017) çalışmalarında sabit ısı akılı yüzeyde ısı transferinin, farklı geometride akış yönlendiriciler ve çarpan akışkan jetin birlikte kullanılması sonucu iyileştirilmesini sayısal olarak incelemişlerdir. Çalışmada, akış yönlendirici kullanılarak ve kullanılmayarak kanal içindeki akış ve ısı transferi farklı Reynolds sayıları ve kanal yüksekliği jet hidrolik çapı (H/D_h) oranları için incelenmiştir. Sonuç olarak; çarpan akışkan jet ile farklı geometride akış yönlendiricilerin birlikte kullanılarak; ısı transferinde akış yönlendirici kullanılmaması durumuna göre %28'e kadar bir artış sağlanabildiğini gözlemlemişlerdir. Re sayısının artması ile ısı transferinin artış gösterdiği tespit edilmiştir. Çarpan akışkan jetlerin akış yönlendiricilerle ve kanatçıklı yüzeylerle kullanılması diğer önemli ısı transferini artırma yöntemleridir (Çalışır vd., 2017).

Wahba (2011) çalışmasında akışın dik olarak yönlendirildiği bir kanalda ani genişlemenin akış yapısındaki ve ısıtma soğutma üzerindeki etkilerini sayısal olarak inceleyen bir çalışma yapmıştır. Çalışmasında, simetrik olarak ısıtılan kanalda duvarın yakınlardan akış ayrılırken merkezde ters bir akış yapısı oluştuğu, simetrik soğutmada ise dalgalı bir yapı oluşurken ısı transferi jet etkisiyle önemli bir şekilde arttığını tespit etmiştir. Wang ve Vanka (1995)

çalışmalarında periyodik olarak sıralanmış dalgalı bir kanalda akışın ısı transferi düzeylerini sayısal bir çalışma ile incelemiştir. Rosas vd. (2017) çalışmalarında; dik bir kanalda bir tarafı adyabatik ve izole edilmiş bir duvar ile sınırlandırılan diğer tarafında ise belli bir ısı akısına sahip yarı silindirik bir engel bulunan sistemdeki karışık konveksiyon ile elde edilen ısı transferini deneysel olarak incelemiştir. Sonuçlarında, yerel sıcaklık dağılımlarını yarı silindirik engelin açıl pozisyonlarına göre ve kanal içindeki uzunlukları boyunca gösterirken onların 3D vorteks yapılarla ilişkileri ve engele yakın yerdeki gelişimlerini incelemiştir.

Kilic vd. (2017) tek bir çarpan jet ve akış yönlendiriciler kullanarak, elektronik sistemlerden olan ısı transferinin iyileştirilmesini hem deneysel hem de sayısal olarak incelemiştir. Farklı Re sayıları, farklı ısı akıları, farklı jet-çarpma noktası uzaklıkları çalışmada kullanılan parametrelerdir. Sonuç olarak yerel ve ortalama Nu sayıları, akış yönlendiriciler arası mesafe, jet hidrolik çapı-çarpma noktası uzaklığı oranı ve akış yönlendirici yüksekliği-kanal yüksekliği oranının bir fonksiyonu olarak elde edilmiştir. Isı transferinin, akış yönlendiricilerin uzunluğu, konumu ve açıl pozisyonlarına göre hassas bir şekilde değiştiğini görmüşlerdir. Young ve Vafai (1999), çalışmalarında zorlanmış taşınım ile ısı transferinin sayısal olarak incelemiştir. Kanal içinde sıkıştırılmaz akış ile birlikte tek duvara sıralanmış ve ısıtılmış engeller akış geometrisini oluşturmuştur. Engellerin yüksekliği, genişliği, aralarındaki boşluklar, sayıları, ısı iletim katsayıları, ısıtılma metotları ve akışkanın akım oranının değiştirilmesinin ısı transferine etkilerini irdelemiştir.

Young ve Vafai (1998) çalışmalarında bir kanaldaki ısıtılmış engellerin taşınım ile soğutulmasını sayısal olarak incelemiştir. Engel yüksekliğinin, genişliğinin, ısı iletkenliğinin, akış özelliklerinin ısı transferini önemli ölçüde etkilediğini tespit etmişlerdir. Özdemir (2018) dik ve içerisinde ısı akısına sahip yarı silindirik engeller bulunan bir kanaldaki karışık konveksiyonu sayısal olarak incelemiştir. Kanal içerisindeki engellerin konumlarının ve geometrilerinin karışık konveksiyonla olan ısı transferini önemli ölçüde etkilediğinin belirlemiştir.

Yukarıdaki sunulan ayrıntılı çalışmalardan görüldüğü gibi literatürde sunulan çalışmalarda akışkan olarak genellikle hava ve diğer akışkanlar kullanılırken suyun çok az çalışmada analiz edildiği görülmüştür. Bu çalışmada; literatürde fazla örneği olmayan su kullanılmıştır. Akışkan olarak suyun kullanılması hem kolay bulunabilen bir akışkan olması hem de çevreye zarar vermemesi sebebiyle tercih edilmiştir. Ayrıca incelenen sayısal çalışmalarda genellikle zorlanmış

veya doğal konveksiyon incelenirken karışık konveksiyonun çok irdelenmediği görülmüştür.

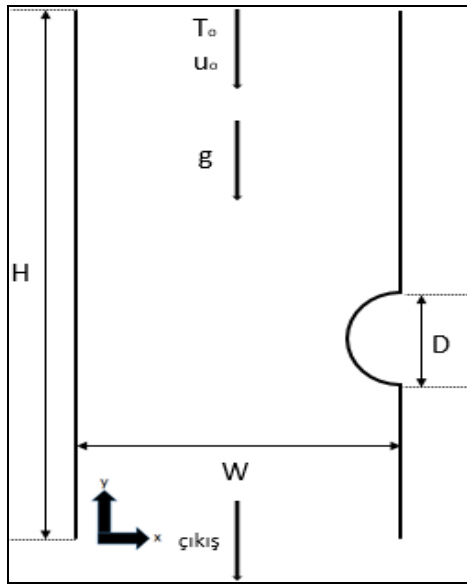
Çalışmamızda karışık konveksiyon incelenmiş ve karışık konveksiyonun avantajlarından yararlanılabilmesi öngörülmüştür. Bunun yanı sıra; literatürdeki çalışmalar incelenirken genellikle Reynolds ve Grashof sayılarının belli değerlerinin ısı transferi ve akış dinamikleri üzerindeki etkileri incelenirken Richardson sayısının etkilerinin incelenmediği görülmüştür. Bu çalışmada; Richardson sayısındaki değişimin ısı transferine olan etkileri incelenmiştir. Ayrıca literatürde kanal genişliklerinin, engellerin boyutlarının ısı transferine olan etkileri detaylı olarak incelenmemiştir. Bu çalışmada; tanımlı uzunlukların değiştirilmesi ile ilgili parametrik çalışmalar yapılarak ısı transferine etkileri detaylı bir şekilde incelenmiştir. Literatürdeki çalışmalarda; Reynolds sayıları genellikle 2300-25900 arasında zorlanmış taşınımın etkin olduğu çalışmalar incelenirken, bizim çalışmamızda Reynolds sayıları 100-200 arasında alınarak karışık konveksiyonun etkilerinin yoğun olduğu bir çalışma ele alınmıştır. Ayrıca literatürdeki çalışmalarda Grashof sayısı 10-1000 aralığında incelenirken bizim çalışmamız kapsamında 10^3 - 10^7 aralığında incelenmiştir. Grashof sayısının bu aralıkta incelenmesiyle kaldırma kuvvetlerinin, akış dinamikleri ve ısı transferi üzerindeki etkilerinin detaylı bir şekilde incelenmesi amaçlanmıştır.

SAYISAL MODEL VE MATEMATİKSEL FORMÜLASYON

Bu bölümde, oluşturulan sayısal model, korunum denklemleri ve sınır şartları sunulmuştur. Bu çalışmada bir sayısal akışkanlar dinamiği (SAD) kodu olan FloEFD paket programı kullanılmıştır. FloEFD, kütle, momentum ve enerji korunumu denklemlerini ihtiva eden Navier-Stokes denklemlerini çözmektedir. Bu denklemler, akışkanın özelliğini tanımlayan hal denklemleri ile desteklenmektedir. FloEFD, verilen sınır şartlarını kullanıp gerekli korunum denklemlerini sonlu hacimler yöntemini kullanarak çözmektedir. Şekil 1'de sayısal çalışma kapsamında incelenmiş olan sayısal model yer almaktadır (Özdemir, 2018). Dik bir kanalda, bir tarafında yarı silindirik engelin bulunduğu, diğer taraflarının ise adyabatik bir duvar ile sınırlandırıldığı, yarı silindirik engelin ise ısı akısına sahip olduğu sayısal modeldeki karışık konveksiyon incelenmiştir. Analiz edilen modelde farklı Reynolds ve Richardson sayılarındaki ısı transferi ve akış karakteristikleri incelenmiştir. Sayısal modelde akışkan olarak su kullanılmıştır. Kanaldaki akış $Pr=7$ sayısında analiz edilmiş olup akış laminar olarak kabul edilmiştir. Su kanalın üst noktasından belli bir hız ile giriş yapmakta ve yer çekimi etkisiyle hareket etmektedir. Akışkanın giriş sıcaklığı $T_0 = 20^\circ\text{C}$ 'dir. Akışkanın giriş sıcaklığı referans sıcaklıktır ve sabit

olarak alınmıştır. Akışkanın giriş hızı u_0 olarak gösterilmiştir.

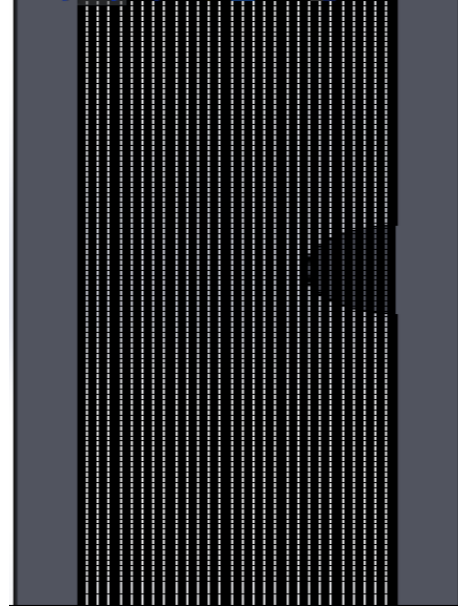
Yarı silindirik engellerden üstteki engel kanalın girişinden itibaren 1m alta konumlandırılmıştır. Kanalın genişliği $W=0,05$ m'dir. Kanalın uzunluğu $H=1,8$ m'dir. Kanaldaki yarı silindirik engelin çapı D olarak gösterilmiştir. Akış oranı (engelin yarıçapının kanal genişliğine oranı) BR olarak gösterilmiştir. Hesaplanan model iki boyutlu olarak incelenmiştir. Problemin sayısal çözümünde x-y koordinat sistemi kullanılmıştır. Her bir parametrenin değişiminin ısı transferine ve akış dinamiklerine olan etkisi incelenmiştir.



Şekil 1. HAD model geometrisi

Sayısal modelde kullanılan hücre yapısı Şekil 2'de sunulmuştur (Özdemir, 2018). Yarı silindirik akış yönlendiriciye yakın yerlerdeki hız ve sıcaklık dağılımlarını daha iyi görmek için bu bölgelere daha yoğun hücre oluşturulmuştur. Bunun sebebi; akış yönlendiriciye yakın yerdeki ısı transferi ve akış değişimlerinin daha fazla olmasıdır.

Sayısal çalışma kapsamında iki boyutlu, sürekli, laminar, sıkıştırılamaz akış incelenmiştir. Çalışmada yer çekimi kuvveti aşağı yönlü olarak modellenmiş ve kaldırma kuvvetlerinin etkisi sayısal çalışmada hesaba katılmıştır.



Şekil 2. Hücre yapısı

Kartezyen koordinatlarda kararlı halde sıkıştırılamaz akışlar için süreklilik, x ve y yönlerindeki momentum ve enerjinin korunum denklemleri aşağıda verilmiştir.

$$\frac{\partial u}{\partial x} + \frac{\partial v}{\partial y} = 0 \quad (1)$$

$$\rho \left(u \frac{\partial u}{\partial x} + v \frac{\partial u}{\partial y} \right) = -\frac{\partial P}{\partial x} + \mu \nabla^2 u \quad (2)$$

$$\rho \left(u \frac{\partial v}{\partial x} + v \frac{\partial v}{\partial y} \right) = -\frac{\partial P}{\partial y} + \mu \nabla^2 v - \rho g \quad (3)$$

$$u \frac{\partial T}{\partial x} + v \frac{\partial T}{\partial y} = \alpha \left[\frac{\partial^2 T}{\partial x^2} + \frac{\partial^2 T}{\partial y^2} \right] \quad (4)$$

Sayısal modelin karşılaştırılmasında kullanılan boyutsuz sayılardan, değiştirilmiş Grashof sayısı Eş. 5'te sunulmuştur.

$$Gr^* = \frac{g \beta q D^4}{k \nu^2} \quad (5)$$

Değiştirilmiş Richardson sayısı aşağıdaki eşitlikte gösterilmiştir.

$$Ri^* = \frac{Gr^*}{Re^2} \quad (6)$$

Reynolds sayısı Eş. 7 ile hesaplanmıştır.

$$Re = \frac{u_0 D}{\nu} \quad (7)$$

Prandtl sayısı Eş. 8'de sunulmuştur.

$$Pr = \frac{\nu}{\alpha} \quad (8)$$

Nusselt sayısı ise aşağıdaki denklemden hesaplanmıştır:

$$Nu = \frac{qD}{k(T_w - T_o)} \quad (9)$$

Burada q ısı akısı, T_w yarı silindirik engelin ortalama sıcaklığı, k ısı iletim katsayısı ve D yarı silindirik akış yönlendiricinin çapıdır. Duvarlarda kayma gerilmesi ve hız sıfır olarak alınmıştır. Akış yönlendiricilerde sabit ısı akısı uygulanmıştır. Problemdede akış dinamikleri ve ısı transferi sürekli akış koşullarında çözümlenmiştir. Radyasyon etkisi dikkate alınmamıştır. Kanal girişindeki suyun sıcaklığı $T_o=20^\circ\text{C}$ olarak alınmıştır. Problemin çözülmesinde uygulanacak sınır şartları Tablo 1’de sunulmuştur (Özdemir, 2018).

Tablo 1. Sınır Şartları

	u	v	T
Giriş	$u = 0$	$v = u_o$	$T = T_o$
Duvar	$u = 0$	$v = 0$	$\partial T / \partial n = 0$
Akış yönlendirici	$u = 0$	$v = 0$	$q'' = \text{ısı akısı}$
Çıkış	$\partial u / \partial y = 0$	$\partial v / \partial y = 0$	$\partial T / \partial y = 0$

SAYISAL SONUÇLARIN DOĞRULANMASI

Bu bölümde FloEFD yazılımı ile gerçekleştirilen sayısal çalışmanın referans olarak alınan çalışmayla karşılaştırılması ve doğrulanması yapılmıştır. Referans olarak Rosas vd. (2017) çalışması alınmıştır. Yazılımda korunum denklemleri sonlu hacimler yöntemine dayalı bir sayısal yöntem ile çözdürülmektedir. Yazılımda kartezyen koordinatlar kullanılmaktadır. Kontrol hacimleri (hücre yapıları) dikdörtgen paralel yüzüldür. Geometri sınırlarında kartezyen “cut cell” yaklaşımı kullanılmaktadır. Bu yaklaşıma göre, sınır yüzeylerine yakın hücreler geometriyi kesmektedir. Dolayısıyla, sınıra yakın hücreler çokgendirler ve gelişigüzel yönde yüzeylere sahiptirler. Bu nedenle, FloEFD dikdörtgen hücrelerin avantajları ile yüksek doğruluğa sahip geometri sınır hücrelerini birleştirmektedir. Bununla birlikte, yerel sıkılaştırmalar yapılarak geometrik ve nümerik çözüm özellikleri dikkate alınmaktadır. Bu genelde, katı/akışkan ara yüzeylerinde, yüksek gradyanlar söz konusu olduğunda, vb. durumlarda kullanılmaktadır. Tüm fiziksel parametreler hücre merkezlerinde depolanmaktadır. Kontrol hacmi yaklaşımı bir önceki bölümde sunulan korunum denklemlerini cebrik ayrıklaştırılmış denklemlere dönüştürmekte ve denklemlerin iteratif olarak çözümü gerçekleştirilmektedir. Uzaysal türevler implicit sonlu fark operatörleri ile ikinci mertebe doğrulukta elde edilmektedir. Zamansal türevler ise implicit birinci mertebe doğrulukta Euler tekniği ile elde edilmektedir. Konvektif akılar için upwind yaklaşımı kullanılmaktadır. Difüzyon terimleri için merkezi farklar yöntemi kullanılmaktadır. Süreklilik ve konveksiyon/difüzyon denklemleri için time-implicit yaklaşımı ile operatör ayrıklaştırma tekniği ile birlikte kullanılmaktadır. Bu yöntem ile basınç-hız bağlantısı

çözümü mümkün hale gelmektedir. Bu işlemi SIMPLE benzeri bir yaklaşımı izleyerek, cebrik işlemler ile eliptik tip ayrık basınç denklemi elde edilmektedir. Çözümlerde öncelikle çözümün doğruluğu araştırılmıştır. Artık değerlerin süreklilik, momentum ve enerji için 10^{-3} oranından daha düşük olması durumunda çözümün yakınsadığı kabul edilmiştir. Tablo 2’de; sayısal çalışma sonuçları giriş ve çıkış bölgesindeki kütle ve enerji değerleri olarak sunulmuş ve fark değeri belirlenmiştir. Kütle ve enerji korunum denklemlerinin sağlandığı ve sonuçların yakınsadığı görülmüştür.

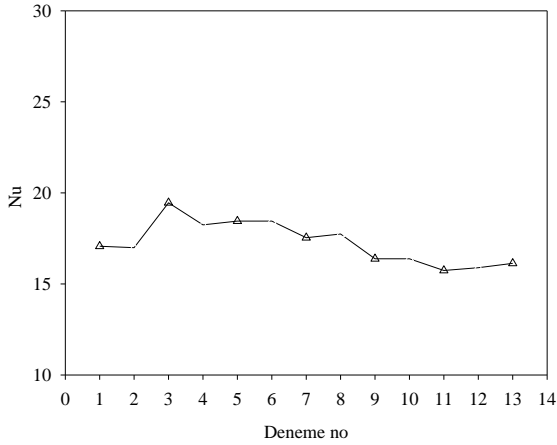
Tablo 2. Sayısal çözümde kütle ve enerjinin korunumu

Hedef	Birim	Kanal Girişi	Kanal Çıkışı	Fark	Yakınsama
Kütle	kg/s	0,0018	0,0018	0	Evet
Enerji	W	2171,521	2171,812	0,291	Evet

Çözümün doğruluğunun araştırılması kapsamında gerçekleştirilen bir diğer çalışma çözümünün hücre sayısından bağımsızlaştırılmasıdır. Bu kapsamda; x ve y koordinat sistemlerinde olmak üzere, $30 \times 145 - 140 \times 475$ aralığında 13 farklı hücre yapısı oluşturulmuş ve bu hücre sayılarında simülasyonlar gerçekleştirilmiş ve çözümlerin hücre sayılarından bağımsız hale getirilmesi sağlanmıştır. Tablo 3’te her deneme için oluşturulan hücre sayısı ve Şekil 3’te Nusselt sayısının hücre sayısı ile değişimi sunulmuştur. Şekil 3’de Nusselt sayısının hücre sayısı ile değişimi sunulmuştur (Özdemir, 2018). Çözüm; 12 numaralı hücre sayısı olan 120×415 ’den sonra yaklaşık olarak sabit hale gelmekte ve hücre sayısından bağımsızlaşmaktadır. Bu nedenle, 120×415 hücre sayısı tüm çözümlerde kullanılmıştır.

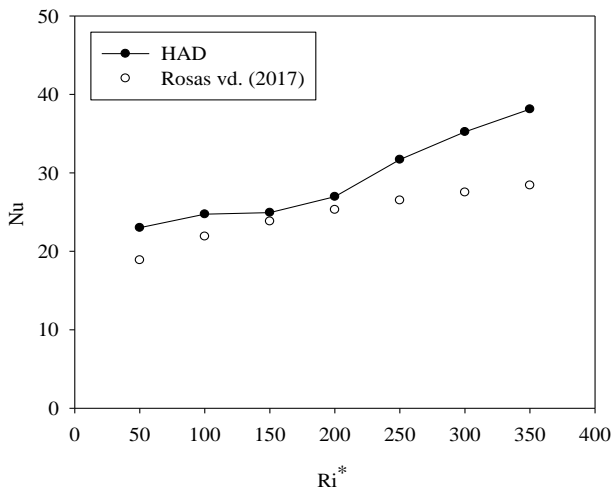
Tablo 3. Her deneme için oluşturulan hücre sayısı

Deneme	x hücre sayısı	y hücre sayısı	Toplam hücre sayısı
1	30	145	4350
2	40	175	7000
3	50	205	10250
4	60	235	14100
5	65	250	16250
6	70	265	18550
7	80	295	23600
8	90	325	29250
9	100	355	35500
10	110	385	42350
11	120	415	49800
12	130	445	57850
13	140	475	66500



Şekil 3. Hücre sayısından bağımsızlaştırma

Sayısal çalışma sonuçları; literatürde yer alan Rosas vd. (2017) deneysel çalışması ile de karşılaştırılmıştır. Şekil 4'te sayısal sonuçlar, deneysel sonuçlarla karşılaştırılmış ve deney sonuçları ile model sonuçları arasındaki farkın ($Ri=50-200$ aralığında) %4,4 ile %17,9 aralığında değiştiği belirlenmiştir. Sayısal sonuçlarla, deneysel sonuçlar arasındaki farkın daha az olduğu aralıkta çalışmak amacıyla; geometrinin daha az karmaşık olduğu 1.nci parametrede (alt alta iki engelin bulunduğu) Ri sayısı $Ri=50-300$ aralığında alınırken, daha fazla engelin bulunduğu (alt alta ve karşılıklı 4 engel) kısmen daha karmaşık geometrilere sahip diğer parametrelerde Ri sayısı $Ri=50-200$ aralığında alınmıştır (Özdemir, 2018).



Şekil 4. Model sonuçlarının deney sonuçları ile karşılaştırılması

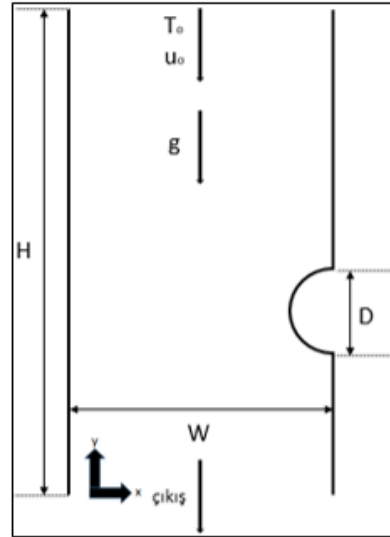
BULGULAR VE TARTIŞMA

Bu bölümde sayısal sonuçlar üç başlık altında incelenmiştir:

- Tek yarı silindirik engel bulunan kanaldaki karışık konveksiyonun incelenmesi
- Alt alta bulunan iki yarı silindirik engeldeki karışık konveksiyonun incelenmesi
- Karşılıklı bulunan iki yarı silindirik engeldeki karışık konveksiyonun incelenmesi

Tek yarı silindirik engel bulunan kanaldaki karışık konveksiyonun incelenmesi

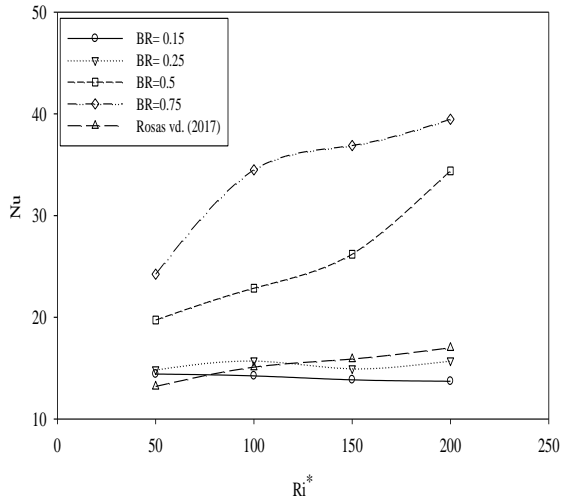
Dik ve içerisinde ısı akısına sahip yarı silindirik bir engel bulunan kanaldaki karışık konveksiyonun incelendiği problemin şematik gösterimi Şekil 5'te gösterilmiştir. Yarı silindirik engelin çapı D olarak gösterilmiştir ve sabit ısı akısına sahip olduğu kabulü yapılmıştır. Kanalın girişindeki suyun sıcaklığı $T_o=20^\circ\text{C}$ olarak alınmıştır. Kanalın genişliği sabit ve W olarak, kanalın uzunluğu ise sabit ve H olarak gösterilmektedir. Bu parametrenin birinci aşamasında BR oranlarının (engel çapının kanal genişliğine oranı (D/W)) değiştirilmesinin, farklı Richardson (Ri) sayılarında, Nu sayısına olan etkileri incelenmiştir. Kanal genişliği sabit tutularak, yarı silindirik engelin çapı değiştirilmiştir. Çalışmada; su, kanalın girişinden belli bir u_o hızıyla girmekte ve yerçekiminin etkisiyle hareket etmektedir.



Şekil 5. Tek yarı silindirik engelin geometrik gösterimi

Şekil 6'da BR oranının değiştirilmesinin, $Re=100$ için Nusselt sayısına olan etkisi gösterilmektedir. Sonuç olarak; BR oranının artırılmasının ısı transferini arttırdığı görülmüştür. Yarı silindirik engelin çapının artırılmasıyla birlikte, yüzey alanının artması ve engelle daha fazla akışkanın temas etmesi sonucunda ısı transferinin arttığı gözlemlenmiştir. $BR=0,15$ değerinde; engelin kanal içerisindeki yüzey alanı çok küçük olduğundan, kaldırma kuvvetleri etkisi arttırıldığında bile (Ri sayısının değerinde artış olmasına rağmen) Nu sayısında belirgin bir artış olmadığı görülmüştür. $BR=0,15$ değerinden $0,75$ değerine yükseltildiğinde; Ri sayısı arttırıldığında ($Ri=50$ 'den $Ri=200$ değerine) ortalama Nu sayısındaki artışın %1 değerinden %58,3 değerine arttığı belirlenmiştir. Hız ve basıncın ise engelin çapının artmasıyla ters orantılı olarak, azaldığı gözlemlenmiştir. Ayrıca elde edilen sonuçlar, grafikte

Rosas ve arkadaşlarının (2017) deneysel çalışma sonuçları ile karşılaştırılmış (Rosas ve arkadaşlarının deneysel çalışmasında BR= 0,285 olarak alınmıştır.) ve oldukça uyumlu olduğu görülmüştür.

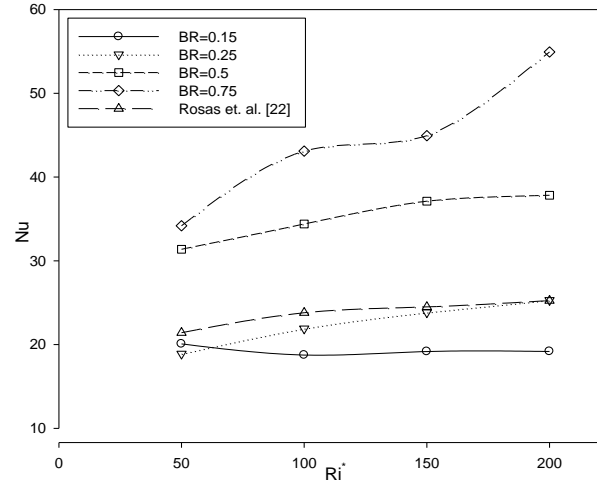


Şekil 6. Nu sayısının farklı Ri sayısı ve farklı BR değerlerine göre, Re=100, W=0,05 m

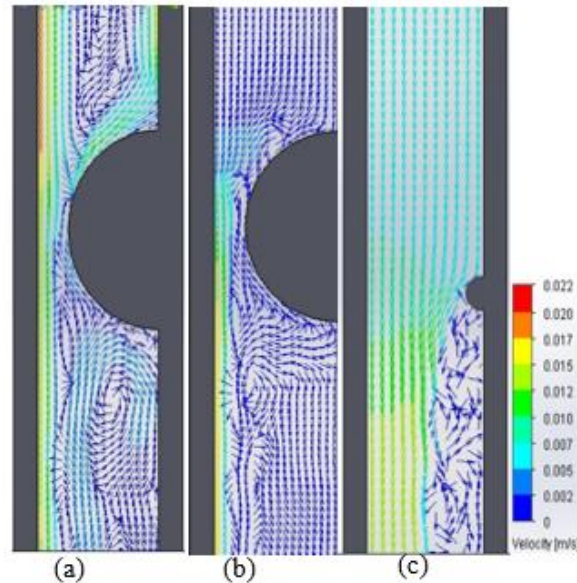
Bu parametrenin ikinci aşamasında Re sayısının etkisinin görülebilmesi amacıyla, Şekil 7’de Nusselt sayısının BR oranına göre değişimi, Re=200 için incelenmiştir. Yarı silindirik engelin çapının artırılmasıyla birlikte yüzey alanı artmış, engelle temas eden akışkan hızının artması ile hidrodinamik sınır tabaka artmış ve ısıl sınır tabakanın azalmasına bağlı olarak ısı transferi artmıştır. Kanal içerisinde akan akışkanın hız ve basıncının ise engelin çapının artmasıyla ters orantılı olarak azaldığı gözlemlenmiştir. Re sayısı artırıldığında; Nu sayısındaki artış düşük Ri sayılarında, yüksek Ri sayılarına göre daha az gerçekleşmiştir. Bunun sebebi; çalışılan geometride yerçekimi etkisiyle oluşan zorlanmış taşınım ile ısı transferi, doğal taşınım ile oluşan ısı transferine azaltıcı (negatif) bir etkiye sahiptir. Zorlanmış taşınım bu geometride doğal taşınımı azaltıcı yönde etkilemektedir. Dolayısıyla; düşük Ri sayılarında zorlanmış taşınımın Nu sayısını azaltıcı etkisi daha fazla olurken, yüksek Ri sayılarında (Ri= 150-200), Gr sayısındaki artışa bağlı olarak, zorlanmış taşınımın azaltıcı etkisi daha az oluşmaktadır.

Şekil 8’de BR oranının ve değiştirilmiş Richardson sayısının vektörel hız dağılımı üzerindeki etkisi gösterilmektedir. BR oranının artması ile yüzey alanı artmakta ve bu durumda akışkanın engele daha fazla teması sağlanmakta ve ısı transferi artmaktadır. Değiştirilmiş Richardson sayısının artırılması ile özellikle akışkan hızının azaldığı engelin üst bölgesinde ve engelin alt bölgesinde daha belirgin şekilde kaldırma kuvvetlerinin etkisi ile girdaplar oluştuğu tespit edilmiştir. Girdap oluşumunun artması ile yüzeye yakın bölgelerde, ısıl sınır tabaka kalınlığı azalmakta ve ısı transferi artmaktadır. Sabit Reynolds

sayısında değiştirilmiş Richardson sayısı Grashof sayısı ile doğru orantılıdır. Değiştirilmiş Richardson sayısının artması, doğal taşınımı arttırdığından (Grashof sayısının artması) sonuç olarak ısı transferini arttırmaktadır.



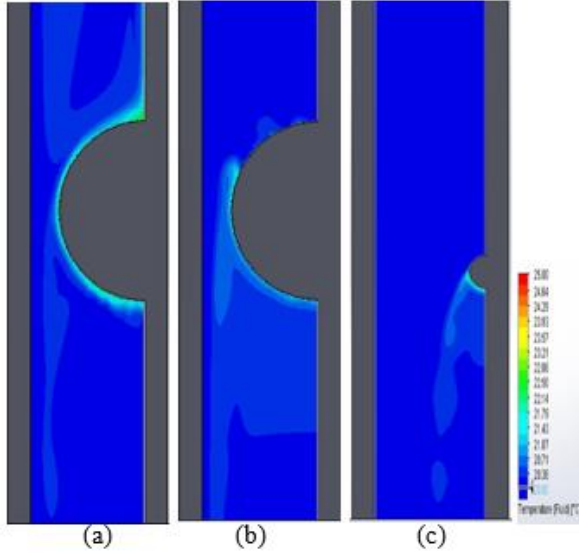
Şekil 7. Nu sayısının Ri sayısı ve farklı BR değerlerine göre, Re=200, W=0,05 m



Şekil 8. Vektörel hız dağılımı, Re=100 (a) BR=0,75, Ri=200, (b) BR=0,75, Ri=50, (c) BR=0,15, Ri=200

Doğal taşınımın etkisinin bir göstergesi olan Grashof sayısının, karışık konveksiyonun etkilerinin incelendiği bu çalışmada, doğal konveksiyonun Re=100 değerinde zorlanmış taşınımına oranla daha etkin olduğu belirlenmiştir. BR oranının azalmasının (BR=0,15’de), yer çekimi yönünde zorlanmış taşınımına bağlı olarak oluşan akışkan hızının arttığı, kaldırma kuvvetlerinin etkisi ile engel yüzeyine yakın bölgelerde oluşan vortekslerin azaldığı ve zorlanmış taşınım etkilerinin, doğal taşınım etkilerine daha baskın geldiği görülmüştür. Şekil 9’da BR oranlarının ve değiştirilmiş Richardson sayısının, sıcaklık konturu dağılımı üzerine etkisi gösterilmiştir. Re=100 için, BR oranının artması, yüzey alanını artırarak ısı transferini arttırmıştır.

Düşük BR oranlarında ($BR=0,15$) yer çekimi yönünde zorlanmış taşınımaya bağlı akışkan hızı arttığı engelin üst bölgesinde ısı sınır tabakanın azalmasına bağlı ısı transferi artmış, hızın azaldığı engelin alt bölgelerinde ise, ısı sınır tabaka kalınlaşmış ve ısı transferi azalmıştır. Yüksek BR oranlarında ise ($BR=0,75$), engelin duvara bağlantı noktasına yakın olan alt ve üst bölgelerde, hızın azalmasına bağlı olarak, ısı sınır tabaka kalınlaşmış ve ısı transferi azalmıştır. Bu bölgelerde, zorlanmış taşınımaya negatif bir etki gösteren doğal taşınım etkisi daha belirgin olarak görülebilmektedir.



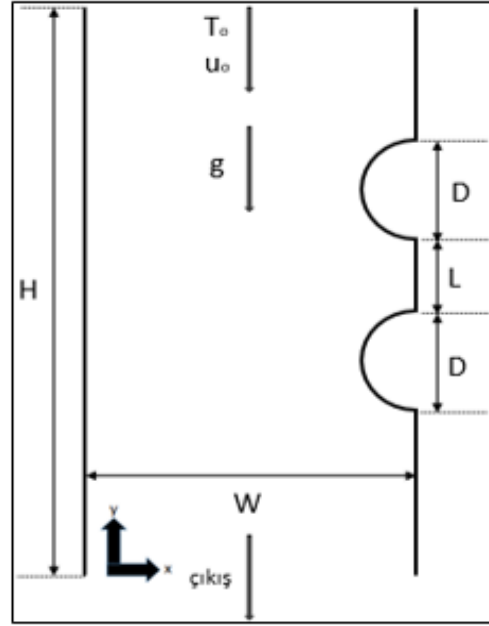
Şekil 9. Sıcaklık konturu dağılımı, $Re=100$ (a) $BR=0,75$, $Ri=200$, (b) $BR=0,75$, $Ri=50$, (c) $BR=0,15$, $Ri=200$

Değiştirilmiş Richardson sayısındaki artış ise; doğal taşınım etkilerinin zorlanmış taşınım etkilerine göre daha belirgin şekilde ortaya çıkmasına sebep olmuş ve bu ısı transferini azaltıcı etki özellikle engelin üst ve alt bölgesinde (akışkan hızını azaldığı bölgelerde) ısı sınır tabakanın artışına sebep olmuştur.

Alt alta bulunan iki yarı silindirik engeldeki karışık taşınımın incelenmesi

Bu bölümde; dik ve iki tarafı adyabatik duvarlarla sınırlandırılmış ve yüzeyinde ısı akışı olan, alt alta bulunan iki yarı silindirik engelin bulunduğu bir kanaldaki ısı transferine ve akış dinamiklerine farklı parametrelerin etkisi incelenmiştir. İncelenen problemin şematik gösterimi Şekil 10'da sunulmuştur. Yarı silindirik engeller aynı çaptadır ve çapları D olarak gösterilmektedir. Yarı silindirik engellere sabit ısı akışı verilmektedir. Kanal girişindeki akışkanın sıcaklığı sabit $T_o=20^\circ C$ 'dir. Engellerin birbirine olan uzaklıkları L , kanalın genişliği W , kanalın uzunluğu H , engellerin birbirine uzaklığının kanal çapına oranı (L/D) olarak gösterilmiştir. Bu bölümde $Re=200$ için, $BR=0,5$ değerinde L/D oranının ve Ri sayısının değiştirilmesinin Nusselt sayısına olan etkisi incelenmiştir. Çalışmada, akışkan kanalın girişinden

belli bir u_o hızıyla girmekte ve yerçekiminin etkisiyle hareket etmektedir. Dolayısıyla; zorlanmış taşınım etkileri, doğal taşınım etkileri ile ters yönde bir etkiye sahiptir.

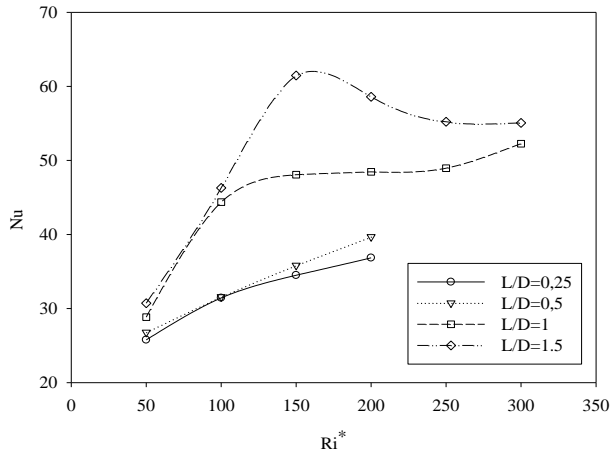


Şekil 10. İki yarı silindirik engelin kanal geometrisi

Üst engel için Nusselt sayısının farklı L/D oranına ve farklı Ri sayılarına göre değişimi, Şekil. 11'de sunulmuştur. Sonuç olarak; Nusselt sayısının engellerin birbirine olan uzaklıkları yani L/D oranlarının artmasıyla birlikte arttığı görülmüştür. $L/D=0,25-0,5$ aralığında engellerin birbirine çok yakın olması sebebiyle, zorlanmış taşınımından kaynaklanan akışkan hareketi engeller arası bölgede yavaşlamaktadır. Bu durum kaldırma kuvvetleri etkisi ile oluşan doğal taşınım etkilerinin (yüzeğe yakın bölgelerde yer çekiminin tersi yönünde oluşan vorteksler) daha belirgin şekilde oluşmasına sebep olmaktadır. Bunun sonucu olarak, engeller arası bölgede hapis olan ve hızı yavaşlayan akışkanın, ısınan akışkanı yüzeyden uzaklaştıramadığı (daha soğuk akışkanın yüzeye yakın bölgedeki daha sıcak akışkanın yerine geçemediğinden), dolayısı ile bu bölgede ısı transferinin artışına sebep olduğu belirlenmiştir. Bu durum Ri sayısı arttıkça Gr sayısının artışına bağlı olarak, Nu sayısının da artmasına sebep olmaktadır. Bu aralıkta $Ri=150$ değerine kadar L/D oranındaki artış Nu sayısında belirgin bir artışa sebep olmaz iken, $Ri=200$ değerinden sonra kaldırma kuvvetlerinin etkisi daha da belirginleşmekte ve Nu sayısı artmaktadır.

$L/D=0,5-1$ aralığında engellerin arasındaki mesafenin artışına bağlı olarak, düşük Ri sayılarında ($Ri=50-150$ aralığında) hem yerçekimi yönündeki zorlanmış taşınım etkileri hem de yerçekiminin aksi yönünde oluşan kaldırma kuvvetlerinin etkisi sebebiyle engellerin arasında oluşan girdapların büyümesine bağlı olarak, Nu sayısı belirgin bir şekilde artmıştır.

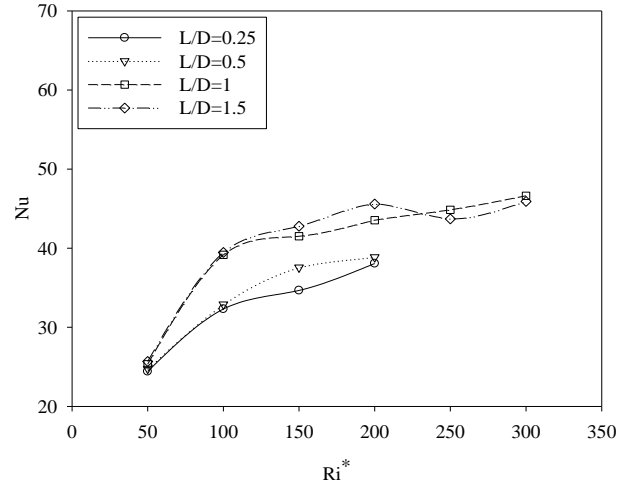
Ancak, $Ri=150-300$ aralığında Gr sayısının artışına bağlı olarak artan kaldırma kuvvetleri etkisi, zorlanmış taşınım etkilerine baskın gelmeye başlamış ve Nu sayısındaki artışı azaltıcı bir etki göstermiştir. Bu aralıkta; $L/D=1,5$ değerinde ortalama Nu sayısındaki azalışın %11,3 olduğu tespit edilmiştir. $Ri=300$ değerinde kaldırma kuvvetleri etkisinin belirgin bir şekilde baskın olması sebebiyle, engeller arasındaki mesafe arttırılsa dahi ($L/D=1-1,5$ aralığında), Nu sayısında belirgin bir değişim olmadığı tespit edilmiştir. $L/D=0,25-1,5$ aralığında arttırıldığında; üst engelde ortalama Nu sayısında %59,4'lük bir artış olduğu, en yüksek Nu sayısının $L/D=1,5$ ve $Ri=150$ olduğu durumda meydana geldiği tespit edilmiştir.



Şekil 11. Üst engeldeki Nu sayısının Ri sayısı ve farklı L/D değerlerine göre değişimi, $Re=200$, $BR=0,5$

Alt engel için Nusselt sayısının farklı L/D oranına ve farklı Ri sayılarına göre değişimi, Şekil 12'de sunulmuştur. Alt engelde de üst engeldeki duruma benzer şekilde, L/D oranı arttıkça ortalama Nu sayısında artış olduğu tespit edilmiştir. Ancak tüm L/D oranları için Nu sayısındaki artış üst engele göre daha az gerçekleşmiştir. Bunun sebebinin; alt engel çevresinde doğal taşınım sonucu oluşan akışkan hareketinin üst engel tarafından engellenmesi ve doğal taşınım etkilerinin tam olarak görülememesinden kaynaklandığı değerlendirilmektedir.

$L/D=0,25-0,5$ aralığında engellerin birbirine çok yakın olması sebebiyle, akışkan hızı azalmakta ve kaldırma kuvvetlerinin etkisi düşük Ri sayılarında ($Ri=50-100$ aralığında) daha belirgin bir şekilde görülmektedir. Bu durumun sebebinin; Ri sayısı arttıkça, Gr sayısının artışına bağlı olarak, Nu sayısının da artması olduğu değerlendirilmiştir. Bu aralıkta; $Ri=150$ değerinde L/D oranındaki artış Nu sayısında belirgin bir artışa sebep olur iken, $Ri=200$ değerinde belirgin bir artışa sebep olmamıştır. Bunun sebebinin; kaldırma kuvvetlerinin etkisinin Ri sayısındaki artışa bağlı olarak artmasına rağmen üst engelin, bu etkiyi azaltıcı bir etki göstererek yer çekimine zıt yöndeki akışkan hızının azalması olarak değerlendirilmiştir.

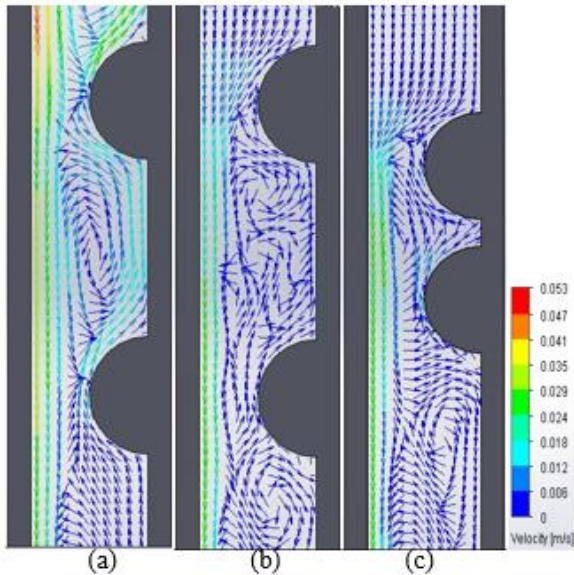


Şekil 12. Alt engeldeki Nu sayısının Ri sayısı ve farklı L/D değerlerine göre değişimi, $Re=200$, $BR=0,5$

$L/D=0,5-1$ aralığında engeller arasındaki mesafenin artışına bağlı olarak, düşük Ri sayılarında ($Ri=50-100$ aralığında) hem yerçekimi yönündeki zorlanmış taşınım etkileri hem de yerçekiminin aksi yönünde oluşan kaldırma kuvvetlerinin etkisi sebebiyle engeller arasında oluşan girdapların büyümesine bağlı olarak, Nu sayısı belirgin bir şekilde, üst engelde olduğu gibi artmıştır. Ancak, bu artış bu bölgede oluşan kaldırma kuvvetlerinin sebep olduğu yer çekimine aksi yöndeki akışkan hareketine bağlı hızın yüksek değerlere çıkamaması sebebiyle Nu sayısı üst engeldekinden farklı olarak belirgin bir şekilde artış göstermemiştir. Bunun sebebi üst engelin kaldırma kuvvetleri sebebiyle oluşan akışkan hareketini engellemesidir. $Ri=150-300$ aralığında Gr sayısının artışına bağlı olarak artan kaldırma kuvvetleri etkisi, zorlanmış taşınım etkilerine, üstteki engelin akışkan hareketini engellemesi sebebiyle kısmen baskın gelmeye başlamış ve Nu sayısındaki artışı azaltarak devam etmiştir. Ancak doğal taşınımın Nu sayısını azaltıcı etkisi üstteki engel sebebiyle yüksek değerlere ulaşmadığından, Nu sayısında yerel olarak bir düşüşe sebep olmamıştır. $Ri=300$ değerinde kaldırma kuvvetleri etkisinin kısmen zorlanmış taşınım etkisine baskın olması sebebiyle, engeller arasındaki mesafe arttırılsa dahi ($L/D=1-1,5$ aralığında), Nu sayısında belirgin bir değişim olmadığı tespit edilmiştir. $L/D=0,25-1,5$ aralığında arttırıldığında; alt engelde ortalama Nu sayısında %25,2'lik bir artış olduğu, en yüksek Nu sayısının $L/D=1$ ve $Ri=300$ olduğu durumda meydana geldiği tespit edilmiştir.

Farklı L/D oranının; $Re=200$, $Ri=200$ ve $BR=0,5$ değerlerinde; kanal içerisinde oluşan hız vektörlerinin dağılımı üzerindeki etkisi Şekil 13'te gösterilmiştir. Richardson sayısının artmasıyla birlikte, kaldırma kuvvetlerinin etkisi artmakta ve bu durumun vorteks oluşumunun artmasına sebep olduğu görülmektedir. Girdap oluşumunun artması, hidrodinamik sınır tabakanın artmasına ve ısı sınır tabakanın azalmasına sebep olmakta ve bu durum ısı transferini

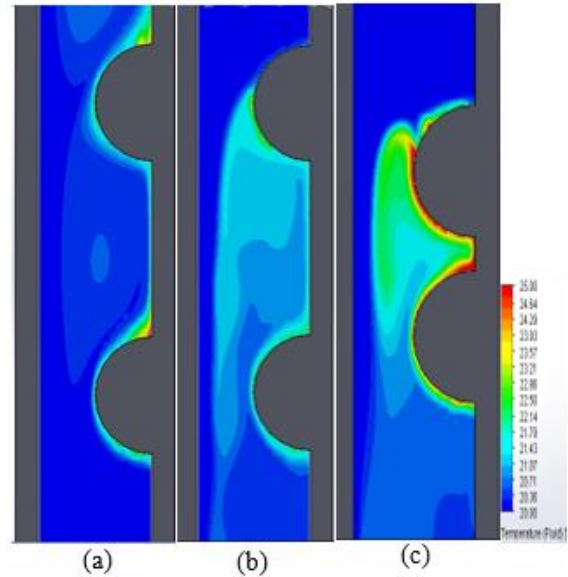
arttırmaktadır. L/D oranının artmasıyla birlikte engeller arası mesafe artmaktadır. $L/D=0,5$ durumunda; doğal taşınımdan kaynaklanan kaldırma kuvvetlerinin etkisiyle oluşan yerçekiminin aksi yönündeki akışkan hareketi hızlanmaktadır. Bu akışkan hareketi zorlanmış taşınımdan kaynaklanan ve yer çekimi yönündeki akışkan hareketiyle etkileşerek, iki engel arasında belirgin girdaplar oluşturmakta ve bu girdaplar engellere yakın bölgelerde hidrodinamik sınır tabakanın kalınlaşmasına sebep olmaktadır. $L/D=0,25$ değerinde engeller arasındaki mesafenin azalmasına bağlı olarak, engeller arasında doğal taşınımdan kaynaklanan akışkan hareketi yavaşlamakta ve buna bağlı olarak hız azalmaktadır. Üstteki engelin de doğal taşınımdan kaynaklanan yerçekiminin aksi yönündeki bu akışı engellemesi sebebiyle bu akış, zorlanmış taşınımdan kaynaklanan akışa baskın gelememekte ve ısınan akışkan bölgeden uzaklaştırılmamaktadır. Bu durumda üst engelin alt bölgesine ve alt engelin üst bölgesinde küçük girdaplar oluşmakta ve hız sınır tabaka kalınlığı azalmaktadır. $L/D=0,15$ değerinde; engeller arasındaki mesafenin daha da azalmasına bağlı olarak, engeller arasındaki akışkan hızı azalmakta ve burada oluşan hidrodinamik hız sınır tabaka kalınlığı daha da azalmaktadır. Bu durumda zorlanmış taşınımdan kaynaklanan akışkan hareketi, engeller arasındaki bölgede oluşan doğal taşınımdan kaynaklanan akışkan hareketine tamamen baskın geldiğinden, yüzeye yakın bölgede oluşan sıcak akışkan bölgeden uzaklaştırılmamaktadır.



Şekil 13. Hız vektörlerinin dağılımı, $Re=200$, $Ri=200$, $BR=0,5$ (a) $L/D= 0,5$ (b) $L/D= 0,25$ (c) $L/D= 0,15$

Farklı L/D oranında; $Re=200$, $Ri=200$ ve $BR=0,5$ değerlerinde; kanal içerisinde oluşan sıcaklık konturlarının dağılımı Şekil 14'te gösterilmiştir. $L/D=0,5$ durumunda; engeller arasındaki mesafe en fazladır. Bu sebeple doğal taşınımdan kaynaklanan akışkan hareketine bağlı akışkan hızı bu durumda en yüksek değerindedir. Zorlanmış taşınımdan

kaynaklanan akışkan hareketi, engellerin zıt yönündeki duvar boyunca yerçekimi yönünde devam etmektedir. Engelle yakın bölgelerdeki doğal taşınımdan kaynaklanan akışkan hareketi, hız sınır tabakayı kalınlaştırmakta ve ısı sınır tabakayı azaltmakta, ve bu durum ısı transferini artırarak iyi bir soğutma sağlamaktadır. $L/D=0,25$ değerinde engeller arasındaki mesafenin azalmasına bağlı olarak, engeller arasında doğal taşınımdan kaynaklanan akışkan hareketi yavaşlamakta ve buna bağlı hız azalmaktadır. Bu durum, hız sınır tabaka kalınlığının azalmasına ve ısı sınır tabaka kalınlığının artmasına ve ısı transferinde azalmaya sebep olmaktadır. Bu sebeple, engeller arasındaki bölgede akışkan sıcaklık değerleri yükselmektedir. $L/D= 0,15$ değerinde; engeller arasındaki mesafenin daha da azalmasına bağlı olarak, engeller arasındaki akışkan hızı azalmakta ve burada oluşan hidrodinamik sınır tabaka kalınlığı daha da azalmakta ve ısı sınır tabaka kalınlığı artmaktadır. Bu durum ısı transferini daha da azaltmakta ve engeller arasındaki bölgede ve engellerin birbirine bakan yüzeylerinde sıcaklıkların, sıcak akışkanın yüzeye yakın bölgelerden uzaklaştırılmaması sebebiyle, belirgin bir şekilde artmasına sebep olmaktadır.

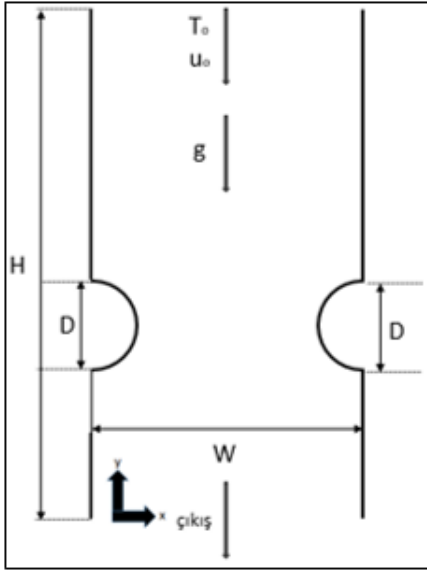


Şekil 14. Sıcaklık konturlarının dağılımı, $Re=200$ $Ri=200$ (a) $L/D= 0,5$ (b) $L/D= 0,25$ (c) $L/D= 0,15$

Karşılıklı bulunan iki yarı silindirik engeldeki karışık konveksiyonun incelenmesi

Bu bölümde; dik ve iki tarafı adyabatik duvarlarla sınırlandırılmış ve yüzeyinde ısı akısı olan, karşılıklı olarak bulunan iki yarı silindirik engelin bulunduğu bir kanaldaki ısı transferine ve akış dinamiklerine farklı parametrelerin etkisi incelenmiştir. İncelenen problemin şematik gösterimi Şekil 15'te sunulmuştur. Yarı silindirik engeller aynı çaptadır (D). Yarı silindirik engellere sabit ısı akısı verilmektedir. Kanal girişindeki akışkanın sıcaklığı sabit $T_o=20^\circ C$ 'dir. İncelenen sayısal çalışma $Re=200$ değeri için

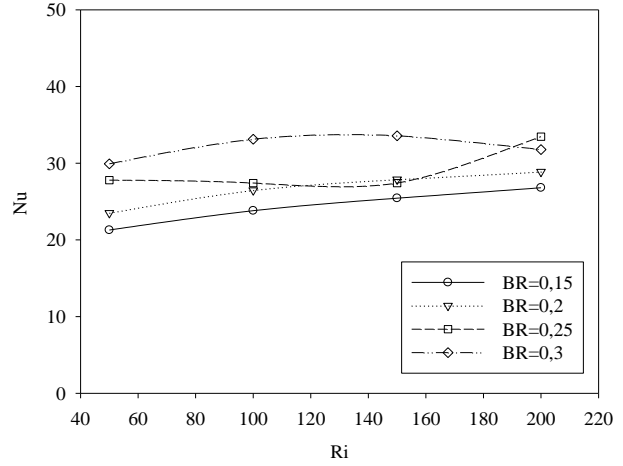
yapılmıştır. BR oranı hesaplanırken engellerin çapı sabit alınarak kanalın genişliği değiştirilmiştir, bunun ısı transferi ve akış dinamikleri üzerindeki etkileri incelenmiştir. Bu çalışmanın ilk aşamasında BR oranı sabit tutularak (BR=0,3) farklı Ri sayılarında akış özellikleri ve ısı transferi incelenmiş, ikinci aşamasında ise; Ri sayısı sabit tutulmuş (Ri=200) ve farklı BR oranlarının akış özellikleri ve ısı transferine etkisi incelenmiştir. Çalışmada su, kanalın girişinden belli bir u_0 hızıyla girmekte ve yerçekiminin etkisiyle hareket etmektedir.



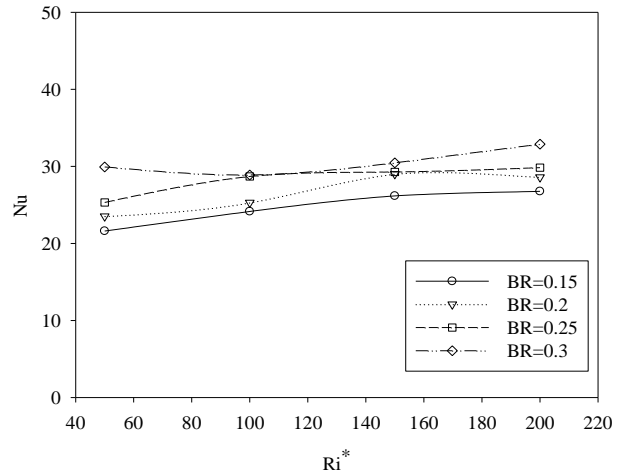
Şekil 15. Karşılıklı bulunan iki yarı silindirik engelin geometrik gösterimi

Şekil 16'da soldaki engel için ve Şekil 17'de sağdaki engel için farklı BR oranlarının ve farklı Ri sayılarının, Nusselt sayısına etkisi gösterilmiştir. BR=0,15-0,25 aralığında; BR oran arttıkça, Ri sayısının artmasına bağlı olarak Nusselt sayısının arttığı tespit edilmiştir. BR=0,3 değerinde ise; Ri=130 değerine kadar Nu sayısının arttığı ancak bu değerden sonra artan Ri sayısına bağlı olarak doğal taşınım etkilerinin, zorlanmış taşınım etkilerini azaltmasına bağlı olarak Nu sayısının azaldığı tespit edilmiştir. BR oranı BR=0,15-0,30 aralığında arttırıldığında; düşük Ri sayılarında (Ri=50) ortalama Nu sayısındaki artış %36,3 olarak belirlenmiş, yüksek Ri sayılarında (Ri=200) ise ortalama Nu sayısındaki artışın %23,1 olarak meydana geldiği tespit edilmiştir. Bu sebeple BR oranı arttıkça artan Ri sayılarında Nu sayısı da genel olarak artmakta ancak bu artış azalarak devam etmektedir. BR=0,15 değerinde; Richardson sayısı Ri=50-200 aralığında arttırıldığında ortalama Nu sayısındaki artış %18,1 olarak tespit edilmiştir. BR=0,30 değerinde ise; Richardson sayısı Ri=50-200 aralığında arttırıldığında ortalama Nu sayısındaki artış %6,6 olarak tespit edilmiştir. Bu durum artan Ri sayısında bağlı olarak kaldırma kuvvetleri etkisinin de arttığı ve bu etkinin zorlanmış taşınım etkilerini azalttığı ve buna bağlı olarak da ortalama Nu sayısının azaldığı tespit edilmiştir. Kanala simetrik olarak

yerleştirilmiş hem sağ hem de sol engelde genel olarak ısı transferi ve akış özelliklerinin benzer şekilde gerçekleştiği tespit edilmiştir. Karışık taşınım etkilerine bağlı olarak meydana gelen en iyi ısı transferinin, BR=0,25-0,30 aralığında Ri=200 değerinde olduğu belirlenmiştir.

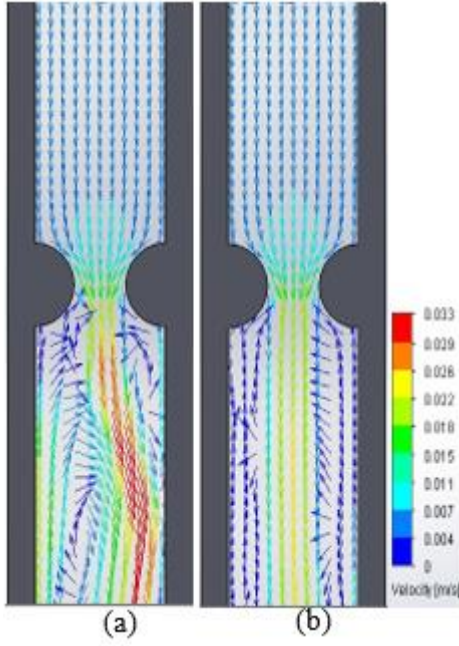


Şekil 16. Sol yarı silindirik engeldeki Nu sayısının farklı Ri sayılarına ve farklı BR değerlerine göre değişimi



Şekil 17. Sağ yarı silindirik engeldeki Nu sayısının farklı Ri sayılarına ve farklı BR değerlerine göre değişimi

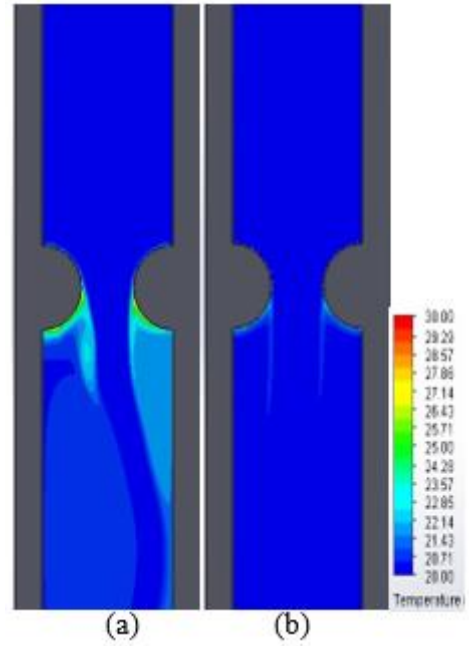
Şekil 18'de Re=200 ve BR=0,3 değerleri için farklı Ri sayılarında hız vektörlerinin dağılımı gösterilmiştir. Ri=50 değerinde zorlanmış taşınım etkilerine bağlı olarak oluşan akışkan hızının doğal taşınım etkilerine bağlı olarak oluşan akışkan hareketine oldukça baskın olduğu, akış hızının kanal orta hattı boyunca yerçekimi yönünde artışına bağlı olarak hidrodinamik sınır tabaka kalınlığının arttığı ve ısıl sınır tabaka kalınlığının azaldığı tespit edilmiştir. Ri=200 değerine arttırıldığında ise; kaldırma kuvvetlerinin etkisine bağlı olarak artan doğal taşınım etkilerinin, zorlanmış taşınım etkilerini azaltmaya başladığı tespit edilmiştir. Engellerin yere bakan tarafında oluşan vortekslerin etkisi ile engele yakın bölgelerde akışkanın hızının azaldığı, bu durumun hidrodinamik sınır tabaka kalınlığının azalmasına ve ısıl sınır tabaka kalınlığının artmasına sebep olduğu belirlenmiştir.



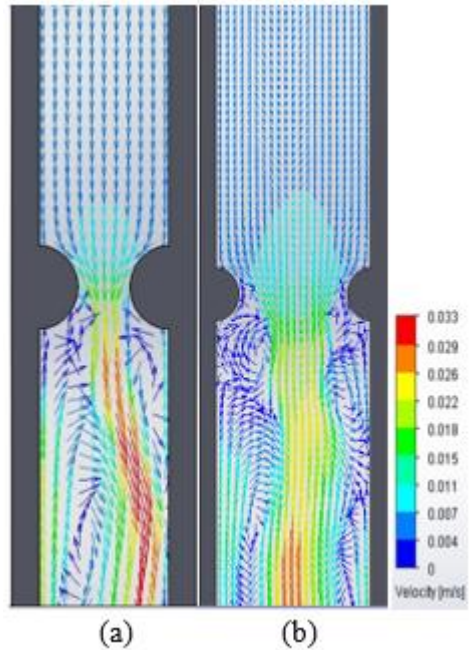
Şekil 18. $Re=200$, $BR=0,3$ için farklı Ri sayılarında hız vektörlerinin dağılımı, (a) $Ri=200$, (b) $Ri=50$

Şekil 19’da $Re=200$ ve $BR=0,3$ değerleri için farklı Ri sayılarında sıcaklık konturlarının dağılımı gösterilmiştir. $Ri=50$ değerinde; akış hızının kanal orta hattı boyunca yerçekimi yönünde artışına bağlı olarak hidrodinamik sınır tabaka kalınlığının artmasına ve ısıl sınır tabaka kalınlığının azalmasına bağlı olarak, engellerin yere bakan yüzeylerinde sıcaklık değerlerinin düştüğü ve etkin bir ısı transferinin sağlandığı belirlenmiştir. $Ri=200$ değerine artırıldığında ise; kaldırma kuvvetlerinin etkisine bağlı olarak artan doğal taşınım etkilerinin, zorlanmış taşınım etkilerinin azalmasına sebep olması sebebiyle ısıl sınır tabaka kalınlığının artmasına bağlı olarak, engellerin yere bakan yüzeylerinde sıcaklık artışının meydana geldiği, bu sebeple bu bölgelerde ısı transferinin azaldığı tespit edilmiştir.

Şekil 20’de $Re=200$ ve $Ri=200$ değerleri için farklı BR değerlerinde hız vektörlerinin dağılımı gösterilmiştir. Bu bölümde; kanal genişliği aynı kalıp, engel çapı arttığında zorlanmış taşınım yönündeki kanal genişliği azalmakta ve bu durum zorlanmış taşınım kaynaklı akışkan hızının artmasına sebep olmaktadır. Engellerin yüzey alanının artması, daha çok akışkanın yüzeyi soğutmasını sağladığından ısı transferini de arttırmaktadır. $BR=0,15$ değerinde; zorlanmış taşınım kaynaklı akışkan hızının nispeten yavaş olması sebebiyle, doğal taşınım kaynaklı kaldırma kuvvetlerinin etkisi ile engel yüzeylerine yakın bölgelerde vorteksler oluşmakta, bu durum bu bölgelerde akışkan hızını azaltmakta ve hız sınır tabakası kalınlığının azalmasına ve ısıl sınır tabaka kalınlığının artmasına sebep olmaktadır.



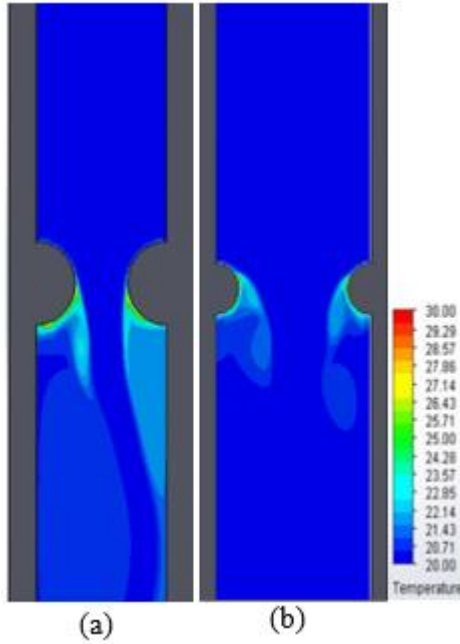
Şekil 19. $Re=200$ ve $BR=0,3$ değerleri için farklı Ri sayılarında sıcaklık konturlarının dağılımı, (a) $Ri=200$ (b) $Ri=50$



Şekil 20. $Re=200$ ve $Ri=200$ değerleri için farklı BR değerlerinde hız vektörlerinin dağılımı (a) $BR=0,3$ (b) $BR=0,15$

$BR=0,3$ değerinde ise; zorlanmış taşınım kaynaklı akışkan hızının artışına bağlı olarak engellerin, yerin aksi yönündeki yüzeylerinde hidrodinamik sınır tabaka kalınlığının arttığı ve ısıl sınır tabaka kalınlığının azaldığı belirlenmiştir. Engellerin yere bakan yüzeylerinde ise; doğal taşınım kaynaklı kaldırma kuvvetlerinin etkisi ile oluşan vortekslerin bu bölgedeki akışkan hızını azaltmasına bağlı olarak; hız sınır tabaka kalınlığı azalmakta ve ısıl sınır tabaka kalınlığı artmaktadır.

Şekil 21’de $Re=200$ ve $Ri=200$ değerleri için farklı BR değerlerinde sıcaklık konturlarının dağılımı gösterilmiştir. $BR=0,15$ değerinde; engel yüzeylerine yakın bölgelerde akışkan hızının azalmasına bağlı olarak hız sınır tabaka kalınlığının azalması ve ısıl sınır tabaka kalınlığının artması engel yüzeyindeki sıcaklıkların artmasına ve nispeten iyi bir ısı transferinin sağlanmasına sebep olmaktadır. $BR=0,3$ değerinde ise; zorlanmış taşınımından kaynaklanan akışkan hızının artışına bağlı olarak engellerin yerin aksi yönündeki yüzeylerinde ısıl sınır tabaka kalınlığının azalması sebebiyle yüzey sıcaklıklarının azaldığı ve etkin bir ısı transferinin sağlandığı tespit edilmiştir. Engellerin yere bakan yüzeylerinde ise; doğal taşınımından kaynaklanan kaldırma kuvvetlerinin etkisi ile oluşan vortekslerin bu bölgedeki akışkan hızını azaltmasına bağlı olarak; ısıl sınır tabaka kalınlığının artmasına sebep olduğu; bu durumun ısı transferinin azalmasına ve yüzey sıcaklıklarının artmasına sebep olduğu belirlenmiştir.



Şekil 21. $Re=200$ ve $Ri=200$ değerleri için farklı BR değerlerinde sıcaklık konturlarının dağılımı, (Variation of temperature contours for different BR values at $Re=200$, $Ri=200$) (a) $BR=0,3$ (b) $BR=0,15$

SONUÇ

Bu çalışmada; dik ve içinde ısı akısına sahip yarı silindirik engeller bulunan bir kanaldaki karışık konveksiyonun ısı transferine ve akış özelliklerine etkisi sayısal olarak incelenmiştir. Çalışmada; yarı silindirik engellerin birbirlerine olan uzaklıkları, konumları ve sayıları değiştirilerek ısı transferine ve akış özelliklerine etkisi belirlenmeye çalışılmıştır. Çalışmada incelenen parametreler; a. tek yarı silindirik engel bulunan kanaldaki karışık konveksiyonun incelenmesi ($BR=0,15-0,75$ ve $Ri=50-200$ aralığında), b. alt alta bulunan iki yarı silindirik engeldeki karışık

taşınımın incelenmesi ($L/D=0,25-1,5$ ve $Ri=50-300$ aralığında), c. karşılıklı bulunan iki yarı silindirik engeldeki karışık konveksiyonun incelenmesidir ($BR=0,15-3,0$ ve $Ri=50-200$ aralığında). Sonuç olarak;

a. Re sayısı $Re=100-200$ değerine arttırıldığında; zorlanmış taşınım etkisinin, doğal taşınım etkisine daha fazla baskın geldiği ve tüm BR oranlarında ortalama Nu sayılarının artış gösterdiği tespit edilmiştir. BR oranının arttırılmasının ısı transferini arttırdığı görülmüştür. $BR=0,15$ değerinde; engelin kanal içerisindeki yüzey alanı çok küçük olduğundan, kaldırma kuvvetleri etkisi arttırıldığında bile (Ri sayısının değerinde artış olmasına rağmen) Nu sayısında belirgin bir artış olmadığı görülmüştür. $BR=0,15$ 'den $0,75$ değerine değiştirildiğinde; Ri sayısının artışına bağlı olarak ($Ri=50$ den $Ri=200$ değerine) ortalama Nu sayısındaki artışın %1'den, %58,3 değerine yükseldiği belirlenmiştir.

b. Engellerin birbirine olan uzaklıkları arttırdığında (L/D oranlarının artmasıyla birlikte); Nusselt sayısının genel olarak arttığı görülmüştür. $L/D= 0,25-0,5$ aralığında engellerin birbirine çok yakın olması sebebiyle, akışkan hızı azalmakta ve kaldırma kuvvetlerinin etkisi daha belirgin bir şekilde görülmektedir. Bu durum Ri sayısı arttıkça Gr sayısının artışına bağlı olarak, Nu sayısının da artmasına sebep olmaktadır. Bu aralıkta $Ri=150$ değerine kadar L/D oranındaki artış Nu sayısında belirgin bir artışa sebep olmaz iken, $Ri=200$ değerinden sonra kaldırma kuvvetlerinin etkisi daha da belirginleşmekte ve Nu sayısı artmaktadır. $Ri=300$ değerinde ise; kaldırma kuvvetleri etkisinin kısmen zorlanmış taşınım etkisine baskın olması sebebiyle, engeller arasındaki mesafe arttırılsa dahi ($L/D=1-1,5$ aralığında), Nu sayısında belirgin bir değişim olmadığı tespit edilmiştir. $L/D=0,25-1,5$ aralığında arttırıldığında; alt engelde ortalama Nu sayısında %25,2'lik bir artış olduğu, en yüksek Nu sayısının $L/D = 1$ ve $Ri=300$ olduğu durumda meydana geldiği tespit edilmiştir.

c. Karşılıklı bulunan iki yarı silindirik engelin olması durumunda; BR oranı arttıkça, Ri sayısının artmasına bağlı olarak Nusselt sayısının arttığı tespit edilmiştir. $BR=0,15-0,30$ aralığında arttırıldığında; düşük Ri sayılarında ($Ri=50$) ortalama Nu sayısındaki artış %36,3 olarak belirlenmiş, yüksek Ri sayılarında ($Ri=200$) ise ortalama Nu sayısındaki artışın %23,1 olarak meydana geldiği tespit edilmiştir. $BR=0,15$ değerinde; Richardson sayısı $Ri=50-200$ aralığında arttırıldığında ortalama Nu sayısındaki artış %18,1 olarak tespit edilmiştir. $BR=0,30$ değerinde ise; Richardson sayısı $Ri=50-200$ aralığında arttırıldığında ortalama Nu sayısındaki artış %6,6 olarak tespit edilmiştir.

d. Bu alanda yapılacak karışık konveksiyonun incelendiği gelecek çalışmalarda; Reynolds sayıları ve

değiştirilmiş Richardson sayısının aralıkları arttırılarak çözümler yapılmasının, yeni tip akışkanların ısı transferine ve akış özelliklerine etkisinin (nanoakışkanlar vb.) incelenmesinin, farklı kanal ve engel geometrisinin ısı transferine ve akış özelliklerine etkisinin farklı parametreler için incelenmesinin faydalı olacağı değerlendirilmiştir.

KAYNAKLAR

Adachi T. ve Uehara H., 2001, Correlation between heat transfer and pressure drop in channels with periodically grooved parts, *International Journal of Heat and Mass Transfer*, 44, 22, 4333-4343.

Auletta A., Manca O., Morrone B. ve Naso V., 2001, Heat transfer enhancement by the chimney effect in a vertical isoflux channel, *International Journal of Heat and Mass Transfer*, 44, 4345-4357.

Barboy S., Rashkovan A. ve Ziskind G., 2012, Determination of hot spots on a heated wavy wall in channel flow, *International Journal of Heat and Mass Transfer*, 55, 3576-3581.

Barletta A. ve Zanchini E., 1999, On the choice of the reference temperature for fully developed mixed convection in a vertical channel, *International Journal of Heat and Mass Transfer*, 42, 3169-3181.

Bilgin E., Du S. Q. ve Vasseur P., 1998, The mixed convection heat transfer in open ended channels with protruding heaters, *Heat and Mass Transfer*, 34, 4, 263-270.

Boutina L. ve Bessaih R., 2011, Numerical simulation of mixed convection air-cooling of electronic components mounted in an inclined channel, *Applied Thermal Engineering*, 31, 11-12, 2052-2062.

Çalışır T., Çalışkan S., Kilic M. ve Başkaya S., 2017, Numerical investigation of flow field on ribbed surfaces using impinging jets, *Journal of the Faculty of Engineering and Architecture of Gazi University*, 32, 1, 119-130.

Forooghi P. ve Hooman K., 2013, Effect of buoyancy on turbulent convection heat transfer in corrugated channels a numerical study, *International Journal of Heat and Mass Transfer*, 64, 850-862.

Hamouche A. ve Bessaih R., 2009, Mixed convection air cooling of protruding heat sources mounted in a horizontal channel, *International Communications in Heat and Mass Transfer*, 36, 8, 841-849.

Herman I. C. ve Kang E., 2002, Heat transfer enhancement in a grooved channel with curved vanes,

International Journal of Heat and Mass Transfer, 4518, 3741-3757.

Jang J. H. ve Yan W. M., 2004, Mixed convection heat and mass transfer along a vertical wavy surface, *International Journal of Heat and Mass Transfer*, 47, 3, 419-428.

Kilic M. ve Baskaya Ş., 2017, Improvement of heat transfer from high heat flux surfaces by using vortex promoters with different geometries and impinging jets, *Journal of the Faculty of Engineering and Architecture of Gazi University*, 32, 3, 693-707.

Kilic M., Calisir T. ve Baskaya Ş., 2017, Experimental and numerical investigation of vortex promoter effects on heat transfer from heated electronic components in a rectangular channel with an impinging jet, *Heat Transfer Research*, 48, 5, 435-463.

Lakkis I. ve Moukalled F., 2008, Natural convection heat transfer in channels with isothermally heated convex surfaces, *Numeric Heat Transfer, Part A: Applications*, 53, 11, 1176-1194.

Mills Z. G., Warey A. ve Alexeev A., 2016, Heat transfer enhancement and thermal-hydraulic performance in laminar flows through asymmetric wavy walled channels, *International Journal of Heat and Mass Transfer*, 97, 450-460.

Moukalled F., Doughan A. ve Acharya S., 2000, Parametric study of mixed convection in channels with concave and convex surfaces, *International Journal of Heat and Mass Transfer*, 43, 1947-1963.

Oztop H. F., 2005, Numerical study of flow and heat transfer in curvilinear ducts: applications of elliptic grid generation, *Applied Mathematics and Computation*, 168, 1449-1460.

Rao G. ve Narasimham G., 2007, Laminar conjugate mixed convection in a vertical channel with heat generating components, *International Journal of Heat and Mass Transfer*, 50, 3561-3574.

Rosas I. Y., Treviño C. ve Suástegui L., 2017, Experimental study of mixed convection heat transfer in a vertical channel with a one-sided semi cylindrical constriction with prescribed heat flux, *International Journal of Heat and Fluid Flow*, 67, 155-167.

Singh N., Sivan R., Sotoa M., Faizal M. ve Ahmed, M., 2016, Experimental studies on parallel wavy channel heat exchangers with varying channel inclination angles, *Experimental Thermal Fluid Science*, 75, 173-182.

Tanda G., 2004, Heat transfer in rectangular channels with transverse and v-shaped broken ribs, *International Journal of Heat and Mass Transfer*, 47, 229–243.

Wahba E., 2011, Mixed convection flows in a vertical plane duct preceded by a sudden expansion, *International Journal Numeric Method Heat Fluid Flow*, 21, 399–417.

Wang G. ve Vanka S., 1995, Convective heat transfer in periodic wavy passages, *International Journal Heat and Mass Transfer*, 38, 3219–3230.

Young T. ve Vafai K., 1998, Convective cooling of a heated obstacle in a channel, *International Journal Heat and Mass Transfer*, 41, 3131–3148.

Young T. ve Vafai K., 1999, Experimental and numerical investigation of forced convective characteristics of arrays of channel mounted obstacles, *ASME Journal Heat Transfer*, 121, 34–42.

Özdemir S., 2018, Bir dik kanal içerisindeki yarı silindirik yüzeylerden olan karışık taşınım ile ısı transferinin nümerik olarak incelenmesi, Yüksek Lisans Tezi, Gazi Üniversitesi, Fen Bilimleri Enstitüsü, Ankara.



THE DETERMINATION OF THE HEAT EXTRACTION RATIO IN THE SOLAR POND

Hacı SOGUKPINAR* and Ismail BOZKURT**

* Department of Electric and Energy, Vocational School, University of Adiyaman, Adiyaman 02040, Turkey, hsogukpinar@adiyaman.edu.tr, ORCID: 0000-0002-9467-2005

**Department of Mechanical Engineering, Faculty of Engineering, University of Adiyaman, Adiyaman 02040, Turkey, corresponding author, ibozkurt@adiyaman.edu.tr, ORCID: 0000-0002-2126-3710

(Geliş Tarihi: 09.06.2021, Kabul Tarihi: 26.11.2021)

Abstract: In this study heat extraction ratio of a solar pond was investigated numerically by using the Discrete Ordinates Method (DOM) with the direct solver PARDISO by using nested dissection multithreaded preordering algorithm, and the findings without exchanger were compared with experimental data to validate simulation accuracy of numerical approaches in the Mediterranean climatic condition. The solar pond was modeled with the same dimension as a previous experimental system and a heat exchanger was placed in the heat storage zone and simulation to take out the hot water at a certain flow was performed with the commercial software COMSOL. The solar position was defined for Adana and ambient data was obtained by processing the ASHRAE Weather Data Viewer 5.0. As a result, the maximum and minimum heat extraction ratio (HER) is calculated as 13.39 % in July and 2.96 % in September for a flow rate of 0.007 kg/s; 24.27 % in June, and 3.23 % in September for a flow rate of 0.014 kg/s, respectively.

Keywords: Solar energy, solar pond, thermal energy, heat transfer, heat exchanger

GÜNEŞ HAVUZLARINDA ISI ÇEKME ORANININ BELİRLENMESİ

Özet: Bu çalışmada, bir güneş havuzunda ısı çekme oranı, doğrudan çözücü PARDISO ile Ayrık Ordinatlarda Yöntemi kullanılarak iç içe parçalara ayrılıp çok iş parçacıklı ön düzenleme algoritması ile sayısal olarak araştırılmış ve sayısal yaklaşımların simülasyon doğruluğu için eşanjörsüz güneş havuzunda yapılan ön nümerik sonuçlar deneysel verilerle Akdeniz iklim koşullarında karşılaştırılmıştır. Daha sonra, güneş havuzu önceki bir deney sistemi ile aynı boyutta modellenmiş ve ısı depolama bölgesine bir ısı eşanjörü yerleştirilmiş ve COMSOL ticari yazılımı ile sıcak suyun belirli bir akışta dışarı alınması için simülasyon gerçekleştirilmiştir. Adana için güneş konumu tanımlanmış ve ASHRAE Weather Data Viewer 5.0 ile işlenerek ortam verileri elde edilmiştir. Sonuç olarak, 0.007 kg/s debi için maksimum ve minimum ısı çekme oranı Temmuz ayında % 13.39 ve Eylül ayında % 2.96 olarak hesaplanmıştır; 0.014 kg/s debi için sırasıyla Haziran'da %24.27 ve Eylül'de %3.23'tür.

Anahtar kelimeler: Güneş enerjisi, güneş havuzu, ısı enerjisi, ısı transferi, ısı eşanjörü

NOMENCLATURE

E	Energy (J)
exc.	Exchanger
C _p	Specific heat capacity at constant pressure (J/kg°C)
h	Heat transfer coefficient (W/m ² K)
DOM	Discrete Ordinate Method
HSZ	Heat storage zone
I (Ω)	Radiative intensity at a given position following the Ω direction
I _b (T)	Blackbody radiative intensity
I(Ω)	Radiation density in a place in Ω direction
k	Thermal conductivity (W/m K)
NCZ	Non-convective zone
N _r	Refractive index
n	Outward normal vector

p	Pressure (Pa)
S	Strain-rate tensor (1/s)
T	temperature (K)
Q	Heat sources other than viscous heating (W/m ³)
q _r	Heat flux striking the wall
q	Heat flux by conduction (W/m ²)
UCZ	Upper convective zone
u	Velocity vector (m/s)
U	Internal energy (J)

Greek symbols

κ	absorption coefficients
β	extinction coefficients
σ _s	Scattering coefficients
φ	Scattering phase function
τ	Cauchy stress tensor deviator

σ	Stefan-Boltzmann constant
ρ	Density (kg/m ³)

Subscripts

exch	exchanged
ext	extracted
st	stored
sw	side wall

INTRODUCTION

The effects of global warming on the environment have started to emerge as different natural disasters all over the world. Therefore, many countries have made very comprehensive investments in alternative renewable energy sources. On the other hand, global energy costs are quite high and foreign energy-dependent countries economy has been shaken. Due to both economic and environmental factors, it has become a necessity for countries to generate their energy from their own resources. The only renewable energy source that countries can harness equally is solar energy all over the world. Solar energy thermal systems are one of the technologies which have advanced and are widely used for many industrial processes such as heating, cooling, product drying, providing low-grade hot water, water desalination, direct steam provision, and commercial cooking (Renewables 2017 Global Status Report, 2018). Solar ponds are thermal energy systems that convert solar energy into heat and have the capacity to store it for a long time. Solar ponds have many operational advantages, such as: easier to construct and set up, lower maintenance rate and installation cost, and long-term energy storage potential. Many studies have been carried out on the heat energy storage capacity of solar ponds. Bozkurt et al. (2012) studied the efficiency of the solar pond which was integrated with flat plate collectors. The efficiency increase of the integrated system was investigated. The energy and exergy analysis of an experimental solar pond, coupled with solar collectors were calculated and compared by Karakilcik et al. (2013a). Furthermore, Karakilcik et al. (2013b) investigated the shading effect on model solar ponds. The efficiency of the solar ponds with and without shading effect was investigated and the shading coefficients of the model pond were determined. The effect of transparent covers on the performance of the solar pond was investigated in another study by Bozkurt et al. (2014), separately. The energy efficiency of the solar pond was calculated for each cover, and the glass cover was determined as the best for the solar ponds. On the other hand, Bozkurt et al. (2015) have determined the effects of a parameter on the thermal performance of sunshine area rates of a model solar pond of different sizes. The performance of solar ponds was also investigated by Sogukpinar et al. (2016; 2018) for different conditions. The annual seasonal temperature distributions of the solar pond were investigated and the efficiency of the system was

calculated. For the salt-gradient solar pond, heat extraction and its variation were investigated by Alcaraz et al. (2016). The pond was tested and compared to conventional heat exchangers for the sidewall areas. The effect of phase change materials on the efficiency of the pond was investigated experimentally by Assari et al. (2015). In order to improve the thermal energy storage capacity of the solar pond, two models were built with and without phase change material to determine its stability during heat extraction. The performance of NCZ and HSZ was investigated to determine the efficiency of the solar pond by Date et al. (2013). For this, a simple method was proposed to estimate the transient thermal performance of the system when heat is extracted from different parts of the pond. The activity of the shallow solar pond under open and closed cycle modes was studied both experimentally and numerically by El-Sebaï et al. (2013) and heat extraction was optimized and compared to show the availability of solar pond in domestic heating and industrial usage. The effect of heat extraction in the non-convective region on the performance of an experimental solar pond was shown by Leblanc et al. (2011) and the performance of the solar ponds was improved by the conventional heat extraction method. Aramesh et al. (2017) investigated the heat storage and heat extraction processes of solar ponds with a combination of the methods presented in the previous works, theoretically. The impacts of different nano-fluids on the heat extraction operation of solar ponds were studied. Khalilian et al. (2018) developed different heat extraction models to determine the effects on the efficiency of the solar pond. The energetic and exergetic transient performances were compared under different modes of heat extraction. Mansouri et al. (2018) suggested three different heat extraction technics to evaluate the performance of the solar pond. The technics were compared based on outlet temperatures and amounts of energy and exergy extraction. Amirifard et al. (2018) compared temperature changes and thermal energy to determine the latent heat storage in the solar ponds for performance stability without phase change material. The heat extraction from the solar pond and the heat supply processes was evaluated by Alcaraz et al. (2018). The heat extraction and supply tests were carried out for a conventional and lateral wall heat exchanger.

Generally, high concentrated brine has been used in solar ponds. Therefore, heat energy from the system cannot be harnessed directly but exchanger. Therefore, the heat storage efficiency of the solar pond alone has no meaning but integrated with a heat exchanger it expresses something for efficiency. Furthermore, when the heat is extracted, the real behavior of the pond emerges. Thus, the ratio of the energy stored in the pond to the energy coming to the pond surface can be

increased. On the other hand, there is a lot of investigation, are available related to the efficiency of the solar pond with a simple analytic method but it is rare with a comprehensive method like Discrete Ordinate Method (DOM). Therefore in this study, the performance of solar pond with an exchanger under Mediterranean climatic conditions was investigated for the full year of operations by using discrete ordinates method and compared with experimental data to validate numerical approaches. The outflow water temperature of a heat exchanger was calculated for the inflow rate temperature of 20°C and the heat extraction ratio of the system was calculated and discussed.

METHODOLOGY

Heat transfer mechanism

The radiation can interact with the surface or the environment in different ways such as absorption, emissions, scattering, and transmission. Interacted medium absorbs a part of the incident radiation and a fraction of radiation is emitted and scattered in all directions, and a part of it may be transmitted to another medium. Heat energy, transmitted from one medium to another via conduction, convection, and thermal radiation, depending on the state of the systems. Heat conduction happens oscillations of each molecule in fluids, in metals mainly by heat-carrying electrons but in gas which occurs through collisions of molecules. Convection occurs with a net displacement of a heat-transferring fluid. Balance of radiative transfer between source and interacting medium happens. The general radiative transfer equation can be written with Eq.(1) (COMSOL, 2018; Modest, 2013).

$$\Omega \cdot \nabla I(\Omega) = \kappa I_b(T) - \beta I(\Omega) + \frac{\sigma_s}{4\pi} \int_{4\pi} I(\Omega') \varphi(\Omega', \Omega) d\Omega' \quad (1)$$

Where, $I(\Omega)$ represent the radiative intensity in a given (Ω) direction, I_b is the blackbody radiation intensity, κ , β , σ_s are absorption, extinction, and scattering coefficients. Radiative intensity may be defined for any direction Ω due to continuous properties of angular space. This discrete ordinates method is used to approximately solve approximately the radiation transfer equation by discretizing both the xyz-domain and the angular variables that specify the direction of radiation. This method provides a discretization of angular space into $n = N(N + 2)$ in 3D discrete directions. The following Eq.(2) was used for the discretization in 3D (COMSOL, 2018).

$$S_i \cdot \nabla I_i = \kappa I_b(T) - \beta I_i + \frac{\sigma_s}{4\pi} \sum_{j=1}^n w_j I_j \Phi(S_i, S_j) \quad (2)$$

where, S_i is the i^{th} discrete ordinate, w_j , is weight. Rosseland and P1 approximation are another possible radiation discretization method. In this study, DOM was used. Because Rosseland approximation has a

limited impact from a computational point of view and does not provide any extra degree of freedom to the heat equation and P1 approximation provides only one additional degree of freedom. For the current simulation, refractive index (n_r) was taken as 1, the index set to 0.4. The radiation with participating media interactions was calculated by using Eq.(2). Heat transfer in solid and liquid and was calculated by using the following Eq.(3) (COMSOL, 2018).

$$\rho C_p \left(\frac{\partial T}{\partial t} + \rho C_p \mathbf{u} \cdot \nabla T \right) + \nabla \cdot \mathbf{q} = Q + Q_{ted} + Q_r \quad (3)$$

where $\mathbf{q} = -\mathbf{k}\nabla T$, $Q_r = \kappa(\sum_{i=1}^N w_i I_i - 4\pi I_b)$, Q_r is used to calculate heat flux divergence in the participating media. \mathbf{k} is thermal conductivity, ρ is the density of medium which can be solid, liquid and gas depend on the boundary region. C_p is the heat capacity, T is temperature, \mathbf{q} is the heat flux, Q is heat, and Q_{ted} is the thermoelastic damping heat source. Eq.(3) is used to calculate heat transfer and the same equation is used for the liquid but Q_{ted} is replaced by $Q_p + Q_{vd}$. Q_p is work done under pressure, Q_{vd} represents viscous dissipation in the fluid. Heat transfer module was used to calculate heat transfer with radiation in participating media and heat transfer in solid and liquid. For this Eq.(2) and Eq.(3) were used to calculate radiation in participation media, Eq.(2) was used to calculate heat transfer in liquid and solid. Eq.(3) was used for calculation of heat interaction with exchanger.

Boundary conditions

Meteorological data was defined for the experiment period from 2011 to 2012 for Adana. The initial condition was set as average wind speed and temperature. The physical properties of materials were taken from COMSOL library. For the heat flux from the surface to air, convection was defined and meteorological data was defined for outside conditions. For the fluid inside the pipe and heat exchanger, fluid velocity was set from 0-2 cm/s, heat conductivity, the ratio of specific heat, and heat capacity from liquid to solid and solid to liquid was defined from used materials automatically. The inflow velocity of water into the heat exchanger was defined as 293.15 K and the other end of the pipe was defined as outflow. The general layout of the solar pond coupled with the exchanger is as shown in Figure 1. Since the solar pond is semitransparent, a part of the incoming solar ray is reflected and scattered and some of it is absorbed by the saltwater and turned into heat. Part of the stored heat is escaped around the environment by conduction, convection, and radiation.

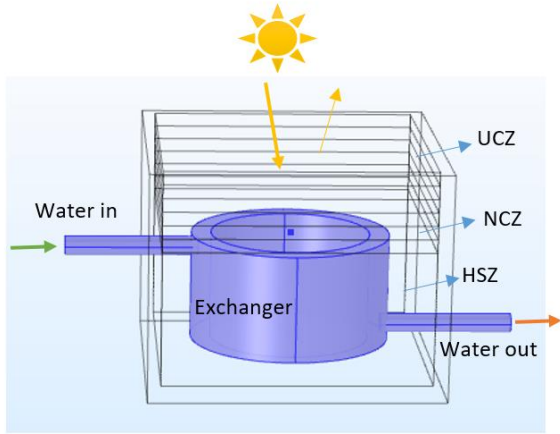


Figure 1. The general layout of the heat exchanger in the solar pond

The Heat Storage Zone (HSZ) is 1 m deep, the Non-Convective Zone (NCZ) consists of 4 layers each has a depth of 0.10 m, and Upper Convective Zone (UCZ) has one layer with 0.10 m deep. The pond was insulated with foam with the thickness of 0.10 m and also inlet and outlet pipes were insulated with 0.05 m thick foam due to their physical size. The NCZ undertakes upstream insulation of the heat storage zone, so with the increasing number of layers at a certain level, which increases the thermal insulation. A shell-type exchanger, with a thickness of 0.15 m and a depth of 0.80 m was designed with inlet and outlet pipes diameter of 0.03 m, and was integrated into the system.

Geometry and Mesh generation

The mesh module in COMSOL was used to create the mesh. Figure 2 shows the mesh distribution in the solar pond. Too sparse mesh distribution may produce calculation error but too dense distribution increase computational time. It was observed that the high mesh distribution greatly increased the computation time but there was no difference compared to the lower mesh distribution. For the numerical calculation in the literature, the only criteria are general compliance with the experiment. Therefore, only the results are more agreement with the experiment were used. 39,693 tetrahedral mesh elements were created. In order to make a more accurate calculation, the mesh distribution in the inlet and outlet sections of the pipe was increased. The mesh quality was determined 0.68 and the minimum was 0.23. Direct solver PARDISO was used for the simulation. Iteration technics and nonlinear methods were used for termination and method. Two other direct solvers in COMSOL are available such as MUMPS and SPOOLES. On the other hand, PARDISO is fast, robust, multi-core capable, and scales better than MUMPS on a single node with many cores but SPOOLES is slow (COMSOL, 2018).

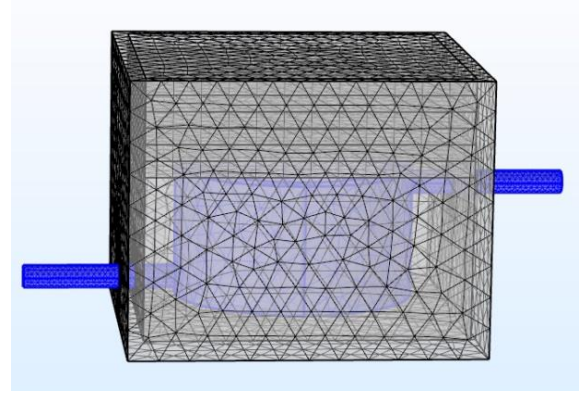


Figure 2. Mesh distribution of the solar pond

Heat Extraction ratio

The heat energy extraction from solar ponds is very important in terms of the efficiency of the pond and heat extraction keeps the temperature in the solar pond at a certain level. Therefore, the heat losses would be reduced. On the other hand, the extracted heat can be used in for various purposes. Solar ponds store the solar energy, coming to the surface of the pond, as heat in the storage zone. The heat is extracted from the solar pond by the heat exchanger in the form of a cylindrical shell, placed in HSZ. The ratio of the extracted heat to incoming solar energy (heat extraction ratio, HER) is calculated as follows.

$$HER = \frac{Q_{ext.}}{Q_{solar}} \quad (4)$$

where $Q_{ext.}$ is the monthly total heat extracted from the solar pond, Q_{solar} is the monthly total solar energy incoming to the surface of the solar pond. The monthly total heat extraction was calculated as;

$$Q_{ext.} = \sum_{\Delta t} \dot{m} c_p (T_{out} - T_{in}) (\Delta t) \quad (5)$$

RESULTS AND DISCUSSIONS

The numerical calculation was conducted by using discrete ordinates method (DOM) and compared with experimental data to validate the simulation accuracy of the numerical approaches. For solar energy and ambient data ASHRAE, Weather Data Viewer 5.0 was used starting from 2010. It is the construction time of the experimental system. The experimental system was built in 2005 and the performance of a solar pond was investigated (Karakilcik et al., 2006), which was integrated with solar collectors (Bozkurt et al., 2012), dynamic exergetic performance assessment of an integrated solar pond (Karakilcik et al., 2013a) was observed, solar pond with and without shading effect (Karakilcik et al., 2013b) was investigated, transparent covers on the performance (Bozkurt et al., 2014), and effect of sunny area ratios on the thermal performance of solar ponds (Bozkurt et al., 2015) and related some

parameter has been investigated and reported since then. On the other hand, varied analytic methods have been used for numerical calculation in addition to experiments but no comprehensive method like DOM has been used. Figure 3 shows yearly solar radiation and ambient temperature distributions for Adana, in Turkey.

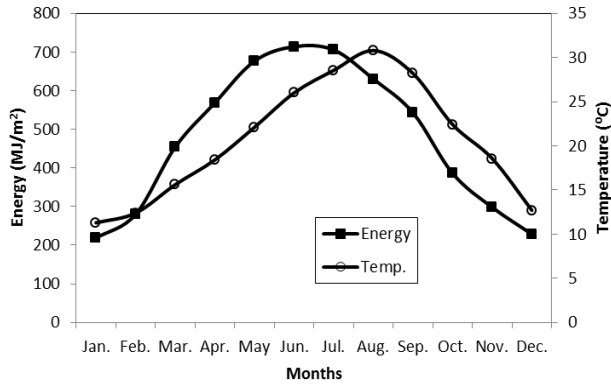


Figure 3. The solar energy and ambient temperature distributions for Adana, Turkey, 2010 (Adana Meteorology Regional Office, 2018) Maximum and minimum incident solar energy on the surface of the solar pond is 713.91 MJ/m² in June and 218.48 MJ/m² in January, and the monthly average maximum and minimum temperatures are observed 30.80 °C in August and 11.30 °C in January, respectively.

The temperature was measured by a sensor for each 0.10 m from the test set and for the numerical model, the temperature was calculated instantaneously at 0.10 m, 0.50 m, and 0.90 m from the base and is presented in Figure 4b. The numerical calculation was carried out for 14 months to see seasonal variation temperature, starting from the first day of March, and is given in Figure 4 with the experimental measurement (Karakilcik et al., 2006). Numerical calculations were carried out in succession for every 30 days and the temperature distribution of the system for May is given in Figure 4a. The numerical study for the whole year is given in Figure 4.b as a line graph in comparison with the experimental study.

There is almost a good agreement between the theoretical data and the experiment. Numerical study results are given for 10, 50, and 90 cm depths of the heat storage zone, and although there are small deviations in winter, they are generally in full agreement. In order to achieve this compliance, meteorological data of the experiment time were defined exactly to the numerical method.

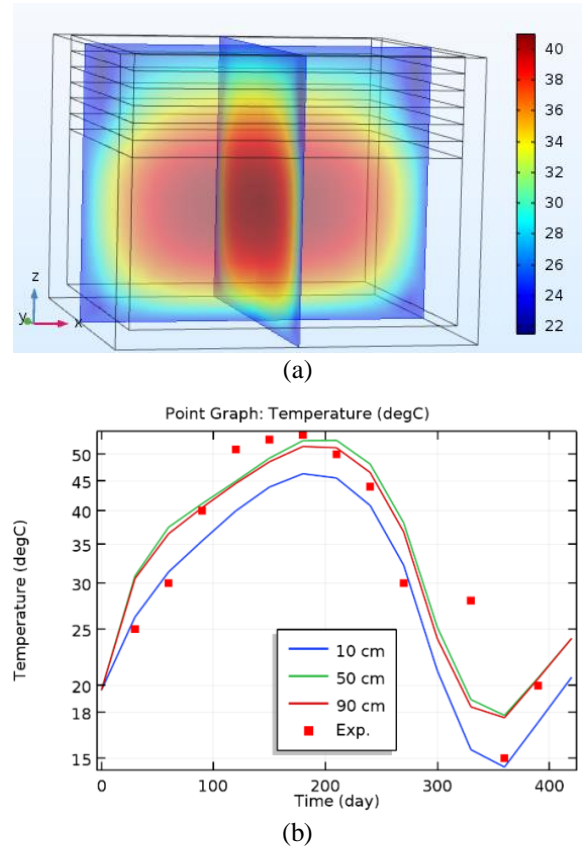


Figure 4. The temperature distribution in the pond without exchanger; (a) temperature distribution (b) temperature point graph for different depths

In preliminary calculations, when the calculation started from January, the calculated solar pond temperature was quite low and bumpy until the end of February. Therefore, to ensure temperature compatibility between experiment and theory, the calculation was started from the first day of March and the numerical method was conducted for 14 months to observe seasonal temperature distribution.

The performance of the solar pond with a heat exchanger was tested by increasing the water flow rate to 0.007 kg/s (1 cm/s) and 0.014 kg/s (2 cm/s). The temperature distribution in different depths of the solar pond for different flow rates is given in Figure 5. It is seen that more heat can be extracted from the system with an increasing flow rate. The maximum water temperature taken out at a speed of 1 cm/s is 42 °C, while the maximum water temperature at a speed of 2 cm/s is around 37 °C. This shows heat can be drawn from the solar pond in summer and spring with the help of an exchanger. however, it was determined that extra heating is not possible at an inlet temperature of 20 °C in winter periods. Fig. 6 shows the outflow temperature distribution of the heat exchanger.

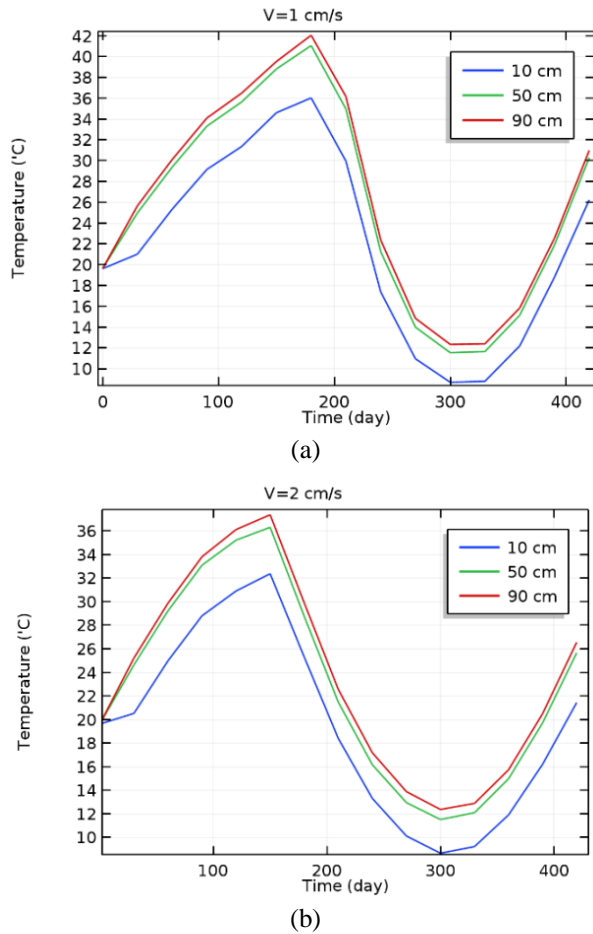


Figure 5. Seasonal temperature variations in different depths of solar pond for different flow rates (a) 1 cm/s (0.007 kg/s) (b) 2 cm/s (0.014 kg/s)

The outflow temperature of the exchanger from March to September is calculated higher than inlet temperature ($20\text{ }^{\circ}\text{C}$) and is calculated lower than the inlet temperature from October to February. Solar ponds can be used for primary heating in winter and some of the autumn months then the inlet temperature ($0\text{ }^{\circ}\text{C}$ to $20\text{ }^{\circ}\text{C}$) might be increased a few degrees up to a maximum $20\text{ }^{\circ}\text{C}$. Then the temperature could be raised to the desired point by using a hybrid system.

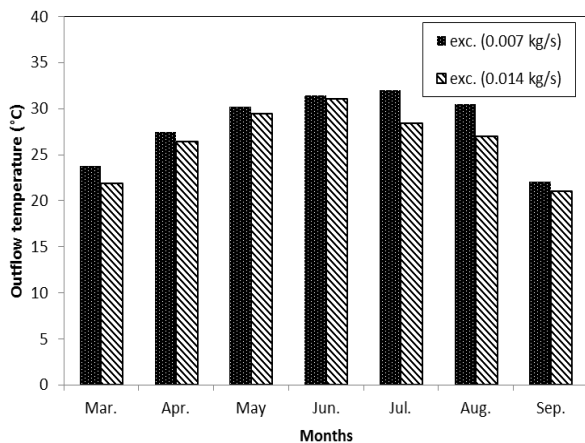


Figure 6. The monthly average outflow temperature of the heat exchanger

Heat loss is one of the most important factors, affecting the performance of the system. The heat losses from the solar pond were calculated separately for the case where the heat was extracted not extracted. Fig.7 shows the heat losses from the solar pond with and without an exchanger. The heat losses reach maximum at the time when the temperature difference between the solar pond and ambient temperatures is maximum. On the other hand, heat losses are reduced by extracting heat from the solar pond.

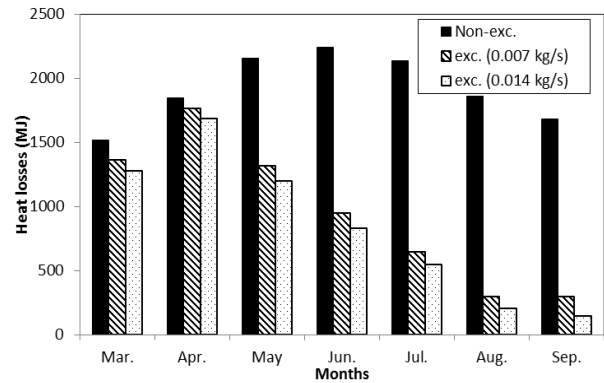


Figure 7. Total heat losses from the solar pond for with and without heat exchanger

The heat was extracted from the solar pond with the cylindrical shell heat exchanger in the heat storage zone of the solar pond. The inlet temperature of the heat exchanger was determined as $20\text{ }^{\circ}\text{C}$, the output temperatures of the heat exchangers were measured for different flow rates. The equation is given in Eq. 5, and the amount of extracted heat from the solar pond was calculated monthly. Figure 8 shows the extracted heat from the solar pond for different flow rates. The maximum and minimum extracted heats are 377.63 MJ in July and 64.29 MJ in September for the flow rate 0.007 kg/s ; 692.99 MJ in June and 70.13 MJ in September for 0.014 kg/s , respectively.

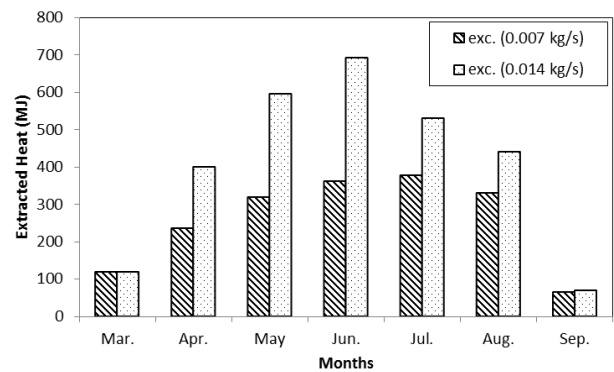


Figure 8. Extracted heat from the solar pond for different flow rates

Some of the solar energy reaching the surface of the solar pond is reflected by the surface of the pond. The rest of the solar radiation is transmitted to the pond and

radiation is absorbed as it passes through the layers. Solar energy, reaching the storage zone of the solar pond is stored thermally. The stored heat energy was extracted by using the heat exchanger. The heat extraction ratio (HER) is calculated by using Eq. 4. The heat extraction rate is important in that it shows how much of the incoming solar energy is extracted. Figure 9 shows the heat extraction ratio for different flow rates. The maximum and minimum heat extraction ratio (HER) is 13.39 % in July and 2.96 % in September for 0.007 kg/s; 24.27 % in June and 3.23 % in September for 0.014 kg/s, respectively. As the system started to operate in March, the heat extraction rate in March was low. The rate of heat extraction increases rapidly after the temperature of the system increases. As the heat is extracted from the solar pond, there is also the possibility of converting more of the solar energy to heat energy.

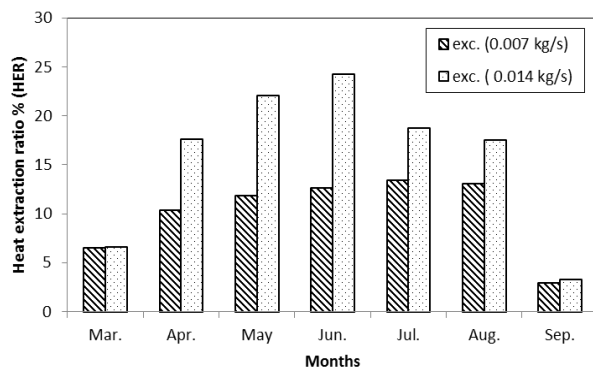


Figure 9. Heat extraction ratio for different flow rates

CONCLUSION

In order to improve the efficiency of solar ponds, the heat conversion rate of solar energy reaching the surface of the pond should be increased. By extracting heat from the solar pond, more solar energy can be converted into heat energy. In this study, a numerical calculation was performed to investigate the performance of the solar pond. Furthermore, the results were compared with an experiment (solar pond 2 m × 2 m × 1.6 m in size) which was built in the university campus of Cukurova. The solar pond with the same dimensions was modeled in a computer environment and simulated with commercial software COMSOL. Daily pressure and temperature values were taken from the meteorology. ASHRAE Weather Data Viewer 5.0 was used for ambient data processing. The maximum and minimum heat extraction ratio (HER) is 13.39 % in July and 2.96 % in September for 0.007 kg/s; 24.27 % in June and 3.23 % in September for 0.014 kg/s, respectively.

In many other studies, since the heat is not taken out by integrating an exchanger into the system, the pond temperature remains constant as the pond temperature reaches stable conditions and heat lost equals heat

absorbed, depending on the solar energy coming in during the day. In this case, it is not possible to estimate exactly how much of the stored heat can actually be used. However, when the heat is extracted, the real behavior of the pond emerges. Thus, the ratio of the energy stored in the pond to the energy coming to the pond surface can be increased. It is observed that from March to the end of September, a positive heat flow is achieved and the solar pond maintains its thermal efficiency. For the other months, the system can be used for primary heating by keeping the inlet temperature low.

ACKNOWLEDGMENT

The authors would like to thank to Adiyaman University and Middle East Technical University for technical support.

REFERENCES

- Adana Meteorology Regional Office, 2018, *Turkish State Meteorological Service*, Ankara, Turkey.
- Alcaraz A., Valderrama C., Cortina J.L., Akbarzadeh A. and Farran A., 2016, Enhancing the efficiency of solar pond heat extraction by using both lateral and bottom heat exchangers, *Solar Energy*, 134, 82-94.
- Alcaraz A., Montalà M., Valderrama C., Cortina J.L., Akbarzadeh A. and Farran A., 2018, Increasing the storage capacity of a solar pond by using solar thermal collectors: Heat extraction and heat supply processes using in-pond heat exchangers, *Solar Energy*, 17, 112-121.
- Amirifard M., Kasaeian A. and Amidpour M., 2018, Integration of a solar pond with a latent heat storage system, *Renewable Energy*, 125, 682-693.
- Aramesh M., Pourfayaz F. and Kasaeian A., 2017, Numerical investigation of the nanofluid effects on the heat extraction process of solar ponds in the transient step, *Solar Energy*, 157, 869-879.
- Assari M.R., Tabrizi H.B. and Beik A.J.G., 2015, Experimental studies on the effect of using phase change material in salinity-gradient solar pond, *Solar Energy*, 122, 204-214.
- Bozkurt I. and Karakilcik M., 2012, The daily performance of a solar pond integrated with solar collectors, *Solar Energy*, 86, 1611-1620.
- Bozkurt I., Atiz A., Karakilcik M. and Dincer I., 2014, An investigation of the effect of transparent covers on the performance of cylindrical solar ponds, *International Journal of Green Energy*, 11, 404-416.

- Bozkurt I. and Karakilcik M., 2015, The effect of sunny area ratios on the thermal performance of solar ponds, *Energy Conversion and Management*, 91, 323–332.
- Bryant H.C. and Colbeck I., 1977, A solar pond for London, *Solar Energy*, 19, 321–322.
- COMSOL, 2018, *Heat Transfer Module*, <https://www.comsol.com> [accessed 30 December 2020]
- Date A., Yaakob Y., Date A., Krishnapillai S. and Akbarzadeh A., 2013, Heat extraction from Non-Convective and Lower Convective Zones of the solar pond: A transient study, *Solar Energy*, 97, 517–528.
- El-Sebaï A.A., Aboul-Enein S., Ramadan M.R.I. and Khallaf A.M., 2013, Thermal performance of shallow solar pond under open and closed cycle modes of heat extraction, *Solar Energy*, 95, 30–41.
- Karakilcik M., Bozkurt I. and Dincer I., 2013a, Dynamic exergetic performance assessment of an integrated solar pond, *Int. J. Exergy*, 12, 70–86.
- Karakilcik M., Dincer I., Bozkurt I. and Atiz A., 2013b, Performance assessment of a solar pond with and without shading effect, *Energy Conversion and Management*, 65, 98–107.
- Karakilcik M., Dincer I. and Rosen M.A., 2006, Performance investigation of a solar pond, *Applied Thermal Engineering*, 26, 727–735.
- Khalilian M., Pourmokhtar H. and Roshan A., 2018, Effect of heat extraction mode on the overall energy and exergy efficiencies of the solar ponds: A transient study, *Energy*, 154, 27–37.
- Leblanc J., Akbarzadeh A., Andrews J., Lu H. and Golding P., 2011, Heat extraction methods from salinity-gradient solar ponds and introduction of a novel system of heat extraction for improved efficiency, *Solar Energy*, 85, 3103–3142.
- Mansouri A.E., Hasnaoui M., Amahmid A. and Dahani Y., 2018, Transient theoretical model for the assessment of three heat exchanger designs in a large-scale salt gradient solar pond: Energy and exergy analysis, *Energy Conversion and Management*, 167, 45–62.
- Modest M.F., 2013, *Radiative Heat Transfer*, 2nd ed., San Diego, California: Academic Press.
- Renewables 2017 *Global Status Report*, 2018, <http://www.ren21.net/gsr-2017/> (accessed 19 September 2018).
- Sogukpinar H., Bozkurt I., Karakilcik M. and Cag S., 2016, Numerical evaluation of the performance increase for a solar pond with glazed and unglazed, *IEEE International Conference on Power and Renewable Energy*, 598–601, doi: 10.1109/ICPRE.2016.7871146
- Sogukpinar H., Bozkurt I. and Karakilcik M., 2018, Performance Comparison of Aboveground and Underground Solar Ponds, *Thermal Science*, 22, 953–961.



MODÜLER HELYUM REAKTÖRÜNÜN KAZA DURUMUNUN ZAMANA BAĞLI ISIL AKIŞ ANALİZİ

Ömür AKBAYIR

Eskişehir Teknik Üniversitesi Ulaştırma MYO 26470 Odunpazarı, Eskişehir, Türkiye
omurakbayir@eskisehir.edu.tr, ORCID: 0000-0002-8747-4238

(Geliş Tarihi: 12.05.2021, Kabul Tarihi: 18.01.2022)

Özet: Modüler Helyum Reaktörü (MHR)'nün en önemli özelliği kaza durumunda aktif soğutma sistemi çalışmadığı zaman kendiliğinden soğuyabilmesidir. Bu çalışmanın ilk amacı; kaza durumunda MHR'nin atık ısı uzaklaştırma yeteneğini incelemek için sayısal bir model geliştirmek ve oluşan tepe sıcaklığı hesaplamaktır. İkinci amacı; grafit iletimi, atık ısı gibi parametrelerdeki değişiminin maksimum aktif kor sıcaklığına etkisini belirlemek için duyarlılık analizleri yapmaktır. Bu çalışmada, aktif soğutmanın çalışmadığı kaza durumunda, atık ısının pasif olarak reaktörden atılmasını simule etmek için bir sayısal model oluşturulmuştur. Zamana bağlı ısı-akış simülasyonları sayısal akışkanlar dinamiği yazılımı Ansys Fluent kullanılarak yapılmıştır. Simule edilen geometri Eşdeğer Silindir Modeli olarak seçilmiştir. Korun içindeki kompleks yapıyı modellemek için gözenekli ortam yaklaşımı kullanılmıştır. Hesaplamalar basınçsız kaza durumu için yapılmıştır. Basınçsız kaza durumunda pasif soğuma 100 saat için nümerik olarak çözülmüştür. Nümerik metodun güvenilirliği diğer çalışmalar ile karşılaştırılarak doğrulanmıştır. Kaza durumunda meydana gelen maksimum sıcaklığın 1492°C olduğu bulunmuştur. Duyarlılık analizlerinin sonuçları kaza durumunda oluşan maksimum sıcaklığa en çok grafit ısı iletim katsayısı ve atık ısı değişiminin etkisi olduğunu göstermektedir.

Anahtar Kelimeler: Modüler helyum reaktörü, kaza, SAD, zamana bağlı, Isıl-akış

TRANSIENT THERMAL HYDRAULIC ANALYSIS OF MODULAR HELIUM REACTOR UNDER ACCIDENT CONDITION

Abstract: The main characteristic of MHR is that it can automatically cool down when the active cooling system does not work under accident condition. The first purpose of the study is to develop a numerical model to analyze the decay heat removal capabilities and evaluate peak temperature in the MHR under accident condition. The second purpose of the study is to perform some sensitivity analyses to evaluate the effect of varying the parameters, i.e. graphite conductivity, decay heat, etc., on the maximum active core temperature. In this study, a numerical model has been constructed to simulate the passive decay heat removal under a loss of active cooling accident. Thermal-hydraulic transient simulations were carried out by using Computational Fluid Dynamics software Ansys Fluent. The simulated geometry was chosen as an Equivalent Cylinder Model. The porous media approach has been applied to model the complex structure in the core. Calculations were performed for loss of forced cooling without pressurization condition. Passive cooldown under depressurized accident is solved numerically for 100 hours. The reliability of the numerical method was validated by comparing with the published data. It was found that the maximum temperature was 1492°C under accident condition. The results of sensitivity analyses show that the graphite thermal conductivity and decay power has a strong effect on the maximum temperature under accident condition.

Keywords: Modular helium reactor, Accident, CFD, Transient, Thermal-hydraulic

SEMBOLLER

E	Toplam enerji
g	Yerçekimi ivmesi
IAEA	International Atomic Energy Agency
k	Isı iletim katsayısı
k_{eff}	Efektif ısı iletim katsayısı [W/mK]
$k_{eff(T)}$	Sıcaklığa bağlı efektif ısı iletim katsayısı [W/mK]
k_g	Grafit ısı iletim katsayısı [W/mK]
k_{He}	Helyum ısı iletim katsayısı [W/mK]
k_{yk}	Yakıt kompaktı ısı iletim katsayısı [W/mK]
MHR	Modüler Helyum Reaktörü

NIST	Ulusal Standartlar ve Teknoloji Enstitüsü
p	Basınç
P	Zamana bağlı atık güç [MW]
P_{or}	Normal çalışma durumunda ısı güç [MW]
RCCS	Reaktör Boşluğu Soğutma Sistemi
\dot{Q}	Isı üretimi
\emptyset	Genel akış değişkeni (örnek: entalpi)
SAD	Sayısal Akışkanlar Dinamiği
S_{\emptyset}	Kaynak terimi
t	Zaman [saniye]
T	Sıcaklık
u	Hız

UDF	Kullanıcı Tanımlı İşlev
VHTR	Çok Yüksek Sıcaklık Reaktörü
α_g	Grafitin hacimsel oranı
α_{He}	Helyumun hacimsel oranı
α_{yk}	Yakıt kompaktının hacimsel oranı
Γ	Difüzyon katsayısı
∇	Del operatörü
μ	Dinamik vizkozite
ρ	Yoğunluk

GİRİŞ

Dünya çapındaki elektrik üretiminin yaklaşık %11,2'si büyük bir kısmı su soğutmalı olan 436 nükleer enerji santrali tarafından sağlanmaktadır. Elektrik üretimi için nükleer enerji kullanımına ilgi birçok ülkede yeni nükleer reaktörlerin kurulmasına yol açmaktadır. Nükleer enerji santralleri için güvenli ve verimli işletmecilik esastır. Nükleer reaktörlerde güvenliğe ve diğer problemlere potansiyel çözüm önerileri IV. Nesil Nükleer Reaktörleri ve diğer ileri reaktör tasarımlarını ortaya çıkarmıştır. IV. Nesil Nükleer Reaktör Forumu (GIF) tarafında yaklaşık 130 reaktör tasarımı çeşitli kriterlere göre incelenmiş ve 6 adet IV. Nesil tasarım grubu/sistemi belirlenmiştir. Bunlar: (1) SFR (Sodium-cooled Fast Reactor), (2) VHTR (Very High Temperature Reactor), (3) GFR (Gas-cooled Fast Reactor), (4) MSR (Molten Salt Reactor), (5) LFR (Lead-cooled Fast Reactor), (6) SCWR (Super Critical Water-cooled Reactor). IV. Nesil Reaktör sistemleri hala tasarım aşamasındadır ve 2030 yılından sonra ticari olarak yaygınlaşması beklenmektedir. VHTR, GFR, LFR ve MSR, 900-1000°C aralığında yüksek çıkış sıcaklığına sahip olduğundan hidrojen üretimi ve endüstriyel proses ısısı uygulamaları için potansiyele sahiptir. Bu çalışmada IV. Nesil Nükleer Reaktör geliştirme çalışmalarına katkı sağlamak amacıyla VHTR tasarımı adaylarından biri olarak belirlenmiş MHR ele alınmıştır (Pioro, 2016).

VHTR'lerin güvenlik açısından en önemli özelliği kaza durumunda atık ısının pasif olarak reaktörden uzaklaştırılmasıdır. Bir kaza olması durumunda aktif soğutma sistemlerinden hiçbiri çalışmadığı takdirde; kor atık ısısı, reaktör içindeki sıcaklık tasarım limitlerini geçmeden iletim, ışınım ve doğal taşınım ile reaktör kabını çevreleyen Reaktör Boşluğu Soğutma Sistemi (RCCS)'ne transfer edilmektedir. Bu özellik şimdilerde VHTR'lerin gelişimine katkı sağlamak amacıyla birçok araştırmacı tarafından incelenmektedir (Huning *vd.*, 2021).

MHR'de korun atık ısısı kaza süresince Kapama Soğutma Sistemi'nin çalışmaması durumunda bağımsız ve pasif olarak uzaklaştırılmaktadır. Aktif soğutma sisteminin çalışmaması durumunda, pasif atık ısı uzaklaştırma sistemi reaktörün soğumasını 2 durumda gerçekleştirmektedir. Bunlar; reaktör kabının çalışma basıncında kaldığı basınçlı soğuma ve reaktör kabının atmosfer basıncında kaldığı basınçsız soğuma kaza durumlarıdır. Basınçsız soğuma Helyumun atmosferik basınçtaki düşük yoğunluğundan dolayı taşınım ile ısı transferinin önemli bir rol oynamadığı en kötü kaza

durumdur. Helyumun doğal taşınım ile ısı transferi sınırlıdır. Bu durumda reaktör daha çok iletim ve ışınım ile soğur. Basınçlı soğuma durumunda reaktör içinde ısı; iletim, doğal taşınım ve ışınım ile transfer olurken; basınçsız soğuma durumunda yalnızca iletim ve taşınım ile transfer olur. Kaza durumunda atık ısı; aktif kordan dış reflektöre, kor kabına ve reaktör kabına, oradan da son olarak pasif RCCS'ye iletilir. Her iki kaza durumunda ısı reaktör kabının dış yüzeyinden ışınım ve doğal taşınım ile reaktörü saran pasif RCCS'ye ulaşır.

Bu çalışmada maksimum sıcaklık açısından daha kötü bir senaryo olduğu için basınçsız kaza durumu ele alınmıştır. 100 saat boyunca kaza durumunu incelemek için Ansys Fluent yazılımı kullanılarak bir model oluşturulmuştur. Kaza durumunda MHR'nin genel davranışını incelemek ve bir metodoloji oluşturmak amaçlanmıştır. Kaza durumundaki belirsizlikler tahmin edilmeye ve kaza durumundaki önemli unsurlar daha iyi anlaşılmasına çalışılmıştır. Böylece reaktör tasarımı ve geliştirilmesinde nerelere dikkat edilmesi gerektiği işaret edilecektir.

MHR'nin ısı-akış analizi ilk olarak General Atomics (GA) tarafından birim hücre modeli kullanılarak POKE kodu ile yapılmıştır (Potter, 1995). Birim hücre modeli basit olmasına rağmen, yakıt elemanı içindeki ısı transferinin aşağı yukarı temel halini anlamak için kullanışlıdır. Birim hücre modeli sadece dik üçgen şeklindeki birim hücrelerden oluşan yakıt elemanlarının içindeki düzenli bölgeyi incelemektedir. Birim hücre yakıt kompakt alanının üçte birinden ve soğutucu deliği alanının altıda birinden oluşur. Birim hücre modeli ile basınçsız kaza durumu için tepe sıcaklığı 1521°C bulunmuştur.

Uluslararası Atom Enerjisi Kurumu (IAEA) tarafından MHR'nin kaza durumu ısı-akış analizi için CRP-3 kıyaslama problemi tanımlanmıştır (IAEA, 2001). CRP-3 kıyaslama probleminde tanımlanmış sınır şartları, malzeme özellikleri ve diğer şartlara göre değişik SAD araçları ve metotları ile 100 saate kadar zamana bağlı basınçsız kaza durumu analizleri yapılmıştır:

Kuzavkov (OKBM-Rusya), GTAS kodu ile yaptığı 2 boyutlu ısı-akış hesaplamalarında pik sıcaklığını 1490°C bulmuştur. Oluşturduğu modelde reaktör kabı ile kor kabı arasındaki akışı hesaba katmamıştır (IAEA, 2001). Mejane (CEA-Fransa), CASTEM kodu ile pik sıcaklığının 1565°C olduğunu hesaplamıştır. Pik sıcaklığı 100.saatten önce oluşması gerektiği halde, ısı iletimi ile ilgili yaptığı varsayımlar nedeniyle pik sıcaklığı 140.saatte oluşmuştur (IAEA, 2001). Siccama ve Koning (ECN-Hollanda)'in ticari CFD yazılımı CFX-F3D ile yaptıkları ısı-akış analizlerinde pik sıcaklığı 1371°C çıkmıştır. Aktif kor içindeki akışı, temsili 4 büyük kanalla modellemesi nedeniyle pik sıcaklığı düşük çıkmıştır (Siccama ve Koning, 1998). Gao (INET-Çin), çakıl yataklı reaktörlerin zamana bağlı ısı-akış analizi için geliştirilmiş olan THERMIX/KONVEK kodu ile pik sıcaklığını 1590°C olarak hesaplamıştır (IAEA, 2001). Ball (ORNL-ABD), ORNL'nin Modüler Helium

Reaktörleri için geliştirdiği MORECA kodunu kullanmıştır. Temsili 3 boyutlu olarak oluşturulan modelde pik sıcaklığı 1552°C çıkmıştır. Oluşturulan model üst boşluğu içermemektedir (IAEA, 2001). Woaye-Hune ve Ehster (Framatome-Fransa), ticari STAR-CD kodu ile pik sıcaklığını 1525°C bulmuşlardır. Efektif ısı iletim katsayısını oluşturdukları başka bir CFD modeli ile hesaplamışlardır (Woaye-Hune ve Ehster, 2002). Haque ve arkadaşları (Framatome-Almanya), MHR'nin THERMIX/KONVEK kodu ile ısı-akış analizini yapmışlardır. Aynı kodu kullanan Gao; pik sıcaklığını 1590°C hesaplamasına rağmen, Woaye-Hune ve Ehster 1560°C olarak hesaplamıştır (Haque *vd.*, 2006, 2004). Woaye-Hune ve Ehster'in elde ettiği sonuçları Mays ve arkadaşları (AREVA-ABD/Fransa/Almanya), ticari STAR-CD kodu ile elde ettikleri sonuçlar ile karşılaştırmışlardır. Elde edilen pik sıcaklığı 1494°C olup, Woaye-Hune ve Ehster'e göre farklılık; RCCS modellemesi, radyal güç yoğunluğu profili ve hesaplama metodlarından kaynaklandığını ifade etmişlerdir (Mays *vd.*, 2004). Shi (Aachen Üni.-Almanya), MGT-3D kodunu GT-MHR'nin ısı-akış analizi için genişletmiştir. Öncesinde MGT-3D kodu çakıl yataklı reaktörlerin hem nötronik hemde ısı-akış analizini yapmak için kullanılmaktadır. Genişletilen MGT-3D kodu ile pik sıcaklığının 1535°C olduğunu hesaplamıştır (Shi, 2015). Hossain (Stuttgart Üni.-Almanya), MHR'nin ısı-akış analizi için yeni geliştirdiği TH3D isimli kodla pik sıcaklığını 1568°C bulmuştur. Elde ettiği sonuçların THERMIX/KONVEK kodu ile elde edilenlerle uyumlu olduğunu göstermiştir (Hossain, 2011; Hossain *vd.*, 2008). Nouri-Borujerdi ve Ghomsheh (Sharif Tekn. Üni.-İran), THPP kodu ile yaptıkları analizlerde 1577°C pik sıcaklığı değerini elde etmişlerdir. Elde ettikleri sonuçları TH3D ve THERMIX/KONVEK kodu ile elde edilenlerle karşılaştırmışlardır (Nouri-Borujerdi ve Tabatabai Ghomsheh, 2015a). Ball (ORNL-ABD), GRSAC kodu ile 1494°C pik sıcaklığı elde etmiştir. Efektif ısı iletim katsayısı fonksiyonlarının önemini vurgulamıştır (Ball, 2006, 2004). Vilim ve arkadaşları (Argonne National Lab.-ABD), bir boyutlu sistem modelleme RELAP5 kodu ile pik sıcaklığını 1471°C elde etmiştir. RELAP5 kodundaki karışık taşınım rejiminin yetersiz olduğunu dile getirmişlerdir (Vilim *vd.*, 2005). Reza ve arkadaşları (Texas Üni./INL/GA-ABD), RELAP5-3D koduna yaptıkları ATHENA kodu eklemesiyle pik sıcaklığını 1437°C hesaplamıştır (Reza *vd.*, 2006). MacDonald ve arkadaşları (INEEL-ABD), RELAP5-3D/ATHENA kodu ile pik sıcaklığını 1514°C bulmuştur. Elde ettikleri değer, GA tarafından POKE kodu ile elde edilen 1521°C pik sıcaklık değerine çok yakın olduğunu

bulmuşlardır. Farklılığın bypass bölgelerinden kaynaklandığını belirtmişlerdir (MacDonald *vd.*, 2003). Bu çalışmada IAEA tarafından tanımlanan CRP-3 kıyaslama problemi çözülmüştür. Daha önceki çalışmalarda oluşturulan modellerin yukarıda belirtilen eksikleri dikkate alınarak, Ansys Fluent yazılımı ile Gözenekli Ortam Modeli ve Eşdeğer Silindir Modeli kullanılarak bir aksi-simetrik model oluşturulmuştur. Modeldeki her bir gözenekli ortam bölgesinin efektif ısı iletim katsayısının belirlenmesinde Maxwell teorisi kullanılmıştır. Zamana bağlı ısı-akış analizleri sonucu elde edilen değerler literatürdeki çalışmalarla karşılaştırmak suretiyle doğrulanmıştır. Ayrıca kaza durumunda grafit ısı iletimi, atık ısı, ışınım yayma katsayısı, RCCS sıcaklığı değişiminin tepe sıcaklığına etkisini inceleyen duyarlılık analizi yapılmıştır. Bu çalışmayla yapılan karşılaştırmalar; analiz araçlarının daha iyi ve detaylı anlaşılmasıyla, VHTR'lerin gelişmesine katkı sağlayacaktır.

METOT

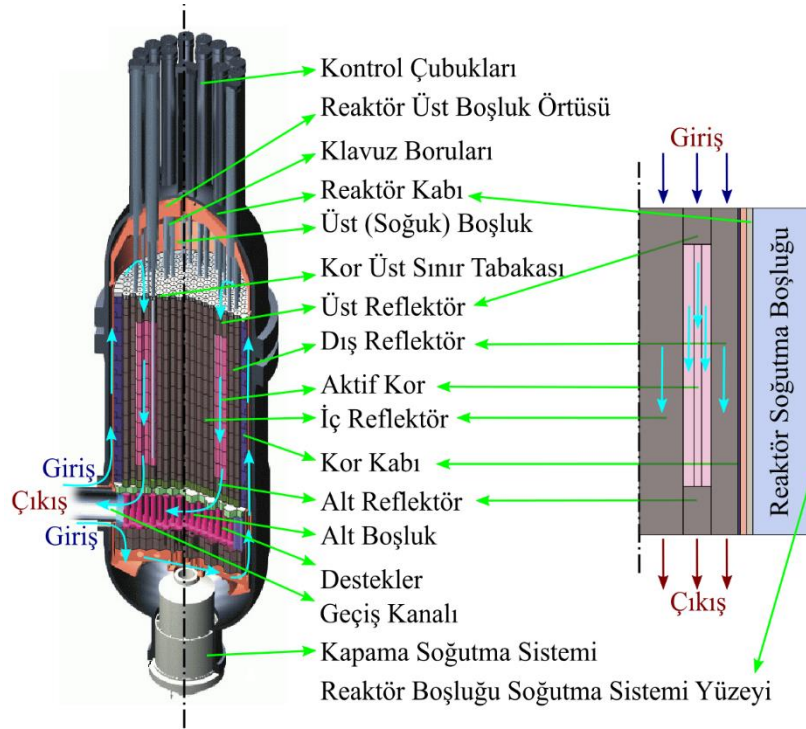
Bu bölümde ilk olarak MHR'nin genel yapısı ele alınmıştır. Daha sonra oluşturulan modelde eşdeğer silindir ve gözenekli ortam yaklaşımı kullanıldığından bunlara ilişkin bilgi verilmiştir. Son olarak; sınır şartları, malzeme özellikleri, teorik temel, çözüm metodu ve varsayımlar verilmiştir.

Modüler Helyum Reaktörü

GT-MHR; Brayton çevrimli gaz türbinli enerji dönüşüm sistemi (GT) ve gaz soğutmalı modüler helyum reaktöründen (MHR) oluşmaktadır. MHR'nin genel özellikleri Tablo 1'de verilmiştir. Şekil 1 'de MHR'nin kesit görünüşü ve oluşturulan model karşılaştırmalı olarak görülmektedir. Helyumun reaktör içindeki akışı ok işaretleri ile gösterilmiştir. Helyum reaktör kabına alt taraftan girmekte, kor kabı ile reaktör kabı arasından yukarı doğru üst boşluğa akmakta, daha sonra üst reflektör, aktif kor, alt reflektör içinden ısınarak aşağıya doğru akmakta, son olarak alt boşluktan çıkmaktadır (Fukuda *vd.*, 2001).

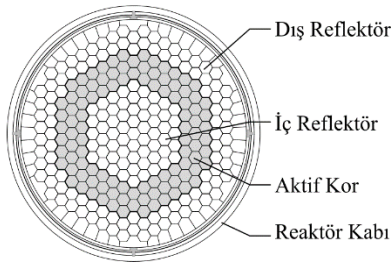
Tablo 1. MHR'nin genel özellikleri (Fukuda *vd.*, 2001)

Özellik	Değer
Kor termal gücü (MWt)	600
Helyum kütleli akış debisi (kg/s)	320
Kor giriş sıcaklığı (°C)	490
Kor çıkış sıcaklığı (°C)	850
Kor basıncı (MPa)	7



Şekil 1. MHR'nin dikey kesit görünüşü (Moses, 2010) ve oluşturulan model

Altıgen şekilli grafit ve yakıt elemanları dairesel kora yerleştirilmiştir. Şekil 2'deki reaktör korunun üstten görünüşüne göre reaktör kora 3 dairesel halkadan oluşmaktadır (Şahin vd., 2012). Bunlar iç reflektör, aktif kor ve dış reflektördür. Aktif kor halkası 102 yakıt sütunundan oluşmaktadır. Her bir standart yakıt sütunu 10 yakıt elemanı, üst ve alt grafit reflektöre sahiptir. Üst ve alt reflektörler sırasıyla 120 cm ve 158 cm yüksekliğindedir. Yakıt elemanı 793 mm yüksekliğe ve 360 mm enine sahiptir. Yakıt elemanında soğutma kanalları ve yakıt kanalları vardır. Bir yakıt elemanı yakıt kompaktları için 210 kanala ve helyum soğutucu için 108 akış kanalına sahiptir. Kompaktlar yakıt kanallarının içine yerleştirilmiştir (Kiryushin vd., 1997; Şahin vd., 2016).



Şekil 2. MHR kor yatay yerleşimi

Eşdeğer Silindir Modeli

Prizmatik reaktör korunu nümerik olarak analiz etmek için basitleştirilmiş hesaplama modelleri vardır. Bunlar; Birim Hücre Modeli, Eşdeğer Silindir Modeli, 3 Boyutlu 1/12 Kesit Modeli, 3 Boyutlu 1/6 Kesit Modelidir. Bu çalışmada SAD analizleri Eşdeğer Silindir Modeli ile yapılmıştır.

Eşdeğer Silindir Model'inde korun altıgen yapısının ortalama yarıçap ile dairesel şekle sahip olduğu varsayılmaktadır. Dairesel şekil Şekil 1'de görüldüğü gibi 2 boyutlu ve aksi-simetrik olarak modellenmiştir. Model; iç reflektörü, aktif kora, dış reflektörü, üst reflektörü, alt reflektörü, kor kabını, reaktör kabını, reaktör içindeki Helyumu ve reaktör soğutma boluğundaki havayı içermektedir. Geçiş kanalı, alt boşluk, üst boşluk, destekler, kor üst sınır yapısı, kontrol çubukları için klavuz boruları ve üst boşluk örtüsü ihmal edilmiştir. Korun iç ve dış yarıçapı sırasıyla 1,48 m ve 2,42 m'dir.

Gözenekli Ortam Modeli

MHR'nin yapısı SAD analizleri için çok karmaşıktır. MHR'deki bir yakıt elemanı yakıt kompaktları için 210 kanala ve helyum soğutucu için 108 akış kanalına sahiptir. Her bir yakıt kompaktını ve akış kanalını doğru olarak simule edebilmek için hücre (mesh) sayısının çok fazla olması gerekmektedir. Tüm yapıyı ayrıntılı olarak temsil edecek model ile çözüm yapmak çok zaman alıcı ve son derece pahalıdır. Bu nedenle MHR'nin kompleks yapısı gözenekli ortam modeli ile basitleştirilmiştir. Bu metot kor içindeki yapının oldukça kaba hücrelerle yani daha az sayıda hücreyle modellenmesine izin vermektedir. Bu metotta bir hücre hem katıyı hem de akışkanı temsil etmektedir. Söz konusu hücrenin akışkan ve yakıt kompaktını temsil eden dağıtılmış direnç ve ısı kaynağı ile simule edilmektedir. Dağıtılmış direnç ve ısı kaynakları korunum eşitliklerinde kaynak terimleri olarak bulunmaktadır (Ansys Inc., 2019). Bu sayede kaba hücrelerle yani daha az sayıda hücreyle modelleme yapılabilmektedir.

Üst reflektör, aktif kor ve alt reflektör gözenekli olarak modellenmiştir. Üst reflektör, aktif kor ve alt reflektör için % 17,9 olarak hesaplanan gözeneklilik oranı tanımlanmıştır. İç ve dış reflektör için ise gözeneklilik oranı % 1,1'dir. Üst reflektör, aktif kor, alt reflektör, iç reflektör ve dış reflektör içinden geçen eksenel ve radyal yöndeki akış için atalet direnci 0 olarak tanımlanmıştır (Ansys Inc., 2019).

Sınır Şartları ve Malzeme Özellikleri

Hesaplamalarda kullanılan malzemelerin fiziksel özellikleri Tablo 2'de verilmiştir (IAEA, 2001). Helyum gazının 1MPa ve 7MPa basınç altındaki özellikleri NIST veri tabanına dayanmaktadır (NIST, 2021). Grafit ve yakıt kompaktının ısı iletim katsayısı sıcaklığa bağlıdır. Grafit ve yakıt kompaktının sıcaklığa bağlı ısı iletim katsayısı değişimi Tablo 3'de görülmektedir.

Tablo 2. Reaktördeki malzemelerin özellikleri (IAEA, 2001).

Malzemeler	Yoğunluk (kg/m ³)	Özgül Isı (J/kg.K)	Isı İletim Katsayısı (W/mK)
Reaktör Kabı	7800	520	33
Kor Kabı	7800	520	24
Grafit	1740	1840	$k_{eff(T)}$
Yakıt Kompaktı	1740	1840	$k_{eff(T)}$

Üst reflektör, aktif kor ve alt reflektör bölgeleri gözenekli ortam yaklaşımıyla oluşturulmuştur. Aktif kor bölgesi; grafit, yakıt kompaktı ve Helyumdan meydana gelmektedir. Üst ve alt reflektör bölgeleri ise; grafit ve

Helyumdan meydana gelmektedir. Üst reflektör, aktif kor ve alt reflektör bölgelerindeki He'nin hacimsel oranı 0,18; aktif kor bölgesindeki yakıt kompaktı hacimsel oranı 0,23'dir. Her bir bölgenin efektif ısı iletim katsayısı hesaplanırken; grafit, yakıt kompaktı ve Helyum'un varlığı dikkate alınmıştır. Tüm bölgeler anizotropik olduğundan radyal ve eksenel yöndeki efektif ısı iletim katsayıları birbirinden farklıdır.

Grafit, yakıt kompaktı ve Helyum'un hacimsel oranı kullanılarak, aktif kor, üst reflektör ve alt reflektörün radyal yönde efektif ısı iletim katsayısı aşağıdaki Maxwell eşitlikleri ile hesaplanmıştır (Nuclear Energy Agency, 2018).

Aktif korun radyal yönde efektif ısı iletim katsayısı Eş. (1) ile hesaplanmıştır (Stainsby *vd.*, 2009).

Üst ve alt reflektörün radyal yönde efektif ısı iletim katsayısı Eş. (2) ile hesaplanmıştır (Pietrak ve Wisniewski, 2015).

Aktif kor, alt reflektör ve üst reflektörün eksenel yöndeki efektif ısı iletim katsayısı Eş. (3) ile hesaplanmıştır (Nuclear Energy Agency, 2018).

Aktif kor, üst reflektör ve alt reflektör bölgelerinin hesaplanan eksenel ve radyal yöndeki efektif ısı iletimi k_{eff} Tablo 3'de verilmiştir. Hesaplanan efektif ısı iletimi değerleri ilgili gözenekli ortam bölgelerindeki iletim ve ışınımın birleşimini temsil etmektedir.

$$k_{eff} = k_g \left\{ 1 - \frac{2[\alpha_{He}(k_g - k_{He})(k_g + k_{yk}) + \alpha_{yk}(k_g - k_{yk})(k_g + k_{He})]}{(k_g + k_{He})(k_g + k_{yk}) + \alpha_{He}(k_g - k_{He})(k_g + k_{yk}) + \alpha_{yk}(k_g - k_{yk})(k_g + k_{He})} \right\} \quad (1)$$

$$k_{eff} = k_g \left[1 + \frac{3\alpha_{He}}{\left(\frac{k_{He} + 2k_g}{k_{He} - k_g}\right) - \alpha_{He}} \right] \quad (2)$$

$$k_{eff} = k_g\alpha_g + k_{yk}\alpha_{yk} + k_{He}\alpha_{He} \quad (3)$$

Tablo 3. Grafit, yakıt kompaktı ısı iletim katsayısı ve gözenekli ortam bölgelerinin hesaplanan ısı iletim katsayıları.

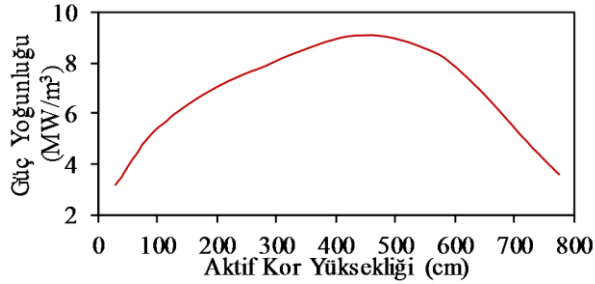
Isı İletim Katsayısı (W/mK)	Sıcaklık (°C)						
	500	600	800	1000	1200	1400	1600
Grafit (Potter, 1995)	29,3	31,4	35,6	37,7	41,4	42,3	43
Yakıt kompaktı (Potter, 1995)	30	27	24	22	20	19	18
k_{eff} aktif kor eksenel yön	23,9	24,5	26,2	27,0	28,7	29,0	29,2
k_{eff} aktif kor radyal yön	16,5	17,7	20,3	22,3	24,7	26,4	27,9
k_{eff} üst/alt reflektör eksenel yön	23,8	25,5	28,9	30,7	33,7	34,4	35,0
k_{eff} üst/alt reflektör radyal yön	16,4	18,2	21,9	24,8	28,7	31,1	33,4
k_{eff} iç/dış reflektör eksenel yön	29,0	31,1	35,2	37,3	40,9	41,8	42,5
k_{eff} iç/dış reflektör radyal yön	21,0	23,3	28,1	31,5	35,9	38,0	39,6

Kaza sırasında 100 saat boyunca zamana bağlı güç üretimi için Eş. (4) kullanılmıştır. Reaktörde fisyon reaksiyonu durdurulduktan sonra güç hemen o anki gücün %10'una düşmektedir. Hesaplamalarda kullanılan

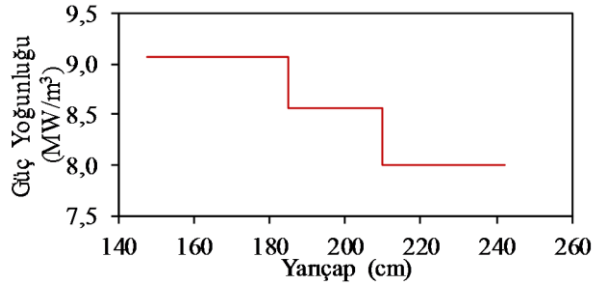
atık ısının zamana bağlı değişimi 30. saniye – 100. saat aralığı için Şekil 8'de görülebilir (Li, 2005).

$$P = P_{or}0,125t^{-0,28} \quad t \geq 1s \quad (4)$$

Reaktör içindeki ısı üretimi dağılımı; yakıt ve reflektör elemanlarının düzeni ve nötronün doğası gereği her yerde aynı değildir. Aktif kordaki güç üretiminin eksenel ve radyal yöndeki değişimi sırasıyla Şekil 3 ve Şekil 4'te görülmektedir (Nouri-Borujerdi ve Tabatabai Ghomsheh, 2015b). Radyal yöndeki güç üretimi değişimini modele girebilmek için aktif kor 3 parçaya bölünmüştür. Güç üretiminin eksenel yöndeki değişimi ve kaza süresince zamana bağlı güç üretimi modele görsel ara yüzden girilemediğinden UDF kullanılmıştır.



Şekil 3. Aktif kordaki eksenel güç yoğunluğu profili.



Şekil 4. Aktif kordaki radyal güç yoğunluğu profili.

CRP-3 kıyaslama probleminde (IAEA, 2001); metalik olan reaktör kabı dış yüzeyinin, kor kabı dış yüzeyinin, reaktör kabı iç yüzeyinin ve RCCS yüzeyinin ısı yalıtım katsayısı 0,8 olarak tanımlanmıştır. RCCS yüzeyi 65°C sıcaklık değerine sahiptir.

Nümerik Hesaplama

Ansys Fluent çözücüsü sonlu hacimler metodu kullanmaktadır. Bölge (domain) sonlu kontrol hacim kümelerine ayrıştırılır (Ansys Inc., 2019). Kütle, momentum, enerji, türler vd. için genel korunum (transport) denklemleri her bir kontrol hacmi üzerinde çözülmektedir. Kısmi diferansiyel denklemler lineer, cebirsel denklemlere dönüştürülür. Daha sonra tüm cebirsel denklemler çözüm alanının oluşturmak için nümerik olarak çözülür (IV ve V, 2019).

Genel korunum (transport) denklemi:

$$\frac{\partial(\rho\phi)}{\partial t} + \text{div}(\rho\phi u) = \text{div}(\Gamma \text{grad } \phi) + S_{\phi} \quad (5)$$

zamana bağlı değişim konveksiyon difüzyon kaynak

Aşağıdaki temel denklemler laminar akış için verilmiştir. Türbülanslı akış için gerekli dönüşümler yapılarak aynı denklemler kullanılır.

Süreklilik denklemi:

$$\frac{\partial \rho}{\partial t} + \nabla(\rho u) = 0 \quad (6)$$

Momentum denklemi:

$$\frac{\partial}{\partial t}(\rho u) + \nabla(\rho u u) = -\nabla p + \mu \nabla^2 u + \rho g \quad (7)$$

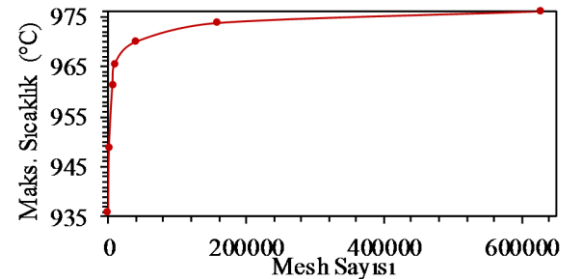
Enerji denklemi:

$$\frac{\partial}{\partial t}(\rho E) + \nabla(u(\rho E + p)) = \nabla(k \nabla T) + \dot{Q} \quad (8)$$

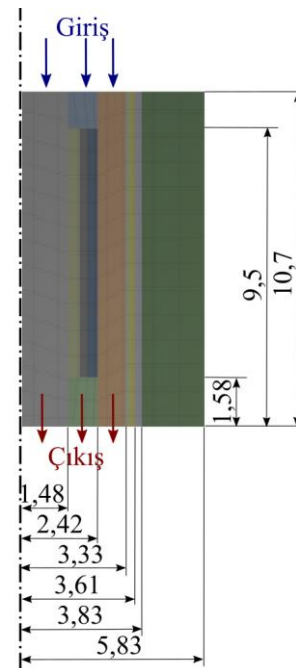
Çözüm Metodu

Eşdeğer Silindir Model kullanılarak, 2 boyutlu ve aksisimetrik model oluşturulmuş ve ısı akış analiz nümerik olarak Ansys Fluent ile yapılmıştır.

Şekil 5'te görüleceği üzere geometri üzerinde küçükten büyüğe farklı hücre (mesh) sayılarında bir dizi analiz yapılmış, 158120 hücre sayısından itibaren maksimum sıcaklığın çok fazla değişmediği görüldüğünden Şekil 6'daki hücre yapısı kullanılmıştır.



Şekil 5. Farklı mesh sayılarına göre tepe sıcaklığı değişimi



Şekil 6. Ağın görünümü ve modelin ölçüleri (m)

Zamana bağılı kaza durumu analizleri için büyükten küçüğe farklı zaman adımlarında (time step) bir dizi analiz yapılmış, 30sn den itibaren tepe sıcaklığının çok fazla değişmediği görüldüğünden bu zaman adımı kullanılmıştır.

Tablo 4’de; hücre sayısına göre hesaplanan maksimum sıcaklıklara göre belirsizlik analizi çalışması yapılmıştır.

Tablo 4. Belirsizlik analizi çalışması

	Element Boyutu	Hücre Sayısı	Maksimum Sıcaklık (°C)
Kaba	0,04	40081	969,797
Orta	0,02	158120	973,558
İnce	0,01	628677	975,882

Simülasyondaki nümerik hataları tespit etmek için; Roache (Roache, 1994) tarafından önerilen belirsizlik değerlendirme prosedürü uygulanmıştır.

$$p = \ln \left(\frac{f_3 - f_2}{f_3 - f_1} \right) / \ln(2) \quad (9)$$

$$f_{h=0} = f_1 + \frac{f_1 - f_2}{2^p - 1} \quad (10)$$

$$GCI_{12} = 1,25 \frac{(f_1 - f_2)}{f_1(2^p - 1)} 100 \quad (11)$$

$$GCI_{23} = 1,25 \frac{(f_2 - f_3)}{f_2(2^p - 1)} 100 \quad (12)$$

$$\frac{GCI_{23}}{2^p GCI_{12}} \cong 1 \quad (13)$$

Burada; Eşitlik 9’den yakınsama mertebesi p , 0,695’dir. $f_{h=0}$, $h=0$ ’daki değeri tahmin etmeye yönelik Richardson ekstrapolasyonu 979,641°C’dir. GCI_{12} , orta ve ince seviyesi için yakınsama indeksi 0,48 ‘dir. GCI_{23} , ince ve kapa seviyesi için yakınsama indeksi 0,78’dir. Asimptotik yakınsama aralığı 1,0024’dür.

Türbülans modeli olarak “Standart k-e”, “Realizable k-e” ve “RNG k-e” türbülans modelleri ile çözüm yapılmıştır. Bütün değişkenlerin kalıntı değerleri diğerlerine göre daha monoton ve değişken bir azalma gösterdiğinden; “Standard Wall Functions” duvar tipi ile “Standart k-e” türbülans modeli tercih edilmiştir. Analizler S2S ve DO ışıınım modelleri ile yapılmış, aynı sonucu daha kısa sürede verdiği için S2S ışıınım modeli tercih edilmiştir.

Ayrıca yapılan analizlerde çözüm yakınsamış, iterasyon sayısından bağımsız hale getirilmiş ve korunum denklemleri sağlanmış. Nükleer reaktör kaza analizlerinin deneysel olarak gerçek boyutlarda yapılması çok zordur. Bu nedenle nükleer reaktör kaza durumu analizleri için tavsiye edilen koddan koda karşılaştırma yapılmıştır. Böylece çözümün doğruluğu ve geçerliliğinin kontrolü tamamlanmıştır.

Hesaplamalar iki basamakta yapılmıştır. Simülasyon ilk olarak sürekli rejimdeki tam güçteki normal çalışma durumu için çalıştırılmıştır. İlk basamağın sonuçları zamana bağılı kaza durumunun başlangıç koşulu olarak tanımlanmıştır. Diğer bir deyişle normal çalışma durumundaki sıcaklık dağılımı kaza durumunun başlangıç şartı olarak kullanılmıştır. Daha sonra zamana bağılı kaza durumu simülasyonu toplam 100 saatlik bir süre için gerçekleştirilmiştir.

Sürekli rejim normal çalışma durumu ve zamana bağılı kaza durumuna ilişkin yöntemler Tablo 5’te görülmektedir.

Tablo 5. Hesaplama yöntemleri

	Sürekli Rejim (Normal Çalışma Durumu)	Zamana Bağılı (Kaza Durumu)
Çözüm metodu	Coupled	PISO
Akış eşitliği	Çözüldü	Çözülmedi
Türbülans eşitliği	Standard k-ε	Çözülmedi
Enerji eşitliği	Çözüldü	Çözüldü
İşınım modeli	S2S	S2S
Yakınsama kriteri	1.0E-6	1.0E-6

Kabuller ve Basitleştirmeler

Modelin karmaşıklığını ve çözüm süresini azaltmak için yukarıda sözü edilenlere ek olarak aşağıdaki varsayımlar ve sadeleştirmeler yapılmıştır:

- Reaktör boşluğunda doğal taşınım ile ısı transferi bulunmamaktadır.
- Reaktör üst ve alt boşluğu modellenmemiştir. Reaktörün üst ve alt dış yüzeyinin adyabatik olduğu varsayılmıştır.
- Aktif kor ve reflektör elemanları arasındaki boşluklarda ve soğutma kanallarındaki boşluklarda ışıınım ile ısı transferi efektif ısı iletimi içerisinde hesaba katılmıştır.
- Soğutma kanalları boşlukları, aktif kor ve reflektör elemanları arasındaki boşluklar içinde meydana gelen doğal taşınım ile ısı transferi başıncısız kaza durumu incelendiğinden ihmal edilmiştir.
- Grafit ve yakıt kompaktı haricindeki malzemelerin fiziksel özellikleri sıcaklıkla değişmemektedir.

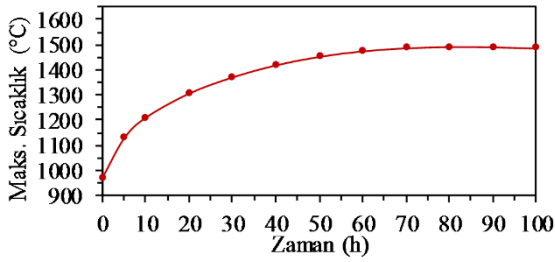
Yapılan kabullerin kaza durumundaki tepe sıcaklığı üzerinde ihmal edilecek kadar az ya da tepe sıcaklığını azaltan etkisi vardır. Bu nedenle; yapılan hesapların konservatif (%95 seviyede güvenilir) olduğu düşünülmektedir.

SONUÇLAR VE TARTIŞMALAR

Bu başlık altında ilk olarak oluşturulan modelin sonuçları sunulmuştur. Daha sonra oluşturulan model yapılan diğer çalışmalarla karşılaştırılarak doğrulanmıştır. Son olarak oluşturulan model üzerinde bazı parametreler değiştirilerek duyarlılık analizi yapılmıştır.

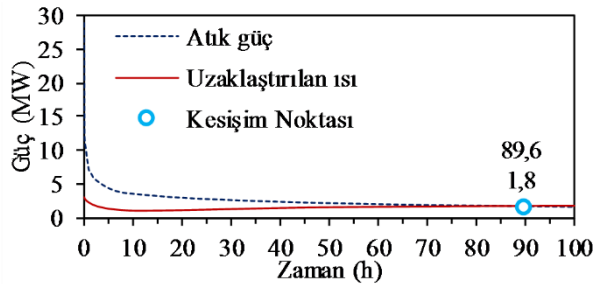
Mevcut Analiz

Normal çalışma durumundaki Helyum akışının aniden kesilmesi ile kaza başlar. Kazanın başlamasından sonra reaktör kapanır ve reaktör koru içerisindeki maksimum sıcaklık reaktör içinde atık ısı ürettiğinden artar. Kazadan sonra ilk olarak; üretilen atık ısı, uzaklaştırılan ısıdan daha büyük olduğundan reaktörün içindeki sıcaklık kademeli olarak artar. Sıcaklık; maksimum değerine ulaşır ve reaktör kabının dış yüzeyinden uzaklaştırılan ısı arttığından ve atık ısı kademeli olarak azaldığından azalmaya başlar. Soğuma sürecinde maksimum sıcaklığın çıktığı en yüksek değer tepe sıcaklığı olarak adlandırılır. Şekil 7'de görüleceği gibi; reaktör tepe sıcaklığı 83. saatte ulaşmış ve daha sonra reaktör yavaşça soğumaya başlamıştır. Reaktör kapandıktan sonra soğuma sürecinde görülen tepe sıcaklık 83. saatte 1492°C dir. Aktif kor tepe sıcaklığı 1600°C olan nominal tasarım sınırı içindedir. Basıncısız kaza durumu incelendiğinden taşınım ile ısı transferi göz ardı edildiği için gerçekte tepe sıcaklığı daha düşük olacaktır.



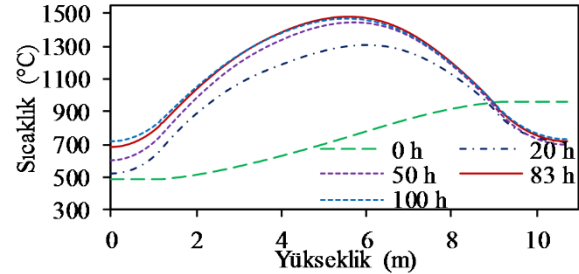
Şekil 7. Mevcut analizin hesaplanan aktif kor maksimum sıcaklık değişimi

MHR doğal güvenlik karakteristiğine sahiptir. Korun içinde çok miktarda grafit bulunduğundan kendiliğinden soğuyabilir. Grafit ısı depolayabilmekte ve hızlı sıcaklık artışını önleyebilmektedir. Bu nedenle MHR içinde en fazla 100 saat içinde maksimum sıcaklık oluşmakta ve sonra reaktör soğuyabilmektedir. Atık ısı reaktör kabının dış yüzeyinden pasif olarak uzaklaştırılır. Şekil 8 hesaplanmış uzaklaştırılan ısıyı göstermektedir. Kor gücü ve uzaklaştırılan ısı oranları 89,6.saatte eşit olmaktadır. Kaza süresince RCCS'ye aktarılan güç 1,2-3,1MW aralığında seyretmektedir.



Şekil 8. 30. saniye - 100. saat aralığında hesaplamalarda kullanılan atık ısı eğrisi ve hesaplanmış uzaklaştırılan ısı oranı

Şekil 9 kaza durumunun 0. 20., 50. 83. ve 100. saatinde korun 1,72m yarıçapındaki eksenel sıcaklık dağılımını göstermektedir. Kazadan önce normal çalışma durumunda maksimum sıcaklık kor çıkışında meydana gelmektedir. Şekilde görüldüğü gibi sıcak bölge zamanla kademeli olarak yukarı doğru aktif korun merkezine kaymaktadır.



Şekil 9. Kaza süresince korun 1,72 m yarıçapındaki eksenel sıcaklık dağılımı

Kor kabı dış yüzeyi ile reaktör kabı iç yüzeyi arasında sıcaklık farkının çok olması nedeniyle ışınlama ile ısı transferinin önemli ölçüde olduğu görülmüştür. Zamana bağlı analizlerde ışınlama modeli çözülmediği zaman; maksimum sıcaklık sürekli yükselmekte, ısı kor içinde kalmakta ve reaktör kabına geçmemektedir.

Nümerik Modelin Doğrulaması

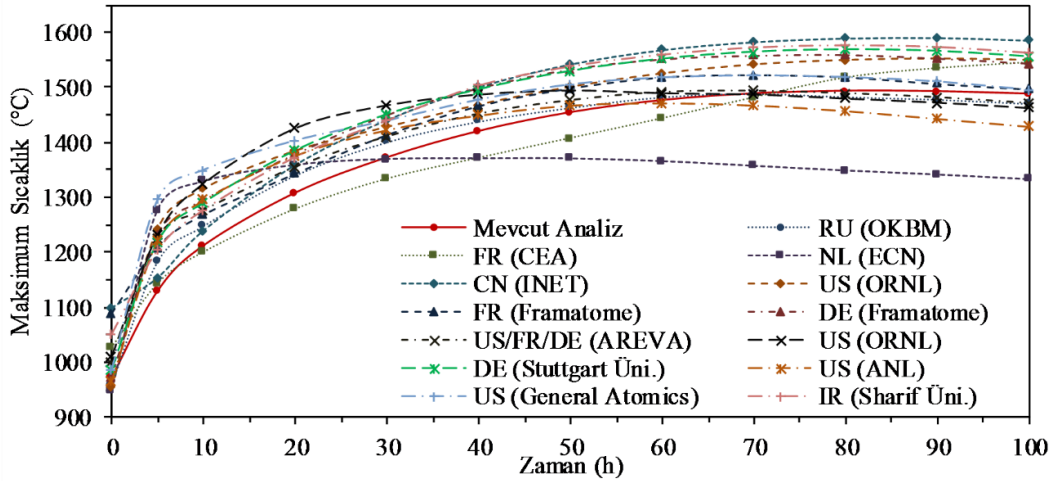
SAD çözümlerde elde edilen sonuçların deneysel sonuçlarla karşılaştırılması, sonuçların doğruluğu ve güvenilirliği açısından gereklidir. Eğer hiçbir şekilde deneysel veri mevcut değilse, bu kesin karşılaştırma literatürde kabul görmüş teorik, analitik veya diğer nümerik çözümlerle yapılabilir. Nükleer reaktörlerin deneysel olarak doğrulamasındaki güçlükler nedeniyle genelde koddan koda kıyaslama yapılmaktadır.

Oluşturulan modelin doğrulaması diğer nümerik çözümlerle karşılaştırmak suretiyle yapılmıştır. Mevcut analizin çok çeşitli araçlar ve yöntemler kullanılarak yapılan diğer analizlerle karşılaştırılması Tablo 6 ve Şekil 10'da verilmiştir.

Şekil 10 kaza süresince zamanla reaktördeki maksimum sıcaklık değişiminin diğer analizlerle karşılaştırılmasını göstermektedir. Mevcut analizde elde edilen maksimum sıcaklık profili, diğer hesaplamalarla uyum göstermektedir. Geliştirilen mevcut modelin nispeten tatmin edici sonuçlar verdiği görülmüştür. Tepe sıcaklığındaki farklılıkların; farklı modellemelerden, malzeme özelliklerinden, güç dağılımından, nümerik yöntemlerden kaynaklanabileceği düşünülmektedir.

Tablo 6. Kıyaslama karşılaştırmasının sonuçları

Kod/Yazılım	Çalışmayı Yapan Kuruluş	Tepe Sıcaklığı (°C)	Tepe Sıcaklığı Zamani (Saat)
POKE/TAC2D (Potter, 1995)	GA-US	1521	72
GTAS (IAEA, 2001)	OKBM-RU	1490	70
CASTEM (IAEA, 2001)	CEA-FR	1565	140
CFX-F3D (Siccama ve Koning, 1998)	ECN-NL	1371	42
THERMIX/KONVEK (IAEA, 2001)	INET-CN	1590	87
MORECA (IAEA, 2001)	ORNL-US	1552	87
STAR CD (Woaye-Hune ve Ehster, 2002)	Framatome-FR	1525	71
THERMIX/KONVEK (Haque vd., 2006, 2004)	Framatome-DE	1560	75
STAR CD (Mays vd., 2004)	AREVA-US/FR/DE	1494	67
MGT-3D (Shi, 2015)	Aachen Üni.-DE	1535	70
TH3D (Hossain, 2011; Hossain vd., 2008)	Stuttgart Üni.-DE	1568	80
THPP (Nouri-Borujerdi ve Tabatabai Ghomsheh, 2015a)	Sharif Tek. Üni.-IR	1577	83
GRSAC (Ball, 2006, 2004)	ORNL-ABD	1494	53
RELAP5 (Vilim vd., 2005)	ARNL-US	1471	61
RELAP5-3D/ATHENA (Reza vd., 2006)	Texas Üni/INL/GA-US	1437	59
RELAP5-3D/ATHENA (MacDonald vd., 2003)	INEEL-US	1514	53
Ansys Fluent	Mevcut Çalışma	1492	83



Şekil 10. Mevcut analiz ve diğer çalışmaların kaza durumunda aktif kor maksimum sıcaklığı değişimi

Duyarlılık Analizi

Grafitin ısı iletim katsayısı; sıcaklığa, grafit türüne ve ayrıca aldığı radyasyona, tavlama miktarına bağlıdır. Reaktör gücünün artırılması atık ısının artmasına neden olmaktadır. Metal ısınım yayma katsayısı reaktörün ömrü boyunca değişebilmektedir. Bu nedenlerden dolayı aşağıdaki parametrelerin aktif kor maksimum sıcaklığı üzerindeki etkileri incelenmek suretiyle duyarlılık analizi yapılmıştır:

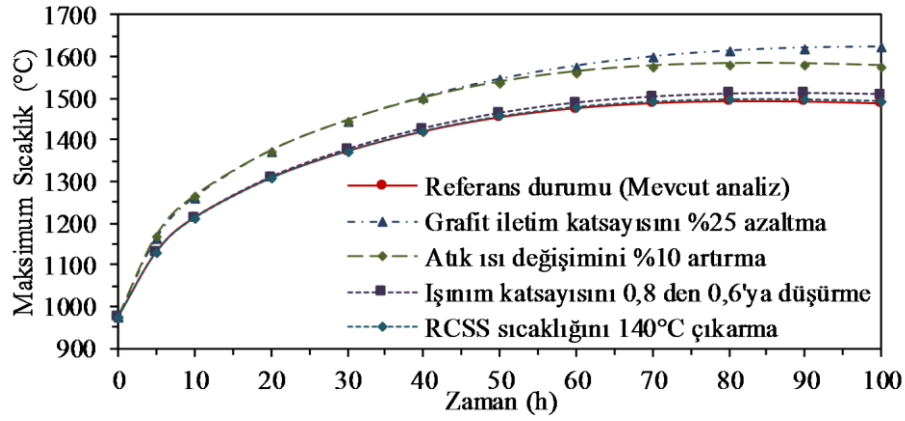
- grafit iletim katsayısını %25 azaltma,
- atık ısı değişimini %10 artırma,
- metal ısınım yayma katsayısını 0,8'den 0,6 ya düşürme,
- RCCS soğutma tüpü sıcaklığını 65°C'den 140°C'ye çıkarma.

Şekil 11 grafit ısı iletimi, atık ısı, metalik yüzey ısınımı ve RCCS soğutma tüplerinin sıcaklık değişiminin aktif kor maksimum sıcaklığı değişimi üzerindeki etkisini göstermektedir. Duyarlılık analizi aktif kor maksimum

sıcaklığının önemli ölçüde grafit ısı iletimine ve atık ısıya bağlı olduğunu göstermektedir.

Grafitin ısı iletiminin %25 azalması aktif kor tepe sıcaklığının referans durumundan 131°C daha yüksek olan 1624°C'ye kadar yükselmesine yol açmıştır. Aktif kor tepe sıcaklığı, azalan grafit termal iletkenliği ile önemli ölçüde artmıştır. Buna rağmen normal çalışma durumunda reaktörde oluşan maksimum sıcaklık değişimine etkisi olmamıştır. Atık gücün %10 artması, aktif kor tepe sıcaklığının 1583°C'ye kadar yükselmesine neden olmuştur. Metalik yüzey ısınımının 0,8 'den 0,6 'ya azalması ile, aktif kor tepe sıcaklığı 1558°C'ye yükselmiştir. RCCS soğutma tüplerinin 65°C yerine 140°C 'ye yükseltilmesi tepe sıcaklığı üzerinde ihmal edilebilir bir etkiye sahiptir.

Referans durumu diğer duyarlılık analizleri ile karşılaştırılmıştır. Tablo 7 bu analizlerin özeti göstermektedir.



Şekil 11. Duyarlılık analizi

Tablo 7. Değişik duyarlılık analizlerinin karşılaştırma sonuçları

	Çalışmayı Yapan Kuruluş	Tepe Sıcaklığı Artışı (°C)
Grafit iletiminin %25 azalması	INET (IAEA, 2001)	202
	OKBM (IAEA, 2001)	110
	Framatome (IAEA, 2001)	188
	Aachen Üni. (Shi, 2015)	100
	ORNL (Ball, 2006, 2004)	124
	Mevcut analiz	131
Atık ısının %10 artması	INET (IAEA, 2001)	115
	OKBM (IAEA, 2001)	80
	ORNL (IAEA, 2001)	98
	Framatome (Woaye-Hune ve Ehster, 2002)	85
	Aachen Üni. (Shi, 2015)	127
	Mevcut analiz	90
Metalik yüzey ışınımını 0,8 'den 0,6 'ya düşürme	INET (IAEA, 2001)	62
	OKBM (IAEA, 2001)	25
	Framatome (Woaye-Hune ve Ehster, 2002)	30
	Aachen Üni. (Shi, 2015)	54
	Mevcut analiz	65

SONUÇLAR

VHTR'lerin tasarımında reaktörden yüksek çıkış sıcaklığı elde edilmek istenirken; normal çalışma ve kaza durumunda reaktörde oluşan maksimum sıcaklığın düşük olması istenmektedir. Kaza süresince aktif soğutma sisteminin çalışmaması durumunda reaktörde oluşan tepe sıcaklığın reaktör tasarım sınırlarını geçmemesi tasarım esnasında göz önünde bulundurulması gereken en önemli hususlardan biridir.

Bu çalışmada VHTR tasarımı adaylarından biri olan MHR'nin kaza durumunu incelemek için Ansys Fluent ile bir model geliştirilmiştir. Geliştirilen model diğer çalışmalarla karşılaştırmak suretiyle doğrulanmıştır. Zamana bağlı ısı-akış analizde kaza durumunda reaktörde oluşan maksimum sıcaklık 1492°C bulunmuştur. Söz konusu tepe sıcaklığına kazanın 83. saatinde ulaşıldığı hesaplanmıştır. Oluşan maksimum sıcaklık değeri TRISO kaplamalı yakıt parçası için kaza durumunda radyoaktivite salınımı ile ilgili sınır sıcaklığı olan 1600°C altındadır.

Mevcut çalışma ve literatürde bulunan diğer çalışmalardan elde edilen sonuçlar; MHR'nin kaza durumunda reaktörde oluşan maksimum sıcaklığın 1471°C ile 1590°C arasında, tepe sıcaklığı zamanının ise 53-87 saatleri arasında yoğunlaştığını göstermektedir.

Kaza boyunca reaktör boşluğu ve RCCS'ye aktarılan güç ortalama 2MW'dır. Kaza durumunda atık ısı ile uzaklaştırılan ısı değerlerinin 89,6.saatte eşit olduğu hesaplanmıştır. Kaza durumunda yüksek sıcaklık farklarından dolayı hem reaktör içinde hem de reaktör dışında ışımla ısı transferinin çok etkili olduğu görülmüştür.

Yapılan duyarlılık analizlerinde kaza durumunda oluşan maksimum sıcaklığa en çok grafit ısı iletim katsayısı ve atık ısı değişiminin etkisi olduğu bulunmuştur. Grafit ısı iletim katsayısının %25 azalması; normal çalışma durumunda maksimum sıcaklığa etkisi olmamasına rağmen, kaza durumunda aktif kor tepe sıcaklığını 131°C artırmaktadır. Metal ışınım yayma katsayısı ve RCCS sıcaklığı değişiminin aktif kor tepe sıcaklığı üzerine etkisi azdır.

Oluşturulan sayısal metodoloji diğer çalışmalarla karşılaştırmak suretiyle doğrulanmış ve gelecek VHTR tasarımları için hazır hale getirilmiştir. Sonuçlar VHTR'nin maksimum çıkış sıcaklığı, termal gücü vb. ile ilgili tasarım optimizasyonu için bazı temel bilgiler sağlayacaktır. Bu çalışmanın devamı olarak; oluşturulan model üzerinde giriş sıcaklığı, giriş debisi, reaktör gücü veya boyutsal değişimler yapılarak etkileri incelenebilir.

TEŞEKKÜR

Bu çalışma Gazi Üniversitesinin bilimsel araştırma projesi (BAP 07/2009-22) ile desteklenmiştir.

KAYNAKLAR

ANSYS Inc., 2019, Ansys Fluent Theory Guide, *ANSYS Inc.*, Canonsburg.

ANSYS Inc., 2019, Ansys Fluent User's Guide, *ANSYS Inc.*, Canonsburg.

Ball, S., 2006, Sensitivity Studies of Modular High-Temperature Gas-Cooled Reactor Postulated Accidents, *Nucl. Eng. Des.*, 236, 454–462.

Ball, S., 2004, Sensitivity Studies of Modular High-Temperature Gas-Cooled Reactor (MHTGR) Postulated Accidents, *2nd International Topical Meeting on High Temperature Reactor Technology*, Beijing-China, 1–13.

Fukuda, K., Kendall, J., Kupitz, J., Matzner, D., Mulder, E., Pretorius, P., Shenoy, A., Shiozawa, S., Simon, W., Sun, Y., Uselton, P. ve Xu, Y., 2001, Current Status and Future Development of Modular High Temperature Gas Cooled Reactor Technology, IAEA-TECDOC-1198, IAEA, Vienna.

Haque, H., Feltes, W. ve Brinkmann, G., 2006, Thermal Response of a Modular High Temperature Reactor during Passive Cooldown under Pressurized and Depressurized Conditions, *Nucl. Eng. Des.*, 236, 475–484. <https://doi.org/10.1016/J.NUCENGDES.2005.10.027>

Haque, H., Feltes, W. ve Brinkmann, G., 2004, Thermal Response of a High Temperature Reactor during Passive Cooldown under Pressurized and Depressurized Conditions, *2nd International Topical Meeting on High Temperature Reactor Technology*, Beijing-China, 1–17.

Hossain, A.S.M.K., 2011, *Development of a Fast Running Multidimensional Thermal-Hydraulic Code to be Readily Coupled with Multidimensional Neutronic Tools, Applicable to Modular High Temperature Reactors*, PhD Thesis, University of Stuttgart, Stuttgart.

Hossain, K., Buck, M., Bernnat, W. ve Lohnert, G., 2008, TH3D, A Three-Dimensional Thermal Hydraulic Tool, for Design and Safety Analysis of HTRS, *HTR'2008*, Washington-USA.

Huning, A.J., Chandrasekaran, S. ve Garimella, S., 2021, A Review of Recent Advances in HTGR CFD and Thermal Fluid Analysis, *Nucl. Eng. Des.*, 373, 111013. <https://doi.org/10.1016/j.nucengdes.2020.111013>

IAEA, 2001, Heat Transport and Afterheat Removal for Gas Cooled Reactors under Accident Conditions, IAEA TECDOC-1163, IAEA, Vienna.

Internet, 2021, National Institute of Standards and Technology, *Thermophysical Properties of Fluid Systems*, <https://webbook.nist.gov/chemistry/fluid>.

IV, J.H.L., V, J.H.L., 2019, A Heat Transfer Textbook, *Phlogiston Press*, Cambridge.

Kiryushin, A.I., Kodochigov, N.G., Kouzavkov, N.G., Ponomarev-Stepnoi, N.N., Gloushkov, E.S. ve Grebennik, V.N., 1997, Project of the GT-MHR High-Temperature Helium Reactor with Gas Turbine, *Nucl. Eng. Des.* 173, 119–129. [https://doi.org/10.1016/S0029-5493\(97\)00099-X](https://doi.org/10.1016/S0029-5493(97)00099-X)

Li, S., 2005, Parametric Thermal-Hydraulic Studies of HTGR Reactor Vessel System - Consequences on the Structure Lifetime, *SMIRT 18*, Beijing-China, 4311–4325.

MacDonald, P.E., Sterbentz, J.W., Sant, R.L., Bayless, P.D., Schultz, R.R., Gougar, H.D., Moore, R.L., Ougouag, A.M. ve Terry, W.K., 2003. NGNP Point Design-Results of the Initial Neutronics and Thermal-Hydraulic Assessments During FY-03, INEEL/EXT-03-00870. INEEL, Idaho.

Mays, B.E., Woaye-Hune, A., Simoneau, J.-P., Gabeloteau, T., Lefort, F., Haque, H. ve Lommers, L., 2004, The Effect of Operating Temperature on Depressurized Conduction Cooldown for a High Temperature Reactor, *ICAPP'04*, Pittsburgh-USA, 1–9.

Moses, D.L., 2010, Very High-Temperature Reactor (VHTR) Proliferation Resistance and Physical Protection (PR&PP), ORNL/TM-2010/163, *Oak Ridge National Laboratory*, Oak Ridge.

Nouri-Borujerdi, A. ve Tabatabai Ghomsheh, S.I., 2015a, Porous Media Approach in Thermohydraulic Analysis of High Temperature Reactors in Pressurized/Depressurized Cooldown: An Improvement, *Prog. Nucl. Energy*, 80, 119–127. <https://doi.org/10.1016/J.PNUCENE.2014.11.017>

Nouri-Borujerdi, A. ve Tabatabai Ghomsheh, S.I., 2015b, An Improved Porous Media Approach to Thermal-Hydraulics Analysis of High-Temperature Gas-Cooled Reactors, *Ann. Nucl. Energy*, 76, 485–492. <https://doi.org/10.1016/J.ANUCENE.2014.10.006>

Nuclear Energy Agency, 2018, NEA Benchmark of the Modular High-Temperature Gas-Cooled Reactor-350

MW Core Design Volumes I and II, *NEA/NSC/R(2017)4*, OECD.

Pietrak, K. ve Wisniewski, T.S., 2015, A Review of Models for Effective Thermal Conductivity of Composite Materials, *J. Power Technol*, 95, 14–24.

Pioro, I.L., 2016, Handbook of Generation IV Nuclear Reactors, Handbook of Generation IV Nuclear Reactors, *Elsevier Inc*, <https://doi.org/10.1016/C2014-0-01699-1>

Potter, R.C., 1995, GT-MHR Conceptual Design Description Report, GA Project No. 6302, *General Atomics*, San Diego.

Reza, S.M., Harvego, E.A., Richards, M., Shenoy, A. ve Peddicord, K.L., 2006, Design of an Alternative Coolant Inlet Flow Configuration for the Modular Helium Reactor, *ICAPP'06*, Reno-USA.

Roache, P.J., 1994, Perspective: A Method for Uniform Reporting of Grid Refinement Studies, *J. Fluids Eng*, 116, 405–413.

Şahin, H.M., Erol, Ö. ve Acır, A., 2012, Utilization of Thorium in a Gas Turbine – Modular Helium Reactor, *Energy Convers. Manag*, 63, 25–30. <https://doi.org/10.1016/j.enconman.2012.01.027>

Şahin, S., Erol, Ö. ve Mehmet Şahin, H., 2016, Investigation of a Gas Turbine-Modular Helium Reactor

Using Reactor Grade Plutonium With ^{232}Th And ^{238}U , *Prog. Nucl. Energy*, 89, 110–119. <https://doi.org/10.1016/j.pnucene.2016.02.006>

Shi, D., 2015, *Extension of the Reactor Dynamics Code MGT-3D for Pebblebed and Blocktype High-Temperature-Reactors*, PhD Thesis. RWTH Aachen University, Aachen.

Siccama, N.B. ve Koning, H., 1998, Afterheat Removal from a Helium Reactor under Accident Conditions: CFD Calculations for the Code-to-Code Benchmark Analyses on the Thermal Behavior for the Gas Turbine Modular Helium Reactor, ECN-RX-97-066, *ECN Nucleaire Research/Faciliteiten (NRG)*, Netherlands.

Stainsby, R., Worsley, M., Dawson, F. ve Grief, A., 2009, Investigation of Local Heat Transfer Phenomena in a Prismatic Modular Reactor Core, NR001/RP/001 R02, *AMEC NSS Limited*, Toronto.

Vilim, R.B., Feldman, E.E., Pointer, W.D. ve Wei, T.Y.C., 2005, Generation IV Nuclear Energy System Initiative Initial VHTR Accident Scenario Classification: Models and Data, ANL-GenIV-057, *Argonne National Laboratory*, Lemont.

Woaye-Hune, A. ve Ehster, S., 2002, Calculation of Decay Heat Removal Transient by Passive Means for a Direct Cycle Modular HTR, *HTR2002*, Petten-NL, 1–7.



Ömür AKBAYIR Lise eğitimini Demiryolu Meslek Lisesinde, Lisans ve Yüksek Lisans Eğitimini Eskişehir Osmangazi Üniversitesinde, Doktora eğitimini Gazi Üniversitesinde tamamlamıştır. 15 yıl TCDD'nin çeşitli işyerlerinde çeşitli görevler üstlendikten sonra, 2015 yılından beri Eskişehir Teknik Üniversitesinde Dr. Öğr. Üyesi olarak çalışmaktadır.



NUMERICAL ANALYSIS OF MICROWAVE CANCER THERAPY USING SINGLE AND DOUBLE SLOT ANTENNAS FOR BREAST AND LIVER TISSUES

Aykut EREN*, Zeynep AYTAÇ**, Ođuz TURGUT*** and Burak TIđLI****

*Gazi Üniversitesi Mühendislik Fakültesi Makina Mühendisliđi Bölümü
06570 Maltepe, Ankara

*aykuteren5@gmail.com, ORCID: 0000-0003-2356-9331

**zeynepaytac@gazi.edu.tr, ORCID: 0000-0003-0717-5287

***oturgut@gazi.edu.tr, ORCID: 0000-0001-5480-1039

****buraktigli@gmail.com, ORCID: 0000-0003-1027-9247

(Geliş Tarihi: 22.09.2021, Kabul Tarihi: 21.02.2022)

Abstract: Microwave cancer therapy is an effective method used to destroy cancer cells which eliminates the need for surgical intervention in diseases such as breast and liver cancer. The present study aims to present a methodology for the destruction of killing the malignant cells in a wider periphery by means of burning in a shorter time meanwhile causing minimal damage to the healthy tissues. The study is carried out for a frequency value of 2.45 GHz and for a power value of 10 W using finite element methods. A comparison between coaxial single-slot antenna and double-slot antenna is conducted for liver and breast tissues. Investigated parameters are the slot number, the type of the tissue and the duration of microwave cancer therapy. The specific absorption rate and temperature distribution are the examined parameters. The results of the study show that both peak specific absorption rate and peak temperature value are obtained for microwave coaxial single slot antenna within the liver tissue, and it is observed that the temperature distribution depends on time. Maximum temperature value is attained as 93.9°C and 82.8°C for single and double slot antennas for liver tissue whereas the so-called values are 93.0°C and 69.8°C for breast tissue. New correlations are given for the treatment of liver and breast tissues using coaxial single slot antenna. It is anticipated that the present study makes a contribution in the field of medicine.

Keywords: Microwave ablation technique, Microwave coaxial antenna (MCA), Specific absorption rate (SAR), Effective wavelength, Finite element method

MEME VE KARACİĐER DOKULARINDA TEK VE ÇİFT YUVALI ANTEN KULLANILARAK YAPILAN MİKRODALGA KANSER TEDAVİSİNİN NÜMERİK ANALİZİ

Özet: Mikrodalga tedavisi, meme ve karaciđer kanseri gibi hastalıklarda, kanserli hücreleri yok etmek için cerrahi müdahale ihtiyacını ortadan kaldırabilen etkili bir yöntemdir. Mevcut çalışma, malign hücrelerin daha geniş bir çevrede, daha kısa sürede yakılırken çevre dokulara en az hasara sebep olmayı amaçlayan bir metodoloji sunmayı hedeflemektedir. Bu çalışma, 2.45 GHz frekans ve 10 W güç değeri kullanılarak sonlu eleman metoduyla gerçekleştirilmiştir. Meme ve karaciđer dokularında, eş eksenli tek yuvalı ve çift yuvalı antenler için bir kıyaslama sunulmuştur. Araştırılan parametreler yuva sayısı, doku tipi ve mikrodalga kanser tedavisinin süresi iken sonuçta incelenen parametreler özgül sođrulma oranı ve sıcaklık dağılımıdır. Çalışmanın sonucunda, hem en yüksek özgül sođrulma oranı hem de en yüksek sıcaklık değeri, karaciđerde tek yuvalı antenle elde edilmiştir ve elde edilen sıcaklık dağılımının zamana bađlı olduđu görülmüştür. Karaciđerde elde edilen en yüksek sıcaklık değeri, tek yuvalı antende 93.9°C ve çift yuvalı antende 82.8 °C olmuştur. Aynı değerler meme dokusunda, tek yuvalı antende 93.0 °C ve çift yuvalı antende 69.8 °C olarak kaydedilmiştir. Tek yuvalı anten için, karaciđer ve meme dokularının tedavisinde kullanılmak üzere yeni korelasyonlar sunulmuştur. Yapılan çalışmanın, tıp alanında katkı sağlaması beklenmektedir.

Anahtar Kelimeler: Mikrodalga ablasyon tekniđi, Mikrodalga eş eksenli anten, Özgül sođurma değeri, Efektif dalga boyu, Sonlu elemanlar metodu

NOMENCLATURE

c Speed of light in free space [$m \cdot s^{-1}$]
C Heat capacity of tissue [$J \cdot kg^{-1} \cdot ^\circ C$]
C_b Heat capacity of blood [$J \cdot kg^{-1} \cdot ^\circ C$]

E Electric field [$V \cdot m^{-1}$]
f Microwave frequency [GHz]
H Magnetic field [A/m]
k Propagation constant [m^{-1}]
L Arc length [m]

n	Normal vector
P	Input microwave power [W]
\dot{Q}_{ext}	External heat source [$W \cdot m^{-3}$]
\dot{Q}_{met}	Metabolic heat source [$W \cdot m^{-3}$]
r, z	Components of cylindrical coordinates [m]
r_i	Inner radius of the coaxial cable [m]
r_o	Outer radius of the coaxial cable [m]
t	Time [s]
T	Temperature [$^{\circ}C$]
T_b	Blood Temperature [$^{\circ}C$]
Z	Wave impedance in the dielectric of the coaxial cable [Ω]
ϵ_o	Permittivity of free space [F/m]
ϵ_r	Relative permittivity [-]
λ	Wavelength [m]
λ_{eff}	Effective wavelength [m]
μ_o	Permeability of free space [H/m]
ρ	Density of the tissue [kg/m^3]
ρ_b	Blood density [$kg \cdot m^{-3}$]
σ	Electrical conductivity of tissue [$S \cdot m^{-1}$]
σ_{el}	Electrical conductivity [$S \cdot m^{-1}$]
ω	Angular frequency [rad/s]
ω_b	Blood perfusion rate [s^{-1}]
MCA	Microwave coaxial antenna
PTFE	Polytetrafluoroethylene
SAR	Specific absorption rate

INTRODUCTION

Throughout the world, the most frequently encountered and diagnosed types of cancer are female breast (11.7%), lung (11.4%), colorectal (10%), prostate (7.3%), and stomach (5.6%) cancer while the terminal types are mostly lung (18.0%), colorectal (9.4%), liver (8.3%), stomach (7.7%) and female breast (6.9%) cancers in 2020 (Sung *et al.*, 2021). The traditional treatment methods for liver and breast cancer are surgical operation, heating/hyperthermia (radiofrequency ablation, microwave ablation, laser), freezing (cryosurgery), chemotherapy or radiation therapy (radiotherapy) depending on the current situation of the patient. Hyperthermia method can be implemented to a local point, to a regional area or to the entire body (Rubio *et al.*, 2011). The microwave cancer treatment is a type of the hyperthermia method which is applied locally.

Microwave cancer therapy, also known as thermal therapy/thermotherapy, is one of the methods used in cancer treatment by exposing the malignant tissue to high temperature. Radiofrequency waves which are transmitted from the tip of microwave antenna causes heating as a result of the increased kinetic energy of polar water molecules (Kaur and Mann, 2014).

Damaging the proteins and structures within the cancer cell cause the tumors to shrink, and finally these cells end up dead. The advantages of the microwave cancer therapy method are heating the zone in a shorter time as well as reaching wider lesions with blood perfusion.

Three types of antennas (monopole, dipole, and slot) are commonly encountered in using microwave cancer therapy due to their low cost, simple design and small dimensions. Literature investigation has shown that many researchers have studied the cancer treatment using microwave ablation method with slot antenna.

Rubio *et al.* (Rubio *et al.*, 2011) modeled double slot antenna employing two different numerical methods, the finite element method and a finite-difference time-domain. Kaur and Mann (Kaur and Mann, 2014) conducted a study to compare the results of coaxial single and double slot antennas at a frequency of 2.45 GHz and at a power of 10 W for liver tissue. Rossetto and Staufer (Rossetto and Staufer, 1999) examined the effect of bolus-tissue load on SAR distribution at a frequency of 915 MHz using finite difference time domain method. Hamada *et al.* (Hamada *et al.*, 2000) studied the electric field and the SAR distribution inside the human body (muscle) using finite difference time domain method by using four different antennas. Kim and Rahmat-Samii (Kim and Rahmat-Samii, 2004) numerically studied a cancer cell located in brain using single slot dipole antenna. Keane *et al.* (Keane *et al.*, 2011) examined the thermal profiles for cardiac tissue using monopole antenna at a frequency of 2.45 GHz. Keangin *et al.* (Keangin *et al.*, 2011) investigated the effects of a single and double slot coaxial antennas for liver tissue using finite element method. Jiao *et al.* (Jiao *et al.*, 2012) calculated SAR value and temperature distribution for ex vivo pork liver by means of finite element analysis using coaxial slot antenna. Acikgoz and Turer (Acikgoz and Turer, 2014) conducted a study to investigate the effect of T-ring shape mounted on the outer conductor of the structure using microwave coaxial slot antenna for the treatment of liver cancer; SAR and backward heating effects were investigated. Zafar *et al.* (Zafar *et al.*, 2014) used the single and double slot antennas to compare SAR distribution using finite element method for liver tissue. Rubio *et al.* (Rubio *et al.*, 2015) numerically investigated the microwave ablation in breast cancer using a coaxial slot antenna. Razib *et al.* (Razib *et al.*, 2016) focused on antenna's slot position within the breast tissue. SAR and temperature distribution were studied, and it was stated that the slot position of the antenna is substantial for the treatment of cancer tissue. Keangin and Rattanadecho (Keangin and Rattanadecho, 2013) numerically investigated the heat transport for local thermal non-equilibrium in porous liver during microwave ablation using finite element method. Keangin and Rattanadecho (Keangin and Rattanadecho, 2018) conducted a study presenting a numerical simulation of microwave ablation using single slot antenna on the tumor layer and the normal tissue which made up the layers of porous liver tissue. Uzman *et al.* (Uzman *et al.*, 2020) investigated the problem of backward heating in microwave ablation, and they proposed an electromagnetic solution based on the utilization of high impedance graphene material. They analyzed the effects of graphene layer to the heat dissipation in the malignant tissue and the duration of the treatment.

Selmi et al. (Selmi *et al.*, 2020) presented a study about the utilization of the finite element method for liver tissue. They analyzed the electro-thermal effects, temperature distribution profile, SAR, and the fraction of the necrotic tissue within the malignant cells. Tehrani et al. (Tehrani *et al.*, 2020) searched the effects of the shape and size of the tumor on microwave ablation. The coupled bio-heat and electromagnetic equations were solved to obtain the temperature gradient by using a three-dimensional finite element method. In addition, the distance between two slots in the coaxial double slot antenna was modified targeting the best treatment. They concluded that the treatment of larger tumors is harder than the smaller ones.

Literature review revealed that the effect of body type for the cancer treatment using microwave ablation method with slot antenna has not been studied at the mentioned frequency. Therefore, this study concerns the treatment of cancer located in liver and breast tissues by using antenna at the frequency of 2.45 GHz and power of 10 W (Keangin *et al.*, 2011). The investigated parameters are the number of slots, type of the tissue and the duration of the process. Temperature distribution and SAR are examined. The novelty of this study is the investigation of the effect of body type for the cancer treatment using microwave ablation method with slot antenna. Giving the new correlations for the treatment of liver and breast tissues is another innovative aspect of this study.

MATERIAL PROPERTIES AND MODELS

Figure 1 shows the simulation of antennas embedded in the tissue. The antenna is encased in the catheter. Frequency and microwave power are transmitted by antenna to the tissue. Radiation is dispersed to the cell by the radiation port.

The geometries of single and double slot microwave antennas used in this study are shown in Figure 2 for liver and breast tissues. In Figure 2, z and r represents the insertion depth and arc length, respectively. The utilized antenna has a radius of 0.895 mm, i.e., it is excessively thin, which makes it possible to embed it inside the tissue easily. The material of the inner conductor is silver plated copper, and it has a radius of 0.135 mm. The outer conductor is made from copper, and the radius is 0.335 mm. In addition, the slot has a width of 1 mm. The antenna is enclosed in a catheter as mentioned before.

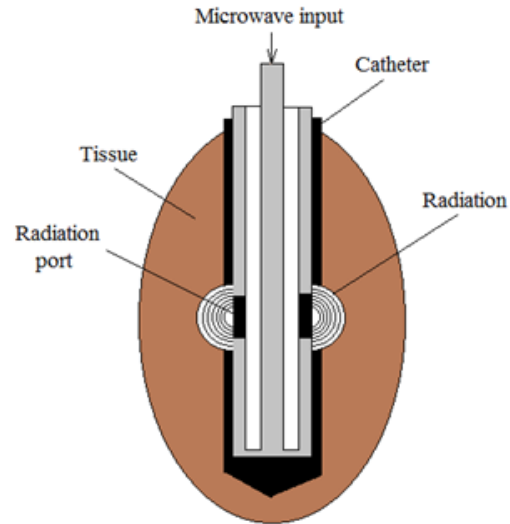


Figure 1. Antenna embedded in a tissue

The catheter is made from polytetrafluoroethylene (PTFE). PTFE has a high dielectric strength, and it is a heat resistant material (-200°C to 260°C). Another advantage of PTFE is that it does not react with any chemicals.

The electric field becomes stronger as the distance to the slot decreases, which causes the maximum temperature to be obtained near the slot. The antenna is based on a 50Ω UT-085B-SS, and it is stainless steel. Microwave frequency operating at 2.45 GHz is applied to heat the tissue (Rubio *et al.*, 2011), (Kaur and Mann, 2014), (Keangin *et al.*, 2011). Microwave ablation therapy transmits energy to the body in shorter wavelengths compared to the other methods. The spacing of slots in the tissue based on the effective wavelength at the frequency of 2.45 GHz is determined by (Rubio *et al.*, 2011), (Keangin *et al.*, 2011).

$$\lambda_{eff} = c/f\sqrt{\epsilon_r} \quad (1)$$

where c is the speed of light in free space, and ϵ_r is the relative permeability of tissue at the operating frequency. f represents the operating frequency of the microwave generator, and it has a value of 2.45 GHz.

The relative permeability of liver and breast tissues are different from each other. In other words, the slot spacing length of the mentioned tissues are not equal. For double slot microwave coaxial antenna, the slot spacing length of the liver tissue is 4.5 mm, whereas it is 13 mm for the breast tissue.

The properties of liver and breast tissues used in the present study are given in Table 1 (Rubio *et al.*, 2011), (Kaur and Mann, 2014), (Razib *et al.*, 2016). The properties of the dielectric material and catheter are represented in Table 2 (Kaur and Mann, 2014), (Razib *et al.*, 2016).

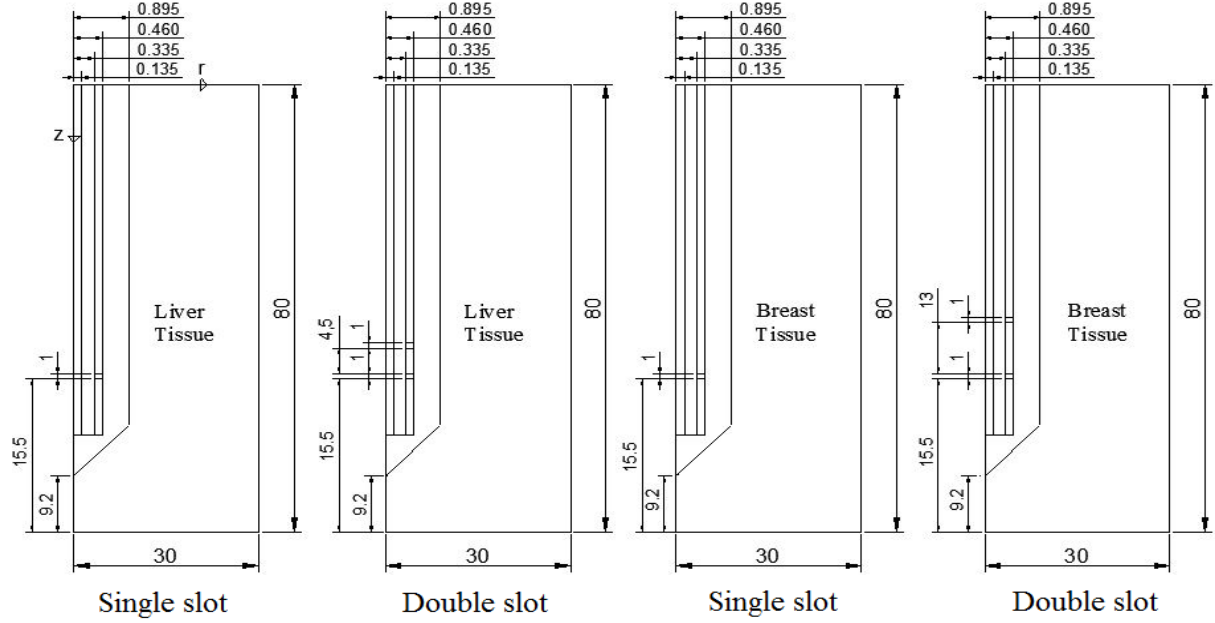


Figure 2. Single and double slot microwave antenna geometries for breast and liver tissues (Dimensions are in mm)

Table 1. The properties of liver and breast tissues

Property Name	Liver	Breast
Heat capacity	4187 (J·kg ⁻¹ ·K)	2960 (J·kg ⁻¹ ·K)
Density	1038 (kg·m ⁻³)	1058 (kg·m ⁻³)
Relative permittivity	45.2	5.14
Electric conductivity	2.12 (S·m ⁻¹)	0.137 (S·m ⁻¹)
Thermal conductivity	0.5 (W·m ⁻¹ ·K ⁻¹)	0.42 (W·m ⁻¹ ·K ⁻¹)
Blood temperature	310K	310K
Blood perfusion rate	3.6×10 ⁻³ s ⁻¹	3.6×10 ⁻³ s ⁻¹

Table 2. The properties of dielectric material and catheter

Property Name	Value
Relative permittivity of dielectric	2.03
Relative permittivity of catheter	2.6
Relative permeability	1
Thermal conductivity of PTFE	0.25 (W·m ⁻¹ ·K ⁻¹)
Density of PTFE	2200 (J·kg ⁻¹ ·K)
Heat capacity of PTFE	1300 (J·kg ⁻¹ ·K)
Microwave power input	10 W
Microwave frequency	2.45 GHZ

Thermal Analysis

The temperature distribution inside the tissue is calculated by Pennes' bioheat equation given by Eq. (2).

$$\rho C \frac{\partial T}{\partial t} = k \nabla^2 T - \rho_b C_b W_b (T - T_b) + \dot{Q}_{met} + \dot{Q}_{ext} \quad (2)$$

where ρ , C , T and k represent the density, heat capacity, temperature, and thermal conductivity of the tissue, respectively, whereas ρ_b , C_b , W_b and T_b indicate the density, specific heat capacity, perfusion rate, and temperature of the blood, respectively. The first term on the right-hand side of Eq. (2) represents the heat conduction inside the tissue, and second term describes the heat caused by convection. \dot{Q}_{met} is the metabolic heat generation within the tissue. \dot{Q}_{ext} is the external heat source (electromagnetic) term which can be calculated by equation

$$\dot{Q}_{ext} = \frac{\sigma E^2}{2} \quad (3)$$

where σ represents the tissue conductivity [S/m], and E is the electric field within the tissue [V/m].

Boundary conditions

Thermal insulation boundary condition is applied to the external boundary of the computational domain, i.e., $n \cdot (k \nabla T) = 0$.

Initial temperature is considered to be $T_0 = T_b = 37^\circ\text{C}$.

Electromagnetic Analysis

The microwave treatment is a multi-physics problem, and it involves the coupling of the temperature and electromagnetic fields. Electric (\vec{E}) and magnetic (\vec{H}) fields are expressed as Keangin *et al.*, 2011), (Keangin and Rattanadecho, 2013), (Keangin and Rattanadecho, 2018), (Bertram *et al.*, 2006), (Liu *et al.*, 2013).

$$\vec{E} = \vec{e}_r \frac{A}{r} e^{\sqrt{-1}(\omega t - kz)} \quad (4a)$$

$$\vec{H} = \vec{e}_\phi \frac{A}{rZ} e^{\sqrt{-1}(\omega t - kz)} \quad (4b)$$

with $Z = \sqrt{\mu_o / \epsilon_r \epsilon_o}$ is the wave impedance in the dielectric of the coaxial cable [Ω], $\mu_o = 4\pi \times 10^{-7}$ is the permeability of free space [H/m], ϵ_r is the relative permittivity of the dielectric, $\epsilon_o = 8.854 \times 10^{-12}$ is the permittivity of free space [F/m], P is the input power [W], r_i and r_o are the inner and outer radii of the coaxial cable [m], $\omega = 2\pi f$ is the angular frequency [rad/s], f is the frequency [Hz], $k = 2\pi / \lambda$ is the propagation constant [m^{-1}], λ is the wavelength [m], and t is the time [s].

At the antenna symmetry axis $\vec{E}_r = 0$ and $\frac{\partial \vec{E}_z}{\partial r} = 0$ boundary conditions are applied. In addition, $\vec{n} \times \sqrt{\epsilon} \vec{E} - \sqrt{\mu} \vec{H}_\phi = -2\sqrt{\mu} \vec{H}_\phi$ boundary condition is applied to the outer boundaries of the computational domain. The local specific absorption rate (SAR) is calculated using the relation

$$SAR = \frac{\sigma}{\rho} |\vec{E}|^2 \quad (5)$$

where σ indicates the tissue conductivity [S/m], ρ is the density of the tissue [kg/m^3], and E represents electric field within the tissue [V/m]. It can be seen from Eq. (5) that the SAR value is dependent on the square of the electric field generated around the antenna. The calculated SAR value is equivalent to the heating source created by the electric field. Although the SAR value does not directly determine the final temperature distribution of the tissue, it causes the temperature to increase (Rubio *et al.*, 2011). This result stems from the application of power for a specific duration.

Computational Method

COMSOL Multiphysics software based on finite element method is used to simulate the problem. A non-uniform mesh distribution is employed, and the typical mesh distribution is shown in Fig. 3 for coaxial single slot antenna. The compactness of the grid structure is increased as getting closer to the antenna in order to enhance the resolution and accuracy of the solution. Mesh independence study is conducted by improving the quality of the mesh structure until the variation in the maximum temperature of the tissue becomes negligible. The computations are performed using a range of element numbers varying from 3114 to 30719 to investigate the effect of the element size on the solution and to ensure that the attained results are independent of the mesh structure. The obtained maximum temperature values for five different grid sizes are given in Table 3. It is observed that the mesh structure having 30719 elements gives the optimum solution, and a similar procedure is followed for double slot antenna.

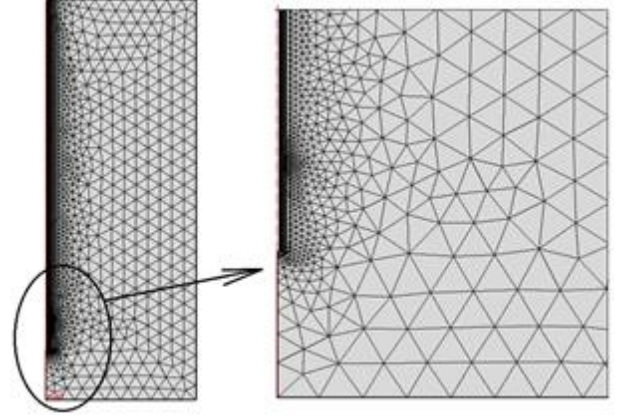


Figure 3. Typical mesh distribution

Table 3. Maximum temperature values for different element numbers

Mesh quality	Normal	Finer	Extra Fine	Extremely Fine	Used Mesh
Element number	3114	3903	5627	13520	30719
Maximum temperature (°C)	93	93.1	93.1	93.1	93.09

RESULTS AND DISCUSSION

Verification of the Numerical Study

The numerical study of Keangin *et al.* (2018) is repeated here to ensure the accuracy of the present numerical study. Verification was carried out for single and double slot coaxial antennas for liver tissue at a frequency of 2.45 GHz and at a power of 10 W. The comparison of the obtained temperature distributions of the current study and of Keangin *et al.*'s (2018) study is represented in Figure 4.

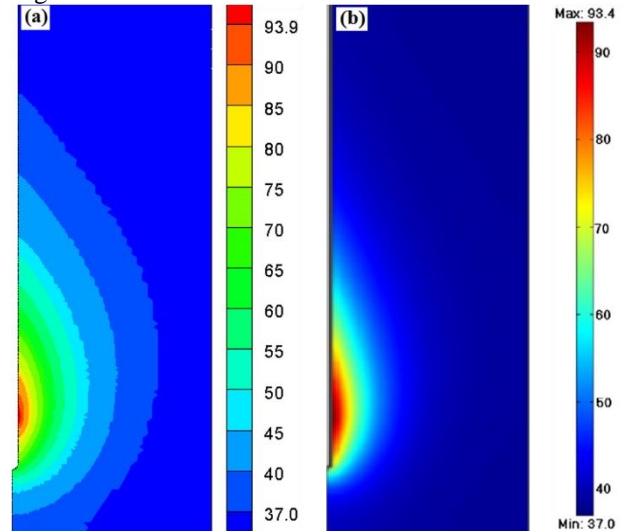


Figure 4. Temperature distribution after 300 second; (a) present and (b) literature study (Keangin *et al.*, 2011)

It is found out that the maximum temperature obtained for single slot after 300 seconds is 93.9°C for the current study, and it is 93.4°C for Keangin *et al.*'s study [8]. In addition, the attained peak SAR value for double slot is

2.49 kW/kg and 2.37 kW/kg for this study and Keangin et al.'s (Keangin *et al.*, 2011) study, respectively. It can be concluded that the results of present study are in good agreement with that of Keangin et al. (Keangin *et al.*, 2011).

SAR Distribution

Figure 5 represents the SAR distribution throughout the insertion depth (z -axis) at 0.895 mm (approximately $r=1$ mm) for single slot and double slot microwave coaxial antenna (MCA) in liver and breast tissues. A microwave power 10 W is applied to the tissues for 300 seconds at a frequency of 2.45 GHz.

Considering the liver tissue, when single and double slot MCAs are compared, it is seen that the peak SAR value is 3058 $W \cdot kg^{-1}$ at the insertion depth of $z=62.8$ mm for single slot MCA. For double slot MCA, it is obtained that the peak SAR value is 2490 $W \cdot kg^{-1}$ at the insertion depth of $z=59.6$ mm. The SAR value decreases abruptly after the peak value, and this trend keeps continuing until the arc length is 80 mm. In addition, it is deduced that the value of SAR depends on the number of slots. It is presumed that a lower SAR value for the double slot antenna is a result of the dispersed frequency from the slots.

For the breast tissue, it is seen that the peak SAR value is 1961 $W \cdot kg^{-1}$ at the insertion depth of $z=68.1$ mm for the single slot. However, two peak SAR values are obtained for double slot MCA. This value is found to be 870 $W \cdot kg^{-1}$ at an insertion depth of 51.1 mm and 1304.5 $W \cdot kg^{-1}$ at that of 68.6 mm. It is seen that the maximum SAR values occur near the slots. After the peak value is passed, SAR decreases suddenly whose minimum value is obtained at an insertion depth of 80 mm, exhibiting a similar behavior to that of the liver tissue.

The distance between the double slots for the liver tissue is smaller than that of breast tissue. Thus, it is foreseeable that the effect of microwave power decreases as the distance between two slots increases.

When the SAR values of the liver and breast tissues are compared, it is seen that a higher SAR value is obtained for the liver tissue for the equal number of slots. Also, when considering the single and double slot antennas, it is observed that utilization of single slot antenna results in a higher SAR value. The cause of having a higher SAR value for liver tissue can be interpreted as having a higher electric conductivity and smaller density. This result also can be validated from Eq. (2).

Temperature Distribution

Figure 6 shows the temperature contours for single and double slot antennas in liver and breast tissues after 300 s. An input power of 10 W was employed for single and double slot antennas with a frequency of 2.45 GHz. The left-hand side of Fig. 6 represents the temperature contours of liver tissue on the top and breast tissue on the bottom whereas the right-hand side represents the results obtained from single and double slot antennas. It is observed that the temperature value decreases as the arc length increases.

For the liver tissue, it is seen that the maximum temperature for single slot antenna is 93.9°C at the location of $r=1$ mm and $z=62.6$ mm. Also, the peak SAR value is obtained at the same coordinates, which means that the microwave input energy is the most effective at this position. For the double slot antenna, the maximum temperature is 82.8°C at the position $r=1$ mm and $z=58.2$ mm. The peak SAR and temperature values are obtained approximately at the same position for double slot antenna. It can be deduced that the SAR value and temperature distribution are related to each other.

When considering the liver tissue, it is seen that maximum temperature is 93.0°C at a position $r=1$ mm and $z=65$ mm for single slot antenna. For double slot antenna the maximum temperature is 69.8°C at a position $r=1$ mm and $z=69$ mm.

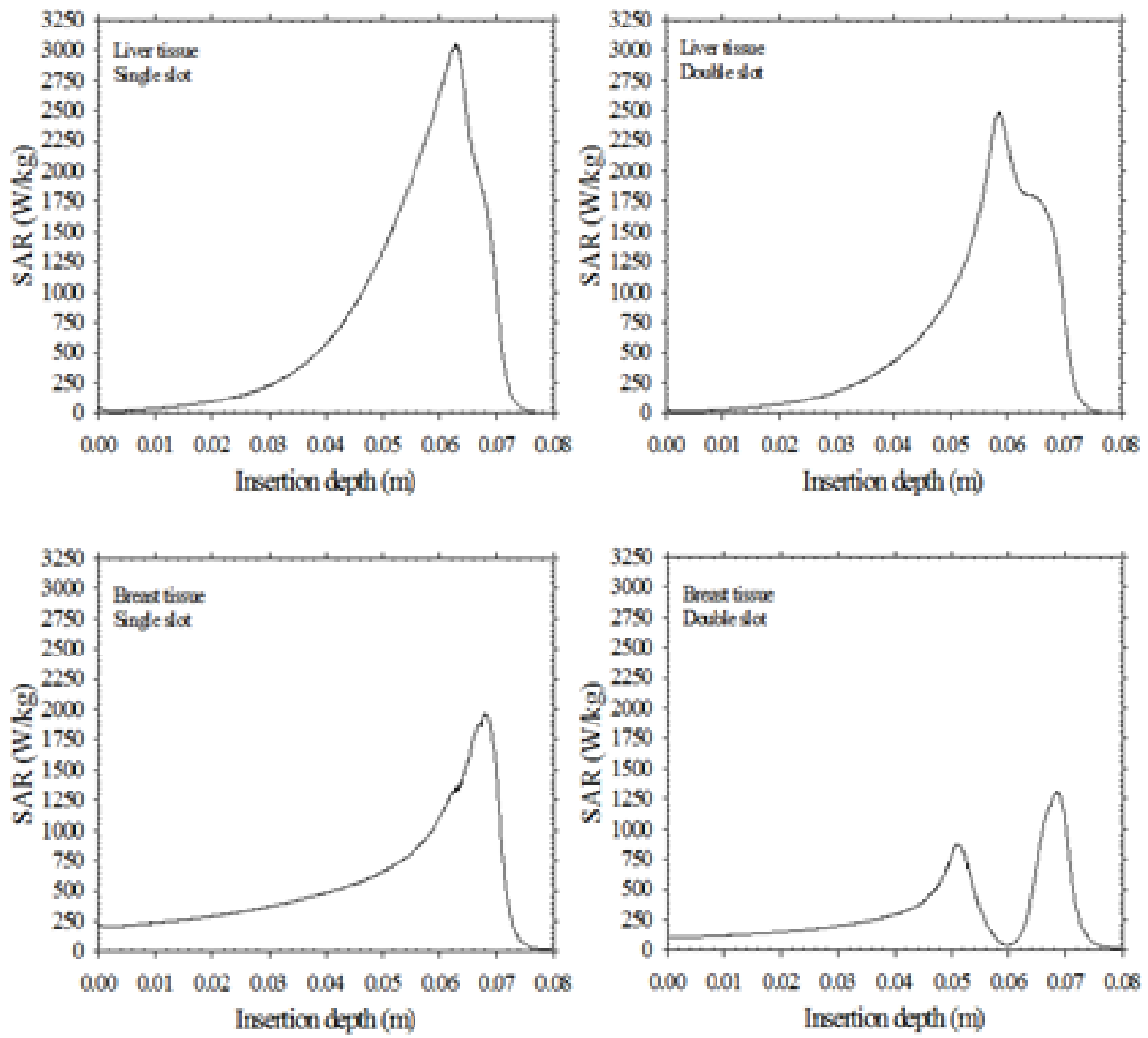


Figure 5. SAR distribution along insertion depth. From top to bottom: liver tissue and breast tissue, respectively. From left to right: single slot and double slot, respectively

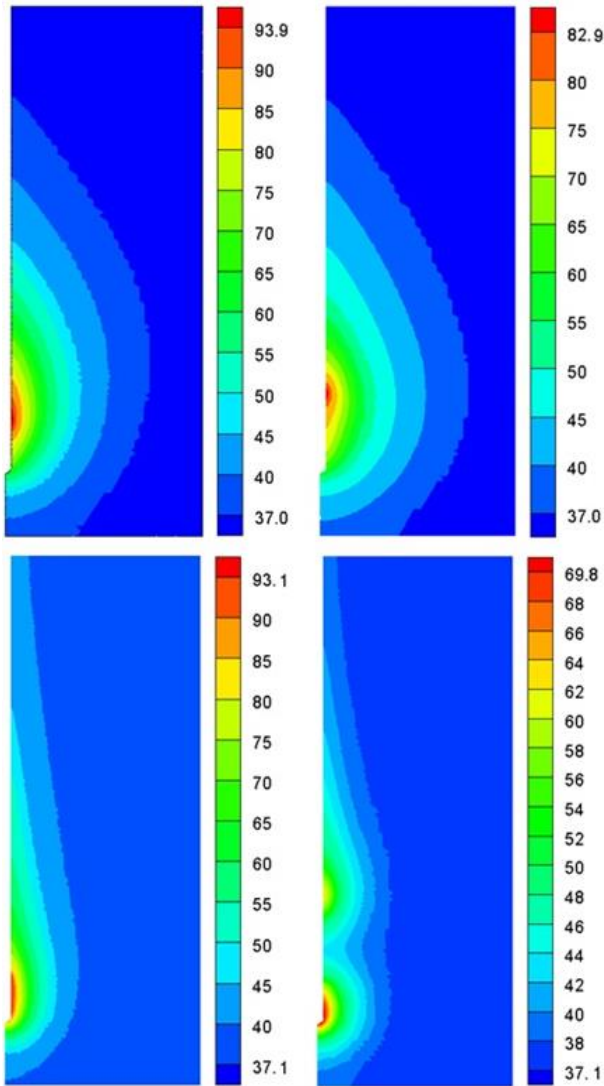


Figure 6. Temperature contour diagram. From top to bottom: liver tissue and breast tissue, respectively. From left to right: single slot and double slot, respectively

Figures 5 and 6 represent the SAR and maximum temperature values for both liver and breast tissues. It is seen that the mentioned values are found to be higher for single slot antenna when comparing to double slot. Consequently, attention will now be paid to single slot antenna. Figure 7 shows the temperature contour after 40, 100 and 300 seconds for breast and liver tissues using single slot antenna. It is seen that the heat in the tissue exhibits an ellipsoidal shape along the arc length as time passes. The maximum temperature occurs around the slot. For liver tissue, the maximum temperature is 67.1°C at the position $r=1$ mm and $z=63$ mm after 40 seconds. After 100 seconds, the maximum temperature is 80.6°C at the position $r=1$ mm and $z=62.8$ mm, and it is 93.9°C after a duration of 300 seconds at the position of $r=1$ mm and $z=62.6$ mm.

For the breast tissue, the maximum temperature is 71.4°C at the position $r=1$ mm and $z=68.5$ mm after 40 seconds.

After 100 seconds, the maximum temperature is 83.0°C at the position $r=1$ mm and $z=65$ mm. This value is found to be 93.5°C at the position of $r=1$ mm and $z=65$ mm after 300 seconds. It is seen that the maximum temperature occurs approximately at the same position with increasing time concerning both tissues. In addition, it is observed that the arc length of the liver tissue is longer than that of breast tissue for the same duration.

In microwave treatments, as mentioned before, the aim is to expose the cancer tissue to heat until the temperature reaches a value of 50°C, damaging proteins and the existing structures within the cancer cell. This procedure causes the tumors to shrink, and eventually they end up dead (Rubio *et al.*, 2011), (Keangin and Rattanadecho, 2013).

Results show that the maximum arc length at a temperature of 50°C is $r=3.9$ mm, 6.5 mm and 9.8 mm, after 40, 100 and 300 seconds of duration in liver tissue, respectively. Regarding the breast tissue, the maximum arc length at the same temperature is $r=3.3$ mm, 4.8 mm and 6.6 mm, respectively, after 40, 100 and 300 seconds. In other words, it is concluded that a larger periphery of the cancer cell can be destroyed by means of increasing the duration of the procedure. It is also seen that temperature increases with increasing time.

In order to represent the temperature distribution along the arc length, temperature values are plotted as a function of arc length in Fig. 8 at an insertion depth where the temperature is maximum.

The insertion depth where temperature has a maximum value is $z=62.6$ mm and $z=59.2$ mm for single and double slot antennas in liver tissue, respectively. As for breast tissue, insertion depth where temperature has a maximum value is $z=65$ mm and $z=69$ mm for single and double slot antennas, respectively. The left-hand side of Fig. 8 represents the temperature values of liver located at the top and breast at the bottom whereas the right-hand side depicts the results obtained from single and double slots. This figure shows that the maximum temperature is obtained at $r=1$ mm, and also it can be deduced from the figure that the temperature decreases along the arc length. It is also seen that the temperature value in tissue for double slot begins with a lower value than that of the one having single slot. As it can be seen from Fig. 8, liver and breast tissues exhibit similar temperature distributions.

Time is plotted in Fig. 9a as a function of maximum arc length where the temperature is 50°C for liver and breast tissues. In Fig. 9a the dash-dot line is for the numerical results of the liver tissue whereas the solid line represents that of breast tissue.

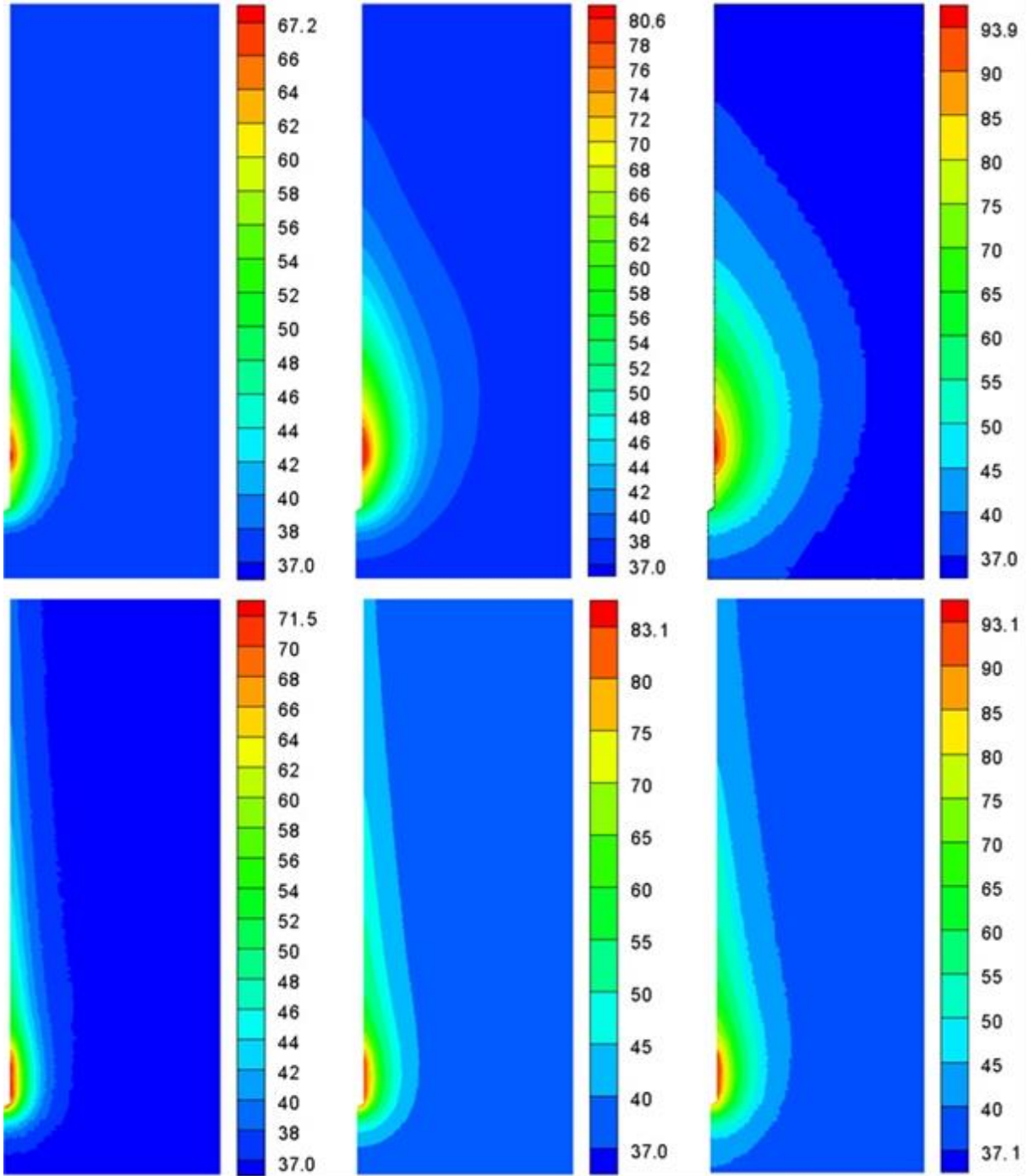


Figure 7. Temperature contour diagram. From top to bottom: liver tissue and breast tissue, respectively. From left to right: after 40s, 100s and 300s, respectively.

The results of numerical study for single slot antenna are represented by an equation in the form of

$$t(s) = aL^3 + bL^2 + cL + d \quad (6)$$

where t is the time in second, L is the maximum arc length at which temperature is 50oC (see Fig. 9b), and the unit of L is mm. In Eq. (6) a , b , c and d are the constants. Correlation equations in the form of Eq. (6) are obtained for liver and breast tissues, respectively, and are given in Eqs. (7) and (8).

$$t(s) = 0.5910L^3 - 5.476L^2 + 28.66L - 22.47 \quad (7)$$

(R2=0.9989)

$$t(s) = 3.819L^3 - 34.00L^2 + 118.9L - 119.1 \quad (8)$$

(R2=0.9989)

Eqs. (7) and (8) are valid for the range of $1.27 \leq L \leq 9.87$ and $1.76 \leq L \leq 6.66$, respectively. When the value of L falls out of these ranges, extrapolation can be used for these equations. The time required to destroy the cancer tissue can be calculated using Eq. (7) for breast cancer and Eq. (8) for liver cancer with knowing the arc length of the malignd tissues.

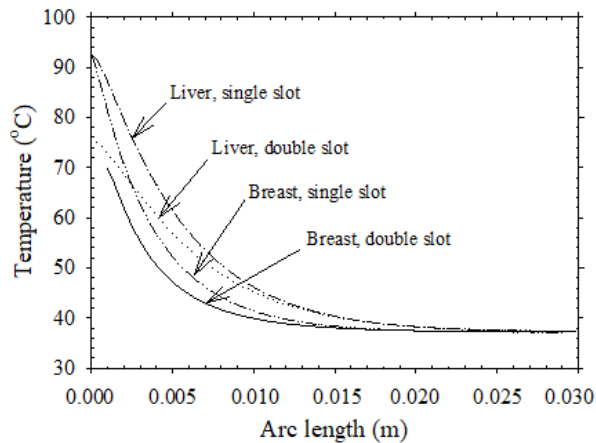


Figure 8. Temperature distribution along arc length. From top to bottom: liver tissue and breast tissue, respectively. From left to right: single slot and double slot, respectively

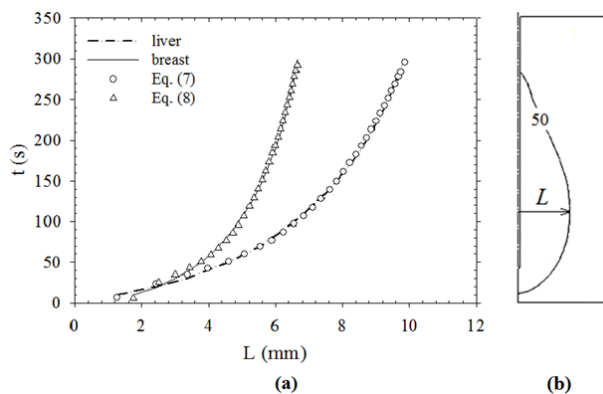


Figure 9. Time as a function of maximum arc length whose temperature is 50°C

CONCLUSION

The present study represents the modeling and analysis of single and double slot microwave coaxial antennas within breast and liver tissues by using finite element method. The study has been carried out for 2.45 GHz and 10 W. The noteworthy results are listed below;

- The temperature of the tissue increases with increasing duration.
- The characteristics of breast and liver tissues are different from each other, which results in different SAR values and temperature distributions.
- For liver tissue, maximum temperature value is 93.90°C and 82.8°C for single and double slot antennas, respectively. As for breast tissue, maximum temperature values are 93.0°C and 69.8°C for single and double slot antennas, respectively.
- The peak SAR value within the liver tissue is 3058 W·kg⁻¹ and 2490 W·kg⁻¹ for single and double slot antennas, respectively. For the breast tissue, the peak SAR value is 1961 W·kg⁻¹ for single slot antenna. However; SAR value has two peak maximum values for double slot antenna in the breast tissue, and the peak SAR values are 870 W·kg⁻¹ and 1304.5 W·kg⁻¹.

- SAR and temperature values decrease along the arc length.
- SAR and temperature distribution strongly depend on the number and position of slot within both tissues.
- When the results of single slot and double slot antennas are compared, maximum SAR and temperature values are obtained for single slot antenna.
- When the results of liver and breast tissues are compared, maximum SAR and temperature values are obtained for liver tissue.
- Single slot antenna is more useful than double slot antenna for microwave cancer treatment. However, double slot microwave coaxial antenna has a larger ablation area.
- New correlations are given in the form of for treatment of liver and breast tissues for coaxial single slot antenna. It is anticipated that the present study makes a contribution in the field of medicine.

ACKNOWLEDGEMENT

The authors would like to thank Nuri Eren TURKOGLU (Politecnico di Milano, Department of Electrical Engineering) for his support during the analyses.

REFERENCES

- Acikgoz H. and Turer I., 2014, A Novel Microwave Coaxial Slot Antenna for Liver Tumor Ablation, *Advanced Electromagnetics*, 3, 1, 20-25.
- Bertram J.M., Yang D., Converse M.C., Webster J.G. and Mahvi D.M., 2006, Antenna design for microwave hepatic ablation using an axisymmetric electromagnetic model, *BioMedical Engineering OnLine*, 5:15.
- Hamada L., Saito K., Yoshimura H. and Ito K., 2000, Dielectric-loaded coaxial-slot antenna for interstitial microwave hyperthermia: Longitudinal control of heating patterns, *International Journal of Hyperthermia*, 16, 3, 219-229.
- Jiao T., Wang H., Zhang Y., Yu X., Xue H., Lv H., Jing X., Zhan H. and Wang J., 2012, A coaxial-slot antenna for invasive microwave hyperthermia therapy, *Journal of Biomedical Science and Engineering*, 5, 198-202.
- Kaur S. and Mann P.S., 2014, Comparison of Single Slot and Double Slot Antenna for the Treatment of Hepatocellular Carcinoma, *International Journal of Research in Computer Applications and Robotics (IJRCAR)*, 2, 5, 86-91.
- Keane D., Ruskin J., Norris N., Chapelon P.A. and Bérubé D., 2004, In Vitro and In Vivo Evaluation of the Thermal Patterns and Lesions of Catheter Ablation with a Microwave Monopole Antenna, *Journal of Interventional Cardiac Electrophysiology*, 10, 111-119.
- Keangin P., Rattanadecho P. and Wessapan T., 2011, An analysis of heat transfer in liver tissue during microwave

ablation using single and double slot antenna, *International Communications in Heat and Mass Transfer*, 38, 757-766.

Keangin P. and Rattanadecho P., 2013, Analysis of heat transport on local thermal non-equilibrium in porous liver during microwave ablation, *International Journal of Heat and Mass Transfer*, 67, 46–60.

Keangin P. and Rattanadecho P., 2018, A numerical investigation of microwave ablation on porous liver tissue, *Advances in Mechanical Engineering*, 10, 8, 1-13.

Liu A.J., Zhou H. and Kang W., 2013, A numerical study on Microwave Coagulation Therapy, *Applied Mathematical Sciences*, 7, 104, 5151-5164.

Razib A., Hossain K.A. and Hossain S., 2016, Microwave ablation technique (MWA) for cancer treatment, *Proceedings of the 2016 International Conference on Medical Engineering, Health Informatics and Technology (MediTec)*, Bangladesh, 1-6.

Rossetto F. and Stauffer P.R., 1999, Effect of complex bolus-tissue load configurations on SAR distributions from dual concentric conductor applicators, *IEEE Transactions on Biomedical Engineering*, 46, 11, 1310-1319.

Rubio M.F.J.C., Hernández A.V., Salas L.L., Ávila-Navarro E. and Navarro E.A., 2011, Coaxial Slot Antenna Design for Microwave Hyperthermia using Finite Difference Time-Domain and Finite Element Method, *The Open Nanomedicine Journal*, 3, 2-9.

Rubio M.F.J.C., López G.D.G., Perezgasga F.V., García F.F., Hernández A.V. and Salas L.L., 2015, Computer modeling for microwave ablation in breast cancer using a coaxial slot antenna, *International Journal of Thermophysics*, 36, 2687–2704.

Selmi M., Dukhyil A.A.B. and Belmabrouk H., 2020, Numerical Analysis of Human Cancer Therapy Using Microwave Ablation, *Applied Sciences*, 10, 1, 211.

Sung H., Ferlay J., Siegel R.L., Laversanne M., Soerjomataram I., Jemal A. and Bray F., 2021, Global Cancer Statistics 2020: GLOBOCAN Estimates of Incidence and Mortality Worldwide for 36 Cancers in 185 Countries, *CA-A Cancer Journal for Clinicians*, 1-41.

Tehrani M.H.H., Soltani M., Kashkooli F.M. and Raahemifar K., 2020, Use of microwave ablation for thermal treatment of solid tumors with different shapes and sizes—A computational approach, *PLOS ONE*, 15, 6.

Uzman B., Yilmaz A., Acikgoz H. and Mitra R., 2020, Graphene-based microwave coaxial antenna for

microwave ablation: thermal analysis, *International Journal of Microwave and Wireless Technologies*, 1-9.

Zafar T., Zafar J. and Zafar H., 2014, Development and microwave analysis of slot antennas for localized hyperthermia treatment of hepatocellular liver tumor, *Australasian Physical & Engineering Sciences in Medicine*, 37, 673–679.



DETERMINATION OF INDOOR DESIGN TEMPERATURE, THERMAL CHARACTERISTICS AND INSULATION THICKNESS UNDER HOT CLIMATE CONDITIONS

Meral ÖZEL

Department of Mechanical Engineering, Firat University, 23279 Elazığ, Turkey
mozel@firat.edu.tr, ORCID: 0000-0002-9516-4715

(Geliş tarihi: 24.06.2021, Kabul tarihi: 06.03.2022)

Abstract: The base purpose of this work is to use interior design temperatures and the heating and cooling periods, which are determined according to different wall orientations in terms of thermal performance throughout the year, in the calculation of heat transfer characteristics and optimum insulation thickness. This work is realized under dynamic thermal conditions for the climatic conditions of Adana, Turkey. Firstly, the transmission loads for both heating and cooling are determined for uninsulated and insulated walls according to indoor design temperatures: 20, 22, 24 °C. Annual transmission loads, annual average dynamic thermal resistance, annual average time lag, and decrement factor for various wall directions are calculated by using indoor design temperatures determined over the whole year from minimum heating and cooling transmission loads point of view. Then, these loads determined overheating and cooling periods are used for the optimization of insulation thickness. In the uninsulated wall, yearly cooling load is obtained to be 221.37, 152.81, 229.14 and 229.14 MJ/m² for the south, north, east and west orientations, respectively while yearly heating load is obtained to be 73.54, 138.44, 117.62 and 117.62 MJ/m². It is observed that the cooling load is more dominant than the heating load under the climate conditions of Adana. It is also observed that the longest cooling period is obtained in south orientation while the shortest cooling period is obtained in north orientation. The optimum thickness of the insulation for Adana is obtained to be 8.4, 8.0, 9.2 and 9.2 cm for south, north, east and west orientations, respectively. The results indicate that the indoor design temperatures and insulation have a significant effect on heating, cooling and total transmission loads. Besides, the results reveal that the wall orientation has an important effect on heating and cooling periods, dynamic thermal resistance, time lag and optimum insulation thickness.

Keywords: Thermal performance, Indoor design temperature, Optimization of insulation thickness, dynamic thermal condition

SICAK İKLİM ŞARTLARI ALTINDA İÇ DİZAYN SICAKLIĞI, TERMAL ÖZELLİKLER VE YALITIM KALINLIĞININ BELİRLENMESİ

Özet: Bu çalışmanın temel amacı, yıl boyunca ısı performans açısından farklı yönlendirmelere göre belirlenen iç dizayn sıcaklıkları ile ısıtma ve soğutma periyotlarını, ısı transfer karakteristikleri ve optimum yalıtım kalınlığının hesabında kullanmaktır. Bu çalışma, Türkiye'nin Adana şehrinin iklim şartları için dinamik termal şartlar altında gerçekleştiriliyor. İlk olarak; 20, 22, 24 °C iç dizayn sıcaklıklarına göre yalıtımsız ve yalıtımlı duvarlar için ısıtma ve soğutma geçiş yükleri belirleniyor. Minimum ısıtma ve soğutma geçiş yükleri açısından bütün yıl üzerinden belirlenen iç dizayn sıcaklıklarını kullanarak değişik duvar yönlendirmeleri için yıllık geçiş yükleri, yıllık ortalama dinamik termal direnç, yıllık ortalama faz kayması ve sönüm oranı belirleniyor. Daha sonra ısıtma ve soğutma periyotları üzerinden belirlenen bu yükler yalıtım kalınlığının optimizasyonu için kullanılıyor. Yalıtımsız duvarda güney, kuzey, doğu ve batı yönleri için yıllık ısıtma yükü sırasıyla 73.54, 138.44, 117.62 ve 117.62 MJ/m² olarak elde edilirken, yıllık soğutma yükü sırasıyla 221.37, 152.81, 229.14 ve 229.14 MJ/m² olarak elde edilmiştir. Adananın iklim şartları altında soğutma yükünün ısıtma yükünden daha baskın olduğu görülüyor. Ayrıca, en kısa soğutma periyodunun kuzeyde elde edildiği, en uzun soğutma periyodunun ise güneyde elde edildiği görülüyor. Adana için optimum yalıtım kalınlığı; güney, kuzey, doğu ve batı yönleri için sırasıyla 8.4, 8.0, 9.2 and 9.2 cm olarak elde edilmiştir. Sonuçlar iç dizayn sıcaklığı ve yalıtımın; ısıtma, soğutma ve toplam geçiş yükleri üzerinde önemli bir etkiye sahip olduğunu gösteriyor. Ayrıca, sonuçlar duvar yönlendirmenin ısıtma ile soğutma periyotları üzerinde ve dinamik termal direnç, faz kayması ve optimum yalıtım kalınlığı üzerinde önemli bir etkiye sahip olduğunu da gösteriyor.

Anahtar Kelimeler: Termal performans, İç dizayn sıcaklığı, Yalıtım kalınlığının optimizasyonu, Dinamik termal şart

NOMENCLATURE

c	specific heat [J/kg K]
C_A	total energy consumption cost [\$/m ² year]
C_i	insulation cost [\$/m ³]
C_E	electricity cost [\$/kWh]
C_F	fuel cost [\$/m ³]
COP	coefficient of performance
h_i	convection heat transfer coefficient at the wall inner surface [W/m ² K]
h_o	convection heat transfer coefficient at the wall outer surface [W/m ² K]
H_u	lower heating value of the fuel [J/m ³]
I_T	total solar radiation for a vertical surface [W/m ²]
k	thermal conductivity [W/m K]
L_i	thickness of insulation [m]
PF	present worth factor
q_i	instantaneous heat flux at the wall indoor surface [W/m ²]
Q_g	heating transmission load [J/m ²]
Q_c	cooling transmission load [J/m ²]
R_n	nominal thermal resistance [m ² .K/W]
R_d	dynamic thermal resistance [m ² .K/W]
$t_{T_{es}(\max)}$	time that external surface temperature are being maximum [h]
$t_{T_{is}(\max)}$	time that internal surface temperature are being maximum [h]
T_{id}	indoor design temperature [°C]
T_o	outdoor environmental temperature [°C]
T_{sa}	sol-air temperature [°C]
$T_{is(\max)}$	maximum internal surface temperature [°C]
$T_{is(\min)}$	minimum internal surface temperature [°C]
$T_{es(\max)}$	maximum external surface temperature [°C]
$T_{es(\min)}$	minimum external surface temperature [°C]

Greek letters

α	wall outdoor surface solar absorptivity
δ	declination angle [deg.]
ϕ	latitude angle [deg.]
Φ	time lag [h]
f	decrement factor
γ	surface azimuth angle [deg.]
η_s	heating system efficiency
ρ	density [kg/m ³]
ω	hour angle [deg.]
θ	incidence angle [deg.]
θ_z	zenith angle [deg.]

INTRODUCTION

Energy consumption which is shared among industrial, transportation, building and agriculture sectors is rising rapidly due to urbanization and population growth (Bolattürk, 2008). The buildings are the biggest energy consumer after the industrial sector and create 40% of the energy consumption. Building envelope plays a major role in maintaining indoor comfort conditions under varying outdoor climatic conditions (Zengin and Kontoleon, 2017; Kontoleon et al., 2013)

The outer envelope that forms the buildings interacts continuously with the changing ambient temperature and solar radiation. In consequence of this interaction, the outer surface temperature of the building envelope and the heat conduction through the wall change continuously depending on the time. This change affects the interior environment considerably. As known, a large amount of the energy consumed in buildings is employed for heating and cooling of buildings to provide internal comfort. Therefore, heating and cooling loads in buildings constitute a significant part of the energy consumption of the buildings. One of the most effective ways to decrease these loads is to use heat insulation in the building envelope. Thermal resistance is increased by using heat insulation on building exterior walls while heat transfer loads are reduced. On the other hand, proper utilization of thermal insulation improves thermal properties such as time lag and decrement factor that expresses the thermal storage capacity of the outer walls. That is, thermal insulation leads to an increase in time lag and reduce in decrement factor. As the insulation thickness applied to the outer walls of buildings rises, the heat transfer reduces, and the insulation cost increases. Therefore, the insulation's optimum thickness should be determined based on a cost analysis.

To estimate the heat transition loads used in the determination of optimization of insulation thickness, many works in the literature applied degree-day or degree-hour method which is a crude and simple model under static conditions (Akan, 2021; Aktemur et al., 2021; Bolattürk, 2008; Dombaycı et al., 2006; Hasan, 1999; Çomaklı and Yüksel, 2003; Sisman et al., 2007; Ozkahraman and Bolattürk, 2006; Çomaklı and Yüksel, 2004; Dombaycı, 2007; Dombaycı et al., 2017; Ertürk, 2016; Ertürk, 2017; Yıldız et al., 2008; Kaynaklı, 2008; Mahlia and Iqbal, 2010; Kurt, 2010; Bolattürk, 2006; Kaynaklı et al., 2015; Yu et al., 2009; Özel et al., 2015; Barrau, 2014; Sundarama and Bhaskaran, 2014). However, a more accurate estimation of heating and cooling transition loads is quite important in the determination of the optimum insulation thickness. Therefore, Dynamic transient models considering the effects of solar radiation and the thermal storage of the building are more reliable for estimating heat loads. In literature, a few studies based on the thermal performance of the building walls used numerical model under dynamic thermal conditions (Al-Sanea et al., 2005; Ozel, 2011; Ozel, 2013a; Ozel, 2013b;

Nematchoua et al., 2017; Huo et al., 2015; Ramin et al., 2016; Ibrahim et al., 2012; Al-Sanea et al., 2003; Al-Sanea and Zedan, 2002) while the others applied an analytical dynamic model based on Complex Finite Fourier Transform (CFFT) method (Daouas, 2011; Daouas et al., 2010).

There are several studies in the literature on determining thermal performance and optimum insulation thicknesses considering different wall orientations. In all of these works, the interior design temperatures and the heating and cooling periods which are determined for the representation day of each month are independent of the wall orientations. The basic aim of this work is to fill this knowledge gap and to analyze the wall insulation both thermally and economically considering many parameters such as heating, cooling, and total transmission loads, static and dynamic thermal resistances, time lag, decrement factor, and optimum insulation thickness. Several studies in the literature include only a few of these parameters. In this study, firstly, the interior design temperatures are numerically determined from minimum heat gain and loss point of view by considering wall orientations under dynamic thermal conditions. Secondly, the interior design temperatures which are determined according to wall

orientations are used to determine thermal parameters such as annual transmission loads, annual average dynamic thermal resistance, annual average time lag, and decrement factor. The transmission loads are separately calculated as hourly, daily, and yearly. Finally, optimum insulation thickness is also calculated by using heating and cooling periods determined according to wall orientations. The results of this work which is realized for the climate conditions of Adana, Turkey are compared with results of other works under various climate conditions.

MATHEMATICAL FORMULATION

The uninsulated and insulated composite wall structures are illustrated schematically in Fig.1. The outer side of the walls is exposed to the external environment temperature and solar radiation changing throughout the day while the inner side is exposed to the indoor design temperature at a fixed temperature. One dimensional transient heat conduction equation in a composite wall with perfect thermal contact is defined as:

$$\frac{\partial T_j}{\partial t} = \frac{k_j}{\rho_j c_j} \frac{\partial^2 T_j}{\partial x^2}, \quad j=1,2,\dots,N \quad (1)$$

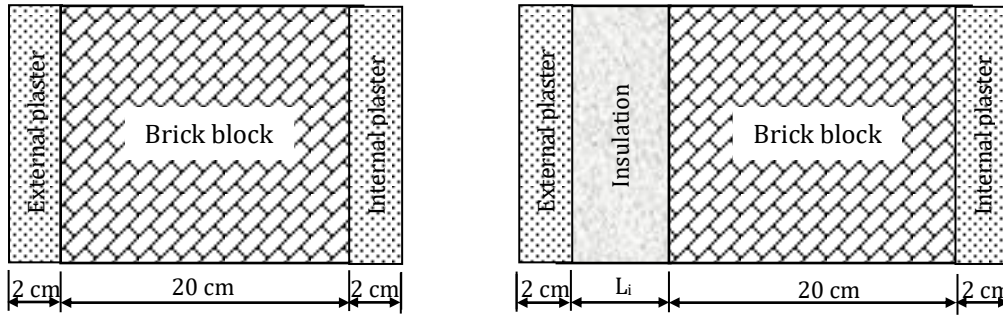


Figure 1. Uninsulated and insulated wall structures

Thermal properties used in the composite wall are given in Table 1. It is considered that there is no heat generation, interface resistance is neglected and change of thermal properties is neglected. One initial condition and two boundary conditions are needed to solve the differential equation. An arbitrary homogeneous temperature range is chosen as the initial condition. The convection boundary conditions on the outer and inner surfaces of the wall are described as follows, respectively:

Table 1. Material properties

Material	k (W/m K)	ρ (kg/m ³)	c (J/kg K)
Brick block	0.620	1800	840
Expanded polystyrene	0.038	18	1500
Cement plaster	0.720	1865	840

$$-k_{EP} \cdot \frac{\partial T(0,t)}{\partial x} = h_o(T_{sa} - T_{es}) \quad (2)$$

$$-k_{IP} \cdot \frac{\partial T(L,t)}{\partial x} = h_i(T_{is} - T_{id}) \quad (3)$$

where k_{EP} and k_{IP} are thermal conductivities of external and internal plaster, respectively. h_o and h_i are convection heat-transfer coefficients at the wall outer and inner surfaces, respectively. T_{es} and T_{is} are the external and internal surface temperatures of wall, respectively. T_{id} is the internal design temperature. T_{sa} is called as sol-air temperature and is described as follows (Threlkeld, 1998):

$$T_{sa} = T_o + \alpha I_T / h_o - \varepsilon \Delta R / h_o \quad (4)$$

T_o and α are external environment temperature changing throughout the day and outer surface solar absorptivity, respectively. The outdoor environment temperatures are given in Table 1. $\varepsilon \Delta R / h_o$ is called as the correction factor and is taken as 0 for vertical wall surfaces. I_T is the total solar radiation and is calculated for vertical wall surfaces as follows (Duffie and Beckman, 1991):

$$I_T = R_b I_b + (I_d + \rho_g I) / 2$$

(5) where I , I_b and I_d are total, beam and diffuse solar radiations on the horizontal surface. ρ_g is the reflectance of the ground and is taken as 0.2. R_b is called as the geometric factor and is calculated depending on incidence angle (θ) and zenith angle (θ_z) as follows:

$$R_b = \cos \theta / \cos \theta_z \quad (6)$$

These angles are given for vertical surfaces as follows:

$$\begin{aligned} \cos \theta = & \cos \delta \cdot \sin \phi \cdot \cos \gamma \cdot \cos \omega \\ & + \cos \delta \cdot \sin \gamma \cdot \sin \omega \\ & - \sin \delta \cdot \cos \phi \cdot \cos \gamma \end{aligned} \quad (7)$$

$$\cos \theta_z = \cos \phi \cdot \cos \delta \cdot \cos \omega + \sin \phi \cdot \sin \delta \quad (8)$$

where ϕ , δ , γ and ω represent latitude angle, declination angle, surface azimuth angle and hour angle, respectively. The surface azimuth angle is taken to be 0 for a south-facing wall, 180 for a north-facing wall, -90 and 90 for east and west orientations, respectively.

For determining the temperature distribution through the composite structure, the heat conduction equation containing boundary conditions was previously solved by employing the implicit finite-difference method (Ozel and Pihili, 2007) and a general-purpose computer program was developed in MATLAB. To achieve a stable periodic solution, it is assumed that the solar air temperature which associates the effects of external environment temperature and solar radiation will be repeated on sequent days.

Environmental Conditions

This work is realized for the climate conditions of Adana (latitude: 36.98°N, longitude: 35.33°E), Turkey. Adana which is placed on Turkey's Mediterranean coast is one of the hottest cities of Turkey. Hourly outdoor environment temperatures are supplied from records for weather data in the meteorological station (2007-2017). These hourly temperatures are obtained by taking the average of the years given and are given in Table 2 for the fifteenth day of each month. The solar radiation on vertical wall surfaces is determined via the isotropic sky model (Duffie and Beckman, 1991). α is accepted as 0.8. h_o and h_i are assumed as 22 and 9 W/m²K, respectively (Ozel, 2013a). Sol-air temperatures are determined depending on the solar radiation intensity and the outdoor air temperatures.

Table 2. Hourly outdoor environment temperatures for the fifteenth day of each month during the year

Time (h)	Hourly outdoor environmental temperatures (°C)											
	Jan.	Feb.	Mar.	Apr.	May	Jun.	Jul.	Aug.	Sep.	Oct..	Nov.	Dec.
1	9.7	11.8	14.3	18.0	21.5	23.1	27.3	27.9	24.0	20.8	15.9	1.5
2	11.1	11.9	14.8	17.5	21.6	22.2	27.0	28.1	23.6	20.3	15.8	0.6
3	9.7	11.8	14.3	17.2	20.6	22.8	26.8	27.9	23.6	21.0	15.6	-0.6
4	8.9	11.5	13.5	16.9	20.4	22.7	26.6	27.9	23.4	18.6	14.9	1.4
5	6.6	11.2	12.8	16.4	21.1	24.3	28.8	27.6	23.4	18.6	14.9	1.4
6	6.4	10.8	12.5	18.0	22.9	25.0	28.1	28.5	24.6	19.8	15.6	1.8
7	6.2	10.7	11.9	19.0	25.3	25.5	29.7	29.3	26.1	23.0	16.3	2.9
8	8.7	10.4	12.6	20.4	26.6	27.1	30.7	32.0	28.3	25.3	17.2	5.4
9	8.1	11.6	14.9	20.6	27.9	27.1	31.8	32.7	29.4	27.0	19.0	7.4
10	11.3	14.0	16.4	21.0	28.2	28.6	32.4	33.7	30.7	28.9	20.8	9.2
11	13.1	16.8	17.7	21.1	28.1	29.8	33.6	34.5	31.4	30.0	22.4	10.6
12	14.4	19.2	18.6	21.8	27.8	29.7	33.6	34.7	31.5	29.6	23.5	11.0
13	16.1	21.4	19.7	21.7	27.8	29.3	34.3	35.0	31.2	30.6	23.4	11.6
14	17.0	22.1	20.2	21.6	26.6	29.6	33.4	34.8	30.6	30.3	23.4	11.0
15	17.2	22.0	20.9	21.6	26.2	29.7	32.6	33.4	27.2	30.0	22.3	9.8
16	17.6	22.3	17.5	21.2	24.0	29.2	31.6	33.0	23.5	27.2	21.4	8.2
17	17.1	22.0	17.5	20.3	22.9	26.7	31.0	31.3	24.0	24.7	20.2	7.6
18	13.6	20.5	17.2	19.2	22.4	25.6	29.5	30.2	21.2	22.7	19.8	7.2
19	10.3	16.7	16.2	18.7	22.3	24.5	29.0	29.5	22.0	23.5	18.9	5.5
20	8.9	14.8	15.0	18.4	22.2	24.2	28.5	28.7	22.3	20.0	17.2	5.1
21	8.8	14.8	14.6	18.3	22.0	24.0	28.3	28.6	22.2	20.1	17.1	4.4
22	8.5	13.4	14.3	18.5	21.5	23.6	28.3	28.2	21.4	19.6	16.3	3.3
23	8.2	13.2	13.7	18.4	21.2	23.6	28.3	27.8	21.2	19.1	16.5	2.1
24	8.1	12.7	13.1	18.3	21.2	22.9	27.9	27.5	21.2	17.3	15.8	2.5

CALCULATION OF THERMAL PARAMETERS

Heating, Cooling, and Total Transmission Loads

In this work, the fifteenth day of each month during the year is taken into consideration as a representative day and hourly heat transmission loads are calculated as follows:

$$q_i = h_i(T_{is} - T_{id}) \quad (9)$$

Daily transmission loads are also calculated by integrating instantaneous load over one day period (24 h) as:

$$Q_{id} = \int_0^{24h} q_i dt \quad (10)$$

To calculate a daily total load, these instantaneous loads are integrated over 24 h periods. The daily value of the representative day of each month is multiplied by the number of days in that month.

Yearly total heating and cooling transmission loads are determined separately from daily heating and cooling loads which are summed up over winter and summer periods.

Nominal and Dynamic Thermal Resistances

Nominal (static) thermal resistance is calculated by summing the convective and conductive resistances as follows (Al-Sanea et al., 2013):

$$R_n = \sum_{j=1}^N (L/k)_j + (1/h_i) + (1/h_o) \quad (11)$$

The average daily dynamic resistance for each month's fifteenth day is obtained as follows (Al-Sanea et al., 2013):

$$R_d = \frac{\int_0^{24h} |(T_o - T_i)| dt}{\int_0^{24h} |q_i| dt} \quad (12)$$

The annual average dynamic resistance is calculated to be the weighted average of monthly values according to transmission loads.

Time Lag and Decrement Factor

There are two features that are beneficial to express the thermal storage capabilities of the outer walls of the building. These features are named as time lag and decrement factor. The time lag is the time when sinusoidal temperature fluctuation achieves from external surface to internal surface of the wall and is defined as follows (Ozel and Pihitli, 2007):

$$\Phi = t_{T_{es}(\max)} - t_{T_{is}(\max)} \quad (13)$$

Where $t_{T_{es}(\max)}$ and $t_{T_{is}(\max)}$ symbolize the time that external and internal surface temperatures are being maximum, respectively. The decrement factor is the

ratio of the internal surface temperature amplitude to the outer surface temperature amplitude, and is defined as follows (Ozel and Pihitli 2007):

$$f = [T_{is(\max)} - T_{is(\min)}] / [T_{es(\max)} - T_{es(\min)}] \quad (14)$$

Where $T_{es(\max)}$, $T_{is(\max)}$, $T_{es(\min)}$ and $T_{is(\min)}$ are the highest and the lowest temperatures on the external and internal surfaces of the wall. Values of the time lag and decrement factor are determined for each month's fifteenth day. Then, annual values are calculated by taking the arithmetic average of monthly values throughout the year.

Optimization of Insulation Thickness

The optimization of the insulation thickness is based on a cost analysis which includes the cost of energy consumption and the cost of insulation over the 20-year life of the building. Only heat transmissions from external walls are taken into account for the calculation of the optimum thickness of the insulation. The annual energy consumption cost is calculated as follows considering both the heating and cooling loads:

$$C_A = \frac{Q_h \cdot C_F}{H_u \cdot \eta_s} + \frac{Q_c \cdot C_E}{3.6 \times 10^6 \cdot COP} \quad (15)$$

where Q_h and Q_c are heating and cooling transmission loads per year of the insulated wall, respectively. C_F and C_E are fuel cost and electricity cost, respectively. H_u is the lower calorific value of the fuel, η_s is the heating system efficiency and COP is the performance coefficient. The total cost is determined by adding the insulation cost to the present worth of the energy consumption cost over the lifetime of the building and is defined as follows:

$$C_t = C_A \cdot PWF + C_i \cdot L_i \quad (16)$$

where C_i and L_i are the insulation cost and thickness. PWF is Present Worth Factor. PWF is determined based on inflation and interest rates over the 20-year life of the building (Ozel, 2013). Table 3 gives parameters used in cost analysis.

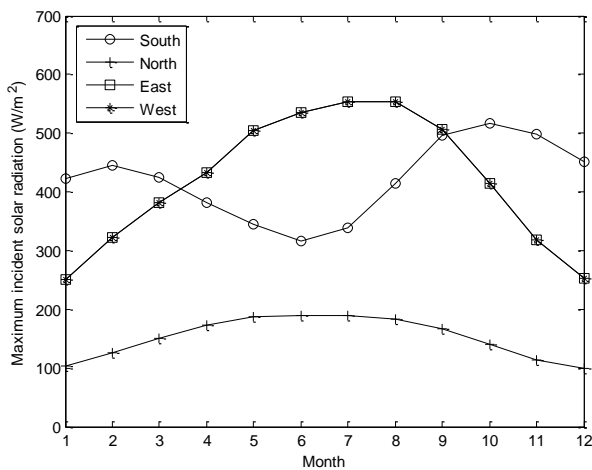
Table 3. The parameters used in calculations

Parameter	Value
Natural gas (in heating)	
C_F	0.4919 \$/m ³
H_u	34.541 * 10 ⁶ J/m ³
η_s	% 93
Electricity (in cooling)	
C_E	0.1894 \$/kWh
COP	2.5
Insulation	
Expanded polystyrene	
C_i	188.419 \$/m ³
PWF	17.75

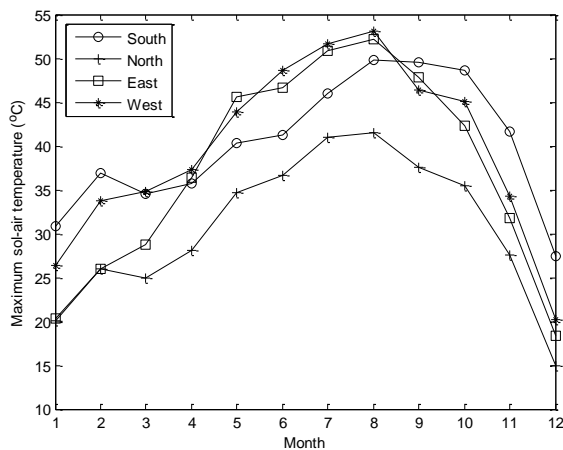
RESULTS AND DISCUSSION

Determination of Solar Radiation and Sol-air Temperature

Fig. 2(a-b) presents the maximum of the solar radiation and sol-air temperature according to months for different wall orientations. It is revealed that the highest values of maximum solar radiation appear in the south-facing wall for October, November, December, January, February and March months while they appear in east and west orientations for April, May, June, July, August and September. The results show that the highest value of maximum solar radiation for all months is obtained to be 553.88 W/m^2 in the east (or west) facing wall while the lowest value of maximum solar radiation is obtained as 98.72 W/m^2 in the north-facing wall. It is seen that for all months, the minimum solar radiation constitutes in north-facing wall. It is also seen in Fig. 2b that the highest value of sol-air temperature for all orientations is obtained in August month that maximum outdoor temperature occurs.



(a)



(b)

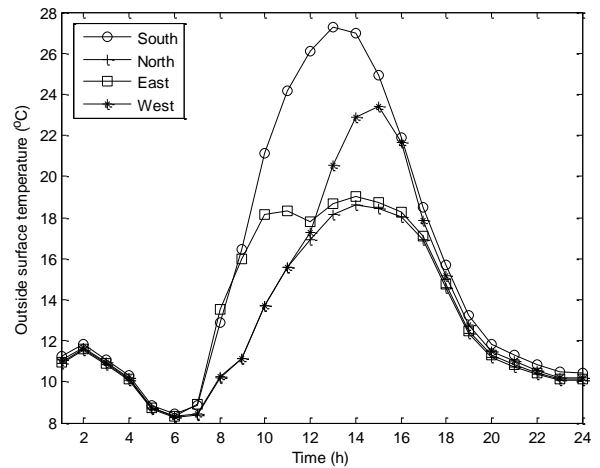
Figure 2 (a-b). Maximum values of the incident solar radiation and sol-air temperature according to months for different orientations

Fig. 4(a-b) presents the hourly change of internal surface temperatures according to wall orientations for

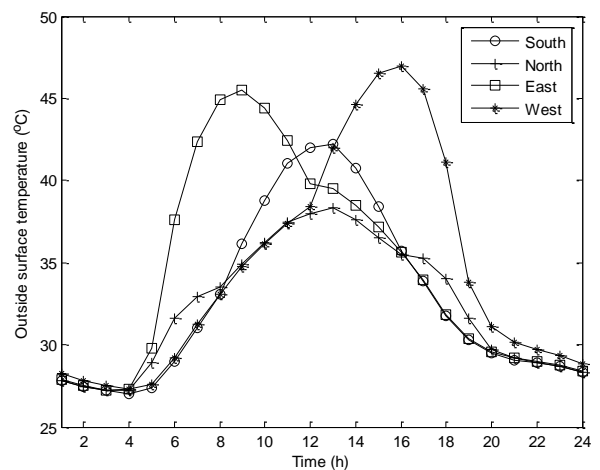
The results indicate that the maximum of sol-air temperatures for west orientation is higher compared to the other orientations. It is obvious that this is due to the time at which the highest external temperature occurs.

Determination of Outdoor and Indoor Surface Temperatures

Fig. 3(a-b) indicates the hourly variation of outside surface temperature for January 15 and July 15, respectively. The conclusions show that on January 15, the highest value of outside surface temperatures is obtained to be $27.26 \text{ }^\circ\text{C}$ at 13:00 for the south-facing wall while on July 15, it is obtained to be $46.99 \text{ }^\circ\text{C}$ at 16:00 for the west-facing wall. Besides, it is seen that in summer, the time that outdoor surface temperature is maximum is obtained to be 13:00, 13:00, 9:00 and 16:00 for the south, north, east and west orientations, respectively. The conclusions indicate that the highest value of the outer surface temperature is reached at the earliest east wall.



(a)

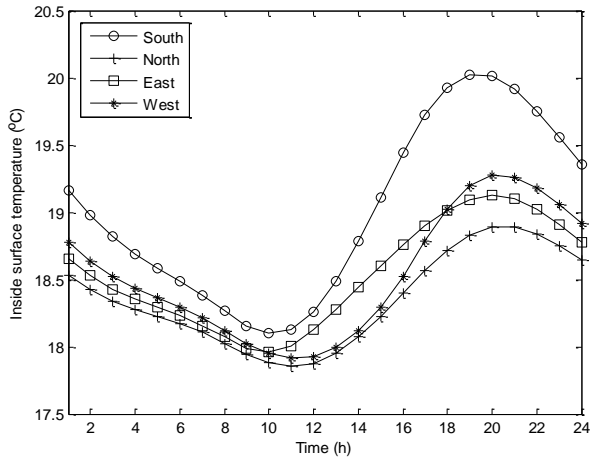


(b)

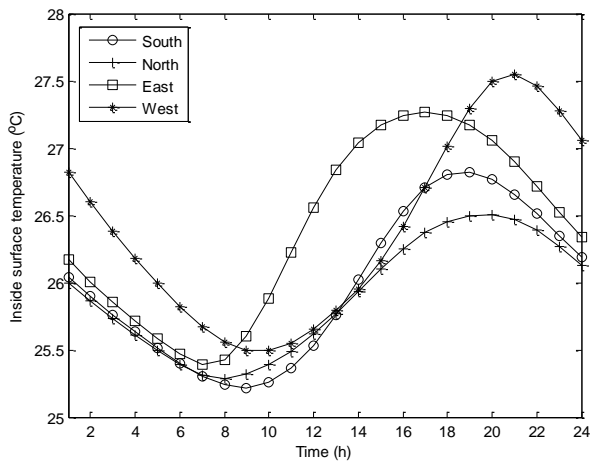
Figure 3. Hourly variation of outside surface temperature for a) January 15 and b) July 15

winter and summer conditions, respectively. It is seen that on July 15, maximum values of inside surface

temperatures are obtained to be 26.82, 26.50, 27.24 and 27.55 °C, respectively while on January 15, they are obtained to be 20.02, 18.89, 19.13 and 19.27 °C for south, north, east and west orientations. The results show that for winter, the maximum peak of inside surface temperature achieves in the south-facing wall while for summer, it achieves in the west-facing wall.



(a)



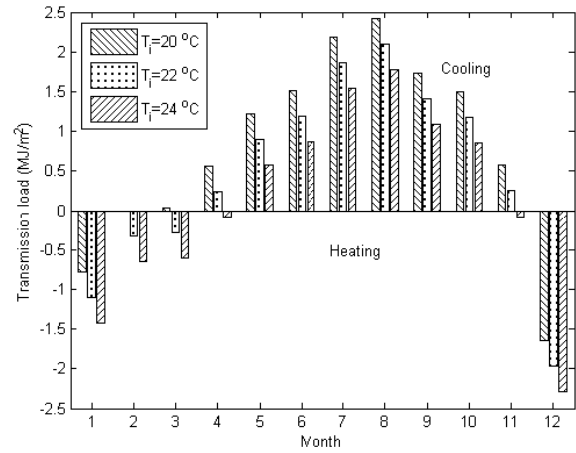
(b)

Figure 4. Hourly variation of inside surface temperature for a) January 15 and b) July 15

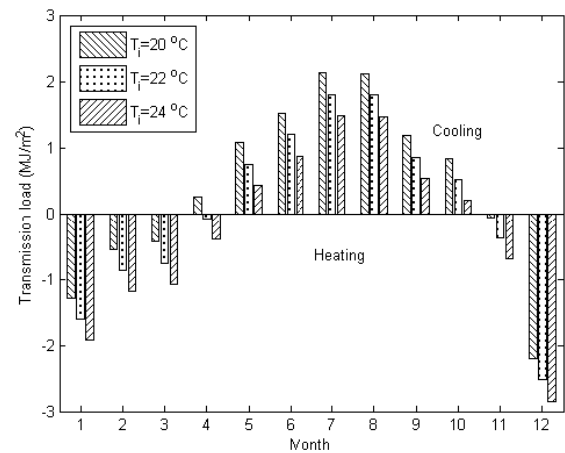
Determination of Indoor Design Temperatures

Fig. 5 (a-c) indicates daily transmission loads in the uninsulated wall for each month's fifteenth day according to different wall orientations and indoor design temperatures: 20, 22 and 24 °C. These loads for the 6 cm insulated wall are also shown in Fig. 6 (a-c). It is observed that the cooling and heating loads are importantly reduced when the wall is insulated. This reduction is obtained to be 74.7% for all wall orientations and three different indoor design temperatures. In both uninsulated and insulated walls, it is obvious that the highest heating load is reached in December for all orientations while the highest cooling load is reached in August for the south, east and west orientations. But, the highest cooling load for the north-facing wall is obtained in July. The results show that both heating and cooling requests occur in April and

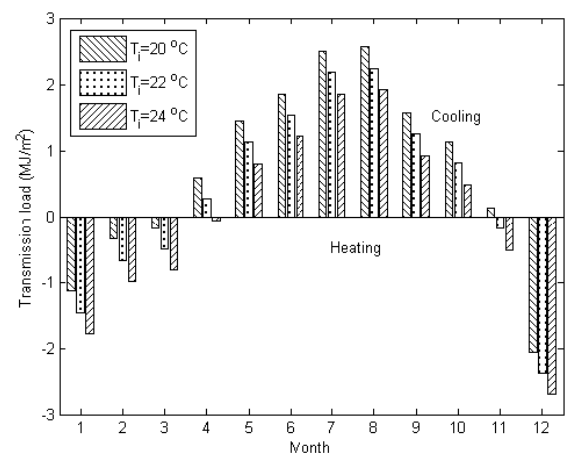
November months according to indoor design temperatures. This indicates that there may be cooling during the day period and heating during the night period.



(a)

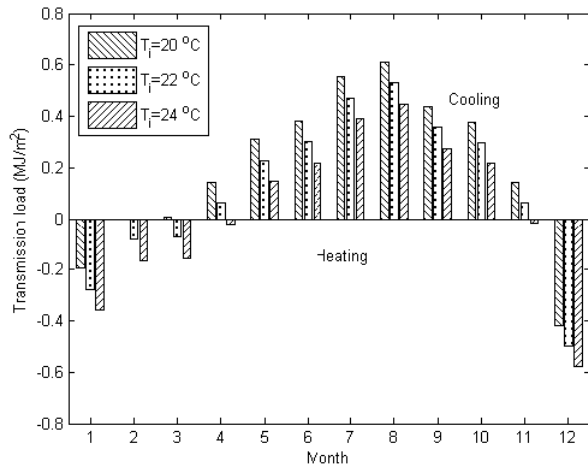


(b)

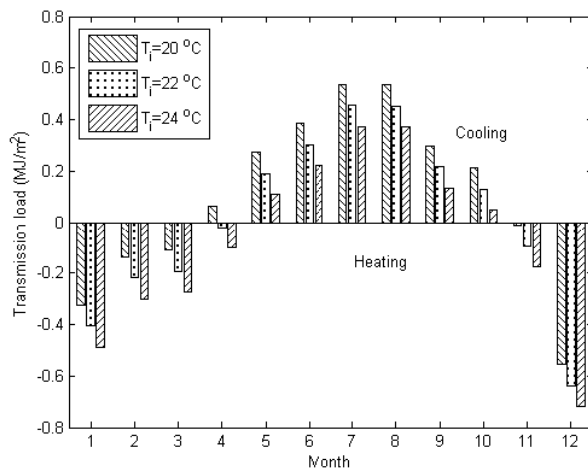


(c)

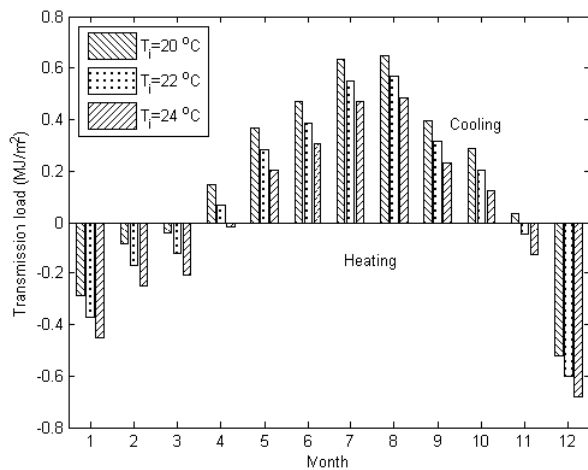
Figure 5. The daily total cooling and heating transmission loads for the 15th day of each month with respect to different indoor design temperatures in the uninsulated wall for (a) south, (b) north and (c) east (or west) orientations.



(a)



(b)



(c)

Figure 6. The daily total cooling and heating transmission loads for the 15th day of each month with respect to different indoor design temperatures in 6 cm insulated wall for (a) south, (b) north and (c) east (or west) orientations.

Table 4 shows yearly heating, yearly cooling and yearly total transmission loads according to indoor design temperatures for different wall orientations. The results indicate that minimum heating load is obtained in the south-facing wall while the minimum cooling load is obtained in the north-facing wall. The same conclusion was previously obtained for the climatic conditions of Elazığ, Turkey (Ozel, 2016). The results also indicate that as indoor design temperature rises, the cooling load and total load decrease while the heating load increases. It is obvious that total transmission load is reduced since the cooling load is more dominant than the heating load under the climatic conditions of Adana, Turkey. It is also obvious that the wall orientation, indoor design temperatures and insulation have a significant effect on heating, cooling and total transmission loads.

Table 4. The effect of indoor design temperatures on the yearly cooling, heating and total transmission loads for different wall orientations

Indoor design temp. (°C)	Wall orientation	The yearly transmission loads (MJ/m ² year)					
		Uninsulated wall			Insulated wall		
		Heat.	Cool.	Total	Heat.	Cool.	Total
20	South	73.5	359.7	433.2	18.6	91.0	109.6
	North	136.2	279.2	415.4	34.4	70.6	105.1
	East/West	112.0	361.9	473.9	28.3	91.5	119.9
22	South	111.3	279.8	391.1	28.2	70.8	98.9
	North	186.9	212.3	399.2	47.3	53.7	100.9
	East/West	156.4	288.6	445.0	39.6	73.0	112.6
24	South	154.7	205.6	360.3	39.1	52.0	91.1
	North	245.1	152.8	397.9	62.0	38.6	100.6
	East/West	206.6	221.2	427.7	52.3	55.9	108.2

Indoor design temperatures and the heating and cooling periods which are determined from the thermal performance point of view are given in Table 5 for each month's representative day according to wall orientations. These results indicate that for the south wall, yearly heating load is obtained during the heating period (December, January and February) while the yearly cooling load is obtained during the cooling period (from March to November). For a north-facing wall, the heating period consists of November, December, January, February, March and April months while the cooling period consists of May, June, July, August, September and October months. On the other hand, it is seen that for east (or west) orientations, the heating period consists of November, December, January, February and March months while the cooling period consists of April, May, June, July, August, September and October months. It is seen that the longest cooling period is obtained in south orientation while the shortest cooling period is obtained in north orientation. It is also seen that the shortest heating period is obtained in south orientation.

Table 5. The indoor design temperatures and the heating and cooling periods which are determined for the representative day of each month according to different wall orientations

Orientation	Indoor design temperatures $T_i(^{\circ}\text{C})$											
	Jan	Feb	Mar	Apr	May	Jun	Jul	Aug	Sep	Oct	Nov	Dec
South	20 ^h	20 ^h	20 ^c	22 ^c	24 ^c	24 ^c	24 ^c	24 ^c	24 ^c	24 ^c	22 ^c	20 ^h
North	20 ^h	20 ^h	20 ^h	22 ^h	24 ^c	24 ^c	24 ^c	24 ^c	24 ^c	24 ^c	22 ^h	20 ^h
East/West	20 ^h	20 ^h	20 ^h	22 ^c	24 ^c	24 ^c	24 ^c	24 ^c	24 ^c	24 ^c	22 ^h	20 ^h

^hheating
^ccooling

Determination of Daily and Yearly Transmission Loads

Fig. 7 presents variation of daily total cooling and heating transmission loads according to months for different wall orientations in 6 cm insulated wall. These transmissions are determined by using the interior design temperatures given in Table 5. It is revealed that the minimum heating load is obtained in February for the south-facing wall while the maximum heating load is obtained in December for the north-facing wall.

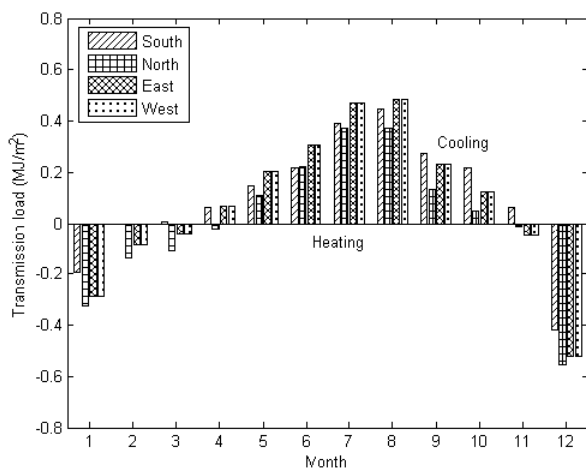


Figure 7. The daily total cooling and heating transmission loads for the 15th day of each month with respect to different wall orientations in 6 cm insulated wall

Fig. 8 indicates yearly cooling and heating loads to insulation thicknesses for different wall orientations. The yearly total transmission load is also shown in Fig. 9. It is seen that in the uninsulated wall, yearly cooling load is obtained to be 221.37, 152.81, 229.14 and 229.14 MJ/m² for the south, north, east and west orientations, respectively while yearly heating load is obtained to be 73.54, 138.44, 117.62 and 117.62 MJ/m². The results show that the cooling load is greater than the heating load. Besides, it is obvious that all transmission loads decrease against increased insulation thickness. This reduction is greater in the smaller insulation thickness values. With the increase of the insulation thickness, the transmission loads approach each other for all wall orientations. It is seen that in 10 cm insulated wall, yearly cooling load is obtained to be 37.37, 25.79, 38.68 and 38.68 MJ/m² for south, north, east and west orientations, respectively while yearly

heating load is obtained to be 12.41, 23.36, 19.85 and 19.85 MJ/m². The results show that the amount of reduction in heating, cooling and total loads is 83.12% for all wall orientations when the wall is insulated as 10 cm. The results also show that the transmission loads are the same for east and west orientations. The other orientations have almost equal cooling loads while the north-facing wall gives the lowest cooling load. It is obvious that inside surface temperature swings and peak loads as seen in Fig.4 are different for south, north, east and west orientations because of solar radiation. However, these loads are obtained as equal for the east and west orientations since yearly transmission loads are calculated from the sum of the instant loads. This is because the incident solar radiation is symmetrical for the east and west orientations, and these orientations receive the same amount of total solar radiation. The north-facing wall gives maximum heating load while the south-facing wall gives minimum heating load. Same trends and similar results were achieved by references (Ozel, 2011; Al-Sanea and Zedan, 2002; Daouas, 2011) for different climates. At lower insulation thicknesses, the total transmission load of the north-facing wall is slightly smaller than that of the south-facing wall. With the increase of the insulation thickness, total transmission loads of south and north-facing walls begin to be the same. The highest values of total transmission load are obtained in east and west-facing walls as obtained in cooling load.

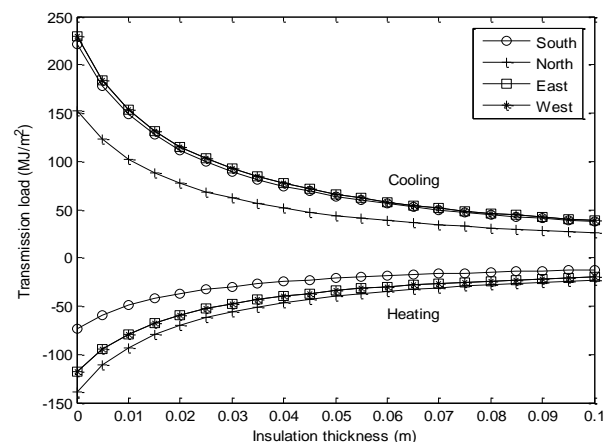


Figure 8. Variation of yearly cooling and heating transmission loads versus insulation thickness for different wall orientations

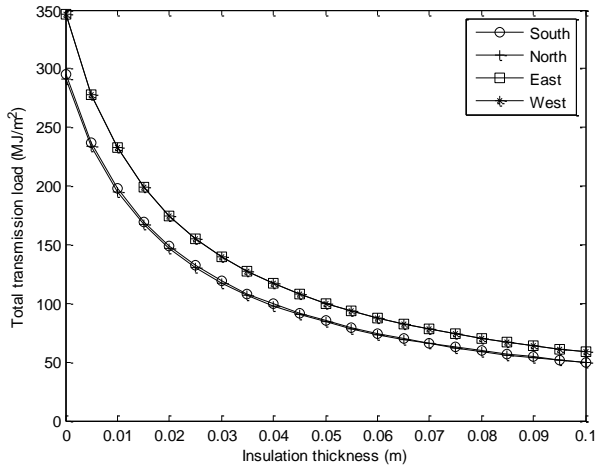
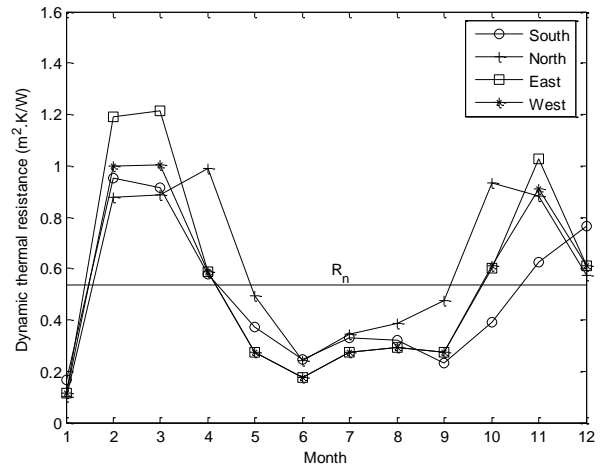


Figure 9. Variation of yearly total transmission loads versus insulation thickness for different wall orientations.

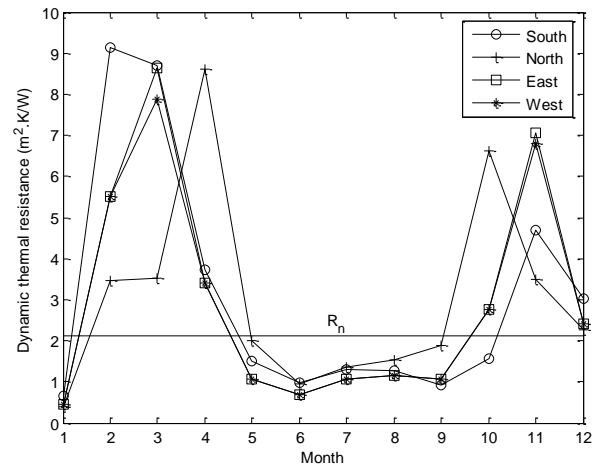
Determination of Dynamic Thermal Resistance

Fig. 10 (a-b) demonstrates the variation of thermal resistance values versus the 15th day of each month according to different wall orientations for uninsulated and insulated walls, respectively. Fig. 10 also demonstrates nominal resistance (R_n) to compare with dynamic resistance. The static resistance does not vary according to the wall orientations as it does not include the effects of solar radiation and heat storage. Besides, it has the same value for all months since the static resistance is the sum of conductive and convective resistances. It is seen that the static resistance is obtained to be $0.5347 \text{ m}^2\text{K/W}$ in the uninsulated wall for all months while it is obtained to be $2.1136 \text{ m}^2\text{K/W}$ in the insulated wall. The results show that the dynamic resistance varies according to the wall orientations and months. It is seen that the static resistance is greater than the dynamic resistance for all wall orientations in January, May, June, July, August, September months while it is smaller than the dynamic resistance in November, December, February, March and April months. It is also seen that dynamic and static thermal resistances increase when the wall is insulated.

The dynamic thermal resistance values of uninsulated and insulated walls are compared in Fig. 11 (a-d). It is seen that peak resistance values in some months of the year are obtained if the wall is insulated. For example, when the wall is 6 cm insulated, the maximum peak value of dynamic resistance is obtained in February for the south-facing wall, in April for the north-facing wall and in March for the east (or west)-facing walls because of minimum heating loads. These months correspond to months of minimum heating as shown in Fig. 7. The results show that dynamic thermal resistance is minimum in months that heating and cooling loads are maximum. It is seen that for south orientation and February month, dynamic thermal resistance is obtained to be $9.1234 \text{ m}^2\text{K/W}$ in the insulated wall while it is obtained to be $0.9511 \text{ m}^2\text{K/W}$ in the uninsulated wall.



(a)



(b)

Figure 10. Variation of thermal resistance values versus months according to different wall orientations for a) uninsulated wall and b) 6 cm insulated wall.

Fig. 12 shows the variation of thermal resistance values versus insulation thickness according to all months for the south-facing wall. It is seen that the static resistance is higher than the dynamic resistance for some months of the year. It is also seen that the dynamic resistances for all months and nominal resistance linearly increase with the increase of insulation thickness. The results demonstrate that the gradient of the resistance versus insulation thickness is different for each month. It is seen that for the south-facing wall, the gradient of the resistance is maximum in February month while it is minimum in January month.

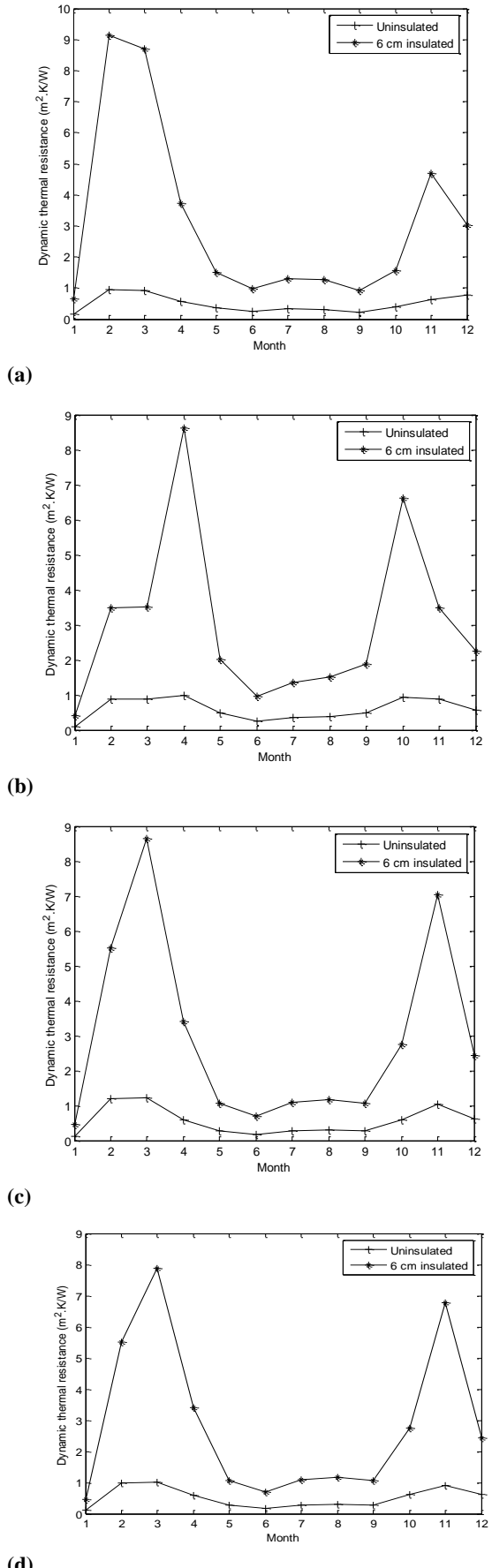


Figure 11. Variation of dynamic thermal resistance versus months according to uninsulated and insulated walls for a) south b) north c) east and d) west orientations

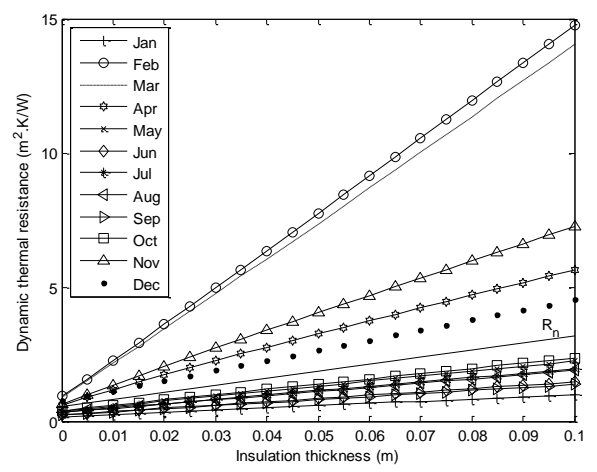


Figure 12. Variation of thermal resistance values versus insulation thickness according to all months for south-facing wall.

Fig. 13 shows the variation of annual averaged dynamic thermal resistance to increasing insulation thickness for different wall orientations. The dynamic resistance differs according to wall orientations since it contains the effects of heat storage and solar radiation. It is seen that in 6 cm insulated wall, the dynamic resistance values are obtained to be 1.956, 1.937, 1.708 and 1.705 m^2K/W while in the uninsulated wall, they are obtained to be 0.480, 0.446, 0.412 and 0.406 m^2K/W for the north, south, east and west orientations, respectively. The results demonstrate that the highest dynamic resistance is obtained in the north-facing wall then the south-facing wall while the lowest dynamic resistance is obtained in east and west-facing walls.

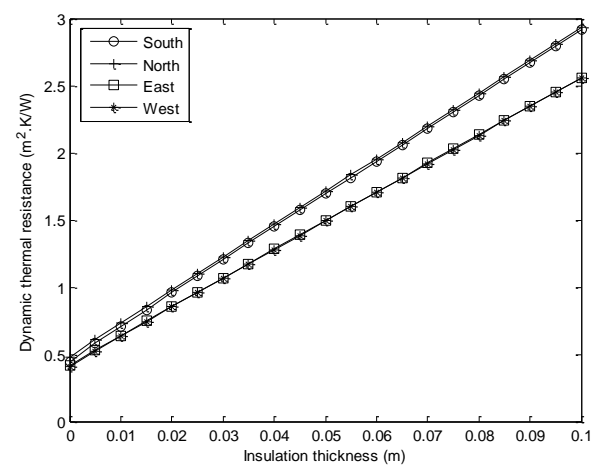
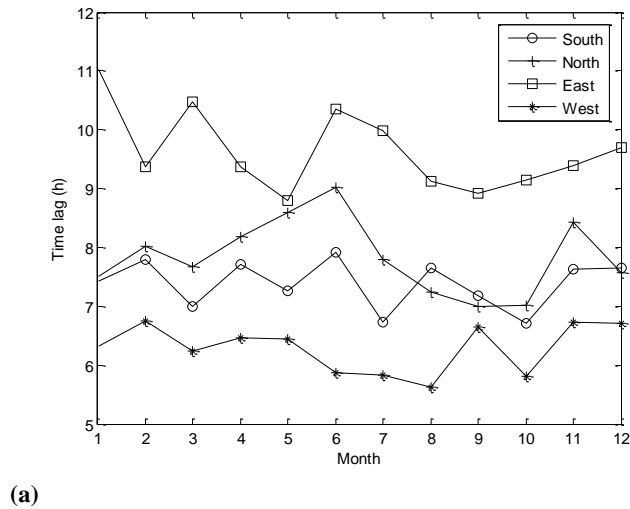


Figure 13. Variation of dynamic thermal resistance versus insulation thickness for different wall orientations

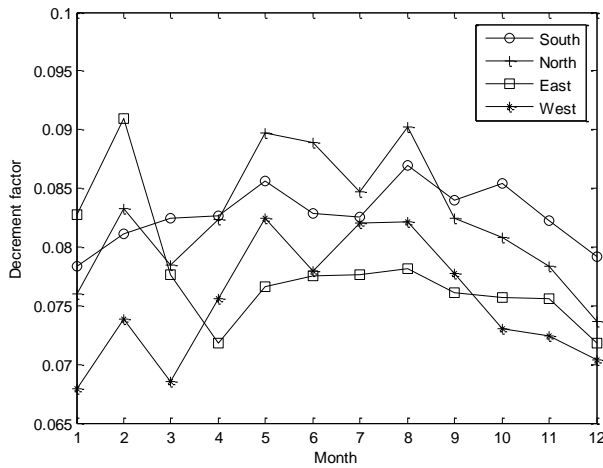
Determination of Time Lag and Decrement Factor

Fig. 14 (a-b) shows the time lag and decrement factor for the 15th day of each month according to different wall orientations. It is revealed that for all months, maximum time lag appears in the east wall while minimum time lag appears in the west wall. Besides, it is seen that the minimum decrement factor is obtained

in the west-facing wall for January, February, March, October, November and December months while it is obtained in the east-facing wall for April, May, June, July, August and September months.



(a)

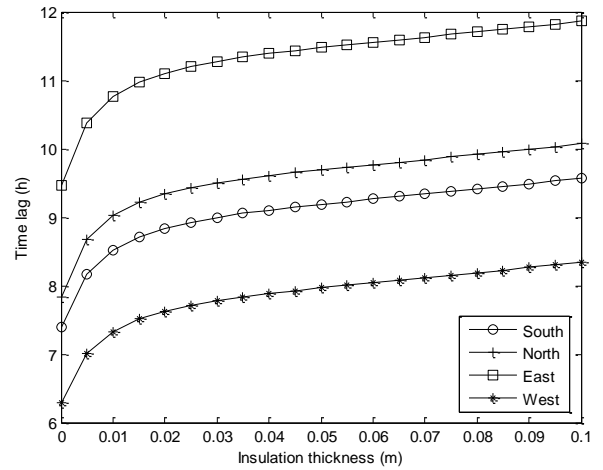


(b)

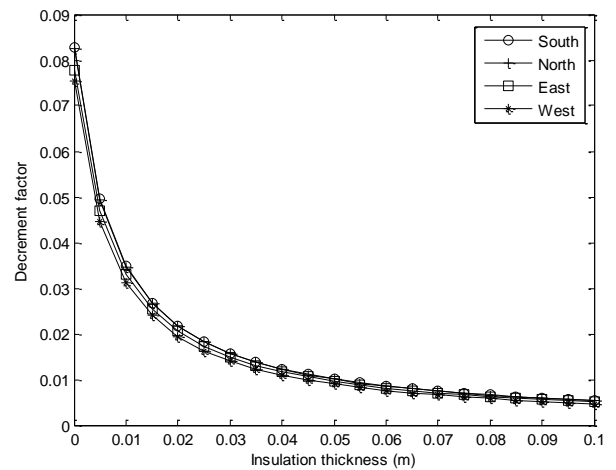
Figure 14 (a-b). Variation of time lag and decrement factor for the 15th day of each month according to different wall orientations

Fig. 15 (a-b) presents the variation of time lag and decrement factor according to increasing insulation thickness for wall orientations. The results indicate that as insulation thickness rises, time lag increase for whole wall orientations while the decrement factor decreases, as expected. The east-oriented wall gives maximum time lag while west oriented wall gives minimum time lag. This is because the maximum peak value of outside surface temperature reaches earlier for the east-facing wall and reaches later for the west-facing wall as seen in Fig.3. However, it is seen that at the lower thickness of insulation, the west-facing wall gives a slightly lower decrement factor than the other orientations. As the thickness of insulation rises, decrement factors for all wall orientations approach each other. Similar conclusions were obtained for different insulation materials under different climatic conditions (Al-Sanea and Zedan 2002). The best result from the maximum time lag point of view is achieved in the east-facing wall

while the worst result from the minimum time lag point of view is obtained in the west-facing wall. The conclusions of this study are consistent with those obtained by employing different climate conditions (Ozel 2013a; Ozel 2013b; Ramin, et al. 2016; Al-Sanea and Zedan 2002).



(a)



(b)

Figure 15 (a-b). Variations of time lag and decrement factor with insulation thickness for different wall orientations.

Change of time lag and decrement factor according to different orientations for uninsulated and insulated walls is presented in Fig. 16 (a-b). For uninsulated walls, the time lag is obtained to be 7.39, 7.84, 9.47 and 6.29 h for the same orientations while the decrement factor is obtained to be 0.0828, 0.0824, 0.0777 and 0.0753 for the south, north, east and west orientations, respectively. The results indicate that the wall orientation has a very small effect on the decrement factor, but has a large effect on the time lag. The results also indicate that the decrement factor is reduced while the time lag rises if the wall is insulated. For 6 cm insulation thickness, it is seen that this increase in time lag is 25.4%, 10.95%, 22.01% and 27.83% while this reduction in decrement factor is 89.61%, 89.68%, 89.58% and 89.91% for the south, north, east and west orientations, respectively.

The results show that the effect of insulation on the decrement factor is greater than its effect on time lag.

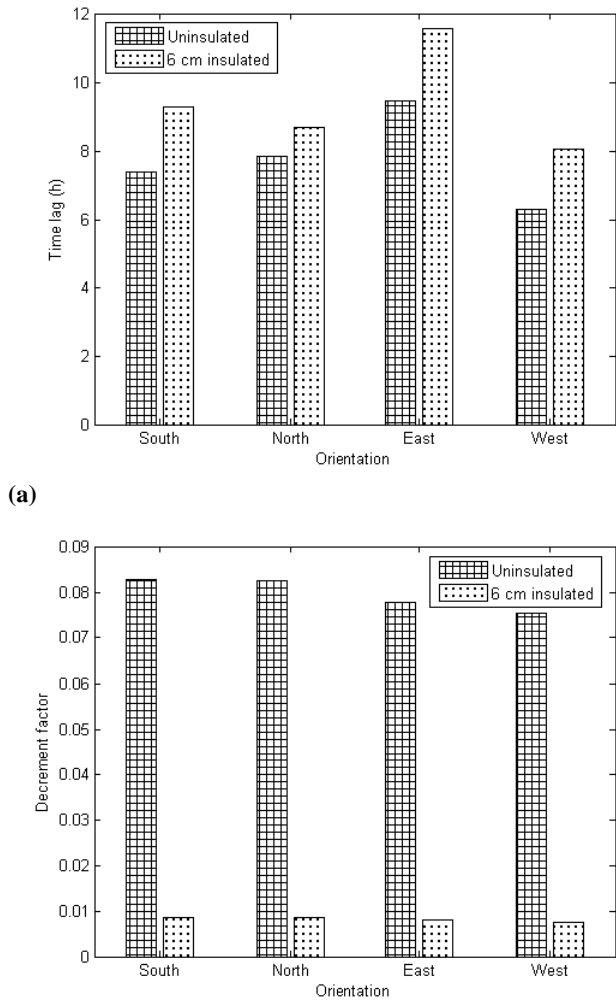


Figure 16 (a-b). Variation of time lag and decrement factor according to different wall orientations

Determination of Optimum Insulation Thickness

Fig. 17 indicates the variation of costs versus increased insulation thickness for the south-facing wall. It is seen that with increasing the insulation thickness, the cost of the insulation rises linearly while the cost of the energy decreases. It is also seen that the total cost which consists of the cost of energy and insulation diminishes up to a certain value of insulation thickness and then started to increase. The variation of total cost according to increasing insulation thickness for all wall orientations is shown in Fig. 18. The optimum insulation thickness is insulation thickness where the total cost is the minimum. The conclusions indicate that the optimum thickness of the insulation is obtained to be 8.4 cm for the south, 8.0 cm for north, 9.2 cm for east and west orientations, respectively. The results of the present study on the optimum insulation thickness according to the different wall orientations are compared with the results of other studies in Table 6. It is obvious that optimum insulation thicknesses of east

and west-facing walls which have the same yearly heating and cooling loads are the same. The results illustrate that for some climatic conditions, the lowest insulation thickness is achieved on the north-facing wall while for other climatic conditions, it is achieved on the south-facing wall. However, it is seen that for most climates, east and west orientations give the greatest insulation thickness. In warm climates such as Adana, it is clear that the minimum insulation thickness is achieved for the north wall. In this study, it is seen that the north orientation provides the lowest insulation thickness while east (or west) orientation provides the highest insulation thickness.

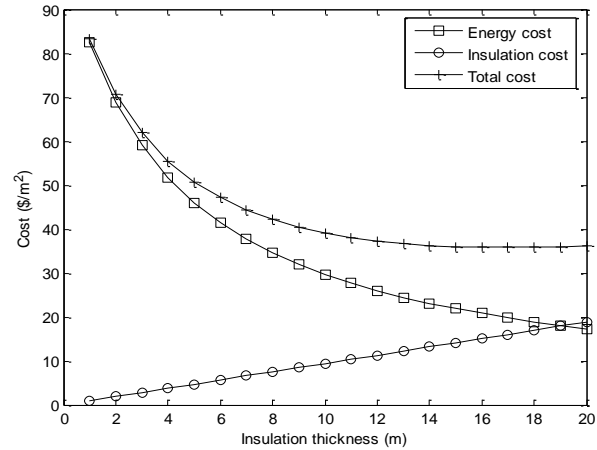


Figure 17. Variation of costs with insulation thickness for a south-facing wall.

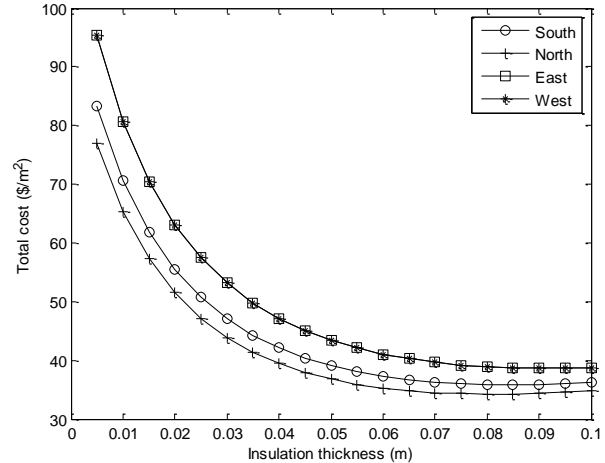


Figure 18. Variation of total cost with insulation thickness for different wall orientations.

Table 6. Comparison of the results of the present study with the results of other studies on the optimum insulation thickness according to the different wall orientations

Reference study	Location	Insulation materials	Optimum insulation thickness (cm)			
			South	North	East	West
Present study (heating+cooling)	Adana, Turkey	Expanded polystyrene	8.4	8.0	9.2	9.2
Ozel, (2011) (heating+cooling)	Elazığ, Turkey	Extruded polystyrene	5.5	6.0	6.0	6.0
Ozel, (2013) (heating)	Kars, Turkey	Expanded polystyrene	13.6	15.0	14.4	14.4
	Kars, Turkey	Extruded polystyrene	9.2	10.2	9.8	9.8
Ozel, (2013) (cooling)	Antalya, Turkey	Extruded polystyrene	3.6	3.1	4.0	4.0
Nematchoua et. al. (2017) (cooling)	Yaounde, Cameroon	Expanded polystyrene	8.0	7.0	8.0	8.0
	Garoua, Cameroon	Expanded polystyrene	12.0	11.0	12.5	12.5
Huo et. al. (2015)(heating+cooling)	Chengdu, China	Expanded polystyrene	6.1	6.1	6.2	6.2
	Changsha, China	Expanded polystyrene	7.3	7.5	7.7	7.7
	Hefeie, China	Expanded polystyrene	7.9	8.2	8.3	8.3
	Shanghai, China	Expanded polystyrene	6.8	7.2	7.2	7.2
Ramin et. al. (2016) heating+cooling)	Tehran, Iran	Expanded polystyrene	5.66	6.04	6.30	6.30
	Tehran, Iran	Extruded polystyrene	3.06	3.24	3.37	3.37
Ibrahim et. al. (2012) (heating)	Zahle, Lebanon	Expanded polystyrene	3.4	4.7	3.9	4.0
Ibrahim et. al. (2012) (cooling)	Beirut, Lebanon	Expanded polystyrene	4.1	1.9	4.8	4.9
Al-Sanea and Zedan(2002)(heating+cooling)	Riyadh	Molded polystyrene	8.75	8.88	9.2	9.25
Daouas, (2011) (heating+cooling)	Tunisia	Expanded polystyrene	10.10	10.1	11.7	11.6

CONCLUSION

This study is realized for the climatic conditions of Adana which is one of the hottest cities of Turkey. Firstly, heating and cooling periods for different wall orientations are determined by calculating the transmission loads according to indoor design temperatures under dynamic thermal conditions. It is seen that for a south-facing wall, the heating period consists of December, January and February months while the cooling period consists from March to November. For a north-facing wall, the heating period consists from November to April while the cooling period consists from May to October. On the other hand, it is seen that for east (or west) orientations, the heating period consists from November to March while the cooling period consists from April to October. The results show that the longest cooling period is obtained in south orientation while the shortest cooling period is obtained in north orientation. The results also show that the wall orientation has an important effect on heating and cooling periods.

Secondly, thermal parameters such as transmission loads, dynamic thermal resistance, time lag and decrement factor are calculated for all wall orientations by using indoor design temperatures determined over the whole year. The results show that the other orientations have almost equal cooling loads while the minimum cooling load is obtained for the north-facing wall. Besides, it is seen that maximum heating load is obtained in the north wall while the minimum heating load is obtained in the south wall.

It is revealed that the dynamic resistance is inversely proportional to the total transmission load. That is, the maximum thermal resistance corresponds to the minimum transmission load. The results show that the north-facing wall then the south-facing wall give the

lowest yearly total transmission load, the lowest insulation thickness and the highest dynamic thermal resistance. On the other hand, west and east-facing walls give the highest yearly total transmission load, the highest insulation thickness and the lowest dynamic thermal resistance.

Besides, the results show that the east-facing wall has the longest time lag since the maximum value of the outer surface temperature is reached at the earliest east wall. It is seen that the effect of the wall orientation on the decrement factor is unimportant while the wall orientation has an important effect on time lag. Finally, the optimum thickness of insulation is determined by using both heating and cooling loads. The results obtained for different wall orientations are compared with the results of other studies under different climatic conditions.

Consequently, it is seen that wall orientation has a noticeable effect on time lag, dynamic thermal resistance, transmission loads and optimum insulation thickness while the effect of wall orientation on decrement factor and static thermal resistance are insignificant.

REFERENCES

- Akan A. E., 2021, Determination and Modeling of Optimum Insulation Thickness for Thermal Insulation of Buildings in All-City Centers of Turkey, *International Journal of Thermophysics*, 42, 49, 1-34.
- Aktemur C., Bilgin F. and Tunçkol S., 2021, Optimization on the Thermal Insulation Layer Thickness in Buildings with Environmental Analysis: an Updated Comprehensive Study for Turkey's all Provinces, *Journal of Thermal Engineering*, 7, 5, 1239–1256.

- Al-Sanea S.A., Zedan M. F., and Al-Ajlan S. A., 2003, Heat Transfer Characteristics and Optimum Insulation Thickness for Cavity Walls, *Journal of Thermal Envelope and Building Science*, 26, 3, 285-307.
- Al-Sanea S.A., and Zedan M. F., 2002, Optimum Insulation Thickness for Building Walls in a Hot-Dry Climate, *International Journal of Ambient Energy*, 23, 3, 115-126.
- Al-Sanea S.A., Zedan M. F. and Al-Hussain S. N., 2013, Effect of Masonry Material and Surface Absorptivity on Critical Thermal Mass in Insulated Building Walls, *Applied Energy*, 102, 1063-1070.
- Al-Sanea S.A., Zedan M. F. and Al-Ajlan, S. A., 2005, Effect of Electricity Tariff on The Optimum Insulation-Thickness in Building Walls as Determined by a Dynamic Heat-Transfer Model, *Applied Energy*, 82, 313-330.
- Barrau J., Ibanez M. and Badia F., 2014, Impact of the Insulation Materials' Features on The Determination of Optimum Insulation Thickness, *International Journal of Energy and Environmental Engineering*, 5, 2-3, 1-9.
- Bolattürk A., 2008, Optimum Insulation Thicknesses For Building Walls with Respect to Cooling and Heating Degree-Hours in the Warmest Zone of Turkey, *Building and Environment*, 43, 1055-1064.
- Bolattürk A., 2006, Determination of Optimum Insulation Thickness for Building Walls with respect to Various Fuels and Climate Zones in Turkey, *Applied Thermal Engineering*, 26, 1301-1309.
- Çomaklı K. and Yüksel B., 2003, Optimum Insulation Thickness of External Walls for Energy Saving, *Applied Thermal Engineering*, 23, 473-479.
- Çomaklı K. and Yüksel B., 2004, Environmental Impact of Thermal Insulation Thickness in Buildings, *Applied Thermal Engineering*, 24, 933-940.
- Daouas N., Hassen Z. and Aissia H. B., 2010, Analytical Periodic Solution for The Study of Thermal Performance and Optimum Insulation Thickness of Building Walls in Tunisia, *Applied Thermal Engineering*, 30, 319-326.
- Daouas N., 2011, A Study on Optimum Insulation Thickness i Walls and Energy Savings in Tunisian Buildings based on Analytical Calculation of Cooling and Heating Transmission Loads, *Applied Energy*, 88, 156-164.
- Dombaycı Ö. A., Gölcü M. and Pancar Y., 2006, Optimization of Insulation Thickness for External Walls for Different Energy-Sources, *Applied Energy*, 83, 9, 921-928.
- Dombaycı Ö. A., 2007, The Environmental Impact of Optimum Insulation Thickness for External Walls of Buildings, *Energy and Buildings*, 42, 3855-3859.
- Dombaycı Ö. A., Atalay Ö., Acar S. G., Ulu E. Y. and Ozturk H. K., 2017, Thermo-economic Method for Determination of Optimum Insulation Thickness of External Walls for The Houses: Case Study for Turkey, *Sustainable Energy Technologies and Assessments*, 22, 1-8.
- Duffie J. A., & Beckman W. A., 1991, Solar Engineering Of Thermal Processes, John Wiley and Sons, inc., New York.
- Ertürk M., 2016, A New Approach to Calculate The Energy Saving Per Unit Area and Emission Per Person in Exterior Wall of Building using Different Insulation Materials and Air Gap, *Journal of the Faculty of Engineering and Architecture of Gazi University*, 31(2), 395-406.
- Ertürk M., 2017, A New Model for Exergetic Optimum Insulation Thickness, *International Journal of Exergy*, 22, 3, 309-330.
- Hasan A., 1999, Optimizing Insulation Thickness for Buildings using Life Cycle Cost, *Applied Energy*, 63, 115-124.
- Huo H., Jing C. and Huo H., 2015, Effect of Natural Ventilation on Transmission Load of Building External Walls and Optimization of Insulation Thickness, *Journal of thermal science and technology*, 10, 2, 1-17.
- Ibrahim M., Ghaddar N. and Ghali K., 2012, Optimum Location And Thickness of Insulation Layers for Minimizing Building Energy Consumption, *Journal of Building Performance Simulation*, 5, 6, 384-398.
- Kaynaklı O., 2008, A Study on Residential Heating Energy Requirement and Optimum Insulation Thickness, *Renewable Energy*, 33, 1164-1172.
- Kaynaklı O., Yüce C., Dogan O., and Kaynaklı Z., 2015, A Study on Determination of Optimum Thermal Insulation Thickness using Life Cycle Cost Analysis, *International Journal of Advances in Mechanical and Civil Engineering*, 2, 6, 1-5.
- Kontoleon K. J., Theodosiou ThG. and Tsikaloudaki K. G., 2013, The Influence of Concrete Density and Conductivity on Walls' Thermal Inertia Parameters Under a Variety of Masonry and Insulation Placements, *Applied Energy*, 112, 325-337.
- Kurt H., 2010, The Usage of Air Gap in The Composite Wall for Energy Saving and Air Pollution, *Environmental Progress and Sustainable Energy* 30, 450-458.

- Mahlia T. M. I. and Iqbal A., 2010, Cost Benefits Analysis and Emission Reductions of Optimum Thickness and Air Gaps for Selected Insulation Materials for Building Walls Maldives, *Energy*, 35, 2242-2250.
- Nematchoua M. K., Ricciardi P., Reiter S., and Yvon A., 2017, A Comparative Study on Optimum Insulation Thickness of Walls and Energy Savings in Equatorial and Tropical Climate, *International Journal of Sustainable Built Environment*, 6, 170-182.
- Ozel M., 2011, Effect of Wall Orientation on The Optimum Insulation Thickness by Using a Dynamic Method, *Applied Energy*, 88, 2429-2435.
- Ozel M., 2013a, Thermal, Economical and Environmental Analysis of Insulated Building Walls in a Cold Climate. *Energy Conversion and Management*, 76, 674-684.
- Ozel M., 2013b, Determination of Optimum Insulation Thickness Based on Cooling Transmission Load for Building Walls in a Hot Climate, *Energy Conversion and Management*, 66, 106-114.
- Ozel, M., & Pihtili, K. (2007). Optimum Location and Distribution of Insulation Layers on Building Walls with Various Orientations. *Building and Environment*, 42, 3051-3059.
- Ozel, M. (2016). Effect of Indoor Design Temperature on The Heating and Cooling Transmission Loads. *Journal of Building Engineering*, 7, 46-52.
- Ozkahraman H. T. and Bolattürk A., 2006, The Use of Tuff Stone Cladding in Buildings for Energy Conservation, *Construction and Building Materials*, 20, 435-440.
- Özel G., Açıklık E., Görgün B., Yamık H. and Caner N., 2015, Optimum Insulation Thickness Determination Using The Environmental and Life Cycle Cost Analyses based Entropy Approach, *Sustainable Energy Technologies and Assessments*, 11, 87-91.
- Ramin H., Hanafizadeh P. and Akhavan-Behabadi M. A., 2016, Determination of Optimum Insulation Thickness in Different Wall Orientations and Locations in Iran, *Advances in Building Energy Research*, 10, s2, 149-171.
- Sisman N., Kahya E., Aras N. and Aras H., 2007, Determination of Optimum Insulation Thicknesses of The External Walls and Roof (Ceiling) for Turkey's Different Degree-Day Regions, *Energy Policy*, 35, 5151-5155.
- State Meteorological Station, Records for weather data, Turkey, 2007-2017.
- Sundarama, A. S. and Bhaskaran A., 2014, Optimum Insulation Thickness of Walls for Energy-Saving in Hot Regions of India, *International Journal of Sustainable Energy*, 33, 1, 213-226.
- Threlkeld J. L., 1998, Thermal environmental engineering. Englewood Cliffs, NJ: Prentice-Hall.
- Yıldız A., Gürlek G., Erkek M. and Özbaltı N., 2008, Economical and Environmental Analyses of Thermal Insulation Thickness in Buildings, *Journal of Thermal Science and technology*, 28, 2, 25-34.
- Yu J., Yang C., Tian L. and Liao D., 2009, A Study on Optimum Insulation Thicknesses of External Walls in Hot Summer and Cold Winter Zone of China, *Applied Energy*, 86, 2520-2529.
- Zengin D. G. and Kontoleon K. J., 2018, Influence of Orientation, Glazing Proportion and Zone Aspect Ratio on The Thermal Performance of Buildings During The Winter Period, *Environmental Science and Pollution Research*, 25, 27, 26736-26746.



Meral ÖZEL graduated from Department of Mechanical Engineering of Fırat University in 1992. She received his M.Sc. and Ph.D. degrees in Mechanical Engineering from Fırat University in 1996 and 2003, respectively. She became Associate Professor in 2014 and Professor in 2021. Currently, she is working as a faculty member at the same university.



ANALYSIS AND OPTIMIZATION OF ACTIVATED CARBON COATED HEAT SINKS

A. Alperen GÜNAY*

*Orta Doğu Teknik Üniversitesi Mühendislik Fakültesi Makina Mühendisliği Bölümü
06800 Çankaya, Ankara
gunaya@metu.edu.tr, ORCID: 0000-0002-2013-9101

(Geliş Tarihi: 21.01.2022, Kabul Tarihi: 12.03.2022)

Abstract: With the enhancements in nanotechnology, electronic devices shrank in size which led to a necessity to develop efficient thermal management strategies. These small electronic devices could be thermally managed through passive systems provided that effective materials are developed. Here, we use a layer of activated carbon on top of anodized aluminum heat sinks to utilize the sorption cycle of atmospheric water to create a desorption induced evaporative cooling effect. The material properties of the activated carbon lead to enhanced cooling by radiation and desorption, while the geometry of the heat sinks ensure surface area maximization. We develop a numerical simulation platform to determine the optimum geometry and the optimal activated carbon coating mass. Our results show that as the fin diameter and spacing shrink, and as the activated carbon mass increases within the considered range (0-100 mg), effective cooling of the chip could be achieved. We further employ our simulations to decouple the effects of desorption, radiation, and convection. Our analyses reveal that desorption only plays a vital role during the initial periods of operation, while cooling due to radiation and convection leads to an $\approx 20\%$ increase in the overall steady-state heat transfer coefficient. This study goes beyond introducing a passive thermal management strategy for small electronic chips by providing a link between mass diffusion and thermal processes for effective transient operation of thermal devices.

Keywords: Thermal management, Activated carbon, Passive device, Heat sink.

AKTİF KARBON KAPLAMALI SOĞUTUCULARIN ANALİZ VE OPTİMİZASYONU

Özet: Nanoteknolojideki son gelişmeler, elektronik cihazların boyutlarının küçülmesine yol açtı ve bu durum randımanlı ısı yönetim stratejilerinin geliştirilmesini bir zorunluluk haline getirdi. Küçülen bu cihazların ısı yönetimlerinin geliştirilecek olan verimli pasif cihazlar vasıtasıyla etkili bir şekilde gerçekleştirilebileceği öngörülmektedir. Bu çalışmada, atmosferdeki su buharının sorpsiyon döngüsü kullanılarak yapay bir buharlaşmalı soğutma etkisi oluşturulması amacıyla anotlanmış alüminyum soğutucuların üzerine bir aktif karbon tabakası kaplanmıştır. Aktif karbonun malzeme özellikleri radyasyon ve desorpsiyon ile daha fazla soğutmaya olanak sağlarken, ısı emicilerinin geometrileri yüzey alanının en üst seviyeye çıkarılmasını sağlamaktadır. İdeal soğutucu geometrisini ve optimum aktif karbon kaplama kütlelerini belirlemek için sayısal benzetim platformları geliştirilmiş ve kullanılmıştır. Analiz sonuçlarına göre kanatçık çapı ve aralığı küçüldükçe, ve aktif karbon kütlesi çalışılan aralıkta (0-100 mg) arttıkça, elektronik çipin etkili bir şekilde soğutulabileceği görülmektedir. Desorpsiyon, radyasyon ve konveksiyonun etkilerini ayrı ayrı çalışabilmek için belirli girdilerle benzetme algoritmaları tekrar kullanılmıştır. Analizlerimiz, desorpsiyonun sadece erken fazlarda önemli bir rol oynadığını, radyasyon ve konveksiyon temelli soğutmanın ise denge durumundaki toplam ısı transfer katsayısında ortalama %20'lik bir artışa yol açtığını ortaya koymaktadır. Bu çalışma küçük elektronik cihazların pasif yöntemlerle soğutulmalarına yönelik stratejiler geliştirmenin ötesinde, ısı cihazların zamana bağlı etkili bir şekilde çalışmalarını için kütle difüzyonu ve ısı prosesi arasında bir bağlantı kurmaktadır.

Anahtar Kelimeler: Isı yönetim, Aktif karbon, Pasif cihazlar, Isı emici.

NOMENCLATURE

A	Area [m ²]	IoT	Internet of Things
AC	Activated Carbon	k	Thermal Conductivity [W/m·K]
C	Concentration [mol/mol]	L	Length of the Fin [mm]
c_p	Specific Heat Capacity [kJ/kg·K]	L_1	Length of the Chip [mm]
D	Fin Diameter [mm]	L_2	Width of the Chip [mm]
D_C	Intramolecular Diffusivity [m ² /s]	L_C	Characteristic Length [m]
g	Gravitational Acceleration (m/s ²)	m_w	Mass of Adsorbed Water [mg]
h	Heat Transfer Coefficient [W/m ² ·K]	m_{AC}	Mass of AC Coating [mg]
		MOF	Metal-Organic Framework
		N	Number of Fins

Nu	Nusselt Number [$=h \cdot L/k$]
P	Perimeter [mm]
q_c	Heat Supply [W/m^2]
r	Radius [m]
R	Thermal Resistance[K/W]
R_s	Particle Radius [nm]
Ra_L	Rayleigh Number [$=\beta \cdot g \cdot \Delta T \cdot (L_C)^3/\nu \cdot \alpha$]
RK4	4 th Order Runge-Kutta Algorithm
S	Fin Spacing [mm]
t	Time [s]
T	Temperature [K]
t_C	Thickness of the Chip [mm]
α	Thermal Diffusivity (m^2/s)
β	Thermal Expansion Coefficient (1/K)
ν	Kinematic Viscosity (m^2/s)
ΔT	Temperature Gradient [$^{\circ}C$]
ϵ	Emissivity
η	Fin Efficiency
σ	Stefan-Boltzmann Constant [$W/m^2 \cdot K^4$]

Subscripts

air	Air
des	Desorption
E	Inside the Silicon Chip
f	Fin
hot	Hot Side of the Silicon Chip
i	i th Body
nat	Natural Convection
o	Overall State
rad	Radiation
s	Surface
t	Total
∞	Ambient

INTRODUCTION

With the recent advancements in nanotechnology, efficient small electronic devices to power Internet-of-Things (IoT) devices have proliferated (Yoon et al., 2015). While scaling down on the size brought about a plethora of advantages, it also led to certain engineering challenges to address to keep the output power at an acceptable range (Zhu et al., 2013). One of the bottlenecks of reducing the size of power electronics and IoT devices is the sheer thermal stresses arising from large thermal gradients, leading to material failures if not properly addressed (Yang et al., 2018). Therefore, thermal management of small devices has been a popular topic of research over the last few decades (Moore and Shi, 2014). Thermal management has been traditionally performed through heat sinks, where the exposed surface area is enhanced through elongated fins with optimized geometries to effectively decrease the temperature of power electronic devices (Hetsroni et al., 2002). While heat sinks enhanced the heat transfer with the surroundings significantly when a liquid flow was present, the enhancements were limited in the absence of a flow (Christen et al., 2016). Hence, other mechanisms of thermal management were introduced including radiative cooling (Zhou et al., 2016) and phase change heat transfer (Cho et al., 2016).

Radiative cooling refers to enhancing the emissivity of a body at the desired spectral range such that the emitted radiation from the surface is increased (Hossain and Gu, 2016). While this approach proves effective for systems that are not exposed to a running flow, design of selective emitters is a challenging task (Hahn, 2010). Thus, the operation of such systems is limited. Furthermore, exposing these devices to sunlight could result in the opposite effect (i.e. heating instead of cooling) since absorption and emission are equal at a spectral level (Hu et al., 2018). Therefore, performance enhancement stemming from radiative cooling is highly application specific.

Another technique to efficiently cool power electronics is to utilize the latent heat of phase change on hot spots of interest (Oh et al., 2017). High latent-to-specific heat ratio values of most liquids make phase change induced thermal management attractive for different applications (Günay et al., 2017). Hence, it has been extensively studied in the past (Attinger et al., 2014), especially through evaporative cooling (Günay et al., 2021), and boiling (Li et al., 2019). While boiling is effective due to significantly larger heat transfer coefficient stemming from bubble dynamics (Zhou et al., 2021), it is only meaningfully useful at high output power electronics due to the required high temperature spots to catalyze boiling (Birbarah et al., 2020). Therefore, evaporative cooling is much more desirable for small electronics where the temperatures are kept close to the standard room temperature or the human body temperature. Thankfully, evaporative cooling also results in significant enhancements in the heat transfer coefficient (Yang et al., 2019). In fact, studies attained as much as 91% enhancement through evaporative cooling due to efficient utilization of the latent heat of water evaporation (Kabeel et al., 2017). Therefore, evaporative cooling remains as a thermal management technique with a significant potential (Yang et al., 2019). On the other hand, while phase change heat transfer comes with many advantages, there are certain bottlenecks associated with it. A constant supply of fresh liquid needs to be integrated into the system, adding to the complexity, cost, and size (Birbarah et al., 2020). Furthermore, droplets have to be actively directed onto the hot spots, resulting in expenditure of energy to decrease the total conversion efficiency (Shahriari et al., 2017). Therefore, these bottlenecks have made it difficult for evaporative cooling inducing systems to be integrated into small electronics and IoT devices.

Recently, passive coatings that could utilize the sorption cycles of atmospheric water have been introduced (Rezk et al., 2012). These coatings constantly adsorb and desorb the humidity in the air to create sorption cycles due to their material properties (Kim et al., 2018). Silica gels (Ng et al., 2001), metal-organic frameworks (MOFs) (Kim et al., 2017), and zeolites (Henninger et al., 2010) have been primarily used for this purpose. While the main use of these materials and their corresponding sorption cycles has been to collect fresh water from the atmosphere (Fathieh et al., 2018), they were also shown

to act as effective evaporative coolers since desorption creates a pseudo-evaporative cooling effect on the surfaces (Karamanis et al., 2012). Researchers from Shanghai Jiao Tong University in China used MIL-101 (a Chromium based MOF) to effectively thermally manage a 1W power generator, decreasing the maximum temperature as much as 8.6°C (Wang et al., 2020). Similarly, researchers from The University of Tokyo parametrically studied three different types of MOFs to display as much as 300% enhancement in thermoelectric power output for a device operating near room temperature (Günay et al., 2022). Though these results are promising, MOF powders are typically expensive and difficult to procure (Stock and Biswas, 2012). Therefore, a long way has to be covered before making these materials fully attractive for small scale operations.

Activated carbon (also termed activated charcoal) is another material with the ability to create water sorption cycles due to the material properties it possesses (Do and Do, 2000). It is cost effective compared to MOFs due to its vast availability and ease of procurement (González-García, 2018). Furthermore, activated carbon (AC) powders could be made to possess characteristic sizes in the microscale or nanoscale (Juárez-Galán et al., 2009). Furthermore, they could easily be applied onto surfaces through spraying (Jang et al., 2013). Since AC possesses a high radiative emissivity ($\epsilon \approx 1$) (Subrenat and Le Cloirec, 2003), they could also be used as radiative coolers. Hence, AC coatings could be tailored as combined radiative and sorbent coolers.

In this study, we numerically investigate the use of AC coatings as efficient thermal management options. We consider aluminum pin fins coated with activated carbon powders to maximize the surface area, radiative cooling, and desorption from the surface. We determine the optimum fin diameter, spacing, and sorbent coating mass through numerical optimization considering the thermal management of a hot silicon chip. Our results show that low diameter and low spacing leads to the optimum geometry due to the maximization of the exposed surface area. Additionally, the results of our optimization reveal that the mass of the AC coating should be maximized within the studied range due to the enhancements in radiative cooling and the benefits of desorption cooling. We further utilize our numerical algorithms to determine the physical mechanism of enhancement. Our results reveal that while desorption plays a role in the early stages of operation, it has a negligible contribution to the performance in the steady- state. Rather, increased radiation and natural convection from the surface result in an $\approx 20\%$ increase in the overall heat transfer coefficient for the AC coated heat sinks compared to the plain anodized aluminum ones. This study not only sheds light onto the use of AC coatings as an effective thermal management strategy but also provides design priorities for the next generation of sorbent based thermal systems.

SYSTEM MODEL

The system of interest consists of an aluminum heat sink with pin fins coated with a thin layer of AC (Figure 1). Aluminum is chosen because of its relatively high thermal conductivity for a fraction of the cost of other metals (Sommer, 1997). Furthermore, aluminum heat sinks could be anodized to increase their overall emissivity (Gustavsen and Berdahl, 2003). The heat sinks to be modeled in this manuscript are all anodized in order to obtain a fair comparison between the AC coated heat sinks and the plain ones. The heat sink serves as a thermally conductive mold with a high surface area, while the thin AC layer that takes the shape of the heat sink serves to create water sorption cycles to induce evaporative cooling, as well as to enhance the overall emissivity of the surface to increase cooling by radiation. The inputs for the numerical model related to AC were obtained from the literature and are summarized in Table 1 (Uddin et al., 2018, Verma et al., 2019).

AC was selected as the coating material due to its cost effectiveness and coatability. AC could be synthesized through many different techniques in vast amounts, leading to a low cost (Nor et al., 2013, González-García, 2018). In fact, commercial AC powders could be purchased from commercial vendors at around 0.132 \$/g (7440-44-0, Sigma Aldrich), which places the cost of coating for this application to 0.013 \$. Furthermore, bulk coatings could be easily applied following a procedure similar to the one given in previous studies (Günay et al., 2022). Therefore, considering the offered advantages of enhanced thermal performance and passive operatability at a low cost, AC coatings could potentially render the anodization process irrelevant for applications where the heat sinks are not subjected to heavy rain or flows.

A total silicon nanowire based chip size of 30x30 mm ($L_1 \times L_2$) was selected as a reference. The size of the heat sink was identical. The thicknesses of the base plate of the heat sink and the silicon chip were both 1 mm (t_c), while the fin length was selected as 3 mm (L). The spacing (S) and the fin diameter (D) were parametrically varied in the analyses to obtain the optimum fin geometry. Furthermore, the mass of the AC layer was altered along with the geometric parameters to determine the optimal coating thickness. All inputs were provided to the numerical code developed in MATLAB to obtain the temperature reduction and the heat transfer enhancement.

THEORETICAL MODELING

The theoretical model consisted of two main parts, namely; 1) mass diffusion model to obtain the desorption characteristics of water vapor on the AC layer, 2) a 1D transient heat transfer model to obtain the temperature gradients and the heat fluxes on the system. Assuming spherical particles undergoing homogeneous diffusion at a given temperature, the change in concentration is given by Fick's Law as (Stebe and Lin, 2001):

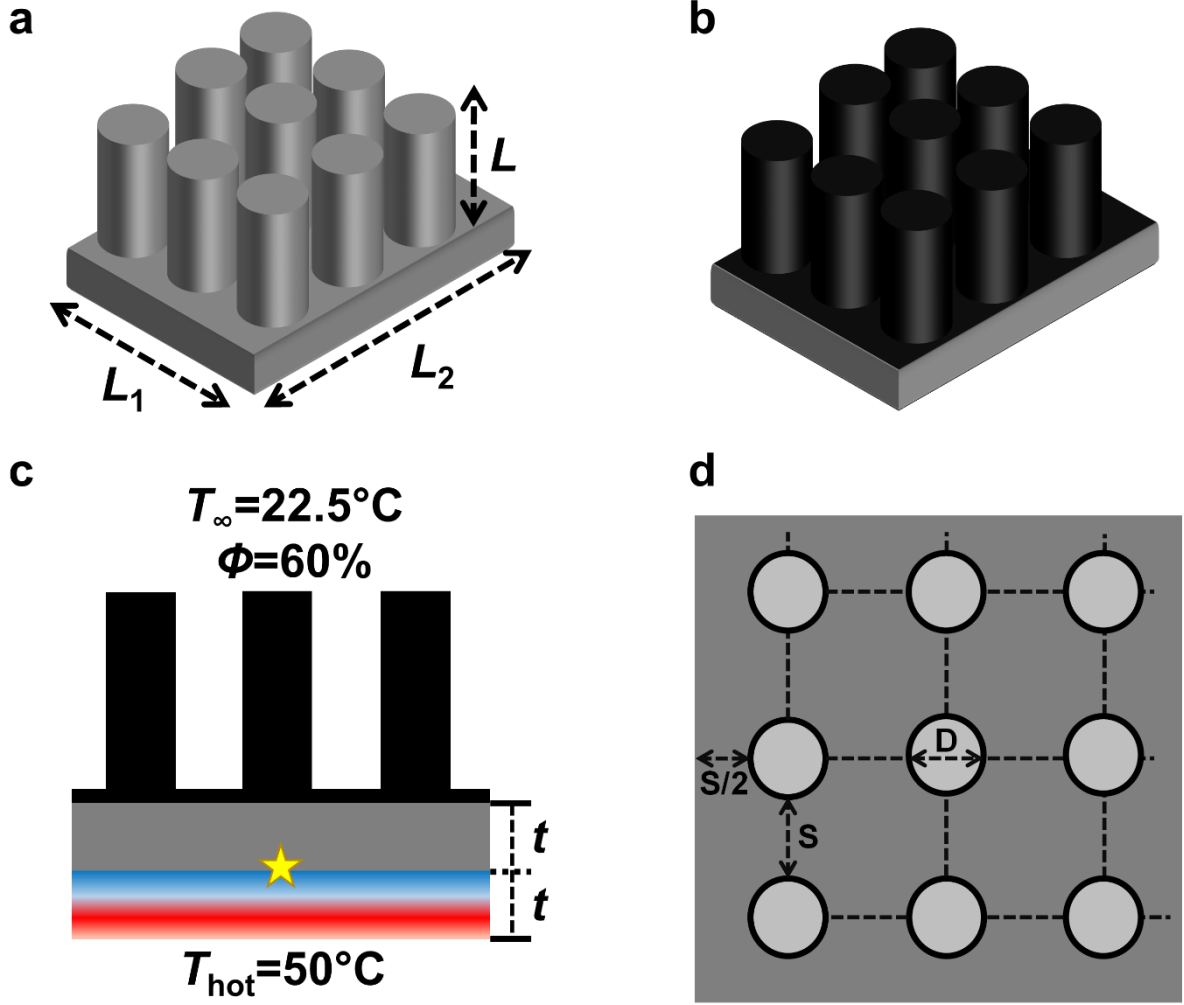


Figure 1. Schematics of the modeled system. a) The anodized aluminum heat sink with the corresponding dimensions, b) activated carbon coated anodized aluminum heat sink, c) side view of the modeled system including the electronic chip, the base of the anodized aluminum heat sink, and the activated carbon coating. The star represents the top side of the electronic chip which is the spot (the whole top surface) to be cooled. d) Top view of the modeled system with the corresponding geometric shape factors.

$$\frac{\delta C}{\delta t} = \frac{D_c}{r^2} \frac{\delta}{\delta r} r^2 \frac{\delta C}{\delta r}, \quad (1)$$

Assuming constant surface concentration, diffusivity, and intermolecular radius, the solution of Eq. (1) reduces to (Kim et al., 2018):

$$\frac{m_w}{m_{AC}} = \left[1 - \frac{6}{\pi^2} \sum_{n=1}^{\infty} \frac{1}{n^2} \exp\left(-\frac{n^2 \pi^2 D_c}{R_s^2} t\right) \right], \quad (2)$$

where the left hand side of Eq. (2) refers to the adsorption capacity of AC (14% at 60% relative humidity on average) (Rodríguez-Mirasol et al., 2005). We determined $R_s=9.5$ nm from the literature (Yuan et al., 2016) and subsequently obtained $D_c=1.4 \times 10^{-21}$ m²/s through fitting Eq.(2) to match the adsorption capacity of AC. After obtaining the mass diffusion dynamics, the next step was to use them as inputs of the heat transfer calculations. Thermal information could be obtained at any given time by a mathematical balance of the total unsteady heat, radiation, convection, mass diffusion induced heat fluxes, and the total heat supply into the

system. Assuming 1-D transport and that the spatial variations do not lead to any temporal changes in the thermal behavior, we could obtain the resulting governing equation with the corresponding boundary conditions as:

$$\sum_i m_i c_{p,i} \frac{dT_i}{dt} = A_s [q_c - h_{nat}(T_s - T_{\infty}) - \varepsilon \sigma (T_s^4 - T_{\infty}^4)] - \dot{m} h_{des}, \quad (3)$$

$$T_s(t=0) = T_{\infty}, \quad (4)$$

$$q_c - h_{nat}(T_s(t=\infty) - T_{\infty}) - \varepsilon \sigma (T_s^4(t=\infty) - T_{\infty}^4) = 0 \quad (5)$$

The 1-D assumption allowed us to effectively carry each intermediary temperature to the surface through the heat supplied from the silicon chip given by:

$$q_c = \frac{T_{hot} - T_s(t)}{\sum_i R_i}, \quad (6)$$

The resistance term was obtained by treating the silicon chip, the base of the heat sink, and the AC layer as slabs

Table 1. Property inputs for the numerical algorithm.

	Silicon Chip	AC	Anodized Aluminum
c_p (kJ/kg·K)	720	850	900
k (W/m·K)	0.25	0.63	205
ρ (kg/m ³)	2330	400	2700
ε	-	0.99	0.8

($R_i=L_i/k_i\cdot A_i$, with their corresponding cross sectional areas), obtaining the resistance of the extended fins (AC coated or plain) through fin efficiency analogy, and considering a 200 μm thick air gap as a contact resistance between the heat sink and the silicon chip (Günay et al., 2022). Thermal parameters that are necessary for the simulation of each layer are given in Table 1. Total fin efficiency and the corresponding thermal resistance were obtained from (Bergman et al., 2011):

$$\eta_o = 1 - \frac{NA_f}{A_t}(1 - \eta_f) = \frac{1}{R_o h A_t}, \quad (7)$$

where the subscript o represents the overall state (array of fins and the base), f represents the fin, and t represents the total. The individual fin efficiency for a pin fin was obtained from (Bergman et al., 2011):

$$\eta_f = \frac{\tanh\left[\left(\frac{4h}{kD}\right)^{0.5} L_c\right]}{\left(\frac{4h}{kD}\right)^{0.5} L_c}, \quad (8)$$

where $L_c=L+(D/4)$ is the characteristic length. Natural convection term was obtained through Nusselt-Rayleigh analogy for a heat plane facing upward given by (Bergman et al., 2011):

$$h_{\text{nat}} = \frac{Nu L_c}{k_{\text{air}}} = (0.54 Ra_L^{0.25}) \frac{L_c}{k_{\text{air}}}, \quad (9)$$

Where $L_c=A_s/P$ was the characteristic length of the heat exchanging surfaces (fins). Finally, the mass information obtained by Eq. (2) was not enough for the solution of Eq. (3). We numerically differentiated Eq.(2) at each instant of interest to obtain the rates of desorption and used it as an input for Eq. (3). The latent heat of desorption of water from the surface was determined to be 55 kJ/mol from the literature which was lower compared to the 135 kJ/mol for evaporation of water (Kim et al., 2016).

The solution scheme of Eq. (3) consisted of a 4th order Runge-Kutta algorithm (RK4) solving Eq.(3) bounded by Eq.s (4)-(5). The effects of the intermediary temperatures (i.e. everything other than T_s) was transformed into the heat supply from the silicon chip using the resistances and effective parameters, and the corresponding surface temperatures were iteratively obtained for each second. The RK4 algorithm was tested with reference cases and validated before the implementation for this study. The reference cases for validation included heat sink scenarios with analytical solutions (without the effects of desorption), comparison to previously performed experiments with heat sinks and flat plates with sorbent coatings (without the effects of desorption), and

comparison to previously performed experiments with sorbent coatings undergoing regular thermal operation (Günay et al., 2022). After we ensured that the algorithm was in perfect agreement with the analytical solutions (i.e. $\approx 0\%$ deviation) and in good agreement with the experiments (within $\approx 10\%$ of the experimental measurements), we implemented our numerical platform to carry out the thermal simulations.

RESULTS AND DISCUSSION

The main goal of this study is to minimize the temperature of the top surface of the silicon chip (Depicted with a star on Figure 1c). Therefore, the temperature reduction inside the silicon chip (ΔT_E) should be maximized. In other words, the effective heat transfer coefficient based on the top surface of the silicon chip (h_E) needs to be maximized. For that purpose, an optimization algorithm was carried out on top of Eq. (3) to determine the optimum geometry of the heat sink and the optimal AC layer mass. The analyses were carried out for a fin diameter range (D) of 0.5-10 mm, fin spacing to fin diameter ratio (S/D) of 0.1-29 with the condition the combination returned integer values of total number of fins (N), and an AC coating mass range of 0-100 mg (0 mg represents plain heat sink without any coating). Here it should be noted that 100 mg was chosen as an average practical maximum value for the applied coatings. Application of more mass would result in a higher activated carbon thickness, reducing the effective thermal conductivity, or increasing the packing ratio to decrease the ability to desorb effectively. Optimization was performed for maximum average temperature reduction inside the silicon chip (ΔT_E) over a period of 60 min. The results are given in Figure 2a. The results reveal that the optimal case ($\Delta T_E=5.9$ °C, enabled by average $h_E\approx 67$ W/m²·K) happens when the fin spacing and the fin diameter are equal (specifically for a fin diameter of 0.5 mm, yielding 900 fins) and for an AC coating mass of 100 mg. This is attributed to the enhancements in the surface area owing to the use of fins, and the increased cooling enabled by desorption and radiation owing to the presence of the AC layer. It is further seen that low S/D typically yields better cooling performance due to the increased number of fins, effectively increasing the exposed surface area. Furthermore, increasing the AC coating mass results in better cooling from the surface owing to the enhanced emissivity and the utilization of the sorption cycle of water. Therefore, we could postulate that the reduction in the effective thermal conductivity because of the presence of the AC layer does not contribute negatively to the cooling performance. On the other hand, our numerical analyses show that the maximum heat transfer coefficient is achieved for a coating mass of 115 mg for the determined optimal geometry, yielding an average overall heat transfer coefficient of $h_E\approx 68$ W/m²·K. Furthermore, a coating mass of 166.2 mg further reduces the heat transfer coefficient to the value without the AC coating ($h_E\approx 56$ W/m²·K), and 180 mg coating leads to the case of a flat plate ($h_E\approx 15$ W/m²·K) due to the lower effective thermal conductivity of AC, leading to less

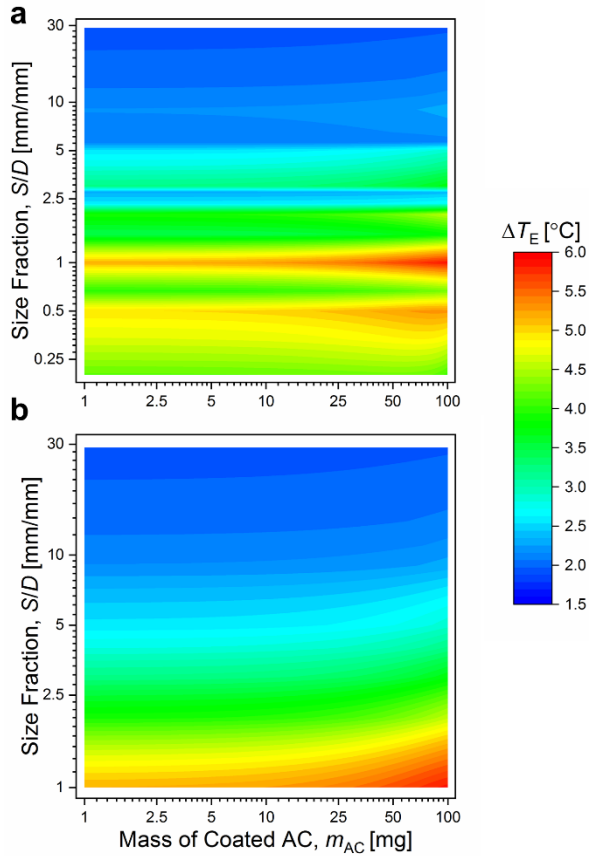


Figure 2. Results of the optimization analysis. The y-axis represents the geometry of the heat sink, the x-axis represents the activated carbon coating layer, and the colors represent the cooling performance (blue denoting minimum performance and red denoting maximum performance). a) The optimization results for all of the considered diameters, b) the optimization results for $D=0.5$ mm.

effective cooling from the surface. Hence, the practical limits should be carefully observed before applying the coatings on the heat sinks. Further investigation of Figure 2a reveals that the data does not follow a specific trend (especially for a S/D range of 1-5) due to thermal dynamics related to the changing diameter of the fin. Therefore, it is more useful to look at each studied diameter individually. For this purpose, we plot the optimization curves of the ideal diameter ($D=0.5$ mm) in Figure 2b. Results show that the cooling performance is reduced as the fin spacing increases, and the cooling performance is enhanced with a thicker AC coating due to the added desorption and radiation. Additionally, it is seen that the shortcomings of the fin geometry could be reversed through AC coatings (i.e. same temperature reduction could be obtained by depositing more AC). Therefore, we can conclude from our analyses that AC coated heat sinks hold great potential for commercial use as chip coolers.

After having obtained the optimal geometry and the AC mass, it was mandatory to get the physical reasoning behind this scenario. For that purpose, we determined the water desorption dynamics from the AC layer. The water uptake information of AC powders was obtained through the solution of Eq. (2) with the given parameters ($R_s=14$

nm and $D_c=3 \times 10^{-21}$ m²/s) and is shown in Figure 3. We can clearly notice from the results that the low adsorption capacity of AC limits extra desorption from the surface. The rate of desorption is high at the initial contact owing to the rapid increase in the layer temperature; however, it becomes insignificant after 5-10 min. If the commercial AC powders could be treated to enhance their water uptake capacities through chemical treatments, the performance of these heat sinks could be drastically increased. Hence, further studies are needed to procure AC powders suitable for water harvesting.

Figure 4 shows the transient behavior of the temperature reduction inside the silicon chip (ΔT_E) and the heat transfer coefficient at the top side of the silicon chip (h_E) both for a plain heat sink with the optimal geometry (dotted lines) and the identical heat sink coated with 100 mg AC (solid lines).

Results reveal that while the plain heat sink itself is highly effective, reaching an average temperature gradient of ≈ 5 °C, the AC coating prevails in terms of performance due to the added radiation and desorption despite the lower effective thermal conductivity it possesses. Additionally, the overall heat transfer coefficient of the AC coated heat sink at the steady-state is 20% higher than that of the plain heat sink, proving the effective cooling capacity of the proposed devices. Considering all these benefits in terms of cooling performance, AC coated heat sinks can be deployed as cheap and effective thermal management solutions to replace the anodized aluminum heat sinks.

A breakdown of the mechanisms contributing to the enhancement in the cooling performance is given in Figure 5. A close investigation reveals that desorption plays a minor role in terms of enhancing the cooling performance, only contributing significantly within the first few minutes. This could be attributed to the low adsorption capacity of AC and the high temperature of the silicon chip. This contribution could be enhanced by increasing the coating mass, chemically treating the AC

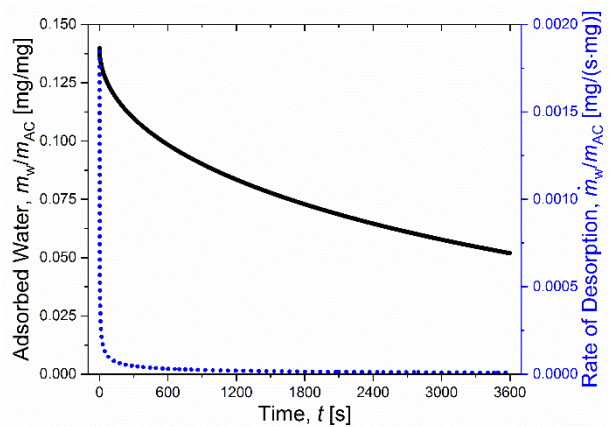


Figure 3. Dynamics of desorption in the activated carbon layer. The black curve (left-side) represents the transient desorption of the adsorbed water from the layer (normalized). The blue dots (right side) represent the corresponding dimensionless rate of desorption.

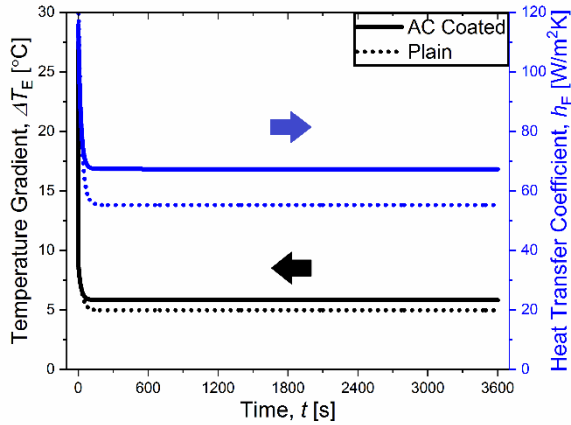


Figure 4. The transient cooling performance of the studied heat sinks. Black color (left-side) represents the temperature gradient within the electronic chip. Blue color (right-side) represents the corresponding overall heat transfer coefficient. Solid lines represent the activated carbon coated heat sinks. Dots represent the plain anodized aluminum heat sinks.

to increase its adsorption capacity, and controlling the pore size to regulate the desorption rate of water from the surface. These improvements were beyond the scope of this study. Additionally, we see that the contributions of both natural convection and radiation significantly increased to enhance the overall steady-state heat transfer coefficient by $\approx 20\%$. Additionally, our studies also revealed that anodized aluminum flat plates only displayed a steady-state heat transfer coefficient of $\approx 15 \text{ W/m}^2\cdot\text{K}$, revealing the importance of surface area improvement through the use of extended surfaces (fins). Thus, we can safely postulate that a combination of increased emissivity, increased surface area, and the utilization of sorption cycles of atmospheric water can lead to highly effective passive thermal management of electronics. Furthermore, AC coated heat sinks are more effective than anodized aluminum heat sinks as revealed throughout this manuscript and can be potentially utilized as readily available electronic chip coolers.

CONCLUSIONS

Passive activated carbon coatings were employed as a passive thermal management solution for low output power electronics. We considered anodized aluminum heat sinks with pin fins and coated them with layers of activated carbon to utilize the sorption cycle of atmospheric water to induce a pseudo-evaporative cooling effect on the surface, and to increase cooling by radiation. In order to study the cooling performance of our envisioned heat sinks, we developed a 1D transient optimization model combining mass diffusion due to desorption and thermal contributions due to radiation, heat supply, conduction, and natural convection. Our numerical optimization revealed that a low diameter and low spacing yielded optimal cooling scenarios due to the enhancement of the total number of fins which leads to an increase in the exposed surface area available for heat exchange with the surroundings. Furthermore, our optimization results revealed that the mass of AC coating layer needs to be maximized within the given limits (100

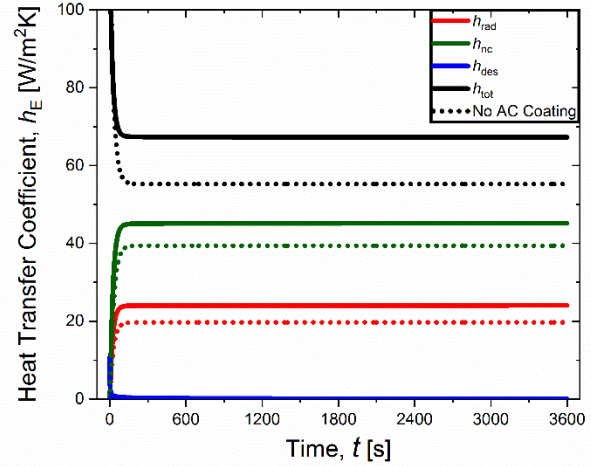


Figure 5. Decoupled effects of radiation, desorption, and natural convection. Solid lines represent the activated carbon coated heat sinks. Dots represent the plain heat sinks. Red denotes radiation, green denotes natural convection, blue denotes desorption, and black denotes the overall heat transfer coefficient.

mg for this study) to effectively employ evaporative cooling in the initial periods of thermal management, and to increase radiative cooling from the surface owing to increased emission. Our optimal heat sink design of 0.5 mm fin spacing, 0.5 mm fin diameter, and 100 mg activated carbon coating displayed a remarkable overall steady-state heat transfer coefficient of $67 \text{ W/m}^2\cdot\text{K}$ in the void of fluid motion (i.e. still air) on the hot side of the electronic chip with room for further improvements through material development. The presence of the AC layer produced an $\approx 20\%$ increase in the cooling performance when compared to the plain anodized case, showing that AC layers could be utilized on aluminum heat sinks instead of the anodized natural oxide layer. We further uncoupled the effects of desorption, natural convection, and radiation and concluded that the enhancement mainly stemmed from radiation and convection with desorption playing a vital role only in the early phases of contact due to the low adsorption capacity of activated carbon and relatively high thermal gradients within the system. Future studies to enhance the adsorption capacity of activated carbon powders would be useful to boost the cooling performance of these layers to the maximum. This study sheds light on the use of sorbents as thermal management coatings and provides design priorities of the new generation of sorbents that could be deployed as passive evaporative coolers.

REFERENCES

- Attinger, D., C. Frankiewicz, A. R. Betz, T. M. Schutzius, R. Ganguly, A. Das, C.-J. Kim and C. M. Megaridis, 2014, Surface engineering for phase change heat transfer: A review, *MRS Energy & Sustainability*, 1.
- Bergman, T. L., F. P. Incropera, D. P. DeWitt and A. S. Lavine, 2011, Fundamentals of heat and mass transfer, *John Wiley & Sons*.

- Birbarah, P., T. Gebrael, T. Foulkes, A. Stillwell, A. Moore, R. Pilawa-Podgurski and N. Miljkovic, 2020, Water immersion cooling of high power density electronics, *International journal of heat and mass transfer*, 147: 118918.
- Cho, H. J., D. J. Preston, Y. Zhu and E. N. Wang, 2016, Nanoengineered materials for liquid–vapour phase-change heat transfer, *Nature Reviews Materials*, 2(2): 1-17.
- Christen, D., M. Stojadinovic and J. Biela, 2016, Energy efficient heat sink design: natural versus forced convection cooling, *IEEE Transactions on Power Electronics*, 32(11): 8693-8704.
- Do, D. and H. Do, 2000, A model for water adsorption in activated carbon, *Carbon*, 38(5): 767-773.
- Fathieh, F., M. J. Kalmutzki, E. A. Kapustin, P. J. Waller, J. Yang and O. M. Yaghi, 2018, Practical water production from desert air, *Science advances*, 4(6): eaat3198.
- González-García, P., 2018, Activated carbon from lignocellulosics precursors: A review of the synthesis methods, characterization techniques and applications, *Renewable and Sustainable Energy Reviews*, 82: 1393-1414.
- Günay, A. A., S. Harish, M. Fuchi, I. Kinefuchi, Y. Lee and J. Shiomi, 2022, Metal–organic framework coated porous structures for enhanced thermoelectric performance, *Energy conversion and management*, 255: 115289.
- Günay, A. A., M.-K. Kim, X. Yan, N. Miljkovic and S. Sett, 2021, Droplet evaporation dynamics on microstructured biphilic, hydrophobic, and smooth surfaces, *Experiments in Fluids*, 62(7): 1-14.
- Günay, A. A., S. Sett, J. Oh and N. Miljkovic, 2017, Steady method for the analysis of evaporation dynamics, *Langmuir*, 33(43): 12007-12015.
- Gustavsen, A. and P. Berdahl, 2003, Spectral emissivity of anodized aluminum and the thermal transmittance of aluminum window frames, *Nordic Journal of Building Physics*, 3(1970): 1-12.
- Hahn, G., 2010. Status of selective emitter technology. *25th European Photovoltaic Solar Energy Conference and Exhibition. 5th World Conference on photovoltaic Energy Conversion*.
- Henninger, S., F. Schmidt and H.-M. Henning, 2010, Water adsorption characteristics of novel materials for heat transformation applications, *Applied Thermal Engineering*, 30(13): 1692-1702.
- Hetsroni, G., A. Mosyak, Z. Segal and G. Ziskind, 2002, A uniform temperature heat sink for cooling of electronic devices, *International journal of heat and mass transfer*, 45(16): 3275-3286.
- Hossain, M. M. and M. Gu, 2016, Radiative cooling: principles, progress, and potentials, *Advanced Science*, 3(7): 1500360.
- Hu, M., B. Zhao, X. Ao, Y. Su and G. Pei, 2018, Numerical study and experimental validation of a combined diurnal solar heating and nocturnal radiative cooling collector, *Applied Thermal Engineering*, 145: 1-13.
- Jang, Y., J. Jo, Y.-M. Choi, I. Kim, S.-H. Lee, D. Kim and S. M. Yoon, 2013, Activated carbon nanocomposite electrodes for high performance supercapacitors, *Electrochimica Acta*, 102: 240-245.
- Juárez-Galán, J., A. Silvestre-Albero, J. Silvestre-Albero and F. Rodríguez-Reinoso, 2009, Synthesis of activated carbon with highly developed “mesoporosity”, *Microporous and Mesoporous Materials*, 117(1-2): 519-521.
- Kabeel, A. E., Y. A. F. El-Samadony and M. H. Khiera, 2017, Performance evaluation of energy efficient evaporatively air-cooled chiller, *Applied Thermal Engineering*, 122: 204-213.
- Karamanis, D., E. Vardoulakis, E. Kyritsi and N. Ökte, 2012, Surface solar cooling through water vapor desorption from photo-responsive sepiolite nanocomposites, *Energy conversion and management*, 63: 118-122.
- Kim, H., H. J. Cho, S. Narayanan, S. Yang, H. Furukawa, S. Schiffres, X. Li, Y.-B. Zhang, J. Jiang and O. M. Yaghi, 2016, Characterization of adsorption enthalpy of novel water-stable zeolites and metal-organic frameworks, *Scientific Reports*, 6(1): 1-8.
- Kim, H., S. R. Rao, E. A. Kapustin, L. Zhao, S. Yang, O. M. Yaghi and E. N. Wang, 2018, Adsorption-based atmospheric water harvesting device for arid climates, *Nature Communications*, 9(1): 1-8.
- Kim, H., S. Yang, S. R. Rao, S. Narayanan, E. A. Kapustin, H. Furukawa, A. S. Umans, O. M. Yaghi and E. N. Wang, 2017, Water harvesting from air with metal-organic frameworks powered by natural sunlight, *Science*, 356(6336): 430-434.
- Li, J., W. Fu, B. Zhang, G. Zhu and N. Miljkovic, 2019, Ultrascalable three-tier hierarchical nanoengineered surfaces for optimized boiling, *ACS Nano*, 13(12): 14080-14093.
- Moore, A. L. and L. Shi, 2014, Emerging challenges and materials for thermal management of electronics, *Materials today*, 17(4): 163-174.

- Ng, K. C., H. Chua, C. Chung, C. Loke, T. Kashiwagi, A. Akisawa and B. B. Saha, 2001, Experimental investigation of the silica gel–water adsorption isotherm characteristics, *Applied Thermal Engineering*, 21(16): 1631-1642.
- Nor, N. M., L. C. Lau, K. T. Lee and A. R. Mohamed, 2013, Synthesis of activated carbon from lignocellulosic biomass and its applications in air pollution control—a review, *Journal of Environmental Chemical Engineering*, 1(4): 658-666.
- Oh, J., P. Birbarah, T. Foulkes, S. L. Yin, M. Rentauskas, J. Neely, R. C. Pilawa-Podgurski and N. Miljkovic, 2017, Jumping-droplet electronics hot-spot cooling, *Applied Physics Letters*, 110(12): 123107.
- Rezk, A., R. Al-Dadah, S. Mahmoud and A. Elsayed, 2012, Characterisation of metal organic frameworks for adsorption cooling, *International journal of heat and mass transfer*, 55(25-26): 7366-7374.
- Rodríguez-Mirasol, J., J. Bedia, T. Cordero and J. J. Rodríguez, 2005, Influence of water vapor on the adsorption of VOCs on Lignin-Based activated carbons, *Separation Science and Technology*, 40(15): 3113-3135.
- Shahriari, A., P. Birbarah, J. Oh, N. Miljkovic and V. Bahadur, 2017, Electric field–based control and enhancement of boiling and condensation, *Nanoscale and Microscale Thermophysical Engineering*, 21(2): 102-121.
- Sommer, J. L., 1997, High Conductivity, Low Cost Aluminum Composite for Thermal Management, Technical Research Associates Inc., Salt Lake City, UT.
- Stebe, K. J. and S.-Y. Lin, 2001, Dynamic surface tension and surfactant mass transfer kinetics: measurement techniques and analysis. *Handbook of Surfaces and Interfaces of Materials*, Elsevier: 55-106.
- Stock, N. and S. Biswas, 2012, Synthesis of metal-organic frameworks (MOFs): routes to various MOF topologies, morphologies, and composites, *Chemical reviews*, 112(2): 933-969.
- Subrenat, A. and P. Le Cloirec, 2003, Thermal behavior of activated carbon cloths heated by Joule effect, *Journal of environmental engineering*, 129(12): 1077-1084.
- Uddin, K., M. Amirul Islam, S. Mitra, J.-b. Lee, K. Thu, B. B. Saha and S. Koyama, 2018, Specific heat capacities of carbon-based adsorbents for adsorption heat pump application, *Applied Thermal Engineering*, 129: 117-126.
- Verma, R., H. Nagendra, S. Kasthuriengan, N. Shivaprakash and U. Behera, 2019. Thermal conductivity studies on activated carbon based cryopanel. *IOP Conference Series: Materials Science and Engineering*, IOP Publishing.
- Wang, C., L. Hua, H. Yan, B. Li, Y. Tu and R. Wang, 2020, A thermal management strategy for electronic devices based on moisture sorption-desorption processes, *Joule*, 4(2): 435-447.
- Yang, X.-H., S.-C. Tan, Z.-Z. He and J. Liu, 2018, Finned heat pipe assisted low melting point metal PCM heat sink against extremely high power thermal shock, *Energy conversion and management*, 160: 467-476.
- Yang, Y., G. Cui and C. Q. Lan, 2019, Developments in evaporative cooling and enhanced evaporative cooling—A review, *Renewable and Sustainable Energy Reviews*, 113: 109230.
- Yoon, S. W., B. Petrov and K. Liu, 2015. Advanced wafer level technology: Enabling innovations in mobile, IoT and wearable electronics. *2015 IEEE 17th Electronics Packaging and Technology Conference (EPTC)*, IEEE.
- Yuan, Y., H. Zhang, F. Yang, N. Zhang and X. Cao, 2016, Inorganic composite sorbents for water vapor sorption: A research progress, *Renewable and Sustainable Energy Reviews*, 54: 761-776.
- Zhou, Y., B. Ji, X. Yan, P. Jin, J. Li and N. Miljkovic, 2021, Asymmetric Bubble Formation at Rectangular Orifices, *Langmuir*, 37(14): 4302-4307.
- Zhou, Z., X. Sun and P. Bermel, 2016. Radiative cooling for thermophotovoltaic systems. *Infrared Remote Sensing and Instrumentation XXIV*, International Society for Optics and Photonics.
- Zhu, G., Z.-H. Lin, Q. Jing, P. Bai, C. Pan, Y. Yang, Y. Zhou and Z. L. Wang, 2013, Toward large-scale energy harvesting by a nanoparticle-enhanced triboelectric nanogenerator, *Nano letters*, 13(2): 847-853.



A. Alperen Günay is an Assistant Professor in the Department of Mechanical Engineering at the Middle East Technical University (METU). Dr. Günay received his B.S. in mechanical engineering from METU in 2014, and his M.S. and Ph.D. in mechanical engineering from the University of Illinois at Urbana – Champaign (UIUC) in 2016 and 2019, respectively. His graduate work focused on thermal management, energy conversion, interfacial science, and renewable energy. Before joining METU, he spent two years as a project researcher at The University of Tokyo where he worked on radiative cooling, silicon-based thermoelectrics, nanoscale energy transport, and sorption dynamics of metal-organic-framework (MOF) coatings. His research efforts are focused on designing self-standing ecological devices for thermal applications and includes a combination of fundamental and applied research on nanomaterials, energy conversion materials and thermal management through phase change.



EXPERIMENTAL INVESTIGATION OF THE EFFECTS OF WATER ADDING INTO THE INTAKE AIR ON THE ENGINE PERFORMANCE AND EXHAUST EMISSIONS IN A SPARK-IGNITION ENGINE

Derya Soysal*, Zehra Şahin** and Orhan Durgun***

*Karadeniz Technical University, Sürmene Abdullah Kanca High School, Trabzon, Türkiye
deyatiryaki@ktu.edu.tr, ORCID: 0000-0003-3371-9540

**Karadeniz Technical University, Faculty of Engineering, Mechanical Engineering Dep., Trabzon, Türkiye
zsahin@ktu.edu.tr, ORCID: 0000-0002-7140-2061

***Avrasya University, Mechanical Engineering Dep., Trabzon, Türkiye
odurgun@ktu.edu.tr, ORCID: 0000-0001-6381-0690

(Geliş Tarihi: 23.06.2021, Kabul Tarihi: 21.03.2022)

Abstract: In the present study, the effects of water addition into intake air (WAIA) on the engine performance and exhaust emissions have been investigated experimentally in an automotive spark-ignition engine (SIE) which is used in Renault Clio vehicles. Experiments have been performed for (3, 6, 9 and 12) % (by vol.) water ratios (WRs) at different engine speeds and different loads. Selected engine speeds were (3000, 4000 5000, and 6000) rpms. 6000 rpm is the maximum speed of this engine. Selected loads were (100, 90, 80, 70, 60, and 50) Nm for (3000, 4000, and 5000) rpms and were (80, 75, 70, 65 and 65) Nm for 6000 rpm, respectively. The test results showed that WAIA decreases significantly brake specific fuel consumption (BSFC) at (3000, 4000, and 5000) rpms, but it increases BSFC at 6000 rpm. The maximum reduction ratios of BSFC at (3000, 4000, and 5000) rpms have been attained at the levels of 28.27 % for 5.60 % WR, 4.160 for 2.67 % WR and 7.19 % for 9.00 % WR, respectively. WAIA generally decreases nitrogen oxides (NO_x) and total hydrocarbon (HC) emissions at all of the selected operating conditions. At (3000, 4000, 5000 and 6000) rpms, the maximum reduction ratios of NO_x have been reached at the levels of 37.80 % for 8.67 % WR, 58.21 % for 12.18 WR, 57.80 % for 12.17 WR and 66.17% for 12.12.WR, respectively. Approximately 9.40 % decrement in HC was achieved by WAIA at the selected engine speeds. Carbon monoxide (CO) emission decreases by applying WAIA at 3000 rpm whereas it generally increases at (4000 and 5000) rpms. Unlike other engine speeds, WAIA increases CO emission significantly at 6000 rpm. Approximately 9 % WR yields the best results for engine performance and exhaust emissions at all of the selected operating conditions.

Keywords: Spark ignition engine, Water addition into intake air, Engine characteristics, Exhaust emissions

BİR BENZİN MOTORUNDA EMME HAVASINA SU EKLENMESİNİN MOTOR PERFORMANSINA VE EGZOZ EMİSYONLARINA ETKİLERİNİN DENEYSEL OLARAK İNCELENMESİ

Özet: Sunulan çalışmada, buji ateşlemeli bir otomobil motorunda (Renault Clio) emme havasına su eklenmesinin (EHSE) motor performansı ve egzoz emisyonları üzerindeki etkileri deneysel olarak incelenmiştir. Deneyler; dört farklı motor devrinde ve % (3, 6, 9 ve 12, hacimsel oran) gibi dört farklı su oranında gerçekleştirilmiştir. Her motor devri için 6 farklı yüklem durumu seçilmiştir. Ayrıca motorun maksimum devri 6000 d/d için 5 tane yük değeri seçilmiştir. Çalışma sonunda; EHSE ile özgül yakıt tüketiminin (ÖYT) (3000, 4000 ve 5000) d/d için azaldığı belirlenmiştir. (3000, 4000 ve 5000) d/d devir sayılarında ÖYT'nde bulunan maksimum azalma oranları sırasıyla % 5.60 su oranında % 28.27, % 2.67 su oranında % 4.160 ve % 9.0 su oranında % 7.19 düzeyinde olduğu belirlenmiştir. Bununla birlikte; ÖYT, 6000 d/d devir sayısında EHSE ile artmıştır. EHSE ile, NO_x'lerin ve HC'lerin ise seçilen tüm çalışma koşullarında genel olarak azaldığı görülmüştür. (3000, 4000, 5000 ve 6000) d/d devir sayılarında; NO_x'lerde elde edilen maksimum azalma oranları sırasıyla, % 8.67 su oranında % 37.80, % 12.18 su oranında % 58.21 ve % 12.17 su oranında % 57.80 % 12.12 su oranında % 66.17 düzeylerinde olmuştur. Aynı devir sayıları için EHSE ile HC'lerde ortalama % 9.40 düzeyinde azalma sağlanmıştır. EHSE ile; 3000 d/d devir sayısında CO emisyonunu azalmasına karşın, (4000 ve 5000) d/d'da CO emisyonu genel olarak artmıştır. 6000 d/d devir sayısında ise CO oranları EHSE ile önemli ölçüde artmıştır. Bu çalışmada deneysel verilerin değerlendirilmesi sonunda, hem motor karakteristikleri ve hem de egzoz emisyonları açısından yaklaşık % 9 su oranının en iyi su oranı olduğu belirlenmiştir.

Anahtar Kelimeler: Buji ateşlemeli motor, Emme havasına su püskürtme, Motor karakteristikleri, Egzoz emisyonu

NOMENCLATURE

be, BSFC	Brake specific fuel consumption (kg/kWh)
CO	Carbon monoxide (vol.%)
HC	Total hydrocarbons (ppm)
Ne	Effective power (kW)
NG	Neat gasoline
NO _x	Oxides of nitrogen (ppm)
SIE	Spark ignition engine
Te	Exhaust temperature (K)
WAIA	Water adding into the intake air
WR	Water ratio
α	Excess air coefficient

INTRODUCTION

It is known from the media and relevant literature that the use of diesel cars in the capitals of some European countries and the major metropolitan cities will be banned after 2020 due to increased environmental pollution (Şahin et al., 2017). In addition, the use of spark-ignition engines (SIEs) would become the most widespread solution for hybrid vehicles, which is considered to be the solution of the near future. However, the vehicles used on highways are noted to be the major emission contributor to the environment, which is dangerous to human health. For this reason, scientists, politicians and automotive companies have been working intensively to reduce environmental pollution nowadays (Nguyen and Wu, 2009; Awad et al., 2018; Bozza et al., 2016).

In this context, many different studies are carried out on the SIEs ((Nguyen and Wu, 2009; Awad et al., 2018; Bozza et al., 2016). The use of different alternative fuels, (Awad et al., 2018; Deng et al., 2018; Li et al., 2018; Wang et al., 2018) and water addition (Nguyen and Wu, 2009; Bozza et al., 2016; Worm, 2017; Wilson, 2011; Mingrui et al., 2017, Tiryaki, 2008) can be given as examples of these studies, and the numbers of these studies have been increased in recent years. Using of many alternative fuels and additives, especially alcohols, and also water in SIEs have shown promising results for engine performance and exhaust emissions (Awad et al., 2018; Li et al., 2018; Arabacı et al., 2015). However, since the use of water in SIEs was examined in the present study, the literature review on water addition in SIEs was briefly presented below.

It is known that the studies on water addition in engines began in the 1950s. The use of water into SIEs has been researched for many years to improve the engine in various ways, including: to increase power output, to boost efficiency, to lower NO_x and CO emissions, to cool the engine and to reduce knock by increasing the octane number (Nguyen and Wu, 2009; Bozza et al., 2016; Worm, 2017; Wilson, 2011; Mingrui et al., 2017). However, it is stated that HC generally increased in some of the water adding studies (Wilson, 2011; Nguyen and Wu, 2009), but it decreased in the other studies (Mingrui et al., 2017; Valentino et al., 2017, Fan et al., 2021; Osama et al., 2019; Babu et al., 2015). In the relevant

literature, water addition is applied in SIEs by three different methods. These are use of direct water–gasoline (fuel) emulsion, water injection into the cylinder by using a separate injector and adding/injecting water into the intake manifold (WAIA) (Wilson, 2011; Tiryaki, 2008; Tiryaki and Durgun, 2010). The water–gasoline emulsion method has been applied lesser than other techniques in SIEs (Nguyen and Wu, 2009; Peters and Stebar, 1976). This method has been usually used in diesel engines (Fahd et al, 2013, Subramanian, 2011). Other water injection methods (port and direct water injection) have been widely investigated by different researchers in SIEs, and the number of these studies has increased in recent years. Some examples of these studies applying the above-mentioned methods are briefly presented in the following paragraphs.

Nguyen and Wu (2009) performed experimental research on the effects of water-gasoline emulsions on engine performance and emissions in a SIE. They found that for 13.23 air-fuel ratio (AFR), 5% and 10% water-gasoline emulsion slightly increase engine torque; otherwise, 15% water-gasoline emulsion decreases. Also, their results showed that water-gasoline emulsions create good reductions in NO_x and CO emissions near the stoichiometric AFR while increases in HC emission occurs. Mingrui et al. (2017) investigated the influence of variable water injection (WI) on the performance and emission characteristics of a gasoline direct injection engine under light load conditions. In this study, water was directly injected into the cylinder by using a different injector. Their results showed that 15% water injection gave the best engine performance. Also, they found that WI decreased NO_x emissions as well as soot emission. Martin Böhm and colleagues (Böhm *et al.*, 2016), who work for BMW, examined the water injection into the combustion chamber in a 1.5 L three-cylinder SIE. In this study, a water-gasoline mixture is injected into the cylinder by using an adapted injection system. Their results show that water injection decreases particulate and CO/HC emissions and BSFC. Fan et al. (2021), investigated port water injection technique in a three-cylinder direct-injection SIE. They explained that adding water to the intake air of gasoline engines could efficiently advance the combustion phase by enhancing the anti-knock capability of the engine and significantly improving thermal efficiency. In this study, they obtained 3.4%–16.7% improvements in the brake-thermal efficiency under different engine operating conditions. Merola et al. (2020), studied water injection effects on engine performance and exhaust emissions in a single-cylinder SIE. In this research, engine performance was found to exhibit a slightly decreasing trend when increasing the injected water quantity in three steps, at 10, 20 and 30% of the mass flow of gasoline. Here, CO emission did not change largely with the water ratio, while NO_x decreased up to 35% for the highest water-fuel ratio.

From the above given literature, it can be seen that the results of these methods are different from each other. The same method may give different results for different

engines. However, by applying all three water adding methods in SIEs, it has been determined that in-cylinder temperatures and NO_x are decreased and the knock resistance is increased (Nguyen and Wu, 2009; Bozza *et al.*, 2016; Worm, 2017; Wilson, 2011; Mingrui *et al.*, 2017; Tiryaki, 2008; Tiryaki and Durgun, 2010). Water using research have been usually carried out in SIE by applying one of these methods. However, the number of studies on the use of water in SIE is less than diesel engines. In addition, selected operating conditions such as engine load, water ratio and engine speed are limited in the water use research for SIEs given in the literature. Therefore, in this study, the effects of the four different WAIA on engine performance and exhaust emissions are investigated experimentally under six different loads at four different engine speeds in an automotive SIE. The experiments were carried out in an automotive SIE currently used in motor vehicles, is very important for providing new information to the industry. In addition, the performing of water adding tests at 6000 rpm, which is higher than nominal engine speed, may contribute some extra information to the literature from a different point of view.

EXPERIMENTAL STUDY

Engine and Experimental Set-up

Experiments for neat gasoline (NG) and water adding into the intake air (WAIA) were conducted in an automotive SIE (Renault Clio). In the present study, water at different ratios has been added into intake air by an adapted variable main jet carburettor placed on the inlet manifold of the engine. The main technical specifications of the engine were given in Table 1 and the schematic diagram of the test system used is presented in Figure 1. The test bed was produced by Cussons. Here, loading was done by a water brake, and the brake moment was measured electronically. Exhaust gases were measured by using an exhaust gas analyzer (MDS 450, AVL). The measurement ranges and uncertainties of the exhaust gas analyzer and test system were given in Table 2.

Table 1. Main technical specifications of the test engine.

Engine	Renault Clio
Number of cylinder	4
Displacement	1.4 L
Stroke and bore	79.5; 70 mm
Compression ratio	9.5
Fuel injection system	Multi point port injection
Maximum power	55 kW @ 5800 rpm
Maximum torque	114 Nm @ 4250 rpm

Test Procedure

In the present study, tests were carried out at (3000, 4000 5000 and 6000) rpms engine speeds and for approximately 3 %, 6 %, 9 %, and 12 % (by vol.) WRs. Also, six different loads of (100, 90, 80, 70, 60, and 50) Nm were selected for 3000, 4000 and 5000 rpms. But at 6000 rpm, five different loads such as (80, 75, 70, 65, and

60) Nm were chosen. Firstly, NG tests were conducted as NG values were required to compare with that of water addition. After NG tests were completed, the adapted carburettor was mounted on the intake manifold of the engine. Figure 1 presents the technical view of the adapted carburettor. Information about the adapted carburettor was given authors' previous studies (Şahin *et al.*, 2014; Şahin *et al.*, 2015). In addition, to introduce water into intake air and to measure the amount of the added water, a small water tank, a scaled glass bulb, and a flexible pipe were used and the water adding unit is shown in Figure 1. Any other change on the experimental system and engine was not done. The main steps of the experiments are briefly given in the following paragraph.

Table 2. Technical specifications of exhaust gas analyser (MDS 450, AVL) and test system

Parameter	Measurement Range	Accuracy
CO (%)	(0-15)	± (0.02-0.03) %
CO ₂ (%)	(0-20)	± 0.3 %
HC (ppm)	(0-3000)	± 4 ppm
O ₂ (%)	(0-25)	± 0.02 %
NO _x (ppm)	(0-5000)	± 5 ppm
Excess air coefficient (α)	0-9.999	α is calculated from CO, CO ₂ , HC ve O ₂
Engine speed (rpm)	Max: 7500	± 5 %
Torque (Nm)	Max: 280	± 5 %

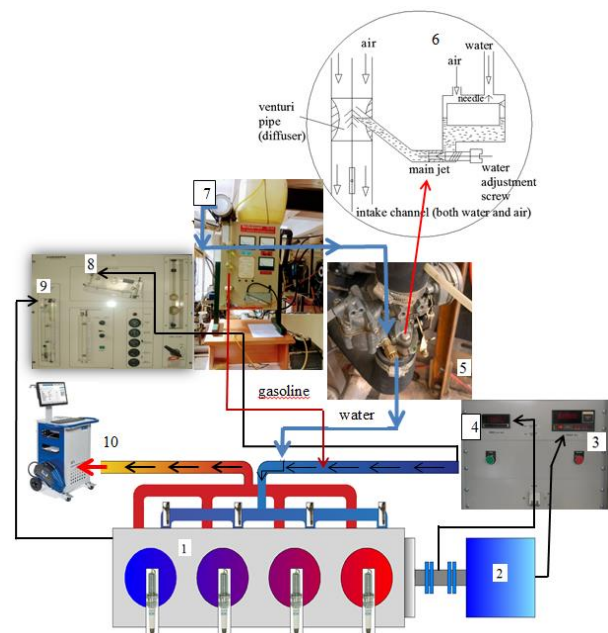


Figure 1. Experimental system. 1-Engine (Renault Clio), 2-Load unit, 3-Torque, 4- Engine speed, 5- Adapted carburettor, 6- Technical drawing of the adapted carburettor, 7- Water tank, 8- Air measurement manometer, 9- Coolant flow meter, 10- Exhaust gas analyzer

The test engine was run for approximately (20-30) minutes before tests, and when the temperature of cooling water becomes (70 ± 5) °C, that is steady-state

conditions were reached, experiments for NG and various WRs have been carried out. For example, at 3000 rpm, firstly, the engine load was adjusted as 100 Nm. Then, the mean jet opening of the carburettor was adjusted to the 1st opening, which gives ~3 % WR. After approximately ~3 % WR tests were carried out for loading moments between (100-50) Nm; by reducing the engine load at 10 Nm steps and simultaneously adjusting gas throttle levels suitably to obtained constant 3000 rpm. Thus, ~3 % WR tests under six different engine loads were performed. After that, for obtaining ~6 % WR, the main jet opening of the carburettor was adjusted to the 2nd opening, and this opening was again retained fixed at the same 3000 rpm. Thus, tests for ~6 % WR were carried out under the above selected six different engine loads. Then, the similar experimental procedure for approximately (~9 % and ~12 %) WRs at 3000 rpm was performed. The similar tests were performed for the same loads and same WRs at (4000, 5000 and 6000) rpms. Calculation of the engine performance parameters, such as effective power, total fuel consumption, BSFC etc. by using experimental values is given briefly in the following paragraphs. Detailed information can be found in the reference (Durgun, 2018; Durgun, 1990).

$$N_e(kW) = \frac{0.1013}{1000} \cdot \frac{T_b \cdot \omega}{P_0} \cdot \sqrt{T_0/293} \cdot X_{hum} \quad (1)$$

$$B(kg/h) = \frac{\Delta m}{\Delta t} = \frac{(\Delta V \cdot \rho) \cdot 3600}{\Delta t \cdot 10^6} \quad (2)$$

$$b_e(kg/kWh) = \frac{B}{N_e} \quad (3)$$

In Eq.1; T_b (Nm) and ω (r/s) are brake torque and angular velocity, respectively. P_0 (MPa) and T_0 (K) are ambient air pressure and ambient air temperatures, respectively. X_{hum} is the humidity correction factor. In Eq. 2; ΔV is the volume of consumed gasoline, Δt (s) is the duration of consumption of ΔV volume (50 mL) of gasoline, ρ (kg/m³) is the density of gasoline.

Here, from the experimental results by applying the error analysis to the measured or derived values (Holman, 2001), uncertainties for effective power and BSFC were computed and it is determined that they took values at the interval of (0.365-1.486) % and (0.995-5.445) %, respectively. Thus, it can be said that these uncertainties are within acceptable limits.

Some of the results obtained from the experimental study are presented in the following section. Here, the variation ratios of BSFC and exhaust emissions in respect of NG were also calculated. For example, variation ratio of BSFC was computed as follows:

$$\frac{\Delta b_e}{b_e} \cdot 100 [\%] = \left[\frac{(b_{e,WAlA} - b_{e,NG})}{b_{e,NG}} \right] \cdot 100 \quad (4)$$

where $b_{e,WAlA}$ and $b_{e,NG}$ are BSFC values for water addition and neat gasoline, respectively.

RESULTS AND DISCUSSION

In this section, the effects of four different WRs on effective power, BSFC, exhaust emissions such as CO, NO_x and HC, excess air coefficient and exhaust temperature (T_e) of this automotive SIE at different loads and engine speeds are presented by comparing with NG. Figures 2 (a-b)-Figures 18 (a-b) present the variation and VRs of effective power, BSFC, CO, NO_x, HC versus WRs under six different loads at (3000, 4000, and 5000) rpms and under five loads at 6000 rpm, respectively. Also, the effects of WAIA on excess air coefficient (α) are shown in Figures 19 (a-d) at selected above engine speeds. Besides, T_e values at (4000, 5000, and 6000) rpms are shown in Figures 20 (a-c). Due to an arising technical problem in the thermocouple when performing experiments at 3000 rpm, T_e values could not be measured.

The effects of WAIA on effective power and BSFC

Figure 2 (a-f) shows the variations and VRs of effective power versus to WRs under different loads at 3000, 4000, 5000 and 6000 rpms, respectively. As can be seen from these figures, WAIA has little influence on effective power. From Figures 2 (a-d), it is observed that the effective power increases at 3000 and 4000 rpm with the addition of water. However, as can be seen in Figures 2 (e-h) that the effective power decreases with the addition of water at 5000 and 6000 rpms. The variation ratios in effective power are very small and they take place within the error limits. Babu et al. (2015) were studied the effects of water mist injected directly into an intake manifold of an SIE. In this study, it has been found that the maximum torque increases by 10%-14% when different water mist is injected into the engine. The improvements in engine performance were explained as follows by these authors. The used water dissociated into molecules of hydrogen and oxygen that assists combustion in the combustion chamber. This may improve engine torque. In the present study, it is thought that the WAIA has created similar effects. Besides, Arabacı et al. (2015) the effects of the water injection quantity and injection advance on engine performance and exhaust emissions were investigated in a six-stroke SIE. In this study, water was injected directly into the cylinder by using a different water injector. They found that brake power was increased 10% by water injection.

Figure 3 (a-b) show the variations and VRs of BSFC versus to WRs under (100, 90, 80, 70, 60, and 50) Nm loads at 3000 rpm, respectively. It is observed that WAIA decreases BSFC at all of the selected operating conditions. From these figures, it can be seen that the reductions ratios in BSFC generally continue up to (5-9) % WRs, but the reductions ratios in BSFC begin to decrease after these WRs. The obtained maximum decrease ratio of BSFC is 28.27% for 6.6% WR at 3000 rpm. Figure 4 (a-b) show the variations and VRs of BSFC versus WRs under (100, 90, 80, 70, 60, and 50) Nm loads at 4000 rpm. It is observed that WAIA generally decreases BSFC at this engine speed. However, BSFC increases for 5.45 % and 9.37 % WRs,

but it decreases for 3.05 % and 12.18 % WRs under 100 Nm. As shown in Figure 4 (a-b), BSFC reduces under the other selected loads; on the other hand, the decrease ratios

in BSFC are low at high WR such as 12%. The attained maximum decrease ratio of BSFC is 4.16% for 2.67% WR at 4000 rpm.

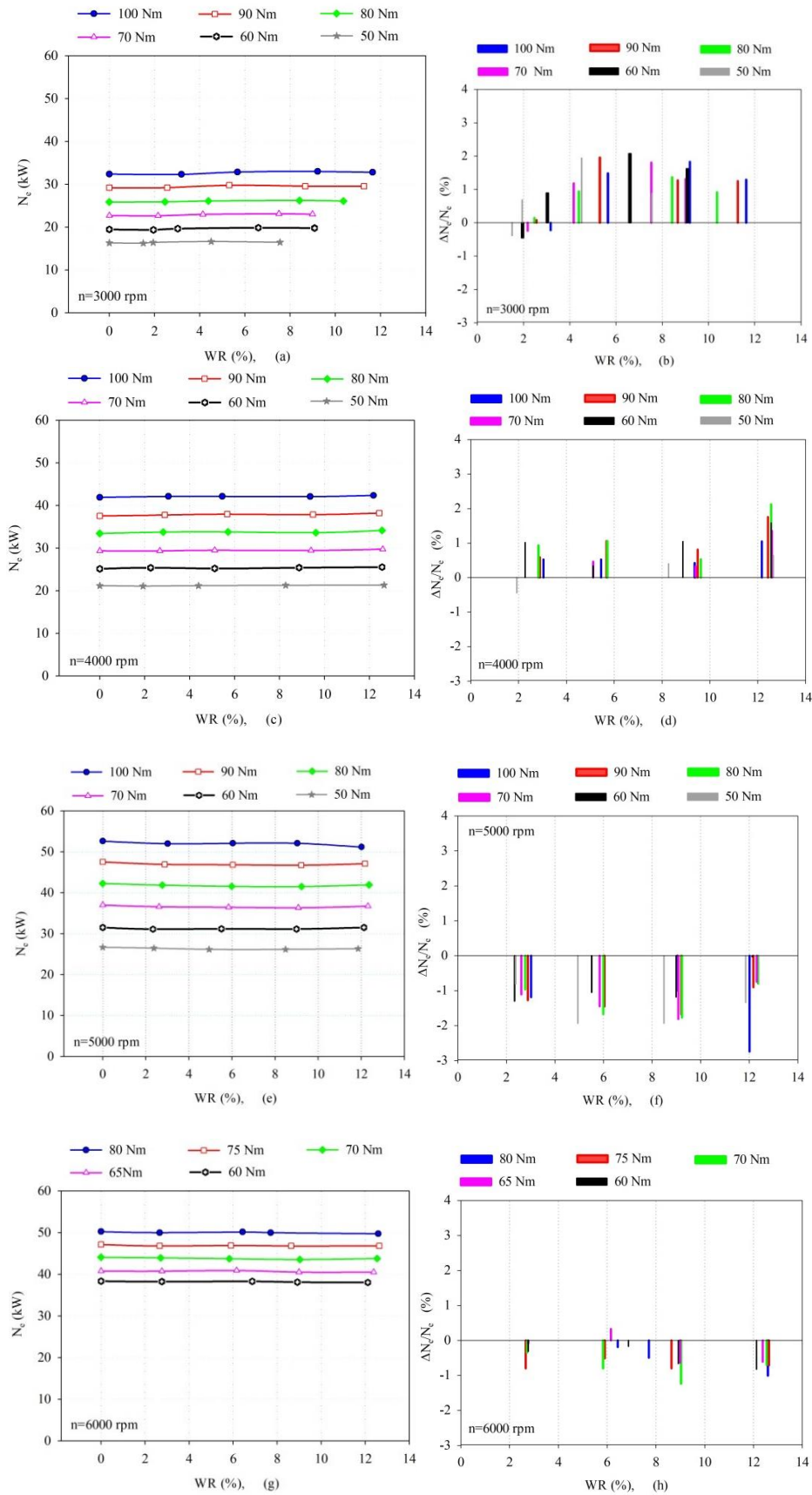


Figure 2 (a-h). Variations and VRs of effective power versus different WRs under different loads at 3000, 4000, 5000 and 6000 rpm, respectively

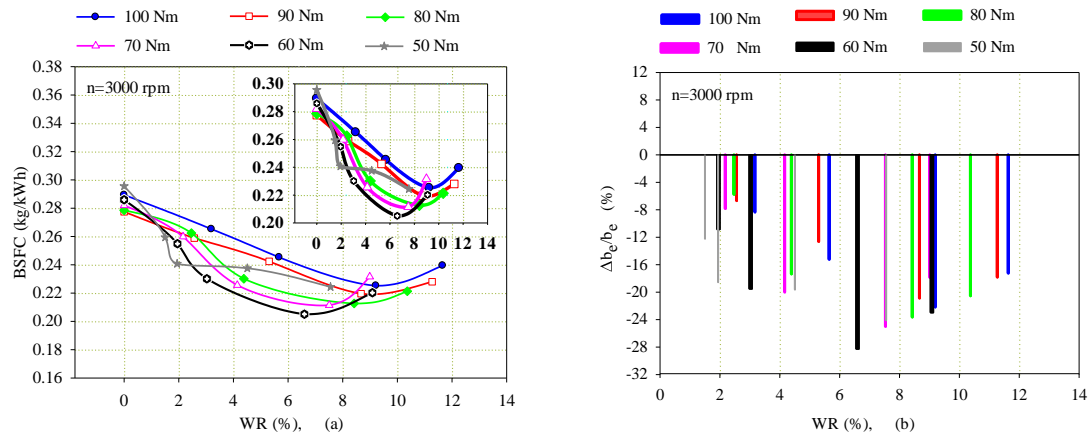


Figure 3 (a-b). Variations and VRs of BSFC versus different WRs under six different loads at 3000 rpm, respectively

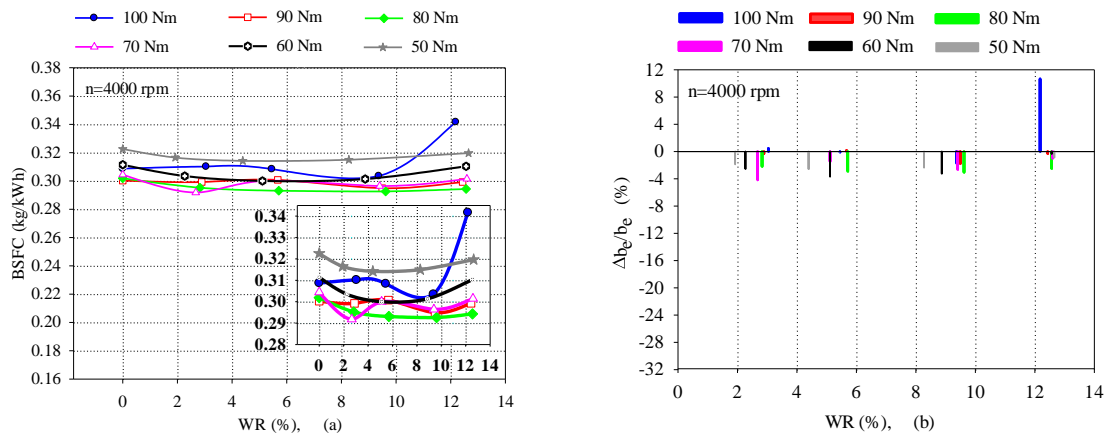


Figure 4 (a-b). Variations and VRs of BSFC versus different WRs under six different loads at 4000 rpm, respectively

Figure 5 (a-b) shows the variations and VRs of BSFC versus WRs under (100, 90, 80, 70, 60, and 50) Nm loads at 5000 rpm. It is observed from the figures that WAIA generally decreases BSFC at all of the selected operating conditions. However, BSFC increases for approximately 12% WRs under 100 Nm and 90 Nm loads. The obtained maximum decrease ratio of BSFC is 7.19% for 9.03% WR at 5000 rpm.

Figure 6 (a-b) shows the variations and VRs of BSFC versus WRs under (80, 75, 70, 65, and 60) Nm loads at 6000 rpm. Unlike to the other engine speeds, WAIA generally increases BSFC at 6000 rpm. This speed is higher than the nominal speed of the experimental engine. For this reason, the expected beneficial effect of water adding did not occur at 6000 rpm, because of higher mechanical losses and smaller combustion duration. At this engine speed, for (6-8) % WRs, the increase ratios of BSFC are lower at low loads in which the engine is less forced. Similar results have also been reported by the earlier researcher (Worm, 2017; Wilson, 2011; Böhm et al., 2016; Fan et al., 2021; Rocha et al., 2021). Martin Böhm and colleagues (Böhm et al., 2016) examined the water injection into the combustion chamber in an SIE. In this study, it was stated that by adding water, BSFC decreased significantly, and 23% decrement ratio in BSFC was determined for 35% WR.

The following interpretations can be made by considering the reduction of BSFC. As water has a very high latent heat of vaporization, evaporating of the added water during intake and compression processes could reduce the cylinder temperature and pressure values. The reduction in pressure values is not only helpful for reducing the compression work but also helps in reducing the suction gas losses resulting from blow-by pass to the piston rings. It is also thought that the charge cooling effect of water addition might also increase volumetric efficiency. Furthermore, the addition of water improves the combustion process, thus increasing the combustion rate of the fuel and enhancing the knocking tendency of the engine. The above effects are thought to contribute to the improvement of BSFC (Wilson, 2011; Worm, 2017; Mingrui et al., 2017; Tiryaki, 2008, Tiryaki and Durgun, 2010).

The effects of WAIA on exhaust emissions

Figure 7 (a-b) shows the variations and VRs of CO emission versus WRs under six different loads at 3000 rpm, respectively. It is observed from these figures that WAIA decreases CO emission at all of the selected operating conditions at this engine speed. As can be seen in Figure 7 (a-b) that as the water addition ratios into the intake air increase, the ratios of reduction in CO emission increase. The obtained maximum decrease ratio of CO emission is 11.65% for 10.5% WR at this engine speed. It can be seen in Figure 19a that WAIA increases the air

excess coefficient, which results in improving the combustion process and reducing of the CO emission (Heywood, 1988; Nguyen and Wu, 2009). However, as shown in Figures 8(a-b) and Figures 9(a-b) that WAIA generally increases the CO emission at 4000 and 5000 rpms. CO emission decreases for about (2-3) % WRs at 4000 rpm. However, after these WRs, CO emission has started to increase. At 5000 rpm, CO emission generally increases for selected WRs, but the increasing ratios in CO emission have remained below 10%. Reductions of

CO emission have been achieved for 12% WR under some loads. As can be shown in Figures 10 (a-b), WAIA increases CO emission significantly at 6000 rpm, which is higher than that of the nominal speed of this engine, As shown in Figures 19 (b-d) that excess air coefficients reduce with WAIA at (4000, 5000, and 6000) rpms. In this condition, combustion occurs in the richer mixture, which could increase CO emission. Similar results have been reported in the literature (Harrington,1982; Babu et al., 2015; Nguyen and Wu, 2009, Osama et al., 2019).

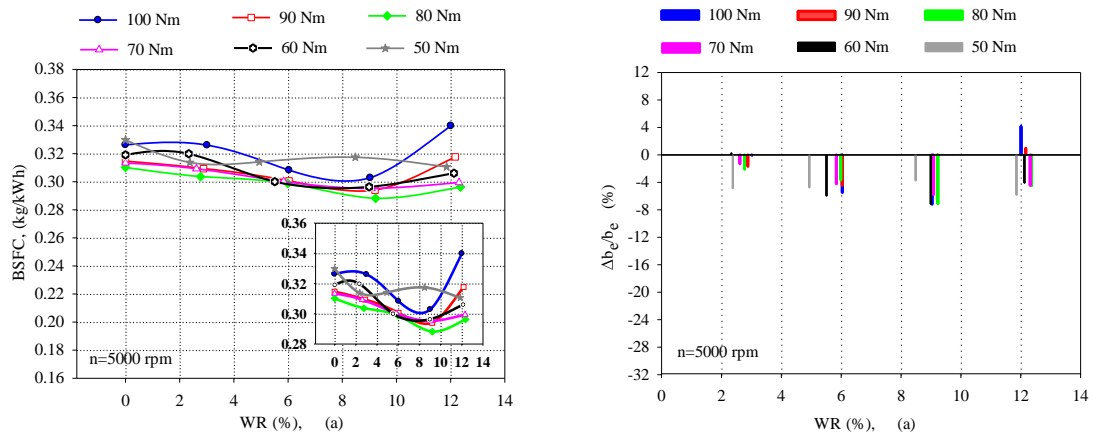


Figure 5 (a-b). Variations and VRs of BSFC versus different WRs under five different loads at 5000 rpm, respectively

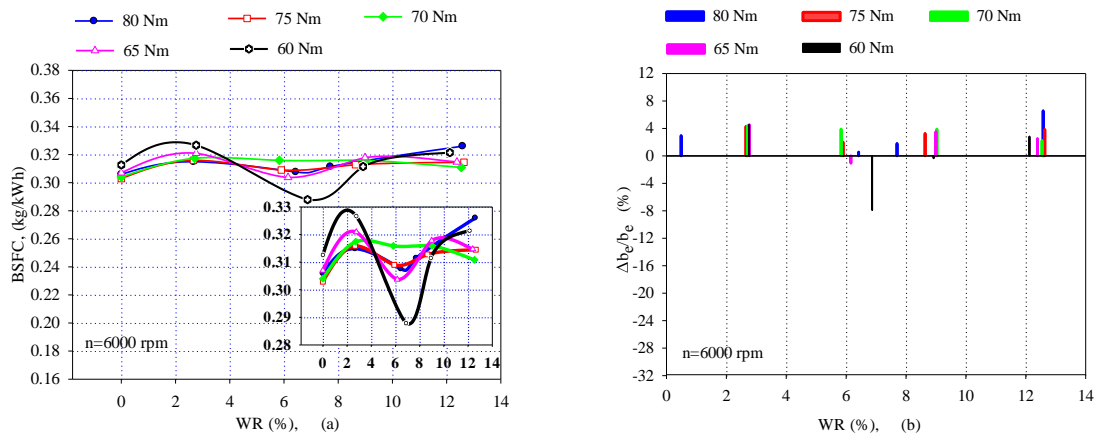


Figure 6 (a-b). Variations and VRs of BSFC versus different WRs under five different loads at 6000 rpm, respectively

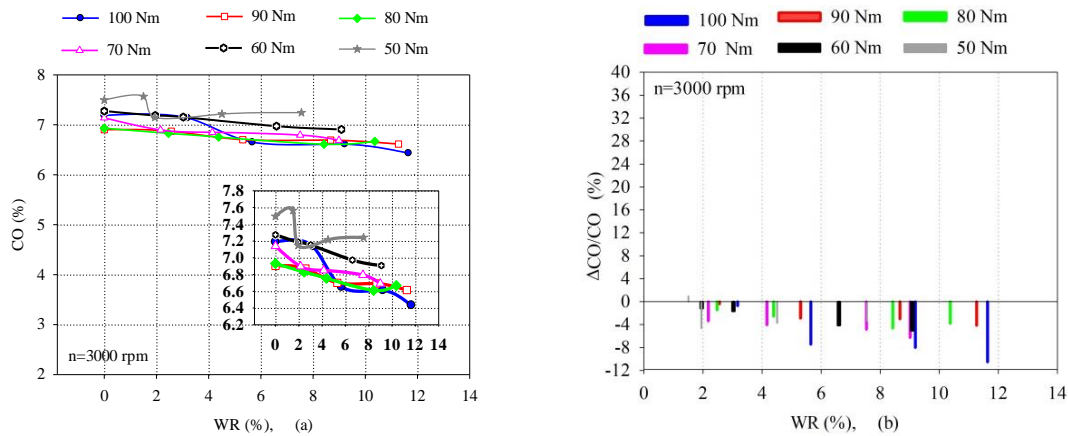


Figure 7 (a-b). Variations and VRs of CO emission versus different WRs under six different loads at 3000 rpm, respectively

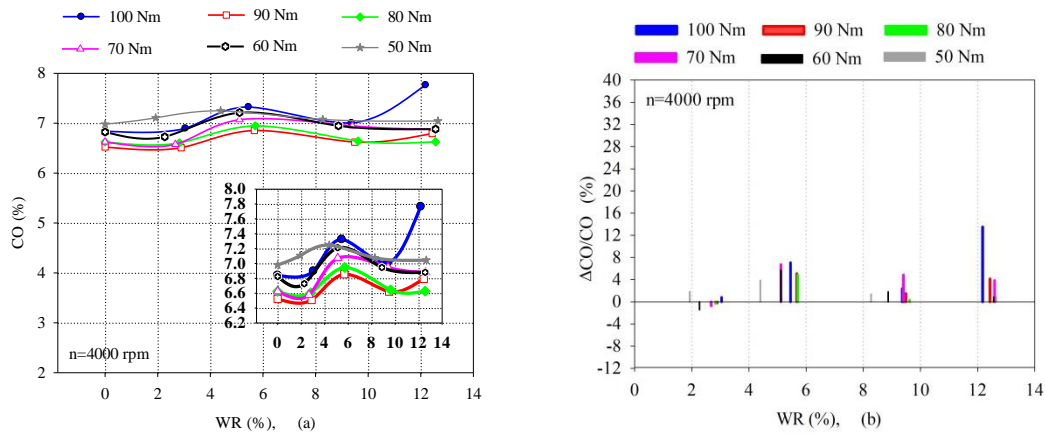


Figure 8 (a-b). Variations and VRs of CO emission versus different WRs under six different loads at 4000 rpm, respectively

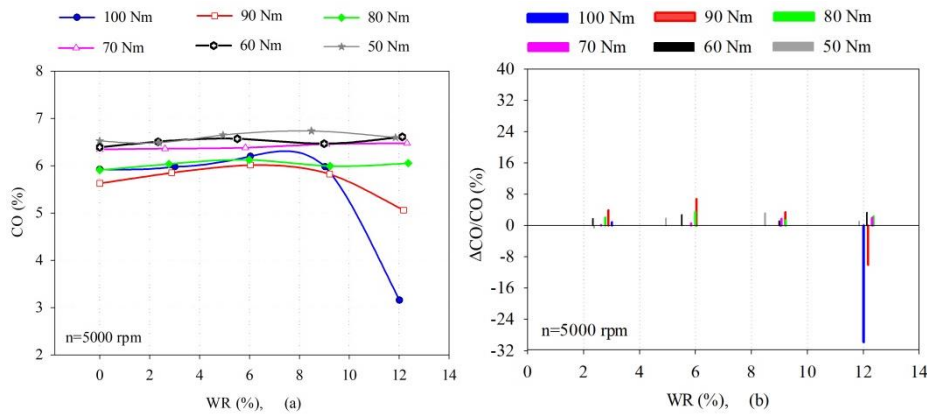


Figure 9 (a-b). Variations and VRs of CO emission versus different WRs under six different loads at 5000 rpm, respectively

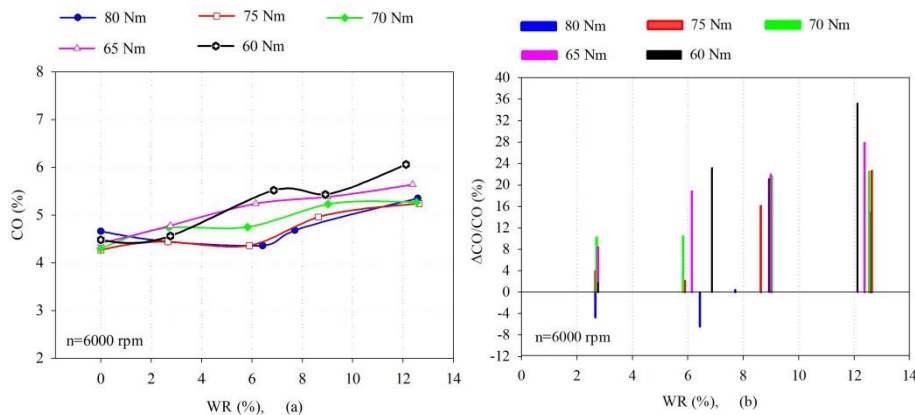


Figure 10 (a-b). Variations and VRs of CO emission versus different WRs under five different loads at 6000 rpm, respectively.

The effects of WAIA on NO_x emissions are presented in Figure 11(a-b), 12(a-b), 13(a-b) and 14(a-b) at (3000, 4000, 5000, and 6000) rpms, respectively. As expected, WAIA decreases the NO_x emissions significantly at most of the selected working conditions. Figures 11 (a-b) show the variations and VRs of NO_x emissions versus WRs under (100, 90, 80, 70, 60, and 50) Nm loads at 3000 rpm, respectively. It could be observed that WAIA increases NO_x emissions at low WRs, such as approximately 3%. However, after this ratio, NO_x emissions are decreased significantly with WRs. The obtained maximum decrease ratio of NO_x emissions reaches to 37.81% for 8.67% WR under 90 Nm load at 3000 rpm.

Figures 12 (a-b) present the variations and VRs of NO_x emissions versus WRs under (100, 90, 80, 70, 60, and 50) Nm loads at 4000 rpm. At this engine speed, NO_x emissions decrease significantly at all of the selected operating conditions. The obtained maximum decrease ratio of NO_x becomes 58.21% for 12.18% WR under 100 Nm load. It is observed that although there NO_x emissions increase somewhat at some water ratios at (5000 and 6000) rpm, NO_x emissions decrease significantly in general. The decrease ratios in NO_x emissions for 12% WR are more prominent than that of low WRs at these engine speeds. The obtained maximum decrease ratios of NO_x emissions are 57.80% for 12.17% WR under 90 Nm and 66.17% for 12.12 WR under 60 Nm at (5000 and 6000) rpm, respectively.

Similar results have been found in the literature (Nguyen et al., 2009; Babu et al., 2015; Mingrui et al., 2017). Nguyen et al. investigated the effects of water-gasoline emulsions in an automotive SIE, and they found that NO_x emissions have been decreased approximately 35.0% by 5% water concentration. Mingrui et al. studied the effects of direct water injection into the cylinder by using different injectors on engine performance and exhaust emissions in a SIE. In this study, the optimum water ratio was determined as 15%. Also, they found that NO emissions were decreased up to 34.6% on average with the water use.

As well from the relevant literature (Heywood, 1988) that, the formation of NO_x emissions depends on the level of maximum temperature and excess air coefficient of the engine. As can be seen in Figures 19 (a-d), Figures 20 (a-c) that WAIA generally decreases excess air coefficient, and it increases the exhaust temperature slightly at all of the selected operating conditions. For this reason, it could be said that excess air coefficient reduction is more dominant than that of exhaust temperature in reducing NO_x formation. Although the exhaust temperature values are higher than that of NG, it is thought that there are lower local combustion zones leading to reduced reaction rates for NO_x in the combustion chamber (Mingrui et al., 2017; Wilson, 2011; Worm, 2017).

HC emissions are formed mainly due to the incomplete combustion of fuel and the quenching effect at the cylinder wall (Galloni et al., 2016; Feng et al., 2015). Also, HC emissions formation depends on engine operating conditions and fuel properties to some extent (Feng et al., 2015).

As shown in Figure 15 (a-b), 16 (a-b), 17 (a-b), and 18 (a-b), the WAIA generally decrease HC emissions formation at all of the selected operating conditions. Figures 15 (a-b) depict that HC emissions decrease with increasing WRs at 3000 rpm. The reduction ratios in HC emissions at high loads are more prominent than that of lower loads. It is thought that higher cylinder temperatures at high loads have an improving effect on the reduction of HC emissions. The obtained maximum decrease ratio of HC emissions becomes 27.34% for 11.27% WR under 90 Nm at this engine speed. At (4000 and 5000) rpms, HC emissions decrease approximately 6% and 9% WRs, but they increase about 3% and 12% WRs. It is thought that for (6 and 9) % WRs, the combustion phase could be improved, which reduces HC emissions. The wall quenching effect may be more dominant for 12% WR due to lower temperatures because of the cooling effect of water. The obtained maximum decrease ratio in HC emissions reaches to 32.80% for 9.37 % WR under 100, Nm and 30.30 for 9.03% WS under 100 Nm at 4000 and 5000 rpms, respectively. WAIA also decreases HC emissions at 6000 rpm. At this engine speed, an average 15.13% reduction has been obtained in HC emissions.

In the present study, it is observed that WAIA generally decreases HC emissions at the selected engine speeds. It

could be thought that water adding into intake air may cause subsequent burning, which results in the reduction of HC emissions during the expansion process. Besides, it can be said that the low quenching effect at the cylinder wall, especially at high loads, contributes to the decrease of HC formation. Similar results have been reported in the literature (Mingrui et al., 2017; Valentino et al., 2017, Fan et al., 2021; Osama et al., 2019; Babu et al., 2015; Arabacı et al., 2015). Mingrui et al. (2017) have explained the reduction of HC as follows. By applying water injection, the steam should be decomposed into hydrogen and oxygen at high temperatures during the combustion stroke. Thus, oxygen atoms were used for fuel oxidation, especially in rich mixture regions. The concentrations of OH and O radicals are increased. This results in a higher oxidation rate. Therefore, the concentrations of the hydrocarbons are reduced dramatically. However, in the existing literature, there are also studies in which it was stated that HC emissions increase with the water adding (Wilson, 2011; Nguyen and Wu, 2009).

The effects of WAIA on excess air coefficient and exhaust temperature

As shown in Figure 19a, WAIA decreases excess air coefficient at 3000 rpm; on the other hand, it increases excess air coefficient values at all of the other selected engine speeds. It is well known from the literature that the excess air coefficient is one of the most important combustion parameters that gives us useful information about the combustion process (Heywood, 1988; Durgun, 2018). As explained above, at 3000 rpm the combustion is become lean because of increasing excess air coefficient values, considerable reduction of BSFC and CO emission. At (4000 and 5000) rpms, excess air coefficient values decrease slightly with WAIA. These reductions are below of 2%. Therefore, as WAIA improves combustion at these engine speeds, BSFC has decreased, and CO emission has also decreased at (5 and 9) % water ratios. At 6000 rpm, BSFC and CO emission increase significantly as the increase ratios of excess air coefficients take higher values by the effect WAIA. It should not be forgotten that the reduction of excess air coefficient has an improving effect on the formation of NO_x emissions (Heywood, 1988).

As shown in Figure 20 (a-c) that WAIA generally increase exhaust temperature at all of the selected engine operating condition. At 4000 rpm, the exhaust temperature decreases for ~12% WR, but it increases for other lower WRs. The increase ratios in exhaust temperature values have remained below of 4% during this engine speed. At 5000 rpm, the exhaust temperature increases for approximately (9 and 12) % WRs and under full load (100 Nm). Exhaust temperature slightly increases at these WRs under other lower loads. For (3 and 6) % WRs, the exhaust temperature has decreased under some loads and contrarily has increased under some loads. However, increases and decreases in exhaust temperature values have not been very high at 5000 rpm.

At 6000 rpm, the exhaust temperature increases significantly at all of the selected operating conditions. As seen in Figure 19d, the engine has operated in rich conditions for WAIA at this engine speed. This might increase the exhaust temperature.

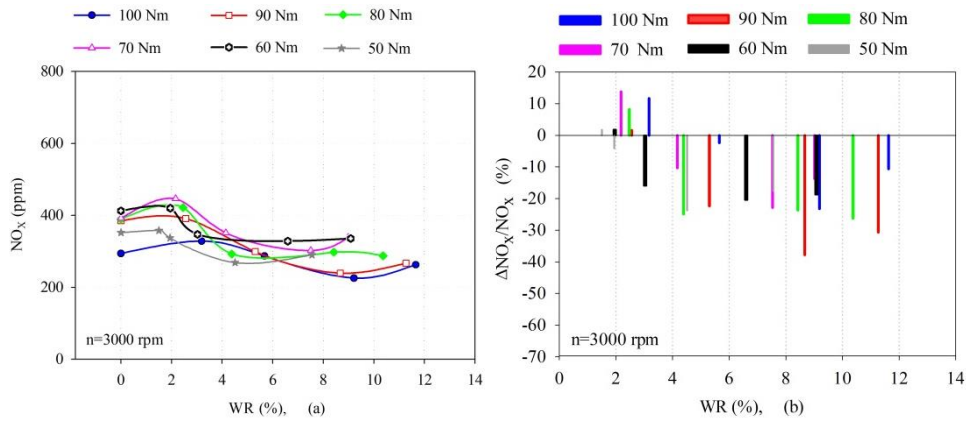


Figure 11 (a-b). Variations and VRs of NO_x emissions versus different WRs under five different loads at 3000 rpm, respectively.

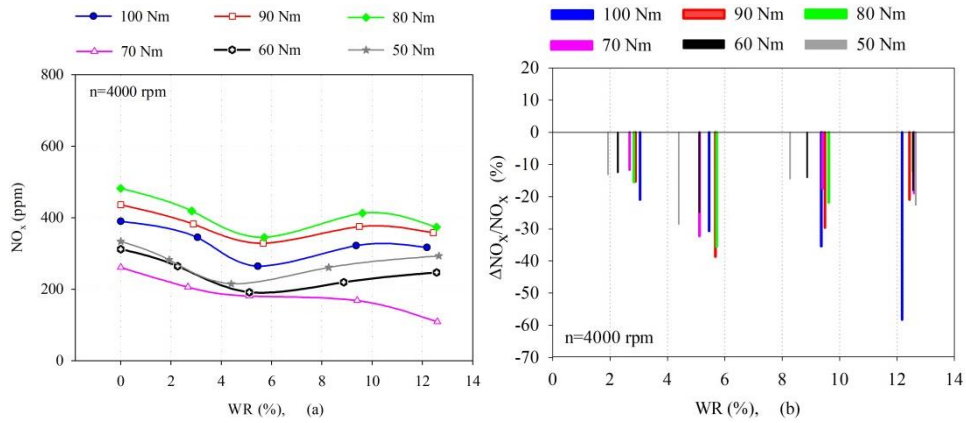


Figure 12(a-b). Variations and VRs of NO_x emissions versus different WRs under five different loads at 4000 rpm, respectively.

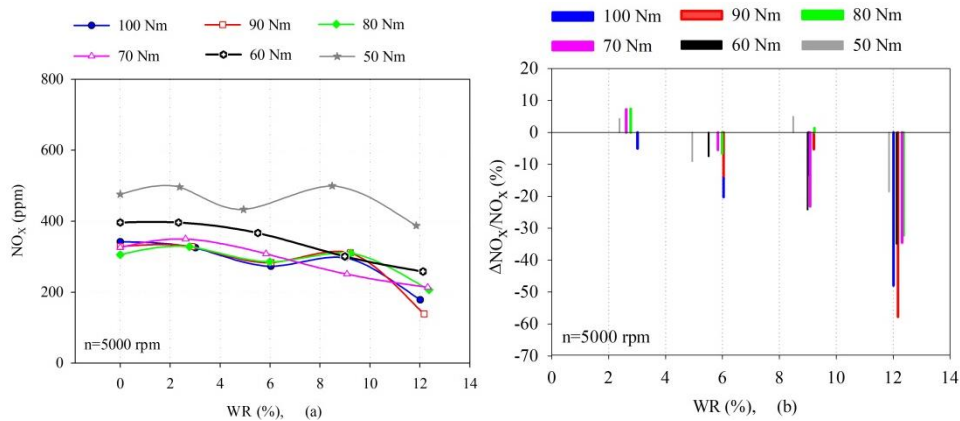


Figure 13 (a-b). Variations and VRs of NO_x emissions versus different WRs under five different loads at 5000 rpm, respectively.

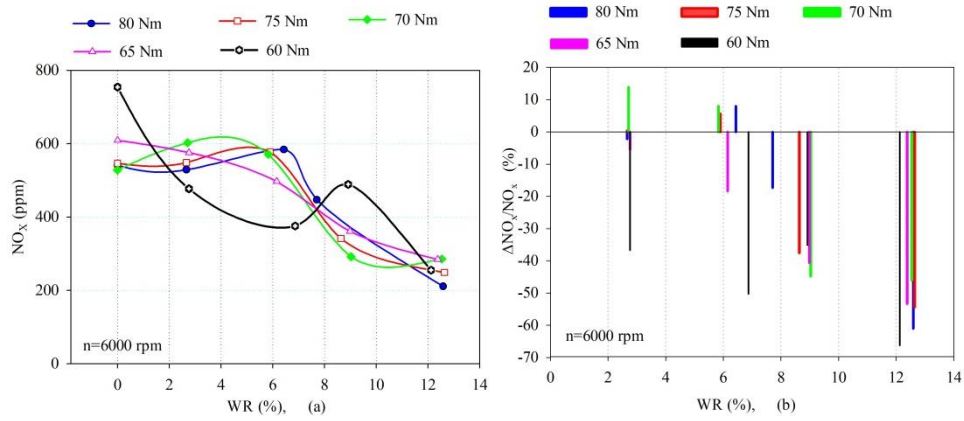


Figure 14 (a-b). Variations and VRs of NO_x emissions versus different WRs under five different loads at 6000 rpm, respectively.

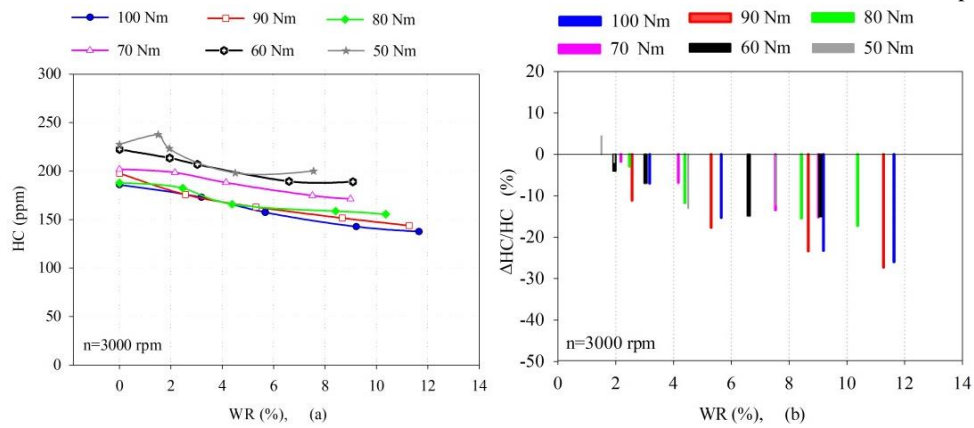


Figure 15 (a-b). Variations and VRs of HC emissions versus different WRs under five different loads at 3000 rpm, respectively.

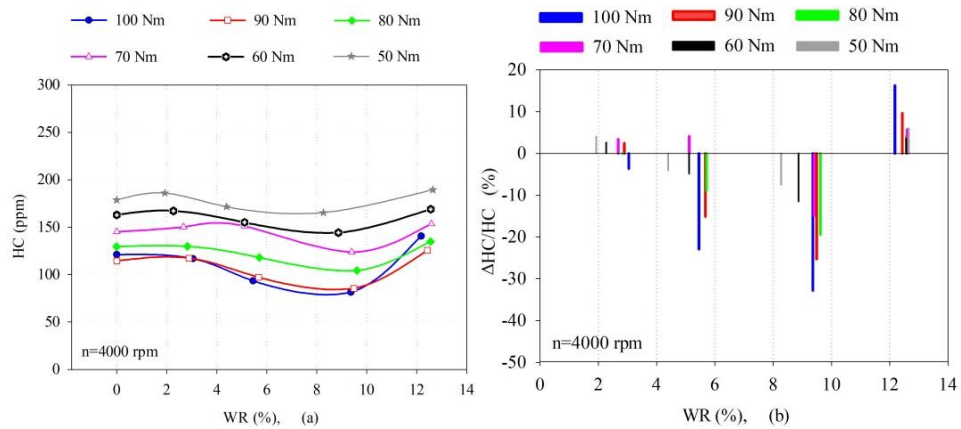


Figure 16 (a-b). Variations and VRs of HC emissions versus different WRs under five different loads at 4000 rpm, respectively.

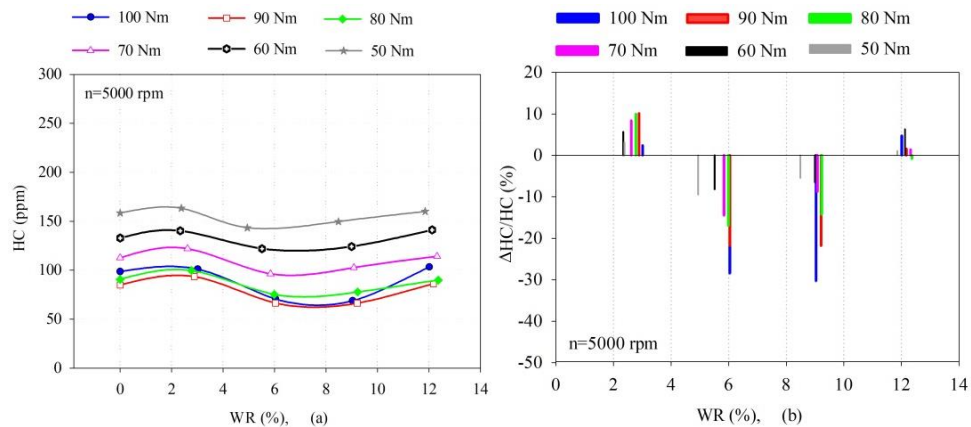


Figure 17 (a-b). Variations and VRs of HC emissions versus different WRs under five different loads at 5000 rpm, respectively.

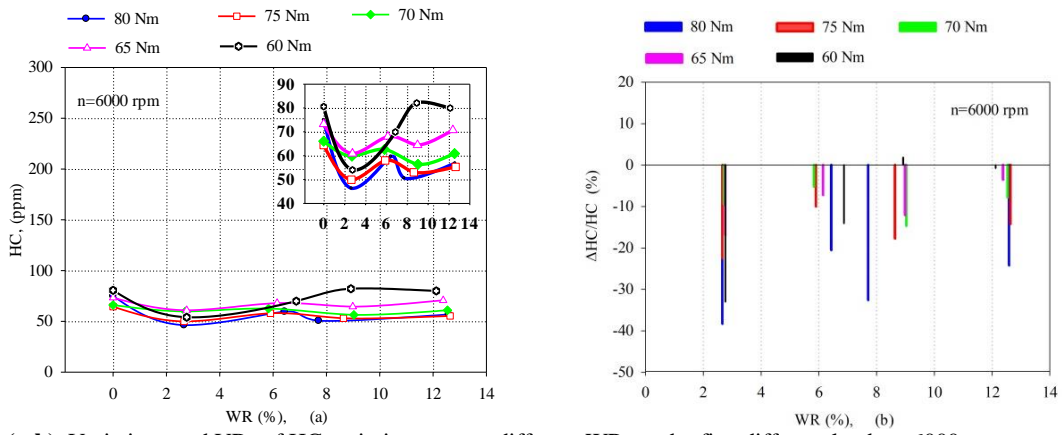


Figure 18 (a-b). Variations and VRs of HC emissions versus different WRs under five different loads at 6000 rpm, respectively.

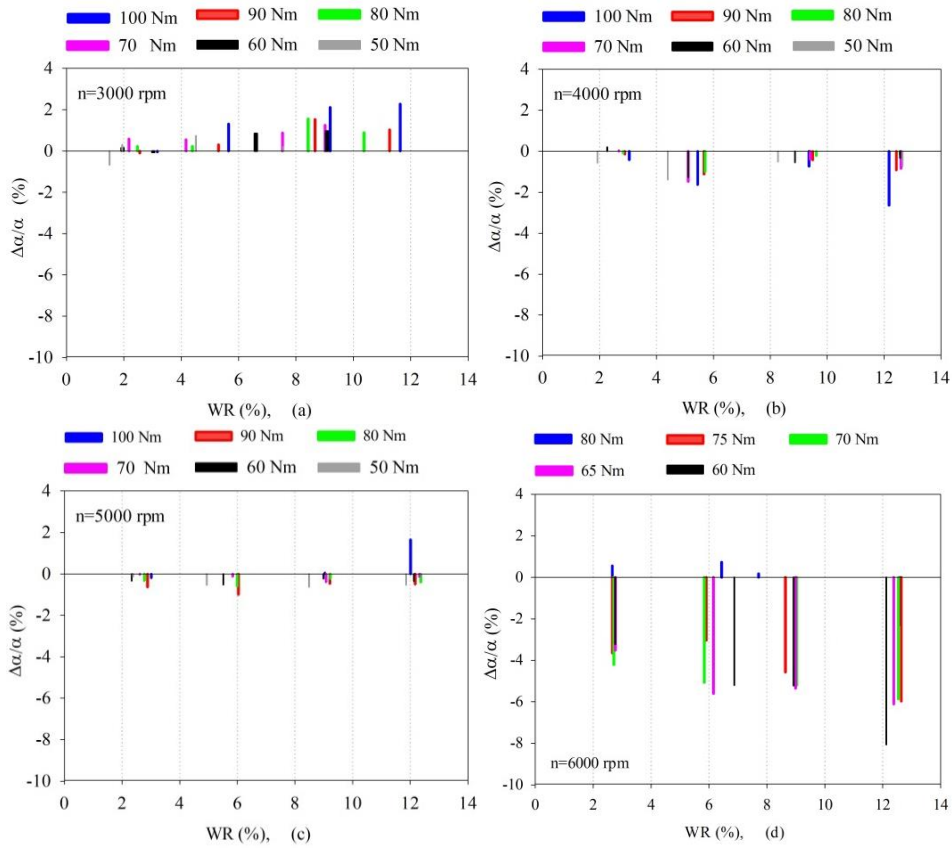
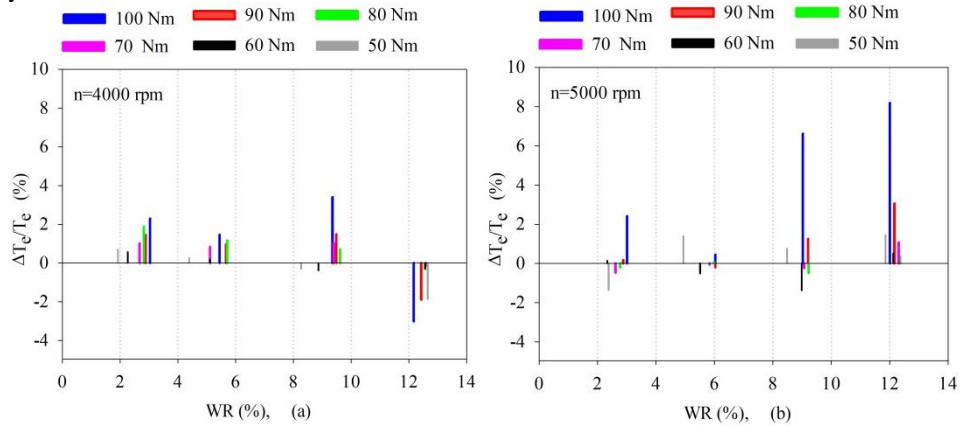


Figure 19 (a-d). VRs of excess air coefficient values versus different WRs under different loads at 3000, 4000, 5000, and 6000 rpm, respectively.



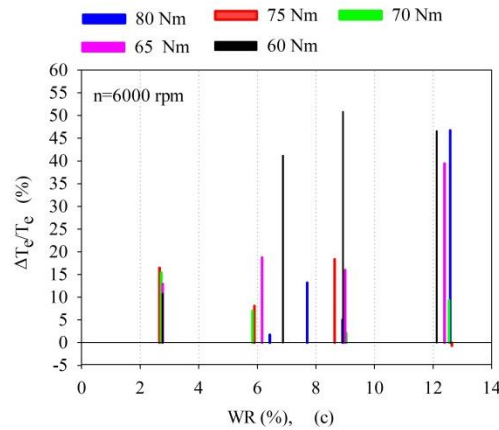


Figure 20 (a-c). VRs of exhaust temperature versus different WRs under different loads at 3000, 4000, 5000, and 6000 rpm, respectively

CONCLUSIONS

In this study, the effects of water addition to intake air on BSFC and emission characteristics were investigated experimentally and compared with that of NG in an automotive SIE. By evaluating of the experimental results, the obtained results can be summarized as follows:

-The water addition into the intake air has little effect on the engine brake effective power at all selected operating conditions.

-The water addition into the intake air decreases the BSFC under selected six different loads at (3000, 4000 and, 5000) rpms. The obtained maximum decrease ratios of BSFC are 28.27% for 6.6% WR at 3000 rpm, 4.16% for 2.67% WR at 4000 rpm and 7.19% for 9.03% WR at 5000 rpm, respectively. Unlike at the other engine speeds, the water addition into the intake air generally increases BSFC at 6000 rpm.

-CO emission decreases by applying water adding into intake air at 3000 rpm whereas it generally increases at (4000 and 5000) rpms. At 6000 rpm, the water addition into the intake air has increased CO emission significantly. The excess air coefficient decrease at (4000, 5000, and 6000) rpms, but it increases at 3000 rpm. Although the excess air coefficient reduction is desirable for NO_x formation, it has a worsening effect on the CO formation and BSFC.

-The water addition into the intake air decreases NO_x under all of the selected six different loads at (3000, 4000, 5000, and 6000) rpms. The obtained maximum decrease ratios of NO_x are 37.81 % for 8.67% WR, 58.21 for 12.18% WR and 57.80 for 12.12 WR, and 66.17% for 12.12.WR at (3000, 4000, 5000, and 6000) rpms.

-The water addition into the intake air generally decreases HC emissions under all of the selected six different loads at 3000, 4000, 5000 and 6000 rpms. The obtained maximum decrease ratios of HC emissions are 27.34 % for 11.27% WR, 32.80% for 9.37% WR, 30.30 for 9.03%

and 38.30% for 2.66 WR at (3000, 4000, 5000, and 6000) rpms.

-The water addition into the intake air exhibits a general tendency to increase the exhaust temperature. It is thought that the increase in the exhaust temperature could be caused by subsequent combustion, which could be occurred by the effect of the water addition during the expansion stroke.

-As a result, it was determined that 9% is the most suitable water ratio in terms of both BSFC and exhaust emissions for this experiment engine. At this WR, BSFC, NO_x and HC values are significantly reduced without any significant deterioration in effective power and CO emissions.

-Adding a suitable amount of water into intake air by using an adapted carburettor or an electronically controlled water injection system could improve considerably of any SIEs performance, BSFC and exhaust emission.

-To obtain general results, more experiments must be done. Also, computer-aided engine combustion and any cycle models must be developed.

ACKNOWLEDGEMENTS

We would like to present our thanks to Karadeniz Technical University which support our study financially and Research Assistant Orhan N. Aksu and Cahit SOoysal who have assisted to the experiments and Mech. Eng. Dep. Internal Comb. Engine Lab. Technician Şenol Dübüş who has helped in the lab. Also, we would like to present our thanks to Dr. Coşkun Bayram who helped to the installation of the test system.

REFERENCES

Arabaci E., İçingür Y., Solmaz H., Uyumaz A., Yılmaz E., 2015, Experimental investigation of the effects of direct water injection parameters on engine performance in a six-stroke engine, *Energy Conversion & Management*, 98, 89-97.

- Awad O. I., Mamata R., Ibrahim T. K., Hammid A. T., Yusria I. M., Hamidi M. A., Humadad A. M., Yusopa A. F., 2018, Overview of the Oxygenated Fuels in Spark Ignition Engine: Environmental and Performance, *Renewable and Sustainable Energy Reviews*, 91, 394-408.
- Babu A. R., Rao G. A. P., Prasad T. H., 2015, Direct Injection of Water Mist in an Intake Manifold Spark Ignition Engine, *International Journal of Automotive and Mechanical Engineering (IJAME)*, 12, 2809-2819.
- Bozza F., Bellis V. D., Teodosio L., 2016, Potentials of Cooled EGR and Water Injection for Knock Resistance and Fuel Consumption Improvements of Gasoline Engines, *Applied Energy*, 169, 112–125.
- Deng X., Chen Z., Wang X., Zhen H., Xie R., 2018, Exhaust Noise, Performance and Emission Characteristics of Spark Ignition Engine Fuelled with Pure Gasoline and Hydrous Ethanol Gasoline Blends, *Case Studies in Thermal Engineering*, 12, 55-63.
- Durgun O., 2018, *İçten Yanmalı Motorlar, Temel İlkeler*, TMMOB Gemi Mühendisleri Odası, İstanbul.
- Durgun O., 1990, *Experimental Methods in Engines, Lecturer Notes for Laboratory*, KTU Engineering Faculty, Mechanical Eng. Dep., Trabzon.
- Fan Y., Wu T., Xiao Di., Xu H., Li X., Xu M., 2021, Effect of port water injection on the characteristics of combustion and emissions in a spark ignition direct injection engine, *Fuel*, 283 (1), 119271.
- Fahd M.E.A., Wenming Y., Lee P. S., Chou S. K., Yap C. R., 2013, Experimental investigation of the perf. and emission characteristics of direct injection diesel engine by water emulsion diesel under varying engine load condition, *Applied Energy*, 102, 1042-1049.
- Feng R., Fu J., Yang J., Wang Y., Li Y., Deng B., 2015, Combustion and emissions study on motorcycle engine fueled with butanol-gasoline blend, *Renewable Energy*, 81:113-122.
- Galloni E., Fontana G., Staccone S., Scala F., 2016, Performance analyses of a spark-ignition engine firing with gasoline–butanol blends at partial load operation, *Energy Conversion & Management*, 110, 319–326.
- Harrington J. A., 1982, Water Addition to Gasoline-Effect on Combustion, Emissions, Performance and Knock, *SAE paper*, 820314.
- Heywood J. B., 1988, *Internal Combustion Engine Fundamental*, McGraw-Hill Book Company.
- Holman J. P., 2001, *Experimental Methods for Engineers*, (7th ed.), McGraw-Hill, New York.
- Internet 2016, Böhm M., Durst B., Unterweger G., Rubbert S., Approaches for On-board Water Provision for Water Injection <https://link.springer.com/content/pdf/10.1007%2Fs38313-015-0073-z.pdf>
- Merola S. S., Irimescu A., Vaglieco B. M., 2020, Influence of water injection on combustion identified through spectroscopy in an optical direct injection spark ignition engine, *Fuel*, 273, 117729.
- Mingrui W., Thanh Sa. N., Turkson R. F., Jinping L., Guanlun G., 2017, Water Injection for Higher Engine Performance and Lower Emissions, *Journal of the Energy Institute*, 90, 285-299.
- Nguyen Q. A., and Wu Y. Y., 2009, Experimental Investigations of Using Water-Gasoline Emulsions as a NO_x Treatment and its Effects on Performance and Emissions of Lean-Burn Spark-Ignition Engine, *Proc of the International Conference on Power Engineering-09 (ICOPE-09)*, November 16-20, Kobe, Japan.
- Osama H. G., Gabriel B., 2019, Use of Water Injection Technique to Improve the Combustion Efficiency of the Spark-Ignition Engine: A Model Study, *JEE Journal of Ecological Engineering*, 20 (2), 226–233.
- Peters B. D., and Stebar R. F., 1976, Water-Gasoline Fuels-Their Effect on Spark Ignition Engine Emissions and Performance, *SAE Transactions*, 85 (3) 760430–760707, 1832-1853.
- Rocha D. D., Radicchi F. C., Lopes G. S., Brunocilla M. F., Gomes P.C.F., Santos N.D.S.A., Malaquias A.C.T., Filho F.A.R., Baeta J.G.C., 2021, Study of the water injection control parameters on combustion performance of a spark-ignition engine, 217 (15), 119346.
- Subramanian K. A., 2011, A comparison of water–diesel emulsion and timed injection of water into the intake manifold of a diesel engine for simultaneous control of NO and smoke emissions, *Energy Conversion and Management*, 52, 849–57.
- Şahin Z., Aksu O. N., Durgun O., 2017, Experimental Investigation of the Effects of n-Butanol Fumigation on Engine Performance and Exhaust Emissions in a Turbocharged DI Diesel Engine, *International Conference of advanced engineering Technology (ICADET)*, 21-23 September, Bayburt.
- Şahin Z., Durgun O., 2015, Aksu O. N., Experimental Investigation of n-Butanol/Diesel Fuel Blends and n-Butanol Fumigation–Evaluation of Engine Performance, Exhaust Emissions, Heat Release and Flammability Analysis, *Energy Conver. and Manag.*, 103, 778–789.
- Şahin Z., Tuti M., Durgun O., 2014, Experimental Investigation of the Effects of Water Adding to the Intake

Air on the Engine Performance and Exhaust Emissions in a DI Automotive Diesel Engine, *Fuel*, 115, 884–895.

Tiryaki D., 2008, *Benzin Motorlarında Emme Havaına Su Eklenmesinin Motor Performansına ve Eksoz Emisyonlarına Etkilerinin Deneysel Olarak İncelenmesi*, Yüksek Lisans Tezi, Karadeniz Teknik Üniversitesi, Fen Bilimleri Enstitüsü, Trabzon.

Tiryaki D., Durgun O., 2010, Experimental Investigation of the Effects of Adding Water to the Intake Air of Gasoline Engines on Engine Performance and Exhaust Emissions, *11th International Combustion Sym.*, Sarajevo.

Valentino G., Siano D., Bozza F., Marchitto L., Tornatore C., 2017, Effect of Water Injection on Performance, Gas Emission and Combustion Noise of a 2-Cylinder Turbocharged SI Engine: Experimental and Numerical Analysis, *40th Meeting of the Italian Section of the Combustion Institute*, June 07-09, Italy.

Wang Y., Yu X., Ding Y., Du Y., Zhao Z., Zuo X., 2018, Experimental Comparative Study on Combustion and Particle Emission of n-Butanol and Gasoline Adopting Different Injection Approaches in a Spark Engine Equipped with Dual-Inj. System, *Fuel*, 211, 837-849.

Wilson J. P., 2011, *Effects of Water Injection and Increased Compression Ratio in a Gasoline Spark Ignition Engine*, Master Thesis, University of Idaho, USA.

Worm J., 2017, *The Impact Of Water Injection On Spark Ignition Engine Perf. Under High Load Operation*, Master Thesis, Michigan Technological University.



AN ACCELERATED NODAL DISCONTINUOUS GALERKIN METHOD FOR THERMAL CONVECTION ON UNSTRUCTURED MESHES: FORMULATION AND VALIDATION

Ali KARAKUS

Department of Mechanical Engineering, Middle East Technical University
06800 Cankaya Ankara

akaragus@metu.edu.tr, ORCID: 0000-0002-9659-6712

(Geliş Tarihi: 04.10.2021, Kabul Tarihi: 04.04.2022)

Abstract: We present a GPU-accelerated method for large scale, coupled incompressible fluid flow and heat transfer problems. A high-order, nodal discontinuous Galerkin method is utilized to discretize governing equations on unstructured triangular meshes. A semi-implicit scheme with explicit treatment of the advective terms and implicit treatment of the split Stokes operators are used for time discretization. The pressure system is solved with a conjugate gradient method together with a fully GPU-accelerated multigrid preconditioner. The code is built on scalable libParanumal solver which is a library of high-performance kernels for high-order discretizations. Performance portability is achieved by using the open concurrent compute abstraction, OCCA. A set of numerical experiments including free and mixed convection problems indicate that our approach experimentally reaches design order of accuracy.

Keywords: discontinuous Galerkin, GPU, parallel, incompressible, heat transfer, high-order.

ISI TAŞINIMI İÇİN YAPISAL OLMAYAN AĞLARDA BİR HIZLANDIRILMIŞ SÜREKSİZ GALERKİN METDU: FORMÜLASYONU VE DOĞRULANMASI

Öz: Bu çalışmada, büyük ölçekli, birleştirilmiş sıkıştırılmaz akış ve ısı transferi problemleri için GPU ile hızlandırılmış bir yöntem sunulmuştur. Yapılandırılmamış üçgen ağlar üzerinde tanımlayıcı denklemlerini ayrıklaştırmak için yüksek dereceli, nodal süreksiz Galerkin yöntemi kullanılmıştır. Zaman ayrıklaştırması, taşınım terimlerinin açık bir şekilde ele alındığı, Stokes operatörlerinin ise örtük olarak çözüldüğü bir yarı-örtük şema kullanılarak elde edilmiştir. Basınç sistemi, tamamen GPU ile hızlandırılmış bir çoklu-ağ ön koşullandırıcının kullanıldığı, eşlenik gradyan yöntemiyle çözülmüştür. Kod, yüksek dereceli ayrıklaştırmalar için yüksek performanslı kerneller sağlayan, ölçeklenebilir kütüphane olan libParanumal üzerine yazılmıştır. Platformdan bağımsız performans taşınabilirliği OCCA (open concurrent compute abstraction) dili ile elde edilmiştir. Yapılan serbest ve karışık taşınım problemlerini içeren bir dizi sayısal test ile sunulan metodun deneysel olarak beklenen, spektral doğruluğa ulaştığını gösterilmiştir.

Anahtar Kelimeler: süreksiz Galerkin, GPU, paralel, sıkıştırılmaz akış, ısı transferi, yüksek seviyeli hesaplama.

NOMANCLATURE

Abbreviations

Gr	Grashof Number $[= g\beta(T - T_r)L_r^3/\nu^2]$
Pr	Prandtl Number $[= \nu/\alpha]$
Ra	Rayleigh Number $[= GrPr]$
Re	Reynolds Number $[= U_r L_r/\nu]$
Ri	Richardson Number $[= Gr/Re^2]$
St	Strouhal Number $[= fL_r/U_r]$
DG	Discontinuous Galerkin
DNS	Direct Numerical Simulation
GPU	Graphical Processing Unit
HPC	High Performance Computing
NS	Navier-Stokes
SIPDG	Symmetric Interior Penalty DG
Subscripts	

u	Velocity Related Value
θ	Temperature Related Value
D	Dirichlet Boundary
N	Neumann Boundary
r	Reference Value
Greek Symbols	
α	Thermal Diffusivity $[= m^2/s]$
β	Expansion Coefficient $[= 1/^\circ C]$
$\nabla \cdot$	Divergence Operator
∇	Gradient Operator
Δ	Laplace Operator
ν	Kinematic Viscosity $[= m^2/s]$
τ	Stabilization Parameter
θ	Non-dimensional Temperature
Superscripts	
e	Element Id

ex	Exact Solution
f	Face Id
$n + 1$	Next Time Level
n	Current Time Level
Symbols	
s_u	Source Term of Momentum Equation
u	Velocity Vector
g_D	Dirichlet Boundary Condition
g_N	Neumann Boundary Condition
h	Characteristics Mesh Size
K	Number of Elements
L_2	L_2 Vector Norm of Error
N	Approximation Order
N_p	Number of Interpolation Nodes
p	Non-dimensional Pressure
s_θ	Source Term of Energy Equation
t	Non-dimensional Time

INTRODUCTION

One of the primary challenges in fluid mechanics and heat transfer is to reflect physical interactions that occurred in a large range of spatial and temporal scales. This type of analysis for real-life applications might require extreme degrees of freedom and high-order discretizations to minimize numerical dissipation. Simulation tools developed for these problems can require large compute times which cannot be provided even by the fastest supercomputers. The principal objective of high-performance computing (HPC) is to bring the extreme runtimes to reasonable levels. Recently, HPC systems use accelerator based on-node parallelism using Graphical Processing Units (GPUs). On the other hand, developing a high-order finite element based flow and heat transfer analysis suit that benefits modern accelerators is complicated due to the need of achieving multi-threaded parallelism with effectively exploiting nonuniform memory hierarchies (Karakus et al., 2019b).

Discontinuous Galerkin (DG) method (we refer Hesthaven and Warburton (2008) and the references therein) is a class of high-order finite element methods. DG method uses completely discontinuous, piecewise polynomial approximations for spatial discretization that leads to weak elemental connectivity and local stencil. These properties of the DG method together with high-order approximations yields highly parallel operators with high arithmetic intensity that makes the method well-suited for GPUs. Because of its attractive properties, DG method has been used to analyze various physical problems (Gandham et al., 2015; Modave et al., 2016; Chan et al., 2016; Karakus et al., 2016a,b, 2019a). The implementation of DG methods on GPUs is well documented for first-order hyperbolic systems with explicit time integrators, but only a few of papers report GPU-optimized DG discretizations for incompressible flows (Roca et al., 2011) or the operators required for

incompressible flows (Swirydowicz et al., 2019). In Karakus et al. (2019b), we recently proposed a GPU-optimized nodal DG method for incompressible flows on unstructured meshes. We extend this efficient approach to thermal convection problems in the present study.

There have been only a couple of studies dealing with incompressible thermal convection using discontinuous or continuous high-order finite element methods. Hossain et al. (Hossain et al., 2021) developed a spectral/hp element method for the Direct Numerical Simulation (DNS) of incompressible thermal convective flows by considering Boussinesq type thermal body-forcing with periodic boundary conditions and enforcing a constant volumetric flow rate. In Kumar and Poth erat (2020), the authors studied the convective patterns that arise in a nearly semi-cylindrical cavity placed in a fluid heated at the upper boundary and bounded by a cold and porous semicircular boundary. They used spectral element method to obtain results and performed a linear stability analysis of the fluid flow. In Saha et al. (2015), a high-order spectral element model is developed for forced thermal convection problems considering incompressible flows and avoiding thermal body-forcing effects.

In this work, we focus on a GPU accelerated, high-order discontinuous Galerkin (DG) based approach for coupled fluid flow and heat transfer problems which is suitable for large scale engineering simulations. In particular, we deal with the formulation of presented method and validation of developed solver for different thermal convection regimes. To the best of our knowledge, there has been no published research on incompressible thermal convection that fully benefits high-order, nodal DG discretization and modern computational architectures relying on-node parallelization.

The remainder of this paper is organized as follows. In the first section, we present the mathematical formulation for the DG scheme to approximate the incompressible Navier-Stokes equations coupled with energy equations, including the spatial discretizations and the temporal splitting scheme. Then, linear solvers and GPU-accelerated p-multigrid preconditioner are briefly explained which is followed by numerical validation test cases. Final section is dedicated to concluding remarks and comments on the future works.

FORMULATION

We consider a closed two-dimensional domain $\Omega \subset R^2$ and denote the boundary of Ω by $\partial\Omega$. Following the notation presented in Karakus et al. (2019b), we assume that $\partial\Omega$ can be partitioned into two non-overlapping regions denoted by $\partial\Omega_D$ and $\partial\Omega_N$ referring prescribed Dirichlet or Neumann boundary conditions, respectively.

We are interested in the approximation of non-isothermal incompressible Navier-Stokes equations coupled by the energy equations through Boussinesq approximation which reads

$$\nabla \cdot \mathbf{u} = 0, \quad (1.1)$$

$$\frac{\partial \mathbf{u}}{\partial t} + (\mathbf{u} \cdot \nabla) \mathbf{u} = -\nabla p + \frac{1}{Re} \Delta \mathbf{u} + \mathbf{s}_u, \quad (1.2)$$

$$\frac{\partial \theta}{\partial t} + (\mathbf{u} \cdot \nabla) \theta = \frac{1}{Re Pr} \Delta \theta + s_\theta, \quad (1.3)$$

in non-dimensional form and space-time domain $\Omega \times (0, \mathcal{T}]$ subject to the initial conditions

$$\mathbf{u} = \mathbf{u}_0, \theta = \theta_0 \text{ for } t = 0, \mathbf{x} \in \Omega, \quad (2)$$

and the boundary conditions

$$\mathbf{u} = \mathbf{g}_D \text{ on } \mathbf{x} \in \partial \Omega_D^u, t \in (0, \mathcal{T}], \quad (3.1)$$

$$\frac{\partial \mathbf{u}}{\partial \mathbf{n}} = 0, p = 0 \text{ on } \mathbf{x} \in \partial \Omega_N^u, t \in (0, \mathcal{T}], \quad (3.2)$$

$$\theta = g_D \text{ on } \mathbf{x} \in \partial \Omega_D^\theta, t \in (0, \mathcal{T}], \quad (3.3)$$

$$\frac{\partial \theta}{\partial \mathbf{n}} = g_N \text{ on } \mathbf{x} \in \partial \Omega_N^\theta, t \in (0, \mathcal{T}]. \quad (3.4)$$

Here u , p and θ are non-dimensional velocity, static pressure and temperature fields, respectively. In the equation, following parameters are used to get dimensionless quantities,

$$\begin{aligned} \mathbf{x} &= \frac{\mathbf{x}^*}{L_r}, t = \frac{t^*}{L_r/U_r}, \mathbf{u} = \frac{\mathbf{u}^*}{U_r}, p = \frac{p^*}{\rho_r U_r^2} \\ \rho &= \frac{\rho^*}{\rho_r}, \nu = \frac{\nu^*}{\nu_r}, \alpha = \frac{\alpha^*}{\alpha_r}, \theta = \frac{T - T_r}{T_s}, \end{aligned} \quad (4)$$

where superscript $*$ denotes the dimensional parameter and the subscript r refers to corresponding reference value i.e. reference length scale L_r , velocity U_r , density ρ_r , viscosity ν_r , thermal diffusivity α_r and temperature T_r . One should note that the temperature scale T_s is problem dependent i.e. in the case of a channel flow with uniformly heated walls, T_s can be defined as the maximum temperature difference between the hot and cold walls in the system.

The non-dimensional Reynolds and Prandtl numbers in the eq. (1) are defined as $Re = U_r L_r / \nu_r$ and $Pr = \nu_r / \alpha_r$. Also, $\mathbf{s}_u = (\mathbf{g} \beta (T - T_r) L_r / U_r) \theta$ is the forcing term for Navier-Stokes, where \mathbf{g} is the gravitational acceleration, β is the expansion coefficient. In free convection problems, the reference velocity is selected as $U_r = \mathbf{g} \beta (T - T_r) L_r$. $s_\theta = s_\theta(\theta, \nabla \theta, \mathbf{u})$ is the generic generation term for the energy equation written in terms of temperature. We would like to emphasize that superscripts u and θ in boundary representation separate

the Dirichlet and Neumann conditions on the physical boundary set for flow and heat transfer equations.

The governing PDE system is discretized by first constructing the spatial discretization using the nodal DG method, then by the temporal discretization using a pressure correction scheme that are covered in the following sections.

Preliminaries

The computational domain Ω is partitioned into K triangular elements \mathcal{E}^e , $e = 1, \dots, K$, such that

$$\Omega = \cup_{e=1}^K \mathcal{E}^e$$

The boundary of the element \mathcal{E}^e is denoted by $\partial \mathcal{E}^e$. Two elements, \mathcal{E}^{e+} and \mathcal{E}^{e-} , are neighbours if they have a common face, i.e., $\partial \mathcal{E}^{e-} \cap \partial \mathcal{E}^{e+} \neq \emptyset$. The unit outward normal vector of $\partial \mathcal{E}$ is showed as \mathbf{n} .

We consider a finite element space on each element \mathcal{E}^e , denoted $V_N^e = \mathcal{P}_N(\mathcal{E}^e)$ where $\mathcal{P}_N(\mathcal{E}^e)$ is the space of polynomial functions of degree N on element \mathcal{E}^e . As a basis of the finite element spaces, we take a set of $N_p = |V_n^e|$ Lagrange polynomials $\{l_n^e\}_{n=0}^{n=N_p}$, interpolating at the Warp & Blend nodes (Warburton, 2006) mapped to the element \mathcal{E}^e .

We have introduced the inner product $(u, v)_{\mathcal{E}^e}$ to denote the integration of the product of arbitrary variables u and v computed over the element \mathcal{E}^e and the inner product $(u, v)_{\partial \mathcal{E}^e}$ to denote the integration along the element boundary $\partial \mathcal{E}^e$. We also define internal and external trace values of a scalar-valued function u^e as u^- and u^+ , respectively. Note that we suppress the use of the e superscript when it is clear which element is the local trace. According to this definition, average and jump operators can be defined as:

$$\{\{u\}\} = \frac{u^+ + u^-}{2}, \quad [[u^e]] = u^+ - u^-. \quad (5)$$

When u is a vector-valued function, the above operators act on it component wise.

Spatial Discretization

The polynomial approximation of the velocity field u , the pressure p and the temperature θ fields are defined on each element as

$$\mathbf{u}^e = \sum_{n=0}^{N_p} \mathbf{u}_n^e l_n^e(\mathbf{x}), p^e = \sum_{n=0}^{N_p} p_n^e l_n^e(\mathbf{x}), \theta^e = \sum_{n=0}^{N_p} \theta_n^e l_n^e(\mathbf{x}),$$

for all $\mathbf{x} = (x, y) \in \mathcal{E}^e$. Then, using the polynomial representation of u^e , p^e and θ^e , the semi-discrete form of PDE system given by the eq. (1) is defined on each element \mathcal{E}^e as

$$D^e \mathbf{u}^e = 0 \quad (6.1)$$

$$\frac{d\mathbf{u}^e}{dt} + \mathbf{N}^e(\mathbf{u}^e) = \mathbf{G}^e p^e + \frac{1}{Re} L^e \mathbf{u}^e + \mathbf{S}_u^e \quad (6.2)$$

$$\frac{d\theta^e}{dt} + N^e(\theta^e) = \frac{1}{RePr} L^e \theta^e + S_\theta^e \quad (6.3)$$

where the operators are defined as follow, $\mathbf{N}^e: (V_N^e)^2 \rightarrow (V_N^e)^2$, $N^e: (V_N^e) \rightarrow (V_N^e)$, $\mathbf{S}_u^e: (V_N^e)^2 \rightarrow (V_N^e)^2$, $S_\theta^e: (V_N^e) \rightarrow (V_N^e)$, $\mathbf{G}^e: V_N^e \rightarrow (V_N^e)^2$, $L^e: V_N^e \rightarrow V_N^e$ and $D^e: (V_N^e)^2 \rightarrow V_N^e$. These terms are discrete versions of the nonlinear term $\mathbf{u} \cdot \nabla \mathbf{u}$, advection term $\mathbf{u} \cdot \nabla \theta$, source terms s_u and s_θ , gradient operator ∇ , Laplacian Δ , and the divergence operator $\nabla \cdot$, in the same order. In the subsequent parts, we define these operators in the nodal DG framework.

We begin with the discretization of nonlinear term, $\mathbf{u} \cdot \nabla \mathbf{u}$ and the advection term $\mathbf{u} \cdot \nabla \theta$. Using the incompressibility condition eq. (1.1), the advection terms are written in divergence form i.e., $\mathbf{u} \cdot \nabla \mathbf{u} = \nabla \cdot \mathbf{F}(\mathbf{u})$ and $\mathbf{u} \cdot \nabla \theta = \nabla \cdot F(\mathbf{u}, \theta)$, where $\mathbf{F}(\mathbf{u}) = \mathbf{u} \otimes \mathbf{u}$ and $F(\theta, \mathbf{u}) = \mathbf{u}\theta$. Multiplying $\mathbf{u} \cdot \nabla \mathbf{u}$ and $\mathbf{u} \cdot \nabla \theta$ by a test function $v \in V_N^e$, integrating over the element \mathcal{E}^e , and performing integration by parts, we define the discrete advective terms $\mathbf{N}^e(\mathbf{u})$ and $N^e(\theta, \mathbf{u})$ via the following variational forms

$$(v, \mathbf{N}^e(\mathbf{u}^e))_{\mathcal{E}^e} = -(\nabla v, \mathbf{F}(\mathbf{u}^e))_{\mathcal{E}^e} + (v, \mathbf{n} \cdot \mathbf{F}^*)_{\partial \mathcal{E}^e},$$

$$(v, N^e(\theta^e, \mathbf{u}^e))_{\mathcal{E}^e} = -(\nabla v, F(\theta^e, \mathbf{u}^e))_{\mathcal{E}^e} + (v, \mathbf{n} \cdot F^*)_{\partial \mathcal{E}^e}$$

Since DG uses discontinuous approximation space, the flux functions \mathbf{F} and F are not uniquely defined on the element boundaries and hence, they are replaced by local Lax-Friedrichs numerical flux functions \mathbf{F}^* and F^* which depend on the local and neighboring trace values,

$$\mathbf{F}^* = \{\{\mathbf{F}(\mathbf{u})\}\} + \frac{1}{2} \mathbf{n} \Lambda_u^e [[\mathbf{u}]], \quad (7.1)$$

$$F^* = \{\{F(\mathbf{u}\theta)\}\} + \frac{1}{2} \Lambda_\theta^e [[\theta]], \quad (7.2)$$

The parameters Λ in the eq. (7) introduce artificial diffusion required to stabilize the numerical discretization of advective terms and are defined to be the maximum eigenvalue of the flux Jacobians in absolute value, i.e.,

$$\Lambda_u = \max_{u \in [u^-, u^+]} \left| \mathbf{n} \cdot \frac{\partial \mathbf{F}}{\partial \mathbf{u}} \right|, \quad \Lambda_\theta = \max_{\theta \in [\theta^-, \theta^+]} \left| \frac{\partial F}{\partial \theta} \right|.$$

Boundary conditions are enforced weakly in flux functions by adjusting exterior trace values i.e. in the case of Dirichlet boundaries $\partial \mathcal{E}^e \cap \Omega_D \neq \emptyset$, the boundary conditions, eq. (3.1) and (3.3) lead $\mathbf{u}^+ = \mathbf{g}_D$ and $\theta^+ = g_D$. For Neumann boundaries eq. (3.2) and (3.4) where $\partial \mathcal{E}^e \cap \Omega_N \neq \emptyset$, we simply choose $\mathbf{u}^+ = \mathbf{u}^-$ and $\theta^+ = \theta^-$.

To obtain discrete gradient and divergence operators, \mathbf{G}^e and D^e , we multiply the pressure gradient ∇p^e and the velocity divergence $\nabla \cdot \mathbf{u}^e$ by a test function $v \in V_N^e$, integrate over the element \mathcal{E}^e . Different from the advection operators, we use integration by parts twice to get strong variational forms and simply utilize central fluxes $p^* = \{\{p\}\}$ and $\mathbf{u}^* = \{\{\mathbf{u}\}\}$ leading

$$(v, \mathbf{G}^e p^e)_{\mathcal{E}^e} = (v, \nabla p^e)_{\mathcal{E}^e} + (v, \mathbf{n}(p^* - p^-))_{\partial \mathcal{E}^e}, \quad (8)$$

$$(v, D^e \mathbf{u}^e)_{\mathcal{E}^e} = (v, \nabla \cdot \mathbf{u}^e)_{\mathcal{E}^e} + (v, \mathbf{n} \cdot (\mathbf{u}^* - \mathbf{u}^-))_{\partial \mathcal{E}^e}, \quad (9)$$

The boundary conditions are imposed for these operators slightly differently than for $\mathbf{N}^e(\mathbf{u})$ and $N^e(\theta, \mathbf{u})$. For Dirichlet boundaries central fluxes become $\mathbf{u}^* = \mathbf{g}_D$ and $p^* = p^-$, and for zero Neumann boundaries, we choose $\mathbf{u}^* = \mathbf{u}^-$ and $p^* = 0$.

To discretize the Laplacian operator L^e , we follow follow the Symmetric Interior Penalty DG (SIPDG) approach (Wheeler, 1978; Arnold, 1982) which reads the following variational definition of the operator for velocity and temperature

$$(v, L^e \mathbf{u}^e)_{\mathcal{E}^e} = -(\nabla v, \nabla \mathbf{u}^e)_{\mathcal{E}^e} + (v, \mathbf{n} \cdot \nabla \mathbf{u})_{\partial \mathcal{E}^e} - \frac{1}{2} (\mathbf{n} \cdot \nabla v, [[\mathbf{u}]])_{\partial \mathcal{E}^e} + (v, \tau [[\mathbf{u}]])_{\partial \mathcal{E}^e} \quad (10.1)$$

$$(v, L^e \theta^e)_{\mathcal{E}^e} = -(\nabla v, \nabla \theta^e)_{\mathcal{E}^e} + (v, \mathbf{n} \cdot \nabla \theta)_{\partial \mathcal{E}^e} - \frac{1}{2} (\mathbf{n} \cdot \nabla v, [[\theta]])_{\partial \mathcal{E}^e} + (v, \tau [[\theta]])_{\partial \mathcal{E}^e} \quad (10.2)$$

where τ is the penalty parameter and must be chosen to be sufficiently large in order to enforce coercivity. On the other hand, selecting large τ increases the condition number of the Laplacian operator and degrades the performance of linear solvers. Along each face of an element shared by its neighbor element, $\partial \mathcal{E}^{ef} = \mathcal{E}^{e+} \cap \mathcal{E}^{e-}$, penalty parameter τ^{ef} is selected using the lower bound estimate derived in in Shahbazi (2005) as

$$\tau^{ef} = \frac{(N+1)(N+2)}{2} \max \left(\frac{1}{h_+^{ef}}, \frac{1}{h_-^{ef}} \right) \quad (11)$$

where h_+^{ef} and h_-^{ef} are characteristic length scales of the elements \mathcal{E}^{e+} and \mathcal{E}^{e-} on either side of the face $\partial \mathcal{E}^{ef}$ and

are defined as $h_+^{ef} = \frac{|\varepsilon^{e+}|}{|\partial\varepsilon^{ef}|}$ and $h_-^{ef} = \frac{|\varepsilon^{e-}|}{|\partial\varepsilon^{ef}|}$. Boundary conditions for the discretized Laplacian operator are imposed in a way analogous to that described for the gradient and divergence operators for pressure and velocity systems. For the heat equation, non-homogeneous temperature Neumann data is imposed as $\nabla\theta^+ = \nabla\theta^- - 2\mathbf{g}_N$.

With the definitions of discrete operators \mathbf{N}^e , N^e , L^e , \mathbf{G}^e and D^e , we complete the semi-discrete form of the scheme given in eq. (6). Assembling the semi-discrete system defined on each element \mathcal{E} into global system, we arrive to following global problem

$$D\mathbf{U} = \mathbf{0}, \quad (12.1)$$

$$\frac{\partial\mathbf{U}}{\partial t} + \mathbf{N}(\mathbf{U}) = -\mathbf{G}\mathbf{P} + \frac{1}{Re}\mathbf{L}\mathbf{U} + \mathbf{S}_U, \quad (12.2)$$

$$\frac{\partial\theta}{\partial t} + N(\theta, \mathbf{U}) = \frac{1}{RePr}L\theta + S_\theta. \quad (12.3)$$

To simplify the notation, we use capital letters and drop the superscript e to denote the global assembled vectors of the degrees of freedom as in Karakus et al. (2019b). In the next section, we proceed to the fully discrete scheme by introducing the semi-explicit time integration method.

Temporal Discretization

A high-order temporal discretization is used for the flow and energy equations by adopting an 3^{rd} order backward differentiation method for the stiff diffusive terms and an 3^{rd} order extrapolation method for advective terms. Then, equation (12) can be advanced from time level t^n to $t^{n+1} = t^n + \Delta t$ by using this formulation as

$$D \cdot \mathbf{U}^{n+1} = 0, \quad (13.1)$$

$$\gamma\mathbf{U}^{n+1} = \sum_{i=0}^2 \beta_i \mathbf{U}^{n-i} - \Delta t \sum_{i=0}^2 \alpha_i (\mathbf{N}(\mathbf{U}^{n-i}) - \mathbf{S}_U^{n-i}) + Re^{-1}\Delta t L\mathbf{U}^{n+1} - \Delta t \mathbf{G}\mathbf{P}^{n+1} \quad (13.2)$$

$$\gamma\theta^{n+1} = \sum_{i=0}^2 \beta_i \theta^{n-i} - \Delta t \sum_{i=0}^2 \alpha_i N(\theta^{n-i}, \mathbf{U}^{n-i}) + \Delta t \sum_{i=0}^2 \alpha_i S_\theta^{n-i} + (RePr)^{-1}\Delta t L\theta^{n+1} \quad (13.3)$$

where β , and γ correspond to the stiffly stable backwards differentiation coefficients and α is the extrapolation scheme coefficients. For the third order scheme, the coefficients are given as $\gamma = 11/6$, $\beta_0 = 3$, $\beta_1 = -3/2$, $\beta_2 = 1/3$ and $\alpha_0 = 3$, $\alpha_1 = -3$, $\alpha_2 = 1$.

Following Shahbazi et al. (2007), the fully discrete scheme eq. (13) is replaced with an algebraically split version in order to avoid solving a fully coupled system for velocity, temperature and pressure which reads six fractional steps as follows

$$\hat{\theta} = \sum_{i=0}^S \beta_i \theta^{n-i} - \Delta t \sum_{i=0}^2 \alpha_i (N(\theta^{n-i}, \mathbf{U}^{n-i}) - S_\theta^{n-i}), \quad (14.1)$$

$$\left(-L + \frac{\gamma RePr}{\Delta t} J\right) \theta^{n+1} = \frac{RePr}{\Delta t} \hat{\theta}, \quad (14.2)$$

$$\hat{\mathbf{U}} = \sum_{i=0}^S \beta_i \mathbf{U}^{n-i} - \Delta t \sum_{i=0}^2 \alpha_i (\mathbf{N}(\mathbf{U}^{n-i}) - \mathbf{S}_U^{n-i}), \quad (14.3)$$

$$\left(-L + \frac{\gamma Re}{\Delta t} J\right) \hat{\mathbf{U}} = \frac{Re}{\Delta t} \hat{\mathbf{U}}, \quad (14.4)$$

$$-LP^{n+1} = -\frac{\gamma}{\Delta t} \mathbf{D} \cdot \hat{\mathbf{U}}, \quad (14.5)$$

$$\mathbf{U}^{n+1} = \hat{\mathbf{U}} - \frac{\Delta t}{\gamma} \mathbf{G}\mathbf{P}^{n+1}. \quad (14.6)$$

In the splitting scheme eq. (14.1) and (14.3) are pure advection evaluations, eq. (14.2) and (14.4) are implicit screened Poisson solves for diffusive terms and eq. (14.5) is a pressure Poisson equation to enforce incompressibility condition. Equation (14.6) corrects the intermediate velocity field incorporating the updated pressure. This splitting scheme reduces the cost of the temporal discretization to a combination of two explicit and three linear elliptic solve steps. Since the advection evaluations are explicitly treated in time, the maximum stable time step size is restricted by Courant-Fredrichs-Lewy (CFL) condition. Although stability of explicit schemes is restricted by a severe time step size, they are computationally inexpensive that conveys the computational load of each time step to elliptic solves. Because of that, effective linear solvers are crucial to obtain fast and scalable coupled flow and energy solvers.

Linear Solvers

Each time step of the temporal splitting discretization (14) requires solving two discrete Helmholtz equations, (14.2), (14.4) and a discrete Poisson problem (14.3). For high resolution solutions, i.e., large meshes and/or high degree N , assembling a full matrix and using a direct solver is not practically applicable. Thus, due to symmetric positive-definite structure of the IPDG discretization (10.1), we choose a preconditioned conjugate gradient (PCG) iterative method to solve the elliptic equations.

For the solution of Helmholtz equations (14.2) and (14.4), we choose the scaled inverse mass matrix on each element for the preconditioner. As the time step size is relatively small and coefficients $Re/\Delta t$ and $RePr/\Delta t$ are large, the Helmholtz operators are dominated by the mass matrix. Since the mass matrix is block diagonal and geometric factors are constant for triangular elements, inverting the mass matrix is computationally cheap and simple which makes the inverse matrix preconditioner very effective for the Helmholtz solves (Karakus et al., 2019b).

For the pressure Poisson problem, we consider a p-multigrid preconditioner (pMG) where we manually coarsen from degree N to degree 1 before setting up the algebraic multigrid (AMG) levels for the degree 1 coarse stiffness matrix. The coarse levels of this AMG method are constructed as unsmoothed aggregations of maximal independent node sets, see (Notay, 2006, 2010), while smoothing is chosen to be a degree 2 Chebyshev iteration (Adams et al., 2003). The multigrid preconditioning cycle itself consists of a K-cycle on the finest two levels, followed by a V-cycle for the remaining coarse levels (Gandham et al., 2014). With this manual coarsening approach, we are able to implement the finest levels of the multigrid cycle in a matrix-free way and avoid the storage of the full degree N stiffness matrix.

RESULTS

We have implemented the solver on the libParanumal (Chalmers et al., 2020) library using C++ together with the OCCA API and OKL kernel language (Medina et al., 2014) and MPI to enable using distributed multi-GPU/CPU platforms. OCCA is an abstracted programming model designed to encapsulate native languages for parallel devices such as CUDA, OpenCL, HIP, and OpenMP. For all the results presented in this section, we have compiled the source code using the GNU GCC 9.3.0 compiler and the Nvidia CUDA V11.0.221 NVCC compiler. The tests were run using Nvidia Tesla P100 GPUs on a machine equipped with an Intel Xeon E5-2680v4 processor.

We solved 2D thermal convection tests to verify the spatial accuracy of the presented algorithm on 2D unstructured triangular grids. To evaluate the accuracy of the numerical scheme, we use L_2 norm of error given as,

$$L_2 = \sum (\phi^e - \phi^{ex}, \phi^e - \phi^{ex})_{\mathcal{E} \in \Omega}, \quad (15)$$

where ϕ is the arbitrary field that error is computed and ϕ^{ex} denotes the exact solution or a very accurate approximation of the exact solution if it is not explicitly known.

Poiseuille Flow

In the first test case, we consider two-dimensional channel flow with a fully developed Poiseuille profile to show the spectral convergence rate of the solver. The channel having the dimension of $[0,2] \times [-1,1]$ is uniformly heated from the lower wall with $\theta_L = 1$ while isothermal upper plate is kept with $\theta_U = 0$. No-slip boundary conditions are imposed for upper and lower walls. The fully developed velocity field with linear

temperature profile is prescribed as the initial condition which reads

$$u = 1 - y^2, \quad v = 0,$$

$$p = \frac{Ra}{2PrRe^2} \left(y - \frac{y^2}{2} \right) - \frac{2x}{Re}, \quad \theta = \frac{1 - y}{2}.$$

Computations are performed on the successively refined meshes by uniformly dividing the initial coarse level grid. The initial mesh, defined with the characteristic scale h_0 , has the element number of $K = 68$ which is constructed by triangles with the edge length of $h = 0.4$ on the boundary of domain $\partial\Omega$. Then the sequence of meshes constructed with the element number of $K = 272$, $K = 1088$ and $K = 4352$ for $h = 0.5h_0$, $h = 0.25h_0$ and $h = 0.125h_0$, respectively. Approximating polynomial order is changed from $N = 1$ to $N = 5$ for all mesh configurations.

Figure 1 shows the computed L_2 norm of the numerical error in the x component of velocity, u and the temperature, θ fields for the flow conditions $Ra = 1000$, $Re = 100$ and $Pr = 0.71$ at the final time $T = 10$. The velocity and the temperature remain unchanged indicating no flow bifurcation in the flow field. The figure clearly demonstrates the expected spectral converge rates in the numerical error i.e. h^{N+1} accuracy for velocity and temperature.

Differentially Heated Square Cavity

We focus on the natural convection problem on a closed enclosure. The cavity width and height are denoted with $W = 1$ and $H = 1$ respectively leading $W:H$ aspect ratio, $A = 1$. The enclosure boundary conditions are simple and consist of no-slip walls, i.e. $u = v = 0$ on all four walls. The thermal boundary conditions on the left and right walls are prescribed as

$$\theta_L = 1, \quad \theta_R = 0$$

and the upper and the lower walls are thermally insulated

$$\frac{\partial \theta}{\partial y} = 0, \quad \text{for } y = 0, y = H.$$

We solved the problem for polynomial order, $N = 4$ on a relatively coarse grid composed of uniformly spaced triangular grids having characteristic length of $h = 0.1$ which leads element number of $K = 242$. The flow conditions are $Pr = 0.71$, $Ra = 10^3, 10^4, 10^5$. Reference velocity is selected as $U_r = \sqrt{h\beta(\theta_L - \theta_R)W}$ so that $Re = \sqrt{Gr}$.

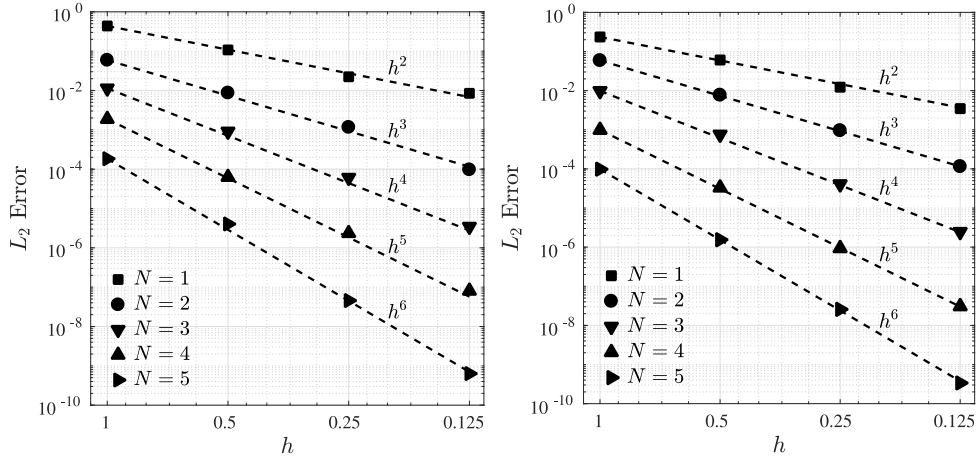


Figure 1. Spatial accuracy test for the Poiseuille test problem using L_2 relative errors on successively refined triangular elements. The error in the x -velocity is shown on the left and the error in the temperature is shown right

Table 1. Maximum and minimum velocities along the center lines of square cavity for $Pr = 0.71$ and $Ra = 10^3, 10^4, 10^5$

	$Ra = 10^3$		$Ra = 10^4$		$Ra = 10^5$	
	u_{max}	v_{max}	u_{max}	v_{max}	u_{max}	v_{max}
Present	0.137	0.139	0.192	0.233	0.129	0.257
Stokos et al. (2015)	0.137	0.139	0.192	0.233	0.130	0.256
De Vahl Davis (1983)	0.136	0.138	0.192	0.234	0.153	0.261

In Table 1, we presented the computed maximum and minimum velocities along the horizontal $y = 0.5$ and the vertical $x = 0.5$ lines. u_{max} stands for the maximum value of x -velocity, u along the vertical line while v_{max} denotes maximum y -velocity, v along the horizontal line. For all simulations, our results compare well with the reported values in the relevant literature (De Vahl Davis, 1983; Stokos et al., 2015). Figure 2 and Figure 3 illustrate temperature contours and velocity profiles on center lines for different Ra numbers. The temperature contours and velocity fields depicted by center lines profiles provide qualitative agreement with those reported in the literature (Stokos et al., 2015; Hossain et al., 2021).

Mixed Convection

The square cylinder test is considered with various channel confinement degrees and aiding ($Ri > 0$) and opposing ($Ri < 0$) buoyancy strengths or without the effect of thermal buoyancy $Ri = 0$. The computational domain is composed of a square cylinder of length, B located at the center of the domain and a vertically aligned channel of width L . The channel blockage ratio $BR = B/L$ defines the degree of channel confinement when imposing no-slip conditions on the left and right sides of the channel. We consider uniform inflow velocity on the lower side and zero Neumann conditions are used on the upper boundary for velocity.

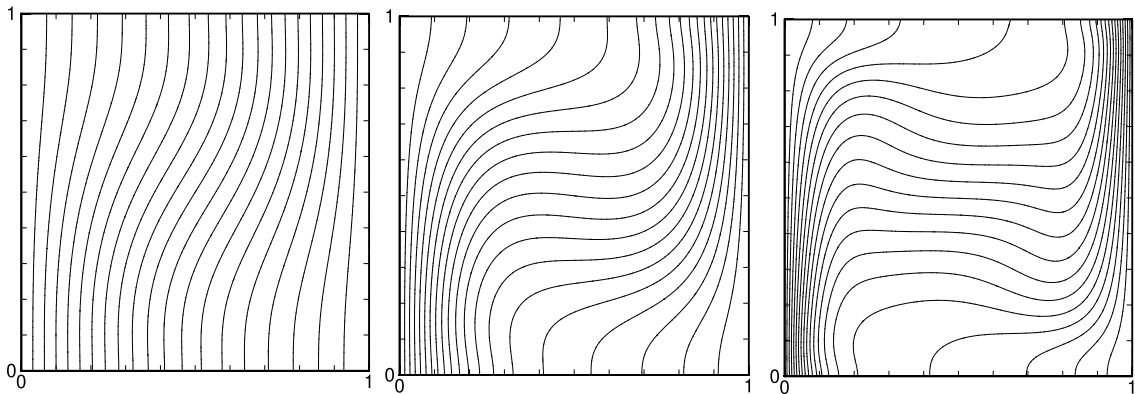


Figure 2. Temperature contours for the square cavity test. The temperature contours drawn between 1 and 0 with the increment of 0.05 for $Ra = 10^3, 10^4, 10^5$ from left to right

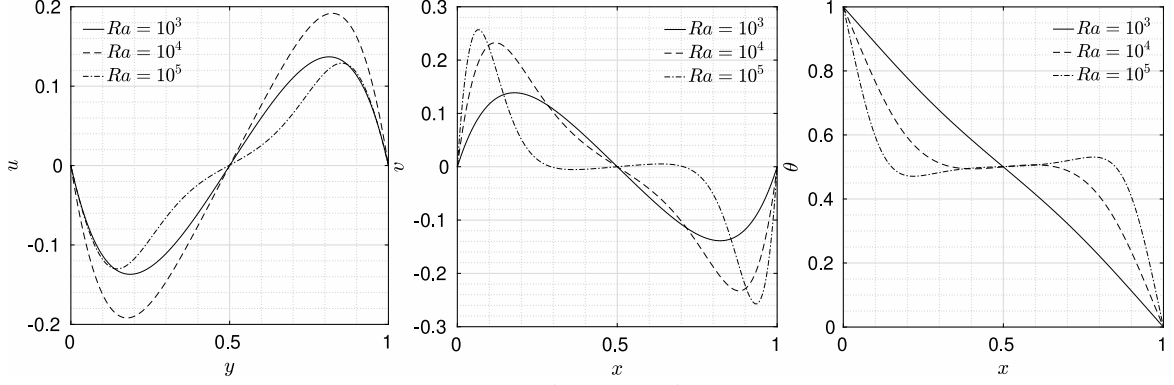


Figure 3. Velocity and temperature profiles along the $y = 0.5$ and $x = 0.5$ lines for the square cavity test

The square cylinder is kept at a fixed temperature of $\theta = 1$ and homogeneous temperature is applied on the channel side walls and the inlet. In this test, we consider following geometric and flow parameters: blockage ratios, $BR = 0\%, 10\%, 30\%, 50\%$, and Richardson number, $Ri = -1.0, -0.5, 0.0$ for the fixed Reynolds number $Re = 100$ and Prandtl number $Pr = 0.71$.

Table 2. Comparison of Strouhal number for flow past a square cylinder test at $Re = 100$ for $BR = 2.3\%$ and $Ri = 0$

	N	St
Present	3	0.144
	5	0.145
Ferrer and Willden (2011)	5	0.144
Darekar and Sherwin (2001)	6	0.145
Shahbazi et al. (2007)	4	0.145

As a preliminary test, we solved the problem without buoyancy forcing, $Ri = 0$ to validate the solver in a complex flow. The flow condition $R = 100$ leads an unsteady Von Karman vortex street with a characteristic vortex shedding frequency which can be represented as a non-dimensional Strouhal number, $St = fB/U_r$, where f , B , and U_r are the non-dimensional vortex shedding frequency, characteristic length as cylinder dimension and the uniform free stream velocity, respectively. We use the same domain and boundary conditions with Darekar and Sherwin (2001); Ferrer and Willden (2011); Shahbazi et al. (2007), with blockage ratio, $BR = 2.3\%$. In order to make direct comparisons between the reference studies, we created identical mesh configuration and used the same non-dimensional time step size which lead to 896 triangular elements and $\Delta t = 0.002$. In Table 2, we report computed St numbers for the approximating polynomial orders, $N = 3$ and $N = 5$. In both cases, we observe that present solver provides good agreement with the reference, high-order numerical results.

Figure 4 shows instantaneous vorticity contours around the square cylinder for $BR = 30\%$ and $Ri = -1.0, -0.5, 0.5$. The free and forced convection effects are comparable under these flow settings which makes the vortex shedding phenomena more complicated. In the figure, the vorticity contours show a wavering motion which increases with increased cooling (decreasing $Ri < 0$) of the cylinder and decreases with increased heating (increasing $Ri > 0$) before it ceases at critical Ri for the given specific blockage ratio. In this work, we only focus on the solver performance in reflecting the flow physics and skip to determine critical $Ri > 0$ numbers that Von Karman vortex street breakdowns.

Table 3. Strouhal numbers for different Ri numbers and blockage ratios at $Re = 100$

BR	Ri		
	-1.0	-0.5	0
10%	0.127	0.137	0.176
30%	0.303	0.312	0.322
50%	0.498	0.508	0.527

In Table 3, Strouhal numbers are listed for different opposing Ri numbers and channel blockage ratios for $N = 5$. A fast Fourier transform of the lift coefficient's time history is used to determine the Strouhal number accurately. For the opposing buoyancy cases, the table shows that the Strouhal number increases monotonically with increasing Ri at a constant blockage ratio before Ri number reaches the critical value where the breakdown of the Karman vortex street is observed. It is also shown that the Strouhal number increases monotonically with increasing blockage ratio due to the acceleration of the cylinder-wall boundary layer.

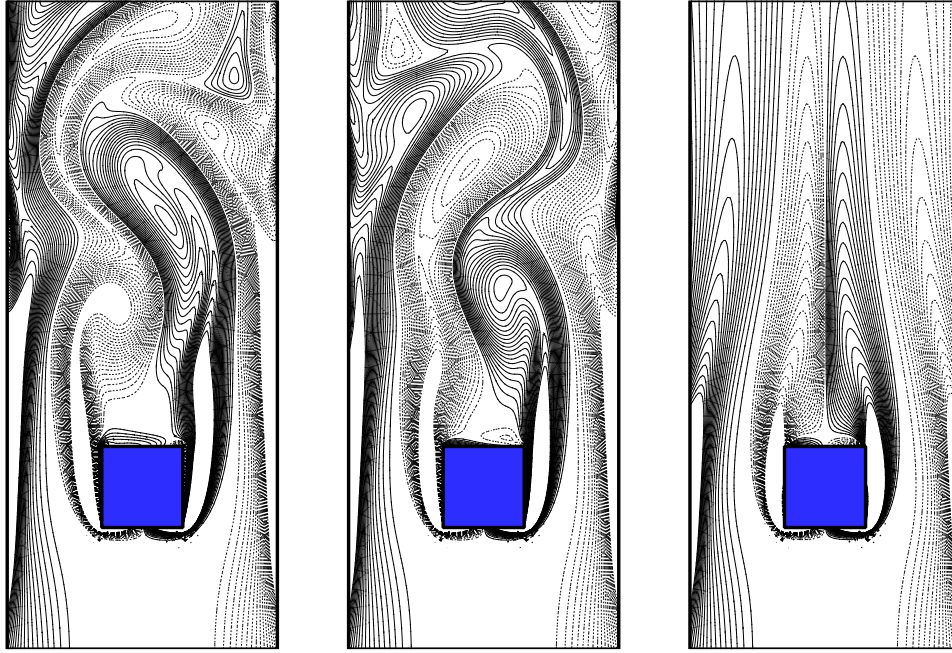


Figure 4. Instantaneous vorticity contours at $t = 100$ for different Ri and the influence of aiding and opposing buoyancy at a blockage ratio of 30% and $Re = 100$. The solid and dashed lines represent positive and negative vorticity contours, respectively. (Only a part of the domain is shown)

CONCLUSION

We have presented a GPU-accelerated, high-order, nodal discontinuous Galerkin approach for the solution of incompressible thermal convection problems on unstructured meshes. The incompressible Navier–Stokes and the energy equation written in terms of temperature are coupled through a Boussinesq type thermal body-forcing term. The equations system is discretized in time using an algebraic splitting scheme where advection terms are evaluated explicitly while diffusive terms together with Poisson equation to impose incompressibility are treated implicitly. This further decouples velocity field from pressure. We showed that the scheme achieves designed order of accuracy and preserves stability for thermal convection problems.

The presented solver is implemented on the open source project libParanumal (LIBrary of PARAllel NUMerical ALgorithms) (Chalmers et al., 2020). libParanumal consists of a collection of mini-apps with high-performance portable implementations of high-order finite element discretizations for a range of different fluid flow models (Karakus et al., 2019a,b).

Extending the scheme to 3D using tetrahedral elements and assessing its performance on multi-GPU systems for triangular/tetrahedral elements remain to be investigated.

ACKNOWLEDGEMENTS

The author thanks to Dr. Noel Chalmers and Prof. Tim Warburton for their helpful discussions and valuable comments.

REFERENCES

- Adams, M., Brezina, M., Hu, J., and Tuminaro, R., 2003, Parallel multigrid smoothing: polynomial versus Gauss–Seidel, *Journal of Computational Physics*, 188(2), 593–610.
- Arnold, D., 1982, An interior penalty finite element method with discontinuous elements. *SIAM Journal on Numerical Analysis*, 19(4), 742–760.
- Chalmers, N., Karakus, A., Austin, A. P., Swirydowicz, K., and Warburton, T., 2020, libParanumal: a performance portable high-order finite element library. *Release 0.4.0*.
- Chan, J., Wang, Z., Modave, A., Remacle, J. F., and Warburton, T., 2016, GPU-accelerated discontinuous Galerkin methods on hybrid meshes, *Journal of Computational Physics*, 318, 142–168.
- Darekar, R. M. and Sherwin, S. J., 2001, Flow past a square-section cylinder with a wavy stagnation face, *Journal of Fluid Mechanics*, 426, 263–295.
- De Vahl Davis, G., 1983, Natural convection of air in a square cavity: A bench mark numerical solution, *International Journal for Numerical Methods in Fluids*, 3(3), 249–264.
- Ferrer, E. and Willden, R. H. J., 2011, A high order discontinuous Galerkin finite element solver for the

- incompressible Navier–Stokes equations, *Computers & Fluids*, 46(1), 224–230.
- Gandham, R., Esler, K., and Zhang, Y., 2014, A GPU accelerated aggregation algebraic multigrid method, *Computers & Mathematics with Applications*, 68(10), 1151–1160.
- Gandham, R., Medina, D., and Warburton, T., 2015, GPU accelerated discontinuous Galerkin methods for shallow water equations, *Communications in Computational Physics*, 18(1), 37–64.
- Hesthaven, J. S. and Warburton, T., 2008, Nodal discontinuous Galerkin methods: algorithms, analysis, and applications, Springer.
- Hossain, M. Z., Cantwell, C. D., and Sherwin, S. J., 2021, A spectral/hp element method for thermal convection, *International Journal for Numerical Methods in Fluids*, 93(7), 2380–2395.
- Karakus, A., Chalmers, N., Hesthaven, J. S., and Warburton, T., 2019a, Discontinuous Galerkin discretizations of the Boltzmann–BGK equations for nearly incompressible flows: Semi-analytic time stepping and absorbing boundary layers, *Journal of Computational Physics*, 390, 175–202.
- Karakus, A., Chalmers, N., Swirydowicz, K., and Warburton, T., 2019b, A GPU accelerated discontinuous Galerkin incompressible flow solver, *Journal of Computational Physics*, 390, 380–404.
- Karakus, A., Warburton, T., Aksel, M. H., and Sert, C., 2016a, A GPU-accelerated adaptive discontinuous Galerkin method for level set equation, *International Journal of Computational Fluid Dynamics*, 30(1), 56–68.
- Karakus, A., Warburton, T., Aksel, M. H., and Sert, C., 2016b, A GPU accelerated level set reinitialization for an adaptive discontinuous Galerkin method, *Computers & Mathematics with Applications*, 72(3), 755–767.
- Kumar, A. and Pothérat, A., 2020, Mixed baroclinic convection in a cavity, *Journal of Fluid Mechanics*, 88. Publisher: Cambridge University Press.
- Medina, D. S., St-Cyr, A., and Warburton, T., 2014, OCCA: A unified approach to multi-threading languages. *arXiv:1403.0968*.
- Modave, A., St-Cyr, A., and Warburton, T., 2016, GPU performance analysis of a nodal discontinuous Galerkin method for acoustic and elastic models, *Computers & Geosciences*, 91, 64–76.
- Notay, Y., 2006, Aggregation-based algebraic multilevel preconditioning, *SIAM journal on matrix analysis and applications*, 27(4), 998–1018.
- Notay, Y., 2010, An aggregation-based algebraic multigrid method, *Electronic transactions on numerical analysis*, 37(6), 123–146.
- Roca, X., Nguyen, N. C., and Peraire, J., 2011, GPU-accelerated sparse matrix-vector product for a hybridizable discontinuous Galerkin method. *In Aerospace Sciences Meetings. American Institute of Aeronautics and Astronautics*, AIAA 2011–687.
- Saha, S., Klewicki, J. C., Ooi, A. S. H., and Blackburn, H. M., 2015, Comparison of thermal scaling properties between turbulent pipe and channel flows via DNS, *International Journal of Thermal Sciences*, 89, 43–57.
- Shahbazi, K., 2005, An explicit expression for the penalty parameter of the interior penalty method, *Journal of Computational Physics*, 205(2), 401–407.
- Shahbazi, K., Fischer, P. F., and Ethier, C. R., 2007, A high-order discontinuous Galerkin method for the unsteady incompressible Navier-Stokes equations, *Journal of Computational Physics*, 222(1), 391–407.
- Stokos, K., Vrahliotis, S., Pappou, T., and Tsangaris, S., 2015, Development and validation of an incompressible Navier-Stokes solver including convective heat transfer, *International Journal of Numerical Methods for Heat & Fluid Flow*, 25(4), 861–886.
- Warburton, T., 2006, An explicit construction of interpolation nodes on the simplex, *Journal of Engineering Mathematics*, 56(3), 247–262.
- Wheeler, M. F., 1978, An elliptic collocation-finite element method with interior penalties, *SIAM Journal on Numerical Analysis*, 15(1), 152–161.
- Swirydowicz, K., Chalmers, N., Karakus, A., and Warburton, T., 2019, Acceleration of tensor-product operations for high-order finite element methods, *The International Journal of High Performance Computing Applications*, 33(4).



EXERGY ANALYSIS OF GRAPHENE-BASED NANOFLUIDS IN A COMPACT HEAT EXCHANGER

Ferhat KILINÇ* and Cihan Zeki UYGUN**

Sivas Cumhuriyet University, Faculty of Engineering, Department of Mechanical Engineering
58140, Sivas, TURKEY

*fkilinc@cumhuriyet.edu.tr, ORCID: 0000-0003-2707-6438

**cihanzekiuygun@gmail.com, ORCID: 0000-0002-1319-1948

(Geliş Tarihi: 21.06.2021, Kabul Tarihi: 04.04. 2022)

Abstract: In this study, the exergy analysis of graphene-based nanofluids in a compact heat exchanger is examined. In experiments using distilled water as the base fluid, graphene nano-ribbon and graphene oxide nanofluids were used at 0.01% and 0.02% of the volume concentrations. The experiments were carried out at 36, 40, and 44 °C fluid inlet temperatures and 0.6, 0.7, 0.8, and 0.9 m³/h mass flow rates. As a result of the calculations made for all temperature and flow rates, it was found that the exergy efficiency values of 0.01% by volume GO nanofluid were higher than the exergy efficiency of the other nanofluids used. Also, the exergy destruction values calculated for %0.01 GO were lower than the value of exergy destruction calculated for other nanofluids. It was concluded that the exergy efficiencies of nanofluids increased with the increase of the fluid flow rates and the inlet temperature of the heat exchanger. When the exergy efficiencies were compared according to the nanofluid concentrations, it was found that the exergy efficiencies decreased with the increase of the fluid concentration. It was examined that the exergy destruction values also increases with the increase of nanofluid flow rates, as well as exergy efficiency. When the exergy destructions were compared to the nanofluid concentrations, it was concluded that the exergy destructions increased with the increase of the nanofluid concentration. It was determined that the amount of increase in exergy destruction of GO nanofluid was higher than that of GNR.

Keywords: Exergy, Second law analysis, Nanofluid, Heat exchanger, Improving heat transfer, Graphene.

KOMPAKT BİR ISI DEĞİŞTİRİCİSİNDE GRAFEN BAZLI NANO AKIŞKANLARIN EKSERJİ ANALİZİ

Özet: Bu çalışmada, kompakt bir ısı değiştiricide grafen bazlı nanoakışkanların ekserji analizi incelenmiştir. Taban akışkan olarak saf su kullanılarak yapılan deneylerde, hacim konsantrasyonlarının %0.01 ve %0.02'inde grafen nano-ribbon ve grafen oksit nanoakışkanlar kullanılmıştır. Deneyler 36, 40 ve 44 °C akışkan giriş sıcaklıklarında, 0.6, 0.7, 0.8 ve 0.9 m³/h kütleli debilerde gerçekleştirilmiştir. Tüm sıcaklık ve debi değerleri için yapılan hesaplamalar sonucunda hacimce %0.01 GO nanoakışkanının ekserji verimi değerlerinin kullanılan diğer nanoakışkanların ekserji verimlerinden daha yüksek olduğu bulunmuştur. Ayrıca %0.01 GO için hesaplanan ekserji yıkım değerleri, diğer nanoakışkanlar için hesaplanan ekserji yıkım değerinden daha düşüktür. Nanoakışkanların ekserji verimlerinin, akışkan debilerinin ve ısı değiştiricinin giriş sıcaklığının artmasıyla arttığı sonucuna varılmıştır. Nanoakışkan konsantrasyonlarına göre ekserji verimleri karşılaştırıldığında, akışkan konsantrasyonunun artmasıyla ekserji verimlerinin azaldığı sonucu bulunmuştur. Nanoakışkan akış hızlarının artması ve ekserji veriminin artmasıyla ekserji yıkım değerlerinin de arttığı sonucu elde edilmiştir. Nanoakışkan konsantrasyonları ile ekserji yıkımları karşılaştırıldığında, nanoakışkan konsantrasyonunun artmasıyla ekserji yıkımlarının arttığı sonucuna varılmıştır. GO nanoakışkanın ekserji yıkımındaki artış miktarının GNR'den daha fazla olduğu belirlenmiştir.

Anahtar Kelimeler: Ekserji, İkinci yasa analizi, Nanoakışkan, Isı değiştiricisi, Isı transferi iyileştirilmesi, Grafen.

NOMENCLATURE

T	Temperature
Ex	Exergy
S	Entropy
h	Enthalpy
η	Second law efficiency
ϕ	Volume fraction

INTRODUCTION

More effective and efficient use of energy is considered as an alternative energy source. In this context, heat exchangers used in all areas of the industry have created remarkable literature in terms of the energy economy in the studies aimed at improving heat transfer. Heat exchangers are the most important components of heating and cooling systems. Many researchers have

done a lot of research to improve heat exchangers' design and operation. Any changes that are made in its design and operation affect the entire system. In this context, the radiators used in vehicle cooling systems are a type of compact heat exchanger and are the main component of the cooling system. In many industrial areas, the studies such as energy efficiency, minimizing energy consumption, optimizing the parts planned to be produced are carried out. While saving energy with these studies, the required performance criteria should also be met. Due to the low thermal properties of conventional fluids, nanofluids have been used in many systems in recent years. Nanofluids with different types, concentrations, and thermal properties have been used numerically and experimentally in many studies in the literature. In almost all of these studies, it was obtained that the use of metallic nanofluids increased the heat transfer (Pantzali *et al.*, 2009; Vajjha *et al.*, 2010; Fard *et al.*, 2011; Peyghambarzadeh *et al.*, 2011; Hung *et al.*, 2012; Pandey *et al.*, 2012; Javadi *et al.*, 2013; Khairul *et al.*, 2014). Also, the effects of several parameters were examined including nanoparticle size, shape, material composition, and acidity (Lomascolo *et al.*, 2015). Graphene particle-based nanofluids have been better properties such as high thermal conductivity, low density, low corrosion, low pumping power, and more stability compared to metallic particle-based nanofluids (Baby and Ramaprabhu, 2011; Sadeghinezhad *et al.*, 2016). In different studies using graphene-based nanofluids reported that thermal conductivity significantly increased up to 86% for 5.0 vol. % graphene dispersion (Yu *et al.*, 2011) and exhibited 47.5% thermal conductivity enhancement at 0.25 wt.% concentration (Hajjar *et al.*, 2014).

Many studies have been investigated the use of nanofluids in different types of heat exchangers. Vajjha *et al.* (2010) numerically investigated heat transfer enhancement of two different nanofluids (Al_2O_3 and CuO) in a flat tube car radiator. The average heat transfer coefficient increased by 94% for the 10% Al_2O_3 and 89% for 6% CuO nanofluids at the Reynolds number of 2000. Hung *et al.* (2012), experimentally investigated the suitability of the alumina nanofluid (Al_2O_3 /water) for heat dissipation in the air-cooled heat exchanger. They reported that the highest heat transfer increase was 40% at the highest mass fraction (1.5%). Kılınç *et al.* (2020), experimentally investigated the cooling performance of a vehicle radiator by using graphene-based nano-fluids. They reported that the average enhancement of the overall heat transfer coefficient was 26.08% for 0.02 vol.% of GO and 20.64% for 0.02 vol.% concentrations of GNR/water nano-fluids. Karabulut *et al.* (2020), numerically and experimentally investigated the convection heat transfer coefficient of a graphene-based nanofluid along a circular copper tube under a turbulent flow regime. They reported that the heat transfer coefficient increment is about 48% for 350 W, heat flux at 0.02 vol.% concentration. The exergy analysis tells us how much is the usable work potential of the system or process. Also, exergy is key to the understanding of the

thermodynamic behavior of energy systems. In recent most, studies were examined to exergy analysis of heat exchangers. Pandey and Nema (2012), were experimentally investigated the heat transfer, frictional losses, and exergy loss in a counter flow corrugated plate heat exchanger by using nanofluids. Esfahani and Languri (2017), were studied the benefits of using graphene oxide nanofluids, regarding their thermal performances in a shell-and-tube heat exchanger. The study was concluded that the increase in the concentration of graphene oxide particles resulted in higher viscosity and aggregate size in nanofluids at room temperature. There are more examples to analyze energy and exergy using nanofluids on various heat exchangers (Khaleduzzaman *et al.*, 2014; Sun *et al.*, 2016; İpek *et al.*, 2017; Singh and Sarkar, 2018; Wang *et al.*, 2018; Bahiraei *et al.*, 2018).

It is generally accepted that two types of losses occur in a heat exchanger: losses due to temperature difference and losses due to frictional losses caused by pressure drop. Both losses can be quantified at once with total entropy generation and to achieve an ideal heat exchanger design, the total entropy generation must be minimized. The second law of thermodynamics is a modern approach for the optimization of a thermal system and the entropy generation is used as the parameter for evaluating the efficiency of the system (Ahammed *et al.*, 2016).

Exergy analysis; is a useful analysis method in order to use the energy and resources efficiently, since it accurately determines the size, shape and location of energy losses. It is also a technique that uses the principles of conservation of mass and energy, together with the second law of thermodynamics, for the analysis, design, and development of energy and other systems (Dinçer and Rosen, 2012). An energy system's efficiency can be improved by using exergy analysis as a tool for design, evaluation, improvement, and optimization. It helps us to understand how thermodynamics phenomena affect effective processes, to compare the importance of different factors, and to determine how to improve the process most effectively (Maddah *et al.*, 2017). The first and second laws of thermodynamics are used to analyze a system's thermal properties. The combined use of both laws is necessary to obtain information about the performance and optimization of the system. To have a good understanding of a heat exchanger's thermal performance, exergy analysis or second law analysis is crucial (Esfahani and Languri, 2017). The analysis of exergy provides insight into the irreversibilities of the system and allows a comprehensive assessment of all the critical aspects of energy use (Rosen, 2002).

The graphene structure, an allotrope of carbon, is two-dimensional on one plane and has an atomic thickness (Singh *et al.*, 2012). Due to its remarkable mechanical, thermal, and electrical properties, graphene attracts the attention of many researchers (Novoselov *et al.*, 2005).

In addition, the hydrophilic nature of graphene makes it superior in terms of many disadvantages seen in metal-based nanofluids. The literature confirms that nanofluids improved heat transfer properties. However, the effects of these improvements in terms of radiator design and exergy analysis have not been evaluated sufficiently. Additionally, a very limited number of studies have been published on graphene-based nanofluids and their performance characteristics in a vehicle radiator (compact heat exchanger).

As a result, different studies have been carried out in the literature that nanofluids improve heat transfer. Although there are studies involving nanofluids and exergy analysis in heat exchangers, most of them are conducted with metal-based nanofluids. The use of graphene-based nanofluids in heat exchangers is less common and is much more limited in terms of exergy analysis. With this study, it is aimed to increase the number of experimental studies on graphene-based nanofluids (known as graphene oxide and graphene nanoribbons) applications in compact heat exchanger systems and to close the consistency and comparability gaps in the literature and based on the authors' knowledge, there is no such research in the corresponding literature. Also with the exergy analysis, it is aimed to reveal what needs to be improved, as well as see the irreversible effects of nanofluids on the system.

MATERIAL AND METHOD

Experimental Setup

The actual photo and schematic diagram of the experimental setup are shown below (Fig. 1) used in this study which includes a reservoir tank, a heater, a



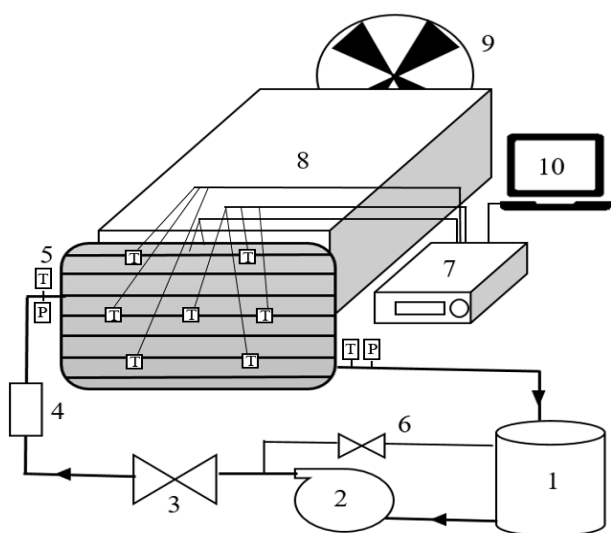
Figure 1. Actual and schematic view of the experimental system (1-storage tank 2-circulation pump 3-ball valve 4-flow meter 5-compact heat exchanger 6-recycle line 7-data logger 8-air flow channel 9-fan 10-computer)

Calculation Method

The schematic view of the compact heat exchanger used in this study is shown in Figure 2, where the red and blue

centrifugal pump, flow lines, a flow meter, an adjustable forced fan, an airflow channel, thermocouples for temperature measurement, a datalogger and a compact heat exchanger (vehicle radiator). Distilled water and nanofluid are used as internal fluid and air is used as external fluid at the heat exchanger. Inlet and outlet temperatures of the distilled water, nanofluids, and air were measured by using J and K-type thermocouples. The nanofluids are heated by a controllable electrical resistance.

The nanofluids are pumped into the tubes of the compact heat exchanger at various rates (0.6-0.9 m³/h) using variable frequency drive equipment. The compact heat exchanger which is used in experiments has a stadium-shaped cross-section and consists of 36 horizontal tubes. The fins and tubes are made from aluminum. The system is cooled by air using a fan. The airflow channel and the fan are placed in a rectangular duct and directed to the radiator. An electric heater (2500 W) is used to heat the heating tank made of stainless steel. The circulation pump is equipped with a frequency converter, which allows it to function from 0 to + 110°C, and has a maximum pumping capacity of 2.7 m³h⁻¹. A flow meter that is capable of withstanding 80°C temperature, with the precision of 0.01 L/min (with ±2% accuracy) is used to measure flow rates. Two K-type and two J-type thermocouples are used to record the inlet and outlet temperatures of the cooling air and fluids, respectively, using a datalogger. Additionally, 7 J-type thermocouples are used to record the surface temperatures of the compact heat exchanger. Nanofluids were synthesized at the Nanotechnology Research Center of Sivas Cumhuriyet University. Nanofluids were prepared by using graphene as a nanoparticle and distilled water as a base fluid.



lines show hot and cold fluids, respectively (Çalışkan and Hepbaşlı, 2013).

The calculations are based on the assumption of one-dimensional, steady-state heat conduction at the base of the aluminum channels and is expressed as follows: fluids and air are assumed to have constant properties, heat rejected by fluids will be fully absorbed by air and

all processes are assumed to be steady-state. Also, based on the assumption that nanoparticles are dispersed within the base fluid.

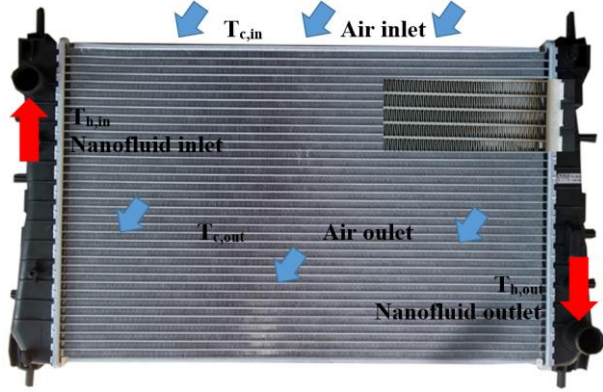


Figure 2. Diagram and detailed tube/fin view of the compact heat exchanger used in the present study

The exergy balance of the heat exchanger is written as follows.

$$(\dot{E}x_{h,in} + \dot{E}x_{c,in}) - (\dot{E}x_{h,out} + \dot{E}x_{c,out}) = \dot{E}x_{dest} \quad (1)$$

where “ $\dot{E}x_{h,in}$ ” ve “ $\dot{E}x_{h,out}$ ” are the exergy input and output for the hot fluids and “ $\dot{E}x_{c,in}$ ” ve “ $\dot{E}x_{c,out}$ ” are the exergy input and output for the cold fluids. “ $\dot{E}x_{dest}$ ” is the exergy destruction.

Exergy flow of the fluid “ $\dot{E}x_f$ ” is written as follows:

$$\dot{E}x_f = \dot{m}_f [(h_f - h_o) - T_0 (s_f - s_o)] = \dot{m}_f C_{p,f} [(T_f - T_0) - T_0 \ln \left(\frac{T_f}{T_0} \right)] \quad (2)$$

where “ \dot{m}_f ” is the mass flow of fluid, “ T_f ” is the fluid temperature, “ $C_{p,f}$ ” is the specific heat capacity of fluid, “ h_f ” is the enthalpy of fluid at fluid temperature, “ s_f ” is the entropy of fluid at fluid temperature, “ T_0 ” is the dead state temperature, “ h_o ” is the enthalpy of fluid at dead state temperature, “ s_o ” is the entropy of fluid at dead state temperature. The above equation is more clearly expressed as follows.

$$\dot{E}x_{h,in} = \dot{m}_{h,in} C_{p,h} [(T_{h,in} - T_0) - T_0 \ln \left(\frac{T_{h,in}}{T_0} \right)] \quad (3)$$

$$\dot{E}x_{h,out} = \dot{m}_{h,out} C_{p,h} [(T_{h,out} - T_0) - T_0 \ln \left(\frac{T_{h,out}}{T_0} \right)] \quad (4)$$

$$\dot{E}x_{c,in} = \dot{m}_{c,in} C_{p,c} [(T_{c,in} - T_0) - T_0 \ln \left(\frac{T_{c,in}}{T_0} \right)] \quad (5)$$

$$\dot{E}x_{c,out} = \dot{m}_{c,out} C_{p,c} [(T_{c,out} - T_0) - T_0 \ln \left(\frac{T_{c,out}}{T_0} \right)] \quad (6)$$

where “in”, “out”, “c”, ve “h” subscripts are meant that input, output, cold and hot, respectively.

The exergy destruction current “ $\dot{E}x_{dest}$ ” of the heat exchanger can be found as follows:

$$\dot{E}x_{dest} = \dot{S}_{gen} T_0 \quad (7)$$

Where “ \dot{S}_{gen} ” is the entropy generation.

There are different ways to calculate exergy efficiency in the literature. According to Hepbaşlı (2008), the most commonly used equation is as follows:

$$\eta_{II} = [(\dot{E}x_{h,out} + \dot{E}x_{c,out}) / (\dot{E}x_{h,in} + \dot{E}x_{c,in})] * 100 \quad (8)$$

where “ η_{II} ” refers to the second law efficiency.

The correlations of nanofluids to be used for exergy analysis can be calculated as follows:

$$c_{nf} = \varphi c_p + (1 - \varphi) c_{bf} \quad (9)$$

where c_p is the specific heat of nanofluids, ρ is the density of nanofluids, and φ is the volume fraction of nanoparticles. Also, nf, p, and bf refer to nanofluid, particle, and base fluid, respectively (Pak and Cho, 1998).

The density of the nanofluids can be calculated as follows (Khanafar and Vafai, 2011):

$$\rho_{nf} = (1 - \varphi_p) \rho_{bf} + \varphi_p \rho_p \quad (10)$$

Also, $\varphi_p = V_p / (V_p + V_{bf})$ is the volumetric concentration of nanoparticles.

Uncertainty analysis

Uncertainty analysis is important in terms of the precision of the measured results and the accuracy of the results obtained. To obtain the uncertainty values the following equation was used (Holman, 2001);

$$w_R = \left[\left(\frac{\partial R}{\partial x_1} w_1 \right)^2 + \left(\frac{\partial R}{\partial x_2} w_2 \right)^2 + \dots + \left(\frac{\partial R}{\partial x_n} w_n \right)^2 \right]^{1/2} \quad (11)$$

where R is a function of independent variables ($x_{1,2,n}$) and resulting from the experimental study. $w_{R,1,2,n}$ can be taken as the uncertainties in the independent variables. According to the uncertainty analysis, the values estimated as $\pm 2.65\%$ for flow rate, $\pm 0.5\%$ for temperature, $\pm 0.65\%$ for circulating pump power input and $\pm 1.25\%$ for heating tank power input.

RESULTS AND DISCUSSION

In the calculations of this study, the data from a previous experimental study were used (Kılınc, 2015). In the experiments, five different fluids as water, graphene oxide (0.01 and 0.02 vol.%) and graphene nanoribbon (0.01 and 0.02 vol.%), three different inlet temperatures (36, 40, and 44 °C), and four different mass flow rates for each temperature (0.6, 0.7, 0.8 and 0.9 m³/h) were used.

Besides, ambient air was used to cool as the fluid passed through the radiator, and it was sent to the radiator with the help of a fan, at a constant flow rate of 0.45 m³/h. The inlet/outlet temperatures of the water and nanofluids, the surface temperature of the radiator, and the outlet temperature of the air passing through the radiator were measured in the experiments. During the experiments, changes in the ambient air are affected by the calculations. The sudden jumps and decreases in different flow transitions are directly proportional to the ambient temperature which is measured and used in the calculations in the graphics below. Since the dataset obtained as a result of calculations are close to each other, exergy efficiencies and exergy destructions have been calculated as two significant steps after the comma (Uygun, 2019).

In Figures 3 and 4, the heat transfer coefficients for water-based nanofluid containing graphene nanoparticles at different concentrations and different inlet temperatures are compared with pure water. The heat transfer coefficients of both GO and GNR nanofluids increased with increasing flow rate, inlet temperature and particle volume concentration. Numerous studies have emphasized the importance of this situation in terms of energy analysis (1st law efficiency) and it provides the basis for the second law efficiency (Vajjha *et al.*, 2010; Peyghambarzadeh *et al.*, 2011; Kılınç *et al.*, 2020).

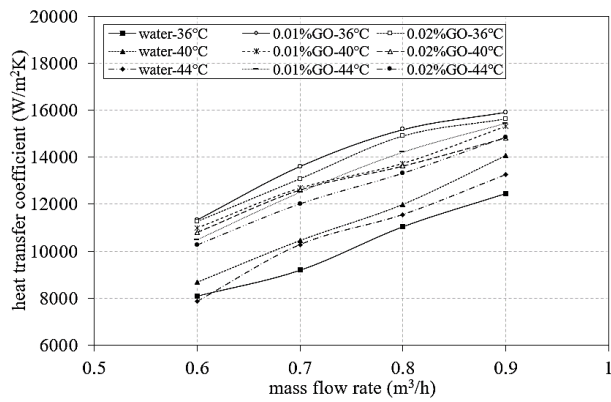


Figure 3. Comparison of heat transfer coefficients for water/GO nanofluids

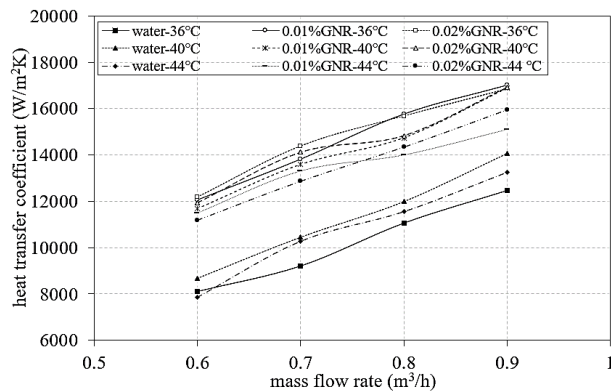


Figure 4. Comparison of heat transfer coefficients for water/GNR nanofluids

Exergy efficiency calculated for different temperatures (36°C, 40°C, and 44°C) from the data obtained after the experiments is given comparatively in Figure 5. As a result of the calculations made for a temperature of 44°C and a flow rate of 0.9 m³/h, the exergy efficiency for water was found to be 95.18%, while the exergy efficiency value for 0.01% GO was 94.93%. At the same temperature and flow rate values, the exergy efficiency was calculated as 92.40% for 0.01% GNR, 91.25% for 0.02% GNR, and 90.10% for 0.02% GO.

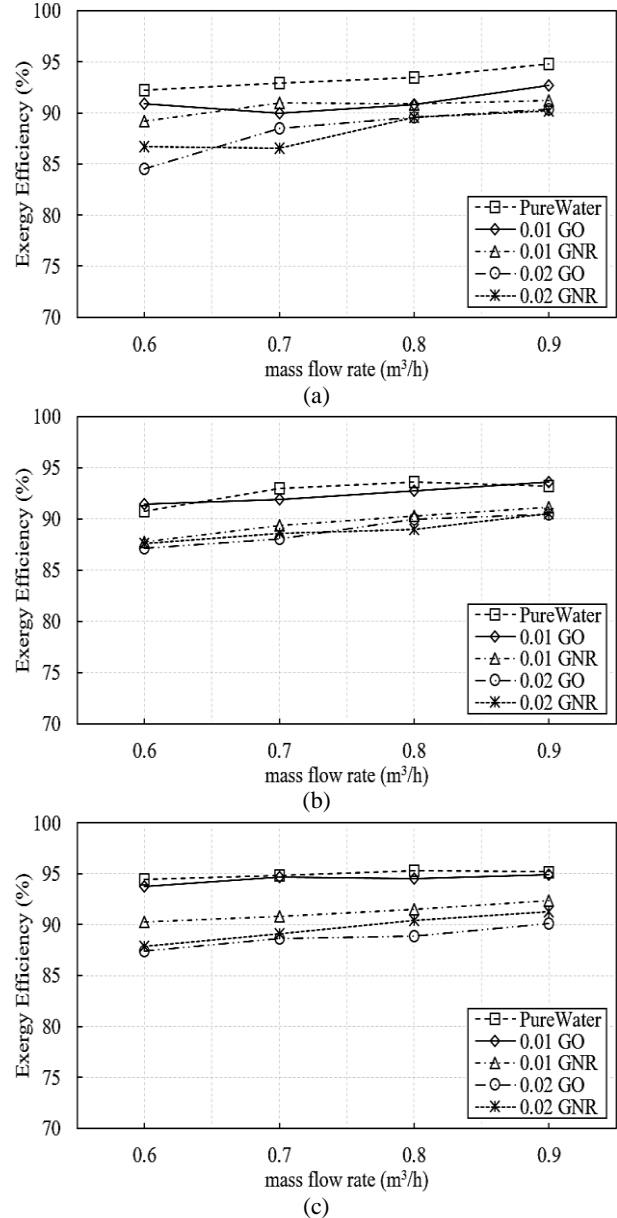


Figure 5. Comparison of exergy efficiencies for all nanofluids at a) 36 °C b) 40 °C c) 44 °C

According to Figure 5(a), it has been obtained that the water exergy efficiency is higher in all flow rates compared to other nanofluids and the highest exergy value has been calculated as 94.79% (Khaleduzzaman *et al.*, 2014). The value of exergy efficiency closest to water was calculated for 0.01% GO and 92.79% for 0.9 m³/h fluid flow. The lowest exergy efficiency was calculated as 84.57% for 0.02% GO at 0.6 m³/h flow rate and 36°C temperature. According to Figure 5(b), the highest

exergy efficiency was obtained as 93.63% at a flow rate of 0.9 m³/h for 0.01% GO. The lowest exergy efficiency was calculated as 87.14% at a flow rate of 0.6 m³/h for 0.02% GO. Exergy efficiencies of water and 0.01% GO were higher compared to other fluids when the fluid temperature was 40 °C. In Figure 5(c), a comparison of exergy efficiencies for four different flow rates of nanofluids at 44 °C is given. Exergy efficiencies for water and 0.01% GO were calculated very close to each other. The highest exergy efficiency for water was calculated as 95.19% at a flow rate of 0.9 m³/h. For 0.01% GO, the exergy efficiency calculated at the same flow rate was 94.93%. The lowest exergy efficiency was calculated as 87.37% again for 0.02% GO at 0.6 m³/h flow rate.

The comparison of exergy destruction for four different flow rates of nanofluids at different temperature are given in Figure 6.

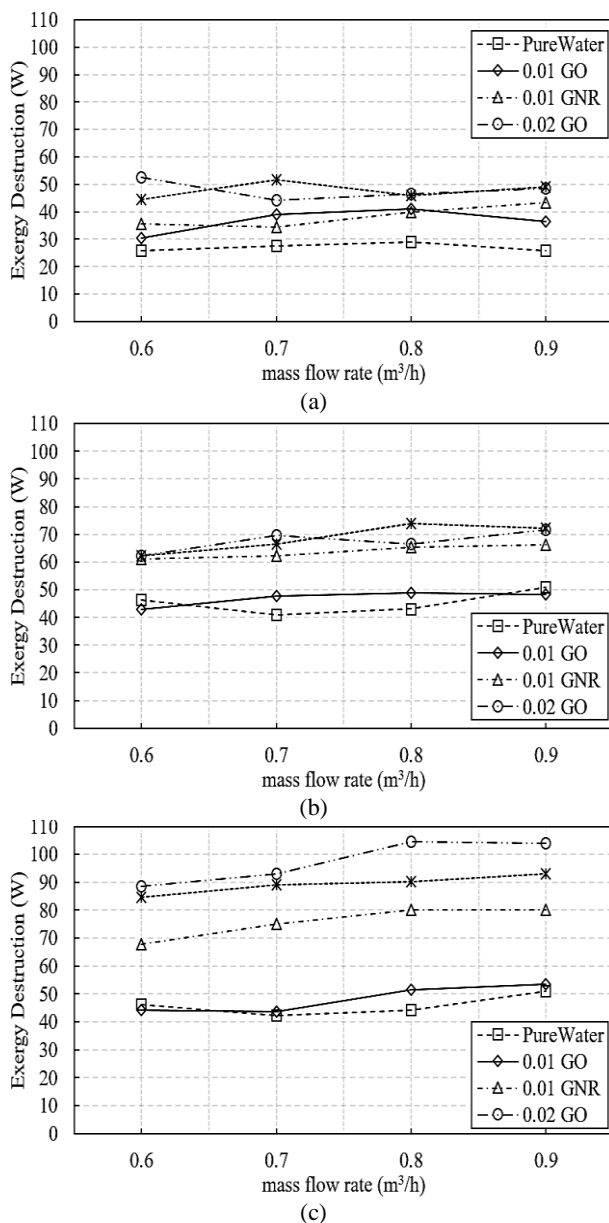


Figure 6. Comparison of exergy destruction for all nanofluids at a) 36 °C b) 40 °C c) 44 °C

According to Figure 6 (a), the highest exergy destruction was 52.42 W for 0.02% GO nanofluid at a flow rate of 0.6 m³/h. The second highest exergy destruction was calculated as 51.77 W for 0.02% GNR nanofluid at 0.7 m³/h flow rate. The lowest exergy destruction was 25.77 W for water at a flow rate of 0.6 m³/h. The lowest exergy destruction value was 30.41 W for 0.01% GO at 0.6 m³/h when compared to each nanofluid at a given temperature. Figure 6(b) shows the changes of exergy destruction of nanofluids at different flow rates at 40 °C. According to obtained data, the lowest exergy destructions were obtained for water at 0.7 m³/h flow and 0.01% GO nanofluid at 0.6 m³/h flow and these values were calculated as 40.84 W and 42.80 W, respectively. Exergy destruction values are close to each other such as exergy efficiency values for water and 0.01% GO nanofluid at 40 °C, and the highest exergy destruction difference is 6.86 W. The highest exergy destruction value is 73.93 W which was obtained at a flow rate of 0.8 m³/h for 0.02% GNR nanofluid (Figure 6(b)). According to Figure 6(c), the lowest exergy destructions obtained at 44 °C fluid inlet temperature were calculated as 42.43 W for water and 43.73 W for 0.01% GO at 0.7 m³/h. The highest exergy destructions were calculated for 0.02% GO as 104.42 W at 0.8 m³/h and 104.01 W at 0.9 m³/h. It has been observed that the exergy destruction values calculated when the fluid inlet temperature is 44 °C are higher than the exergy destruction values calculated for 36 °C and 40 °C fluid inlet temperatures. On the other hand, exergy destruction values for water and 0.01% GO was observed as a result of the calculations concerning the exergy values calculated for water at 40 °C and 0.01% GO oxide.

The graphs of exergy efficiency for water and all nanofluids (0.01% GO, 0.01% GNR, 0.02% GO, 0.02% GNR) are given in Figure 7, comparatively for all flow rates at 36, 40, and 44 °C temperatures.

According to Figure (7), the graphs of exergy efficiency for water and all nanofluids (0.01% GO, 0.01% GNR, 0.02% GO, 0.02% GNR) are given comparatively for all flow rates at 36, 40, and 44 °C temperatures. The highest exergy efficiency among all nanofluids and all temperature values for a flow rate of 0.6 m³/h is 94.48% and 93.73% for water and 0.01% GO at 44 °C, respectively. The lowest exergy efficiency which is 84.57% is obtained for 36 °C temperature and 0.02% GO nanofluid. The highest exergy efficiency among all nanofluids and all temperature values for a flow rate of 0.7 m³/h is 94.85% and 94.68% for water and 0.01% GO at 44 °C, respectively (Khaleduzzaman *et al.*, 2014). The lowest exergy efficiency is obtained for 36 °C temperature and 0.02% GNR nanofluid, and the exergy efficiency is 86.57%. The highest exergy efficiency among all nanofluids and all temperature values for a flow of 0.8 m³/h is 95.29% and 94.53% for water and 0.01% GO at 44 °C, respectively. The highest exergy efficiency among all nanofluids and all temperature values for 0.9 m³/h flow is 95.19% and 94.93% for water and 0.01% GO at 44 °C, respectively. The calculated

exergy efficiency values for 0.01% GO nanofluid were the highest at 6.33% compared to other nanofluids, and water's exergy efficiency was generally between 1% and 2% higher than 0.01% GO compared to water (Gamal *et*

al., 2021). The graphs of comparative exergy destructions for water and all nanofluids are given in Figure 8.

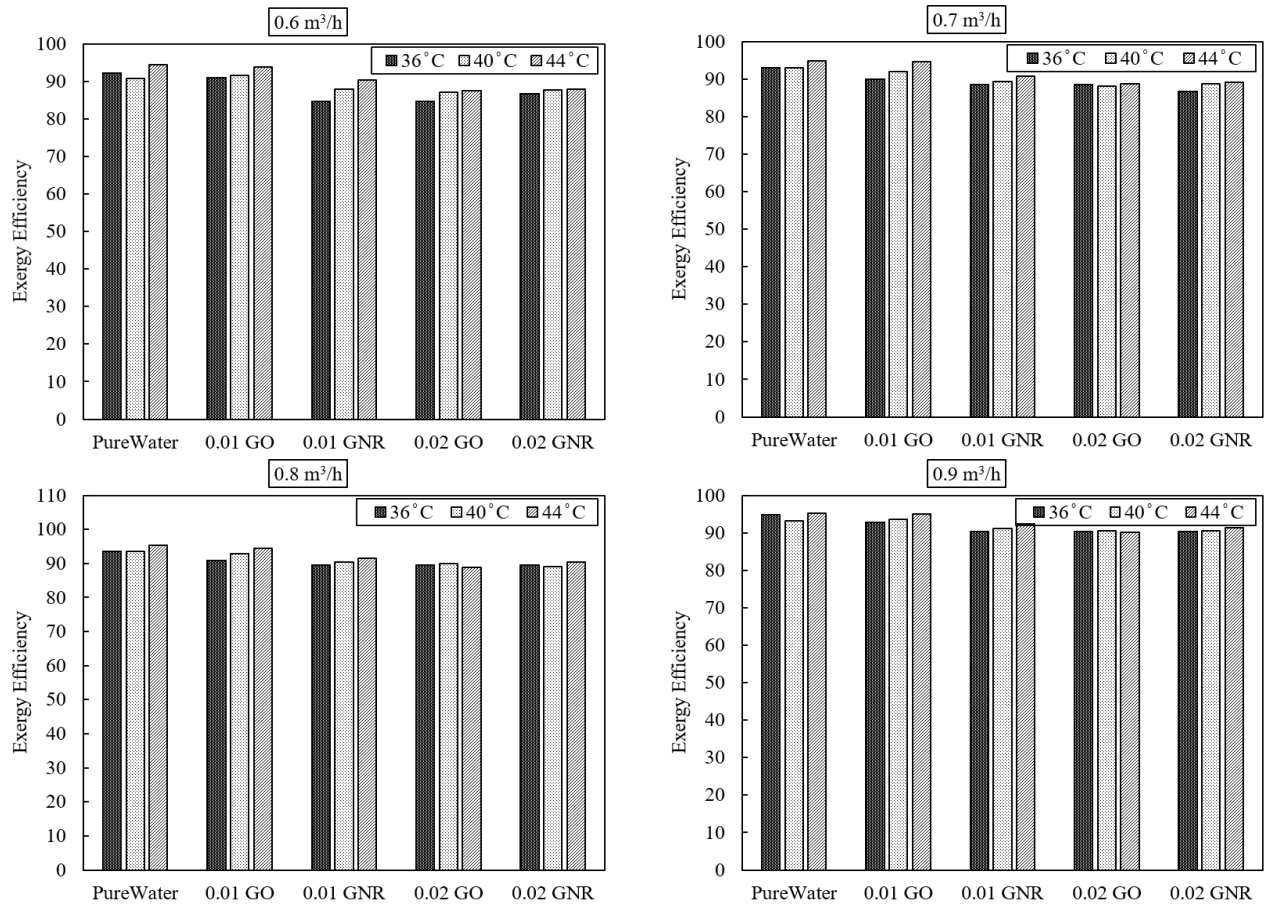


Figure 7. Comparison of the exergy efficiency of water and nanofluids at different temperatures for all flow rates

According to Figure 8, the highest exergy destruction value for a flow of $0.8 \text{ m}^3/\text{h}$ among all temperature values and nanofluids is 88.63 W for 0.02% GO at $44 \text{ }^\circ\text{C}$. The lowest exergy destruction values are at $36 \text{ }^\circ\text{C}$ for water and 0.01% GO, which are 25.77 W and 30.41 W respectively. For the flow rate of $0.7 \text{ m}^3/\text{h}$, the lowest exergy destruction value of $36 \text{ }^\circ\text{C}$ water and 0.01% GNR were obtained, which are 27.58 W and 34.56 W respectively. The highest exergy destruction was calculated as 92.98 W for $44 \text{ }^\circ\text{C}$ temperature and 0.02% GO nanofluid. Also, the exergy destruction value at $44 \text{ }^\circ\text{C}$ calculated for 0.01% GO nanofluid is 43.73 W and the exergy destruction value at $40 \text{ }^\circ\text{C}$ is 47.70 W .

As seen in Figure 8, the highest exergy destruction was calculated as 104.42 W at $44 \text{ }^\circ\text{C}$ for 0.02% GO nanofluid. Among exergy destructions calculated for the flow rate of $0.8 \text{ m}^3/\text{h}$, water has a lower exergy destruction value than nanofluids at all temperature values. The nanofluid with the lowest exergy destruction value at $40 \text{ }^\circ\text{C}$ and $44 \text{ }^\circ\text{C}$ is 0.01% GO. The nanofluid with the lowest exergy destruction value for $36 \text{ }^\circ\text{C}$ is 0.01% GNR. The highest exergy destruction value for the flow rate of $0.8 \text{ m}^3/\text{h}$ was obtained as 104.01 W at $44 \text{ }^\circ\text{C}$ for 0.02% GO. It is seen that the nanofluid with the lowest exergy destruction is

0.01% GO. It has been observed that 0.01% GO has lower exergy destruction at all temperatures and flow rates compared to other nanofluids.

In Table 1, the exergetic analysis results are shown for all fluids at 36 , 40 and $44 \text{ }^\circ\text{C}$. Exergy destruction and exergy efficiency values are summarized in tabular form for a better understanding of the graphs. In addition, entropy generation values are also given. Exergy destruction in a heat exchanger is dependent on the heat exchanger's dead state and its inlet and outlet temperatures. Improvement of these parameters will increase the exergy efficiency of the system by reducing the exergy destruction of the heat exchanger.

In many studies under the heading of exergy analysis, changes in exergy destruction and exergy efficiency have been evaluated in terms of flow rate, inlet temperature, and particle concentration parameters. The positive and negative results obtained as a result of the changes in these parameters are attributed to some factors that occur with the use of nanofluids. Increasing the nanoparticle concentration provides higher thermal conductivity and increases the heat transfer coefficient. In addition, increasing the nanoparticle concentration increases the

viscosity and friction losses. It has been stated that this situation provides an increase in the second law efficiency (Gamal *et al.*, 2021). Similarly, it has been reported that the increase in flow rate and particle loading increases the heat transfer coefficient, and an

improvement in exergy efficiency is observed with the resulting particle migration, molecular level layering of the liquid at liquid particle interface and hydrodynamic effect of Brownian motion of nanoparticles (Khairul *et al.*, 2014; Ahammed *et al.*, 2016)

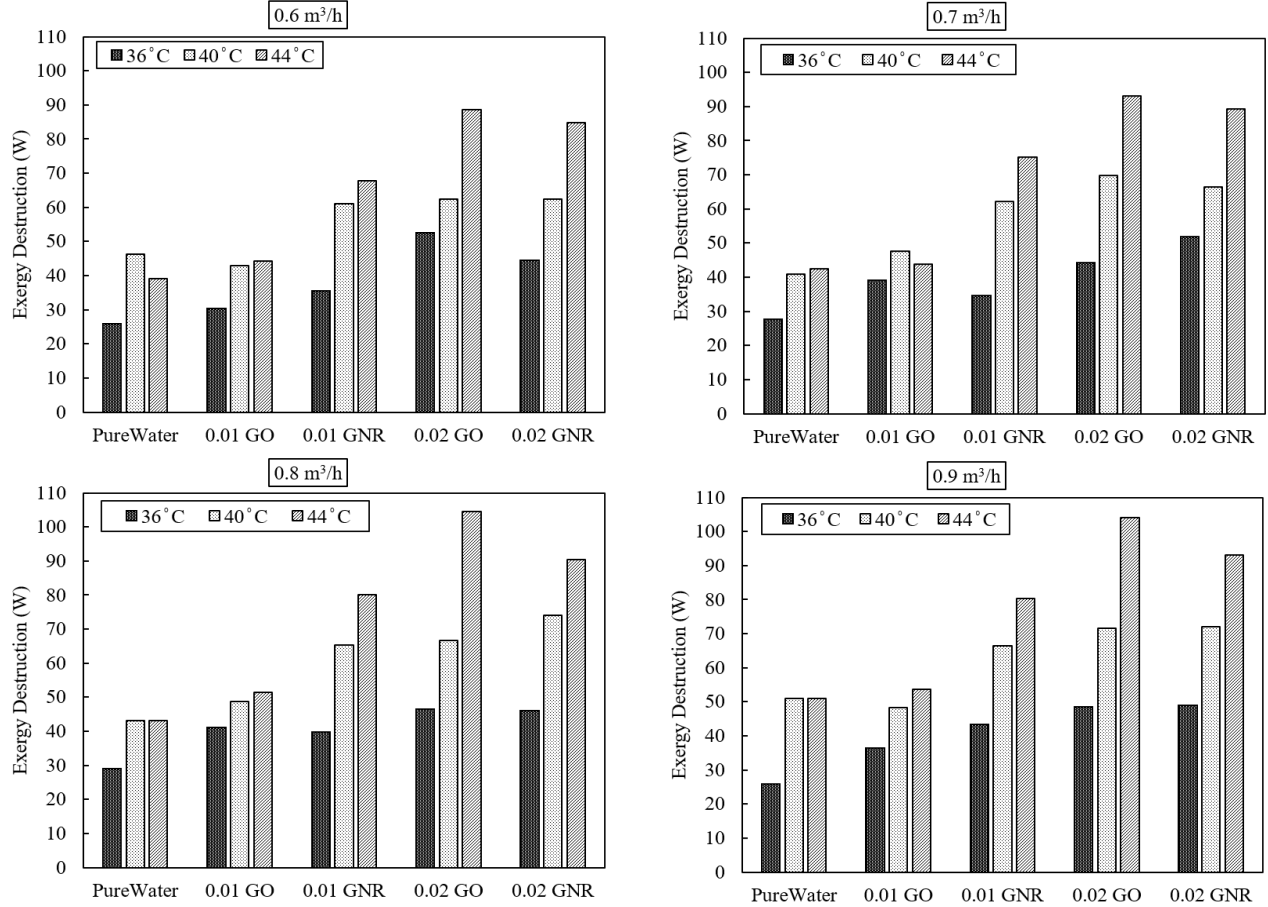


Figure 8. Comparison of the exergy destruction of water and nanofluids at different temperatures for all flow rates

Table 1. Exergetic analysis results for all fluids at 36, 40 and 44 °C

Fluid	\dot{m}_{fluid} (m ³ /h)	36 °C			40 °C			44 °C		
		$\dot{E}x_{dest}$ (W)	\dot{S}_{gen} (W/K)	η_{II} (%)	$\dot{E}x_{dest}$ (W)	\dot{S}_{gen} (W/K)	η_{II} (%)	$\dot{E}x_{dest}$ (W)	\dot{S}_{gen} (W/K)	η_{II} (%)
water	0.6	25.77	0.088	92.24	46.23	0.158	90.78	39.07	0.134	94.48
	0.7	27.58	0.094	92.89	40.84	0.140	93.00	42.43	0.145	94.85
	0.8	29.04	0.099	93.45	43.04	0.147	93.62	44.37	0.152	95.29
	0.9	25.94	0.089	94.79	50.99	0.175	93.25	50.98	0.175	95.19
0.01% GO	0.6	30.41	0.104	90.91	42.80	0.147	91.48	44.30	0.152	93.73
	0.7	39.15	0.134	89.98	47.70	0.163	91.91	43.73	0.150	94.69
	0.8	41.06	0.141	90.84	48.78	0.167	92.78	51.45	0.176	94.53
	0.9	36.48	0.125	92.73	48.33	0.166	93.63	53.57	0.183	94.93
0.02% GO	0.6	52.42	0.180	84.57	62.34	0.213	87.15	88.63	0.304	87.37
	0.7	44.24	0.152	88.49	69.76	0.239	88.06	92.98	0.318	88.63
	0.8	46.58	0.160	89.56	66.57	0.228	90.01	104.42	0.358	88.84
	0.9	48.43	0.166	90.38	71.58	0.245	90.49	104.01	0.356	90.10
0.01% GNR	0.6	35.54	0.122	89.16	60.98	0.209	87.79	67.72	0.232	90.28
	0.7	34.56	0.118	91.00	62.25	0.213	89.37	75.13	0.257	90.81
	0.8	39.83	0.136	90.87	65.27	0.224	90.28	80.03	0.274	91.49
	0.9	43.23	0.148	91.22	66.32	0.227	91.18	80.24	0.275	92.40
0.02% GNR	0.6	44.49	0.152	86.67	62.28	0.213	87.60	84.75	0.290	87.88
	0.7	51.77	0.177	86.57	66.50	0.228	88.60	89.16	0.305	89.13
	0.8	45.94	0.157	89.60	73.93	0.253	88.98	90.29	0.309	90.44
	0.9	48.99	0.168	90.24	72.11	0.247	90.53	93.04	0.319	91.25

When the increase in exergy loss is examined for the inlet temperature, it is concluded that the temperature difference between the hot and cold fluids increases the exergy loss, which is due to the finite temperature difference, and this is the main reason for the exergy loss in the heat exchangers (Dizaji *et al.*, 2017). As the fluid flow rate increases, it increases fluid disruption and destroys the flow boundary layer. Additionally, graphene nanoparticles in nanofluids are subjected to Brownian forces for irregular Brownian diffusion and thermal diffusion. Micro-convection occurs between nanoparticles and the base fluid, energy is transferred from the nanoparticles to the base fluid, the boundary layer is sharply disrupted, disturbance is heightened, and heat transfer is enhanced (Wang *et al.*, 2020).

CONCLUSION

In this study, the exergy analysis of graphene-based nanofluids in a compact heat exchanger is examined. Exergy efficiency and exergy destruction values were calculated comparatively for distilled water and nanofluids. The results of the calculations can be summarized as follows:

It was concluded that the exergy efficiencies of nanofluids increased with the increase of the fluid flow rates and inlet temperature to the heat exchanger (Bahiraei and Mazaheri, 2021; Khairul *et al.*, 2014; Saleh and Sundar, 2021; Gamal *et al.*, 2021; Sadighi *et al.*, 2016; Ahammed *et al.*, 2016). The increase in the number of Nusselt resulted in an increase in heat transfer and an increase in the exergy efficiency of the nanofluid. Enhanced exergy efficiency results from changes in entropy generation of the fluid and irreversibility rates in the system (Saleh and Sundar, 2021).

When the exergy destruction and entropy generation were compared to the nanoparticle concentrations, it was concluded that the exergy destructions increased with the increase of the nanoparticle concentration. It can be explained by the limited heat transfer temperature difference, the fluid viscosity flow resistance, Brownian motion, particle migration, etc. (Wang *et al.*, 2020; Pandya *et al.*, 2020).

It was concluded that the exergy destruction and entropy generation of nanofluids increased with the increase of the flow rates (Bahiraei and Mazaheri, 2021). However, it showed an increasing and decreasing trend by oscillating in some conditions. It was determined that the amount of increase in exergy destruction of GO nanofluid was higher than that of GNR. Graphene nanofluid's lower concentration enhances heat transfer more than fluid viscosity's effect on performance (Wang *et al.*, 2020).

When the exergy destruction values are compared with the fluid temperatures, it was found that the exergy destruction values increase with the increase of fluid inlet

temperatures (Pandya *et al.*, 2020; Esfahani and Languri, 2017; Sadighi *et al.*, 2016).

In this study, it was concluded that the positive effect of the nanofluids prevails to the adverse effects and fluid flow rate, inlet temperature and particle concentration play an important role in heat exchanger efficiency. This shows that the use of the nanofluid is a valuable method to reduce the total irreversibility of the heat exchanger.

As a result, it has been determined that the exergy efficiency of 0.01% GO nanofluid is better and the amount of exergy destruction is less compared to 0.02% GO nanofluid. The calculated values were found to be comparable to previous studies in the literature (Khaleduzzaman *et al.*, 2014; Gamal *et al.*, 2021; Jils and Jesseela, 2021). Considering that the flow structure of nanofluids will cause irreversibilities and entropy generation, the nanoparticles in the fluid will cause a turbulent flow structure, these values are quite remarkable. Finally, further work is required to investigate the effects of the economic efficiency of nanofluids and the use of hybrid nanofluids.

REFERENCES

- Ahammed N., Asirvatham G. L., and Wongwises S., 2016, Entropy Generation Analysis of Graphene–Alumina Hybrid Nanofluid in Multiport Minichannel Heat Exchanger Coupled with Thermoelectric Cooler, *International Journal of Heat and Mass Transfer*, 103, 1084-1097.
- Baby T. T. and Ramaprabhu S., 2011, Enhanced Convective Heat Transfer Using Graphene Dispersed Nanofluids, *Nanoscale Res. Lett.*, 6, 1-9.
- Bahiraei M. and Mazaheri N., A Comprehensive Analysis for Second Law Attributes of Spiral Heat Exchanger Operating with Nanofluid Using Two-Phase Mixture Model: Exergy Destruction Minimization Attitude, *Advanced Powder Technology*, 32, 211-224.
- Bahiraei M., Jamshidmofid M., Amani M. and Barzegarian, R., 2018, Investigating Exergy Destruction And Entropy Generation for Flow of a New Nanofluid Containing Graphene–Silver Nanocomposite in a Micro Heat Exchanger Considering Viscous Dissipation, *Powder Technology*, 336, 298-310.
- Çalışkan H. and Hepbaşlı A., 2013, Isı Değiştiricilerinin Ekserjetik Yönleri, *Mühendis ve Makina*, 54, 645, 28-37.
- Dincer I. and Rosen M. A., 2012, Exergy: Energy, Environment And Sustainable Development, *Elsevier Science*.
- Dizaji H. S., Khalilarya S., Jafarmadar S., Hashemian M. and Khezri M., 2016, A comprehensive second law analysis for tube-in-tube helically coiled heat

- exchangers, *Experimental Thermal and Fluid Science*, 76, 118-125.
- Esfahani M. R. and Languri E. M., 2017, Exergy Analysis of a Shell-and-tube Heat Exchanger Using Graphene Oxide Nanofluids, *Experimental Thermal and Fluid Science*, 83, 100-106.
- Fard M. G., Talaie M. R. and Nasr, S., 2011, Numerical and Experimental Investigation of Heat Transfer of ZnO/Water Nanofluid in The Concentric Tube and Plate Heat Exchangers, *Thermal Science*, 15:1, 183-194.
- Gamal M., Radwan M. S., Elgizawy I. G. and Shedid M. H., 2021, Heat Transfer Performance and Exergy Analyses of MgO and ZnO Nanofluids Using Water/Ethylene Glycol Mixture as Base Fluid, *Numerical Heat Transfer, Part A: Applications*, 80:12, 597-616.
- Hajjar Z., Rashidi A. M. and Ghazatloo A., 2014, Enhanced Thermal Conductivities of Graphene Oxide Nanofluids, *Int. Commun. Heat Mass Transfer*, 57, 28-131.
- Hepbasli A., 2008, A Key Review on Exergetic Analysis and Assessment of Renewable Energy Resources for a Sustainable Future, *Renewable and Sustainable Energy Reviews*, 12, 593-661.
- Holman J. P., 2011, Experimental methods for engineers, 7th edition, *MCGraw-hill*, New York.
- Hung Y. H., Teng T. P., Teng T. C. and Chena J. H., 2012, Assessment of Heat Dissipation Performance for Nanofluid, *Applied Thermal Engineering*, 32, 132-140.
- Ipek O., Kılıç B. and Gürel B., 2017, Experimental Investigation of Exergy Loss Analysis in Newly Designed Compact Heat Exchangers, *Energy*, 124, 330-335.
- Javadi F. S., Sadeghipour S., Saidur R., Boroumandjazi G., Rahmati B., Elias M. M. and Sohel M. R., 2013, The Effects of Nanofluid on Thermophysical Properties and Heat Transfer Characteristics of a Plate Heat Exchanger, *International Communications in Heat and Mass Transfer*, 44, 58-63.
- Jils J. and Jesseela S., 2021, Exergy Analysis in a Minichannel with Nanofluid, *The International Conference on Emerging Trends in Engineering*, Kozhikode, Kerala, India.
- Karabulut K., Buyruk E. and Kılınç F., 2020, Experimental and Numerical Investigation of Convection Heat Transfer in a Circular Copper Tube Using Graphene Oxide Nanofluid, *Journal of the Brazilian Society of Mechanical Sciences and Engineering*, 42:230, 1-16.
- Khairul M. A., Alima M. A., Mahbulul I. M., Saidur R., Hepbasli A. and Hossaina A., 2014, Heat Transfer Performance and Exergy Analyses of a Corrugated Plate Heat Exchanger Using Metal Oxide Nanofluids, *International Communications in Heat and Mass Transfer*, 50, 8-14.
- Khaleduzzaman S. S., Sohel M. R., Saidur R., Mahbulul I. M., Shahrul I. M., Akash B. A. and Selvaraj J., 2014, Energy and Exergy Analysis of Alumina–Water Nanofluid for an Electronic Liquid Cooling System, *International Communications in Heat and Mass Transfer*, 57, 118-127.
- Khanafar K. and Vafai K., 2011, A Critical Synthesis of Thermophysical Characteristics of Nano-Fluids, *Int. Journal of Heat and Mass Transfer*, 54, 4410-4428.
- Kılınç F., 2015, *Enhancement of Heat Transfer Performance by Using Nanofluids in Auto Radiators*, Ph.D. Thesis, Cumhuriyet University, Sivas, Turkey.
- Kılınç F., Buyruk E. and Karabulut K., 2020, Experimental Investigation of Cooling Performance with Graphene Based Nano Fluids in a Vehicle Radiator, *Heat and Mass Transfer*, 56:2, 521-530.
- Lomascolo M., Colangelo G., Milanese M. and Risi A., 2015, Review of Heat Transfer in Nanofluids, Conductive, Convective and Radiative Experimental Results, *Renew. Sustain. Energy*, 43, 1182-1198.
- Maddah H., Ghasemi N., Keyvani B. and Cheraghali R., 2017, Experimental and Numerical Study of Nanofluid in Heat Exchanger Fitted by Modified Twisted Tape: Exergy Analysis and ANN Prediction Model, *Heat and Mass Transfer*, 53:4, 1413-1423.
- Novoselov K., Geim A. K., Morozov S., Jiang D., Grigorieva M. K. I., Dubonos S. and Firsov A., 2005, Two-dimensional Gas of Massless Dirac Fermions in Graphene, *Nature*, 438, 197-200.
- Pak B. C. and Cho Y. I., 1998, Hydrodynamic and Heat Transfer Study of Dispersed Fluids with Submicron Metallic Oxide Particles, *Experimental Heat Transfer*, 11, 151-170.
- Pandey S. D. and Nema V. K., 2012, Experimental Analysis of Heat Transfer and Friction Factor of Nanofluid as a Coolant in a Corrugated Plate Heat Exchanger, *Experimental Thermal and Fluid Science*, 38, 248-256.
- Pandya N. S., Shah H., Molana M. and Tiwari A. K., 2020, Heat Transfer Enhancement with Nanofluids in Plate Heat Exchangers: A Comprehensive Review, *European Journal of Mechanics / B Fluids*, 81, 173-190.
- Pantzali M. N., Kanaris A. G., Antoniadis K. D., Mouza A. A. and Paras S. V., 2009, Effect of Nanofluids on the Performance of a Miniature Plate Heat Exchanger with

- Modulated Surface, *International Journal of Heat and Fluid Flow*, 30, 691-699.
- Peyghambarzadeh S. M., Hashemabadi S. H., Hoseini S. M. and Jamnani M. S., 2011, Experimental Study of Heat Transfer Enhancement Using Water/Ethylene Glycol Based Nanofluids as a New Coolant for Car Radiators, *International Communications in Heat and Mass Transfer*, 38, 1283-1290.
- Rosen M. A., 2002, Assessing Energy Technologies and Environmental Impacts with the Principles of Thermodynamics, *Applied Energy*, 72, 427-441.
- Sadeghinezhad E., Mehrali M., Saidur R., Latibari S. T., Akhiani A. R. and Metselaar H. S. C., 2016, A Comprehensive Review on Graphene Nanofluids, Recent Research, Development and Applications, *Energy Convers. Manage.*, 111, 466-487.
- Saleh B. and Sundar L. S., 2021, Experimental Study on Heat Transfer, Friction Factor, Entropy and Exergy Efficiency Analyses of a Corrugated Plate Heat Exchanger Using Ni/Water Nanofluids, *International Journal of Thermal Sciences*, 165, 106935.
- Singh S. K. and Sarkar J., 2018, Energy, Exergy and Economic Assessments of Shell and Tube Condenser Using Hybrid Nanofluid as Coolant, *International Communications in Heat and Mass Transfer*, 98, 41-48.
- Singh V., Joung D., Zhai L., Das S., Khondaker S. and Seal S., 2012, Graphene Based Materials: Past, Present And Future, *Prog. Mater. Sci.*, 56, 1178-1271.
- Sun B., Peng C., Zuo R., Yang D. and Li H., 2016, Investigation on the Flow and Convective Heat Transfer Characteristics of Nanofluids in the Plate Heat Exchanger, *Experimental Thermal and Fluid Science*, 76, 75-86.
- Uygun C. Z., 2019, *Exergy analysis by used graphen based nanofluid in car radiator*, BSc. Thesis, Sivas Cumhuriyet University, Sivas, Turkey.
- Vajjha R. S., Das D. K. and Namburu P. K., 2010, Numerical Study of Fluid Dynamic and Heat Transfer Performance of Al₂O₃ and CuO Nanofluids in the Flat Tubes of a Radiator, *International Journal of Heat and Fluid Flow*, 31, 613-621.
- Wang Z., Han F., Ji Y. and Li W., 2020, Performance and Exergy Transfer Analysis of Heat Exchangers with Graphene Nanofluids in Seawater Source Marine Heat Pump System, *Energies*, 13 (7), 1762.
- Wang Z., Wu Z., Han F., Wadsö L. and Sundén B., 2018, Experimental Comparative Evaluation of a Graphene Nanofluid Coolant in Miniature Plate Heat Exchanger, *International Journal of Thermal Sciences*, 130, 148-156.
- Yu W., Xie H., Wang X. and Wang X., 2011, Significant Thermal Conductivity Enhancement for Nanofluids Containing Graphene Nanosheets, *Phys. Lett. A*, 375, 1323-1328.



IMPLEMENTATION, VERIFICATION AND ASSESSMENT OF VORTEX CAPTURING CAPABILITIES OF $k-kL$ TURBULENCE MODEL

Erdem DİKBAŞ* and Özgür Uğraş BARAN**

* TÜBİTAK SAGE, Aerodynamics Division, 06270 Mamak, Ankara, Turkey
erdem.dikbas@tubitak.gov.tr, ORCID: 0000-0001-9074-3649

** Middle East Technical University, Mechanical Engineering Department, 06800 Çankaya, Ankara, Turkey
ubarar@metu.edu.tr, ORCID: 0000-0002-8437-7862

(Geliş Tarihi: 08.10.2021, Kabul Tarihi: 08.04.2022)

Abstract: This study presents the first results of a new turbulence model implementation in our compressible finite volume CFD solver. The $k - kL$ turbulence model is one of the newest two-equation models, and it is based on the ideas of Rotta's two-equation model. Various research groups progressively develop the model, and it is maturing rapidly. Reports suggest that the $k - kL$ turbulence model provides superior results compared to the other two-equation turbulence models in specific problems. The improved solutions are observed mainly for the flows with high adverse pressure gradients, the blunt-body wakes and jet interactions. We have implemented the $k - kL$ model (with the standard designation of $k-kL$ -MEAH2015) in our solver, and we are testing it rigorously. This paper presents our results on standard turbulence test cases: subsonic flat plate and subsonic wall-mounted bump. The results compare well with the reference study previously presented and published by model developers. The design of the $k - kL$ model prevents excessive production of turbulence and dissipation; hence it preserves vortices significantly better than the other two-equation models. The implemented model is also tested with a transonic fin trailing vortex case to support this statement. Results show that the $k - kL$ model yields considerably better results than the SST turbulence model in cases including vortices.

Keywords: Turbulence models, $k - kL$ model, Computational Fluid Mechanics

k-kL TÜRBÜLANS MODELİNİN UYGULAMASI, DOĞRULAMASI VE GİRDAP YAKALAMA YETENEKLERİNİN DEĞERLENDİRİLMESİ

Özet: Bu çalışmada, sıkıştırılabilir akış sonlu hacimler çözücümüz üzerinde yeni bir türbülans modeli uygulamasının ilk sonuçları sunulmaktadır. $k - kL$ türbülans modelinin tarihsel kökleri Rotta'nın iki denklemlili modeline dayanmaktadır. Birkaç araştırma grubu üzerinde uzun süreli çalışmalar yapmakta ve bu model günümüzde olgunluğa erişmektedir. Geçmiş çalışmalar $k - kL$ türbülans modelinin diğer iki denklemlili türbülans modellerine göre bazı alanlarda daha iyi sonuçlar verebildiğini göstermiştir. Özellikler ters basınç gradyanlı akışlar, küt gövde arkası iz akışları ve jet etkileşimleri içeren akışlarda bu olumlu etki gözlemlenmiştir. Bu çalışma kapsamında, standart notasyonda $k-kL$ -MEAH2015 olarak geçen $k - kL$ türbülans modeli çözücümüze eklenmiş ve ilk testleri başlamıştır. Ses altı düz levha ve ses altı tümsekli duvar problemleri üzerinde elde edilen sonuçlar sunulmaktadır. Sonuçlar model geliştiricilerinin yayınladığı sonuçlarla örtüşmektedir. $k - kL$ türbülans modelinin, türbülans denklemlerinin çözümü sırasında aşırı yüksek türbülans üretiminin oluşmasını engelleyerek diğer RANS modellerine göre daha iyi girdaplı akış tahminlerinin yapılmasına yardımcı olması beklenmektedir. Bu sebeple, yeni eklenen model ile ses geçiş hızlarında kanat ucu girdap problem üzerinde testler yapılmış ve Menter'in Shear Stress Transport türbülans modeline göre daha iyi sonuçlar elde edilmiştir.

Anahtar Kelimeler: Türbülans modelleri $k-kL$ modeli, Hesaplamalı Akışkanlar Dinamiği

NOMENCLATURE

ARSM Algebraic Reynolds Stress Model

CFD Computational Fluid Dynamics

KSKL $k\sqrt{kL}$

LES Large Eddy Simulation

NS Navier-Stokes

QCR Quadratic Constitutive Relationship

RANS Reynolds Averaged Navier Stokes

SST Shear Stress Transport

C Model constants

δ_{ij} Kronecker delta

k turbulent kinetic energy

L Length scale

t time

x Spatial direction

μ viscosity

μ_t turbulent viscosity

ρ	density
P	Turbulent Production term
u	x - velocity
v	y - velocity
w	z - velocity
τ_{ij}	shear stress tensor

INTRODUCTION

Computational Fluid Dynamics is still a developing area encompassing numerous numerical methods to address different aspects of flow physics. Despite its currently unresolved shortcomings, it is already accepted as a standard design and analysis tool for most engineering flows. CFD methods are based on solving Navier-Stokes equations with various techniques. The discretization of NS equations is often adequate for Laminar flows. Turbulence is one of the essential flow features that conventional CFD methods based on NS discretizations cannot precisely simulate. The main reason for this is the considerable gap between discretization sizes achievable with today's computer capacity and the scales of turbulence. This shortcoming is frequently evaded by applying turbulence models. These models allow replicating turbulence effects into the mean flow on a relatively coarser grid.

Most turbulence models are designed to add turbulence effects by replacing viscosity with an artificial eddy viscosity parameter. The eddy viscosity characterizes the effect of turbulent fluctuations of the flow variables. There are a couple of different turbulence models in the literature with a different number of equations and different complexities. Two-equation models are successfully applied in practical applications. These models rely on the idea that turbulence effects are constituted by two independent scales, obtained from two independent transport equations, as Launder and Spalding (1983) explained.

The $k - kL$ turbulence model was first developed by Rotta (1951), and since then, there has not been widespread use among the CFD community. This slow adaptation is essentially associated with third-order velocity gradient content contained in the equation set (Menter and Egorov, 2010). A third-order gradient is cumbersome to compute in practice for most finite volume schemes; hence, the application of the solver model did not materialize until recently. However, the historical importance of $k - kL$ remains. It should be noted that this model constitutes the roots of major families of two-equation models such as $k - \varepsilon$ and $k - \omega$, which are incorporated in many modern CFD solvers (Rodi, 2006). The model has been becoming prevalent in the last few years after the efforts of Menter and Egorov (2010) and Abdol-Hamid (2013, 2015).

The prominent distinguishing feature of Rotta's model is that it employs the turbulent length scale (L) concept in the turbulence transport equations. According to this model, the kL parameter is driven by the third velocity

gradient with the assumption of homogeneous turbulence. On the other hand, Menter and Egorov (2006) suggest that a second-order velocity gradient should drive the turbulent length scale. This approach helps to avoid tedious computation of third derivatives, especially for three-dimensional domains (Menter and Egorov, 2010). The second-order gradient term appears in the von Karman length scale calculation, through which the two turbulence transport equations are coupled. The revision of the length scale discussion leads to the development of $k - \sqrt{(k)}L$ (KSKL) model, where the preference of $\sqrt{(k)}L$ parameter is based on historical reasons. KSKL model provides an estimation of local breakups at unstable regions of the flow. This feature may result in an unsteady RANS analysis to exhibit an LES-like behavior where several turbulent scales co-exist in the computed flow field.

The most recent efforts have been made by Abdol-Hamid, while he adapted $k - kL$ model into NASA solvers. After applying Menter's idea to Rotta's model, he and his colleagues presented and verified the k-kL-MEAH2015 model (Abdol-Hamid, 2016). It is demonstrated that the $k - kL$ model shows similar or better performance than SST after testing on various problems with different flow regimes. Other variations where quadratic constitutive relationship (QCR) and algebraic Reynolds stress models (ARSM) are incorporated lead to performance improvements (Abdol-Hamid, 2019).

The $k - kL$ turbulence model is a promising method that incorporates several advantages over standard two-equation models. The main advantage of the model is that the method involves several turbulent length scales. This feature may provide an advantage in simulating flows involving large vortices, whereas other two-equation models produce excessive turbulent stresses, and vortices dissipate rapidly. The fin-vortex may severely affect the missile performance, and it is a challenging task in the missile design process. To address this problem, we have decided to implement the method and assess its characteristics in such flow configurations.

In the current study, the k-kL-MEAH2015 turbulence model is implemented into our in-house flow solver. We used subsonic flat plate and subsonic wall-mounted hump problems as initial validation cases. Test results are presented in comparison with the results of the model developers.

Another critical area that the $k - kL$ turbulence model is the inclusion of the turbulent length scale parameter, L . The length scale allows the model to adapt scales of turbulence to local flow characteristics. This feature becomes vital in vortex structures, where the turbulence production is over-predicted in classical models. A compressible-flow fin trailing vortex test case is presented in this study to assess vortex preserving features of the $k - kL$ turbulence model.

METHOD

We have implemented the k - kL -MEAH2015 model in our density-based finite volume solver. Our solver applies the HLLC method as the inviscid flux scheme (Toro et al., 1994) and implicit time integration. The software is suited to widely used turbulence models, e.g., Spalart-Allmaras and $k - \omega$ family. Hybrid RANS-LES models are also supported. Software execution is done fully parallel by MPI libraries. It is possible to input the grids with various element topologies in a wide range of formats. The implementation of the $k - kL$ model is completed, tests are run in parallel and solutions are compared with the SST type $k - \omega$ model.

Theory

The formulation of $k - kL$ model developed by Abdol-Hamid (2015) is utilized to implement the current study. The governing equations and other relations are presented here for completeness. NASA Langley Turbulence Modeling Resource (Rumsey, 2021) is also utilized for necessary equations.

Scalar transport equations of variables k and kL are given as described in k - kL -MEAH2015 in Eqs. 1-2.

$$\frac{\partial(\rho k)}{\partial t} + \frac{\partial(\rho u_j k)}{\partial x_j} = P - C_\mu^{3/4} \rho \frac{k^{5/2}}{(kL)} - 2\mu \frac{k}{d^2} + \frac{\partial}{\partial x_j} \left[(\mu + \sigma_k \mu_t) \frac{\partial k}{\partial x_j} \right] \quad (1)$$

$$\frac{\partial(\rho(kL))}{\partial t} + \frac{\partial(\rho u_j(kL))}{\partial x_j} = C_{\phi 1} \frac{(kL)}{k} P - C_{\phi 2} \rho k^{3/2} - 6\mu \frac{(kL)}{d^2} f_\phi + \frac{\partial}{\partial x_j} \left[(\mu + \sigma_\phi \mu_t) \frac{\partial(kL)}{\partial x_j} \right] \quad (2)$$

Production term P , is computed for both k and kL equations using relations in Eqs. 3 through 6. Here, the production term is expressed in terms of the pure strain tensor S_{ij} . Formulations using the vorticity tensor for the production term are also applicable and can be included as an option in our solver. The production term is limited by the expression given in Eq. 7, as introduced by Abdolhamid.

$$P = \tau_{ij} \frac{\partial u_i}{\partial x_j} \quad (3)$$

$$\tau_{ij} = \mu_t \left(2S_{ij} - \frac{2}{3} \frac{\partial u_k}{\partial x_k} \delta_{ij} \right) - \frac{2}{3} \rho k \delta_{ij} \quad (4)$$

$$S_{ij} = \frac{1}{2} \left(\frac{\partial u_i}{\partial x_j} + \frac{\partial u_j}{\partial x_i} \right) \quad (5)$$

$$\mu_t = C_\mu^{3/4} \frac{\rho(kL)}{k^{1/2}} \quad (6)$$

$$\min \left(P, 20C_\mu^{3/4} \rho \frac{k^{5/2}}{(kL)} \right) \quad (7)$$

Parameters used in kL -equation are given in Eq. 8. The second-order gradient of the velocity field, U'' , is utilized in calculating the von Karman length scale, L_{vk} , which appears in the $C_{\phi 1}$ function. While implementing the turbulence model into the solver, the gradient of the velocity gradient components is constructed throughout all face and cell centers.

$$C_{\phi 1} = \left[\zeta_1 - \zeta_{2l} \left(\frac{(kL)}{kL_{vk}} \right)^2 \right] \quad (8a)$$

$$C_{\phi 2} = \zeta_3 \quad (8b)$$

$$C_{\phi 2} = \zeta_3 \quad (8c)$$

$$L_{vk} = \kappa \left| \frac{U'}{U''} \right| \quad (9a)$$

$$U' = \sqrt{2S_{ij}S_{ij}} \quad (9b)$$

$$U'' = \left[\left(\frac{\partial^2 u}{\partial x^2} + \frac{\partial^2 u}{\partial y^2} + \frac{\partial^2 u}{\partial z^2} \right) + \left(\frac{\partial^2 v}{\partial x^2} + \frac{\partial^2 v}{\partial y^2} + \frac{\partial^2 v}{\partial z^2} \right) + \left(\frac{\partial^2 w}{\partial x^2} + \frac{\partial^2 w}{\partial y^2} + \frac{\partial^2 w}{\partial z^2} \right) \right]^{1/2} \quad (9c)$$

Limiters and constants not given in this paper are used identically with those described in the reference. Boundary conditions for turbulence equations are given in Eqs. 10 and 11 for farfield and wall boundaries, respectively.

$$k_\infty = 9 \times 10^{-9} a_\infty^2 \quad (10a)$$

$$(kL)_\infty = 1.5589 \times 10^{-6} \mu_\infty a_\infty / \rho_\infty \quad (10b)$$

$$k_{wall} = (kL)_{wall} = 0 \quad (11)$$

VERIFICATION TEST CASES

Zero pressure gradient flat plate

The test case of the zero-pressure gradient flat plate is described in Figure 1. As perceived from the inlet boundary condition definitions, the test case is specified for compressible flow solvers despite the low-speed free

stream flow ($M_\infty \sim 0.2$). It is one of the AIAA 5th Drag Prediction Workshop (Levy et al., 2014).

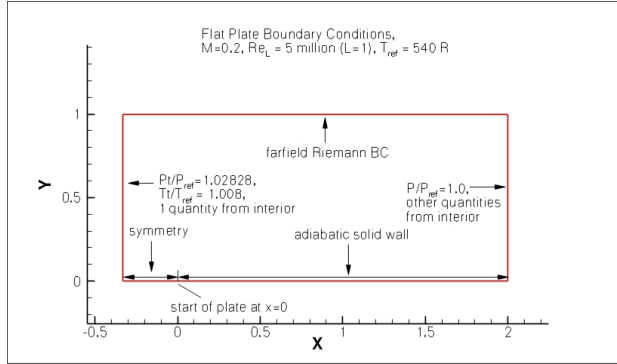


Figure 1. Zero pressure gradient flat plate test case description from Turbulence Modeling Resource website (Rumsey, 2021)

In order to keep all the numerical validation test conditions the same, a grid provided on the NASA Turbulence Modeling Resource website is used (Rumsey, 2021). This test case is used among the researchers, and many results are available. In addition to

the NASA Turbulence Modeling Resource website, two AIAA led workshops used this test case, and extensive reports are available (Rumsey, 2015), (Levy, 2014). We will compare our results only with the reference study. Other results with various turbulence models and solvers are available on the website. The grid borrowed for the current study is the structured hexahedral grid with $2 \times 545 \times 385$ node points on each axis.

Bump-in-channel

The bump-in-channel test case is described in Figure 2. This test case is specified for compressible flow solvers, similar to the previous case. The bump in the middle triggers flow separation, which is accepted as a challenging test case for RANS models. Indeed, many examples of RANS models are not proven to provide credible results in the case of flow separation. In order to keep all the inputs the same, a grid provided on the NASA Turbulence Modeling Resource website is used (Rumsey, 2021). The grid borrowed for the current study is a structured hexahedral grid with $2 \times 705 \times 321$ nodes on each axis.

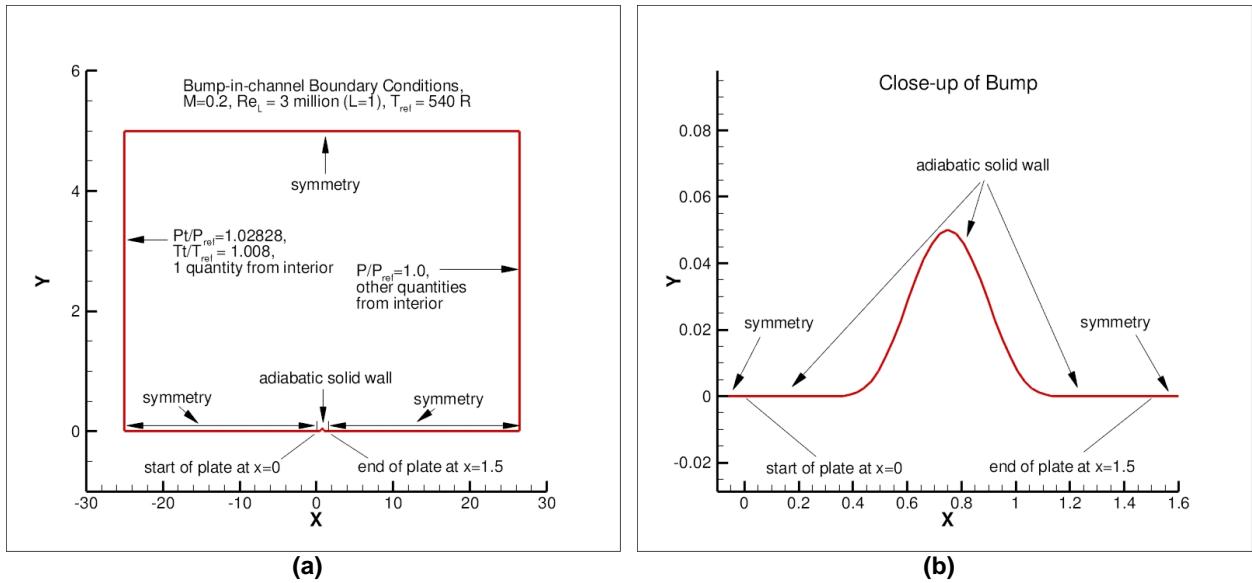


Figure 2. Bump-in-channel test case description from Turbulence Modeling Resource website (Rumsey, 2021). (a) domain dimensions, (b) bump details (x-y scales do not match)

RESULTS

Verification of the implementation

Verification of the new $k - kL$ turbulence model implementation is shown on zero pressure gradient flat plate and bump-in-channel test cases. The data set given in the NASA Langley Center Turbulence Modeling Resource webpage (Rumsey, 2021) is used for comparison purposes. Local flow field variables at reference planes and variations of flow quantities within the boundary layer at definite axial stations constitute the basis of the comparisons. Results are presented and discussed in the respective sub-headings.

Zero-gradient flat plate

The zero pressure gradient flat plate case results have been obtained by utilizing the newly implemented $k - kL$ turbulence model. Verification of current implementation is done via flow field comparison between new results and those presented by Abdol-Hamid (2016). The computed turbulent viscosity ratio within the boundary layer compares well, as given in Figure 3. Note that the vertical axes are exaggerated for assessment. The current result of the skin-friction coefficient throughout the wall surface mostly coincides with the reference results, except for the foremost region where the gradient of this quantity approaches infinity

(Figure 4.(a)). Velocity, k and kL profiles at $x = 0.97$ station also compare very well to the results of the reference study, as seen in Figure 4. Minor differences in

the free stream turbulence quantities do not significantly affect the flow field prediction within the boundary layer.

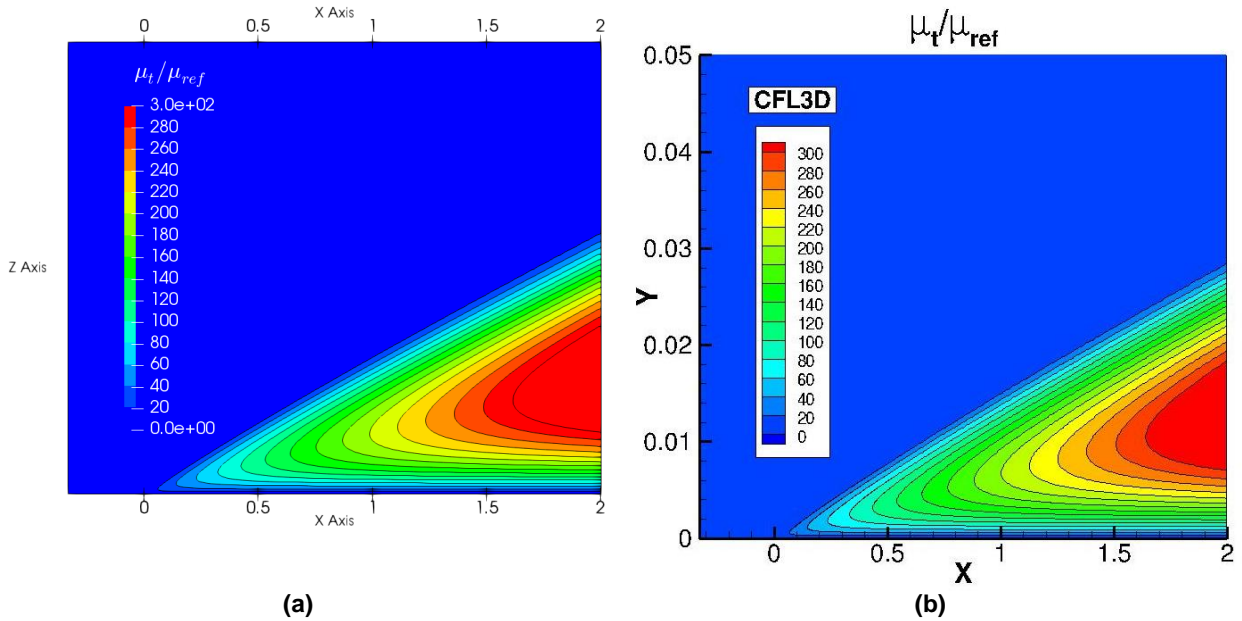


Figure 3. Turbulent viscosity ratio within the boundary layer; zero pressure gradient flat plate; (a) – current, (b) – Abdol- Hamid et al.

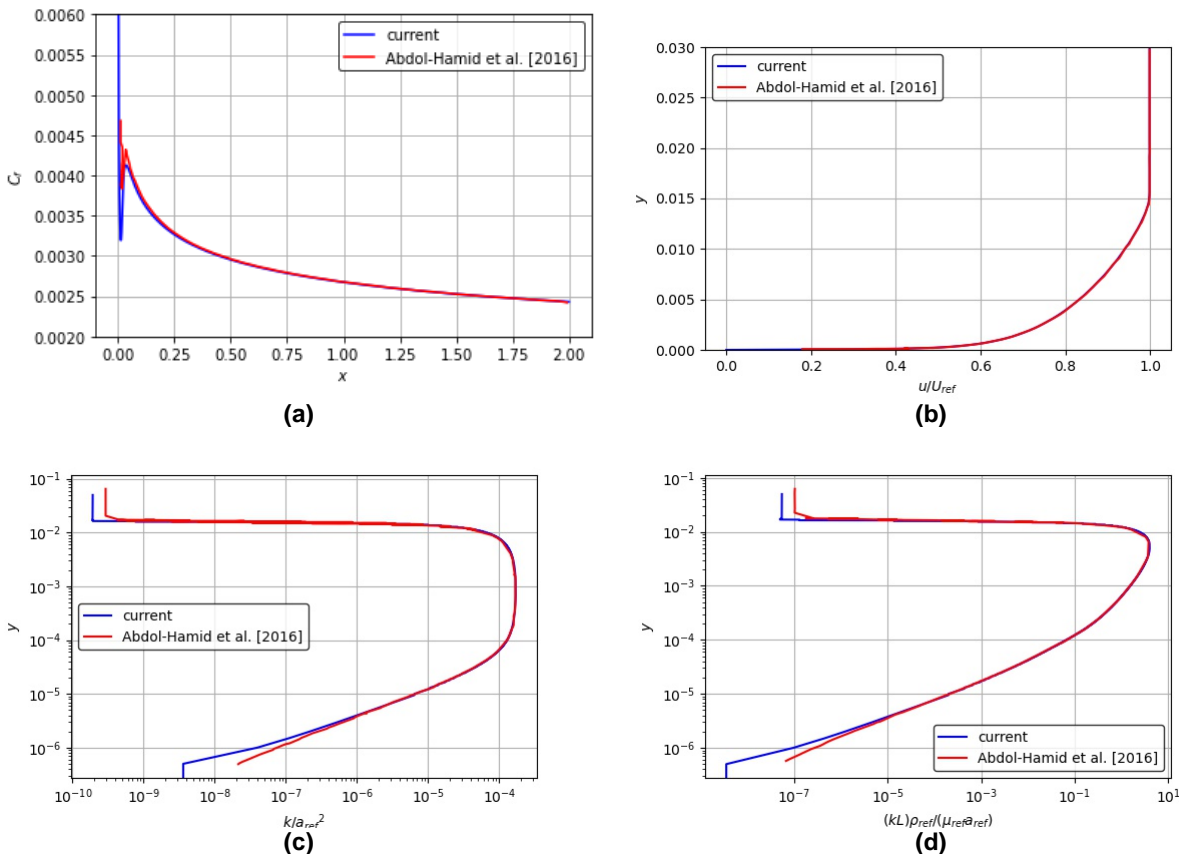


Figure 4. Verification of $k - kL$ implementation; zero pressure gradient flat plate; (a) to (d): skin friction throughout the plate, velocity, k and kL profiles at $x=0.97$

Bump-in-channel

The results of the bump-in-channel case are, at first, examined qualitatively, as in the previous case. Figure 5

shows turbulent viscosity ratio fields computed by the current implementation of Abdol-Hamid (2021). The contour levels are relatively comparable to a particular location near the downstream end of the bump geometry. After this point, slightly higher turbulent viscosity levels

are predicted by the current implementation. The difference between maximum values of turbulent viscosity is considerably small. It should be noted that this region is exposed to adverse pressure gradient effects. Therefore various factors, e.g., flux scheme and wall distance calculation method, may contribute to this minor difference.

The skin friction coefficient is one of the most significant parameters for this test case. This parameter matches very well with the reference study, as seen in Figure 6. The large skin friction coefficient at the end of the solid wall is observed in most validation results with all turbulence models published on the NASA turbulence

page. Therefore deviations at this location can be ignored. The same plot also shows that pressure distribution is not affected, and it compares well with Abdol-Hamid’s results.

This test case is surprisingly challenging due to the adverse pressure gradient after the bump. The NASA turbulence modeling website provides the boundary layer profile plots at $x=0.75$ station, i.e., the peak point of the bump geometry. Profile plots in Figure 7 show a good correlation with the reference study, and minor differences in free-stream turbulence are ineffective on the boundary layer flow field, similar to the zero pressure gradient flat plate case.

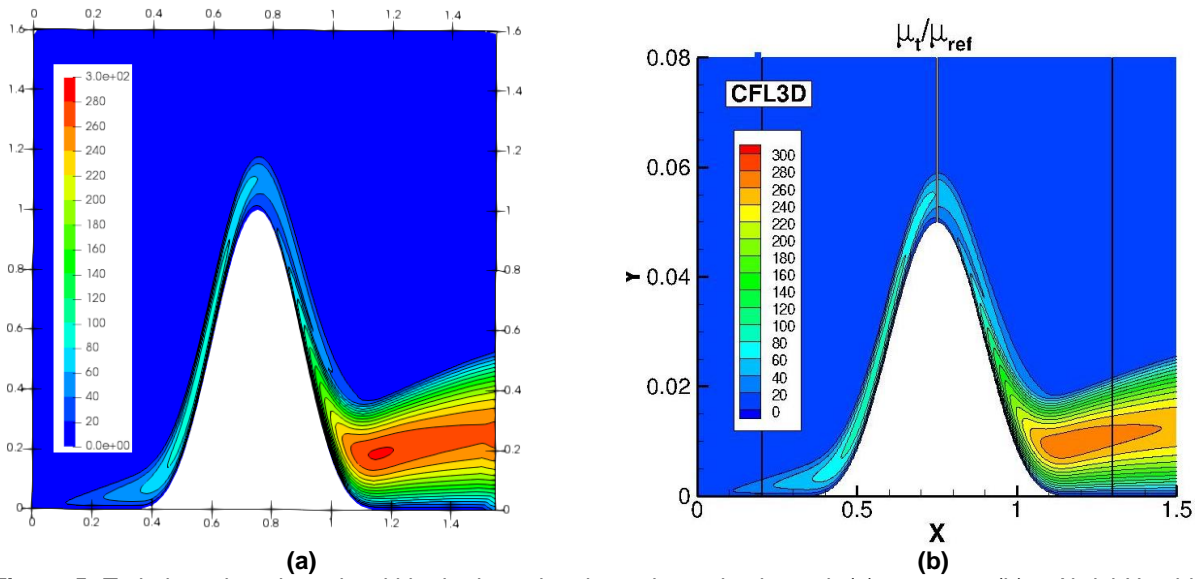


Figure 5. Turbulent viscosity ratio within the boundary layer; bump-in-channel; (a) – current, (b) – Abdol-Hamid et al. (2021)

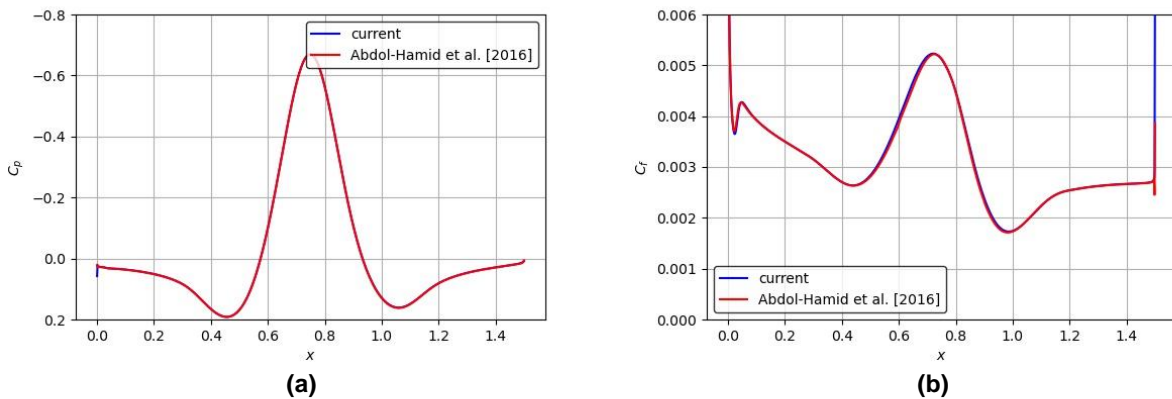


Figure 6. Verification of $k - kL$ implementation; bump-in-channel; pressure (a), and skin friction (b) distributions throughout the plate

Fin Trailing Vortex

An experimental study in Sandia National Laboratories investigated the isolated fin aerodynamics in upstream vortex flow generated by another fin (Beresh et al., 2009). The test was conducted at various speeds in the Mach number range between 0.50 and 0.80. The angles of both fins were adjustable to have different flow conditions. In this study, local flow measurements were conducted without the existence of the aft fin. The outcomes of this effort are considered helpful for assessing the current study thanks to the measurements of local flow quantities via particle image velocimetry (PIV) technique. Various parameters such as local velocity vector were measured in cross-planes at different locations providing the velocity deficit and vorticity quantities (Beresh et al., 2012).

Initial observations focused on the fin-tip vortex development in the PIV planes located at four cross-sections downstream of the fin at $x/c = 0.51, 1.18, 2.18, 4.18$, with c being root chord length. It was seen that the well-known RANS models could not accurately simulate the vortex core region due to overestimated turbulent viscosity and isotropic turbulence assumption. After $k - kL$ implementation, the fin trailing vortex case is repeated with this turbulence model. The velocity fields showing the vortex core behavior are depicted in Figure 10. It is clear that the vortex is more intensively preserved up to the most downstream cross-plane when $k - kL$ turbulence model is utilized. This behavior is much closer to the experimental results at the most downstream cross-plane location.

Turbulent viscosity ratio (TVR) distribution through vortex core explains the better-preserved vortex behavior of the $k - kL$ turbulence model. Figure 8 explicitly shows the influence of utilizing the $k - kL$ turbulence model on computed TVR compared to various forms of Shear Stress Transport (SST) turbulence model (Menter, 1994). In this context, we also applied rotation (R) (Dacles-Mariani et al., 1995) and rotation-curvature (RC) (Shur et al., 2000) correction implementations in order to achieve improved results with the SST turbulence model. The function of either correction is to limit the turbulence generation in the vortex core, where the elements of vorticity tensor are dominant over shear stress tensor. The magnitude of TVR computed by $k - kL$ turbulence model is even below those predicted by the rotational corrections applied on SST.

Tangential velocity profiles through vortex core obtained with all these variants together with those with $k - kL$ are presented in Figure 9. Tangential velocity distribution in the radial direction is significantly better predicted by $k - kL$ compared to all SST versions with and without vortex corrections. This is considered another piece of evidence that $k - kL$ turbulence model better predicts the vortex dynamics compared to SST.

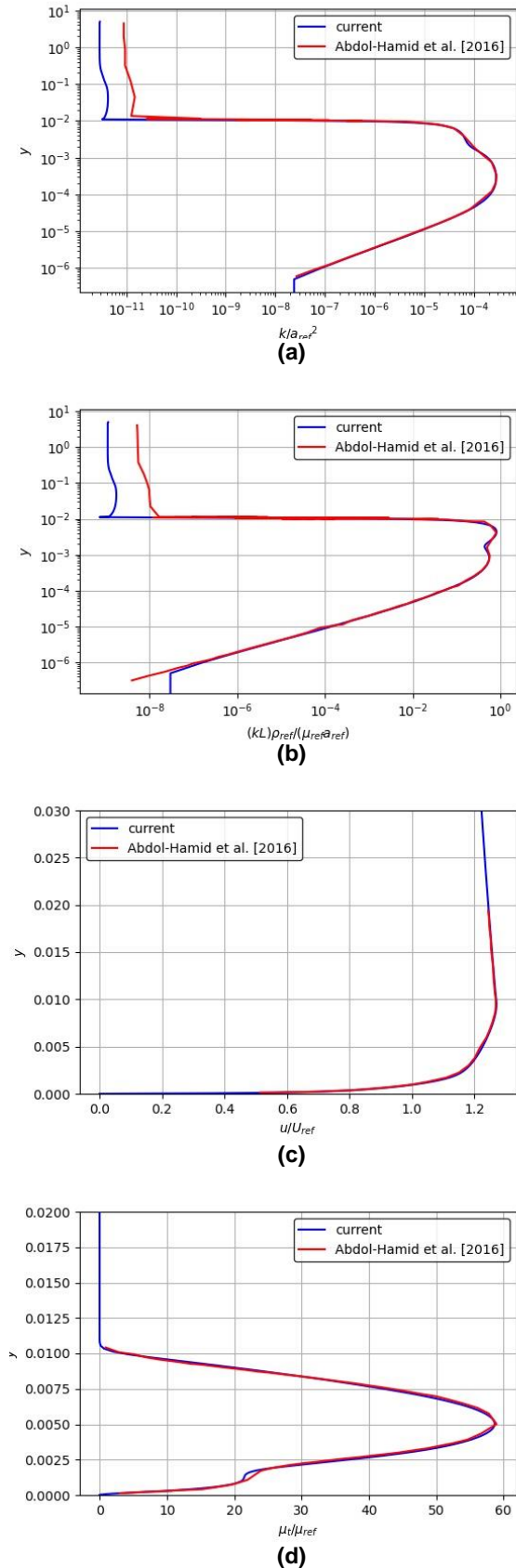


Figure 7. Verification of $k - kL$ implementation; bump-in-channel; (a) to (d): k , kL velocity and turbulent viscosity profiles at bump peak

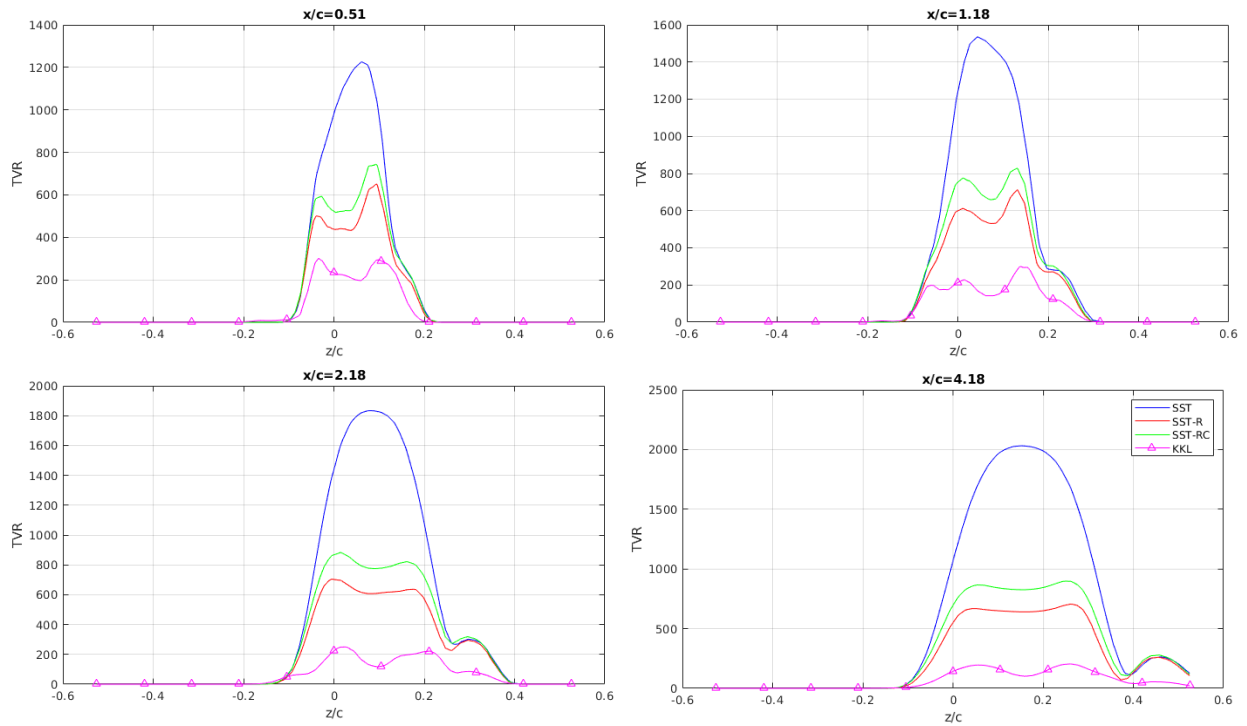


Figure 8. Turbulent viscosity ratio distribution through vortex core at different cross-sections; fin trailing vortex

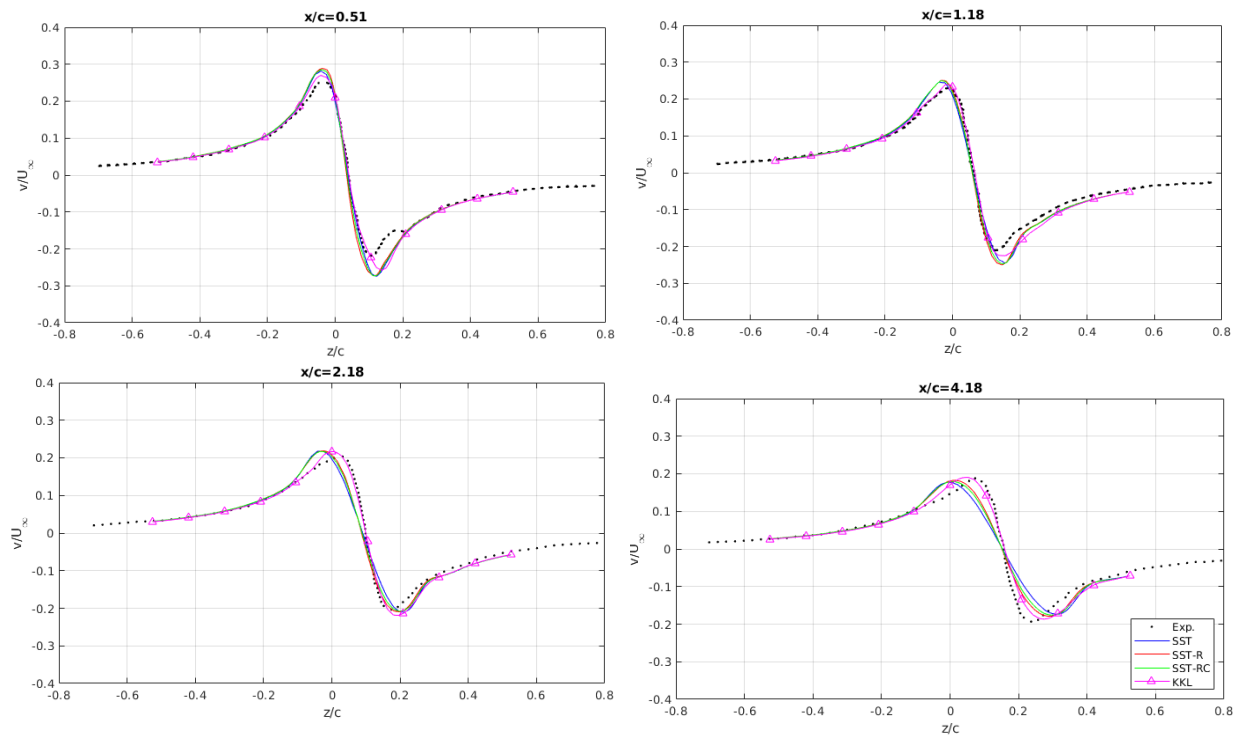


Figure 9. Tangential velocity distribution through vortex core at different cross-sections; fin trailing vortex; experimental results from Beresh et al. (2009)

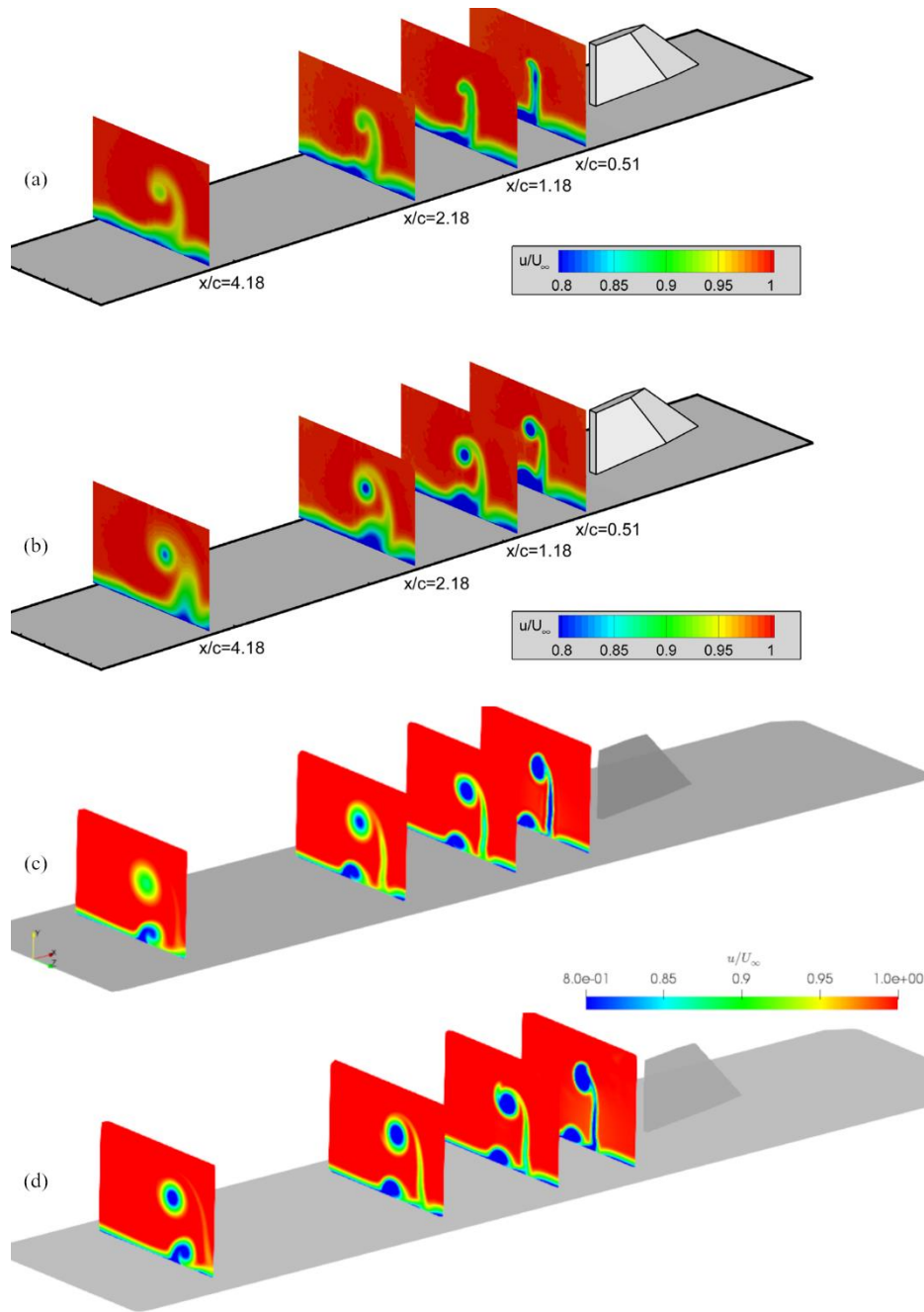


Figure 10. Velocity fields at several cross planes downstream of the fin; (a) experiment (Beresh et al., 2009), (b) SST (DeSpirito, 2016), (c) SST (current), (d) $k - kL$ (current); $M_\infty=0.80$, $Re=19 \times 10^6 m^{-1}$, $\alpha=10$

CONCLUSION

In this study, the first results of $k - kL$ turbulence model implementation in our CFD code are presented. Verification work is held using the data generated by the original developers of the model. The results match with a good margin.

The main aspect of the $k - kL$ turbulence model is the inclusion of the turbulent length scale L . The model developers claim that this feature enables the model to resolve different turbulence scales. This capability can be beneficial to resolve separated flows.

The tip vortex generated by the missile fins is an important and challenging topic. These vortices interact with the missile body and other fin-sets and significantly affect missile stability and flight characteristics. Therefore, we have selected a fin-vortex test case to assess the claimed turbulent length-scale resolution feature of the $k - kL$ model.

The fin trailing-vortex simulation results with $k - kL$ turbulence model predict the velocity profile at the vortex core considerably better than other commonly used two-equation turbulence models. The vortex strength is preserved better, and significantly less dissipation is observed. The reason for this superior vortex prediction capability at vortices is investigated. It is claimed that the

Turbulence Viscosity Ratio through the vortex core is significantly lower than the other two-equation models.

We are currently conducting further validation tests in a broad spectrum. The following studies will encompass challenging industrial problems with intensive vortex interactions.

REFERENCES

Abdol-Hamid, K. S., 2013, Assessments of-turbulence model based on Menter's modification to Rotta's two-equation model, AIAA Paper no: 2013-0341.

Abdol-Hamid, K. S., 2015, Assessments of k-kL turbulence model based on Menter's modification to Rotta's Two-equation model. *International Journal of Aerospace Engineering*, 987682.

Abdol-Hamid, K. S., 2019, Development of kL-based linear, nonlinear, and full Reynolds stress turbulence models. *In AIAA Scitech 2019 Forum*, 1878.

Abdol-Hamid, K. S., Carlson, J.-R., and Rumsey, C. L., 2016, Verification and validation of the k-kL turbulence model in FUN3D and CFL3D codes. *In 46th AIAA Fluid Dynamics Conference*, 3941.

Beresh, S.J., Henfling, J.F. and Spillers, R.W., 2009. Planar velocimetry of a fin trailing vortex in subsonic compressible flow. *AIAA Journal*, 47 (7), 1730-1740.

Beresh, S. J., Henfling, J. F., and Spillers, R. W., 2012, Turbulence of a fin trailing vortex in subsonic compressible flow. *AIAA Journal*, 50 (11), 2609–2622.

Dacles-Mariani, J., Zilliac, G. G., Chow, J. S., and Bradshaw, P., 1995, Numerical/experimental study of a wingtip vortex in the near field. *AIAA Journal*, 33(9), 1561–1568.

DeSpirito, J., 2016, CFD validation of interaction of fin trailing vortex with downstream control surface in high subsonic flow. *In 54th AIAA Aerospace Sciences Meeting*, page 1546.

Egorov, Y., Menter, F., Lechner, R., and Cokljat, D., 2010, The scale-adaptive simulation method for unsteady turbulent flow predictions. part 2: Application to complex flows. *Flow, Turbulence and Combustion*, 85 (1), 139–165.

Launder, B. E. and Spalding, D. B., 1983, The numerical computation of turbulent flows. *In Numerical prediction of flow, heat transfer, turbulence and combustion*, 96–116. Elsevier.

Levy, D. W., Laflin, K. R., Tinoco, E. N., Vassberg, J. C., Mani, M., Rider, B., Rumsey, C. L., Wahls, R. A., Morrison, J. H., Brodersen, O. P., et al., 2014, Summary of data from the fifth computational fluid dynamics drag

prediction workshop. *Journal of Aircraft*, 51 (4), 1194–1213.

Menter, F. R. and Egorov, Y., 2006, Revisiting the turbulent scale equation. *IUTAM Symposium on One Hundred Years of Boundary Layer Research*, 279–290, Dordrecht. Springer Netherlands.

Menter, F. R. and Egorov, Y., 2010, The scale-adaptive simulation method for unsteady turbulent flow predictions. Part 1: Theory and model description. *Flow, Turbulence and Combustion*, 85 (1), 113–138.

Rodi, W., 2006, Turbulence modelling for boundary-layer calculations. *In IUTAM Symposium on One Hundred Years of Boundary Layer Research*, 247–256. Springer.

Rotta, J., 1951, Statistische theorie nichthomogener turbulenz. *Zeitschrift für Physik*, 129(6), 547–572.

Rumsey, C. L., 2021, Turbulence modeling resource. <https://turbmodels.larc.nasa.gov>. (Accessed on 04/12/2022)

Rumsey, C.L. and Slotnick, J.P., 2015, Overview and summary of the second AIAA high-lift prediction workshop. *Journal of Aircraft*, 52 (4), 1006-1025.



DESIGN FIRE CURVE SELECTION OF SMALL SCALE POOL FIRES IN A SCALED METRO STATION

Umud Baris YILMAZ*, Oguz TURGUT**, Nuri YUCEL***, Muhammed İter BERBEROĞLU****

*Yuksel Proje A.S., Birlik Mahallesi 450. Cadde No: 23, 06610 Cankaya, Ankara / Turkey
barisyilmaz@yukselproje.com.tr, ORCID: 0000-0002-6103-7670

** ,***Gazi University, Faculty of Engineering, Department of Mechanical Engineering
06570 Maltepe, Ankara, Turkey

**oturgut@gazi.edu.tr, ORCID: 0000-0001-5480-1039

***nuyucel@gazi.edu.tr, ORCID: 0000-0001-9390-5877

****Turkish Aerospace Industry, Kahramankazan, Ankara, Turkey
militerx@yahoo.com, ORCID: 0000-0003-2957-5185

(Geliş Tarihi: 24.10.2021, Kabul Tarihi: 12.04.2022)

Abstract: n-heptane pool fire was numerically and experimentally investigated in a 1:100 scaled metro station. Fire Dynamics Simulator (FDS v6.7.5) has been applied to investigate smoke and temperature distribution by implementing different design curves in the station. Experimental and numerical studies were performed for 10 ml n-heptane fuel under zero piston effect. To develop performance-based design and to obtain reliable fire simulation results for structures, reasonable input conditions are essential for numerical studies. The aim of the study is to select most suitable fire design curve and make the numerical study independent of the experimental results for small scale hydrocarbon pool fires. In this study, t^2 , tanh, Eurocode 1 (BS EN 1991-1-2), exponential, and quadratic fire curves were investigated and validated with experimental results. The numerical results obtained using FDS were validated with experimental data and good agreement was observed for all design fire curves except quadratic one. It was observed that the exponential design fire curve predicted more similarly to the experimental data over the fire duration including growth, fully developed and decay phases. Regardless of the experimental results, it was seen that the temperature distribution results obtained from the numerical study using exponential fire design curve and the radiation / turbulence parameters obtained from the literature were found to have an average of 5% difference with the experimental results. It was also seen that the t^2 and tanh curves have acceptable differences of 6.92% and 9.02%, respectively, and the Eurocode HC is less suitable than the other curves with a difference of 12.17%. Therefore, it can be said that in small scale hydrocarbon pool fires, fire design can be done using exponential design curve.

Keywords: Fire development, Design fire curve, Pool fire, N-heptane, Fire dynamics simulator (FDS)

ÖLÇEKLENDİRİLMİŞ BİR METRO İSTASYONUNDA KÜÇÜK ÖLÇEKLİ SIVI HAVUZ YANGINLARININ YANGIN TASARIM EĞRİSİ SEÇİMİ

Özet: n-heptan havuz yangını 1:100 ölçekli bir metro istasyonunda sayısal ve deneysel olarak incelenmiştir. Fire Dynamics Simulator (FDS v6.7.5) yazılımı ile istasyonda farklı tasarım eğrileri uygulanarak duman ve sıcaklık dağılımı araştırılmıştır. Sıfır piston etkisi altında 10 ml n-heptan yakıt için deneysel ve sayısal çalışmalar yapılmıştır. Performansa dayalı tasarımı geliştirmek ve yapılar için güvenilir yangın simülasyon sonuçları elde etmek için sayısal çalışmalarda güvenilir girdiler tanımlamak gerekmektedir. Çalışmanın amacı, küçük ölçekli hidrokarbon havuz yangınları için en uygun yangın tasarım eğrisini seçmek ve sayısal çalışmayı deneysel sonuçlardan bağımsız hale getirmektir. Bu çalışmada, t^2 , tanh, Eurocode 1 (BS EN 1991-1-2), eksponansiyel ve ikinci dereceden yangın eğrileri incelenmiş ve deneysel sonuçlarla doğrulanmıştır. FDS kullanılarak elde edilen sayısal sonuçlar deneysel verilerle doğrulanmış ve ikinci dereceden hariç tüm yangın tasarım eğrileri ile uyumlu olduğu gözlenmiştir. Yangın süresi

boyunca büyüme, tam gelişme ve bozunma aşamalarını içeren eksponansiyel yangın tasarımı eğrisinin deneysel verilere daha yakın sonuçlar verdiği gözlemlenmiştir. Deneysel sonuçlardan bağımsız olarak, eksponansiyel yangın tasarımı eğrisi kullanılarak yapılan sayısal çalışmadan elde edilen sıcaklık dağılım sonuçları ile literatürden elde edilen radyasyon/türbülans parametrelerinin deneysel sonuçlarla ortalama %5 farklılık gösterdiği görülmüştür. Ayrıca t^2 ve tanh yangın tasarımı eğrilerinin de deneysel sonuçlarla %6.92 ve %9.02 gibi kabul edilebilir farklılıklar gösterdiği, Eurocode HC'nin ise %12.17'lik fark ile daha uzak olduğu gözlenmiştir. Bu nedenle küçük ölçekli hidrokarbon havuz yangınlarında eksponansiyel tasarımı eğrisi kullanılarak yangın tasarımının yapılabileceği söylenebilir.

Anahtar Kelimeler: Yangın gelişimi, Yangın tasarımı eğrisi, Havuz yangını, N-heptan, Fire dynamics simulator (FDS)

NOMENCLATURE

C_p	Specific heat of air, $J \cdot kg^{-1} \cdot K^{-1}$
C_V	Deardorff model constant, -
D^*	Characteristic fire diameter, m
D_F	Diffusivity of the fuel, $m^2 \cdot s^{-1}$
D_l	Material diffusivity, $m^2 \cdot s^{-1}$
f	Fuel, -
g	Acceleration of gravity, $m \cdot s^{-2}$
\tilde{h}	Favre-filtered enthalpy, $m^2 \cdot s^{-2}$
k	Time width coefficient, -
k_c	Thermal conductivity, $W/m \cdot K$
k_{sgs}	Turbulent kinetic energy, $m^2 \cdot s^{-2}$
L_f	Flame height, m
n	Retard index, -
P	Pressure, Pa
r	Amplitude, -
q^r	Radiative heat flux, $W \cdot m^{-2}$
\dot{Q}	Peak heat release rate, kW
\dot{Q}^*	Fire Froude number, -
S_L	Flame spread, $m \cdot s^{-1}$
t	Time, s
T	Temperature, K
T_∞	Temperature of air, K
u,v,w	Three components of velocity vectors, $m \cdot s^{-1}$
\bar{u}	Average value of u at the grid cell center, $m \cdot s^{-1}$
\hat{u}	Weighted average of u over the adjacent cells, $m \cdot s^{-1}$
\tilde{u}	Favre-filtered velocity, $m \cdot s^{-1}$
U	Overall heat transfer coefficient, $W \cdot m^{-2} \cdot K^{-1}$
\bar{w}_l	Favre-filtered species source term, -
y_s	Soot yield, $kg \cdot kg^{-1}$
\tilde{Y}_l	Favre-filtered mass species concentration, $kg \cdot m^{-3}$
Greek Letters:	
α	Fire growth rate, $kW \cdot s^2$
β_d	Ratio between the integrated energy at time t_d , (E_{tot, t_d}) and total energy released in the fire (E_{tot})
μ_{LES}	Turbulent viscosity, $kg \cdot m^{-1} \cdot s^{-1}$
Δ	LES filter width, m
$\bar{\rho}$	Filtered density, $kg \cdot m^{-3}$
ρ_∞	Density of air, $kg \cdot m^{-3}$
τ	Shear force, $N \cdot m^{-2}$

τ_{mix}	Mixing time, s
τ_{chem}	Chemical time scale, s
δx	Indicator of grid resolution
Subscripts:	
i, j, k	Three directions in co-ordinates
g	Growth
d	Decay

INTRODUCTION

Performance-based fire protection design is one of the most widely used engineering approaches to reduce the damage and devastating disasters caused by fire in structures. Fire simulation is used to determine the damage to the structure and measure the values such as smoke spread, temperature distribution, visibility and the amount of carbon monoxide in the environment, which are necessary for the safe evacuation of people from the structure during the development and propagation of the fire. These design methods give also direction to the building design at the point of taking passive fire precautions and determining escape distances. Combustion characteristics of materials including n-heptane and generation of fire products were investigated in detail in the literature (Tewarson, 1986; Khan et al., 2015).

A pool fire is defined as the turbulent diffusion fire burning above a horizontal pool of vaporizing hydrocarbon fuel where buoyancy is the controlling transport mechanism (Sudheer, 2013). The early works on liquid pool fires were performed by Blinov and Khudiakov (1957). Hottel (1959) and Hall (1973) studied the rates of burning of pools of hydrocarbon liquids for different diameters. Yao et al. (2013) developed a new modeling approach of n-heptane pool fire and validated by experimental data. Bordbar and Hostikka (2019) numerically obtained the spectral characteristics of radiation coming from a pool fire flame. Dobashi et al. (2016) performed experiments for small and middle scale n-heptane pool fires to understand the mechanisms of the flame height growth at fire whirled. Yin et al. (2013) built

an altitude chamber where they configured different dynamic pressure descent rates to simulate n-heptane pool fire behaviors under different low pressures. Burning rate, flame height, and fuel temperature distribution of small scale thin-layer n-heptane pool fires were experimentally studied for different pool diameters by Kang et al. (2010). Xin et al. (2002, 2005a, 2005b, 2005c) used FDS software to work on various pool fire scenarios. Hietaniemi et al. (2004) studied on several diameters of n-heptane pool fires.

In order to obtain reliable fire simulation results, reliable fire design curve and input parameters are essential. In this sense, there are various studies in the literature (Staffansson, 2010; Ciani and Capobellin, 2018; Baek et al., 2017; Ingason, 2009; Drysdale, 2011). Also Numajiri and Furukawa (1998) proposed a mathematical expression of the heat release rate curve by a simple equation. New fire design curves were suggested for the utilization in fire simulations (Baek et al., 2017, 2018). Literature study indicates a lack of knowledge about the small scale (≤ 10 cc) n-heptane pool fire. In this study, a 1/100 scale model of a real metro station was built and heat release rate, temperature distribution and visibility were investigated experimentally and numerically with zero piston effect condition along the station. Fire Dynamics Simulator (FDS v6.7.5) software was used to simulate an n-heptane pool fire development by means of available design fire curves in the literature to obtain the closest results to the experimental data.

The aim of this study is to select most suitable fire design curve and make the numerical study independent of the experimental results by not using the experimental results as numerical analysis input for small scale hydrocarbon pool fires.

EXPERIMENTAL SETUP

The model is a scale of the Maltepe Station on Ankaray Metro line located in Ankara/Turkey with a scale of 1:100. The Maltepe Station, built with the cut-and-cover method, has a 90 m platform and rectangular cross-section connection tunnels. In the design of the model,

platform length was taken as the characteristic length to be scaled. The model consists of three sections: inlet tunnel, station and outlet tunnel. The model constructed with heat resistant 5 cm thick autoclaved aerated concrete block. The ceiling and floors are covered with a 1 cm thick fiber-resin composite layer. In addition, the interior and exterior of the model were plastered in four layers with fireproof, heat-insulating plaster. Heat resistant glass was used on the symmetry plane to view experiments. Variable frequency driven fan located on the inlet tunnel was used to provide different inlet flow velocities. Besides, a honeycomb mesh was located on the inlet tunnel in order to maintain uniform airflow. The experimental setup of metro station consists of 3 rectangular sections including 900 mm x 324 mm x 220 mm (LxWxH) station and 1000 mm x 120 mm x 120 mm (LxWxH) inlet and outlet tunnels as can be seen in Fig. 1 (Berberoğlu, 2008).

During the experiments, the temperatures inside the station were measured by means of a K-type thermocouple located 5 cm above the 10 cm x 5 cm x 4 mm (LxWxH) in size. The pool contains 10 ml n-heptane fuel.

NUMERICAL MODEL

In the present study, Fire Dynamics Simulator (FDS v6.7.5) software was used to simulate an n-heptane pool fire development under different design fire curves. FDS is a computational fluid dynamics (CFD) model of fire-driven fluid flow, which was developed by the National Institute of Standards and Technology (NIST) (McGrattan et al., 2021a). FDS numerically solves low-speed, thermally driven flows, with an emphasis on smoke and heat transport from fires using Navier-Stokes equations (McGrattan et al., 2021a). Based on Navier-Stokes equations and Large Eddy Simulation (LES) model for turbulent flow, the governing equations are presented on the next section.



Figure 1. (a) Front and (b) rear view of the experimental setup

Computational Domain and Mesh Structure

The computational domain as shown in Fig. 2 consists of three rectangular sections including 900 mm x 324 mm x 220 mm ($L \times W \times H$) station and 1000 mm x 120 mm x 120 mm ($L \times W \times H$) inlet and outlet tunnels.

In the present study, n-heptane was used as fuel. The FDS fuel library was used to set the physical and chemical properties. HRRPUA (heat release rate per unit area) approach was used in the study and the agreement with experimental data was analysed. Four thermocouples were placed at the middle and T1:35 mm, T2:50 mm, T3:120 mm and T4:205 mm above the pool in order to trace temperature variations.

The ratio $D^*/\delta x$ is an indicator of grid resolution where D^* is the characteristic fire diameter and δx is the size of a grid cell. The ratio of 5 to 10 usually produces favorable

results at a moderate computational cost (Nureg 1824, 2007), (McGrattan et al., 2021b). D^* is given as

$$D^* = \left(\frac{\dot{Q}}{\rho_{\infty} C_p T_{\infty} \sqrt{g}} \right)^{2/5} \quad (1)$$

where \dot{Q} is heat release rate (HRR), ρ_{∞} is density of the air, T_{∞} is temperature of the air, C_p is specific heat of the air, and g is acceleration of gravity (9.81 m/s^2). Based on Eq. (1), D^* is calculated as 7.8 cm, which corresponds to $D^*/dx = 5$ for 1.56 cm and $D^*/dx = 10$ for 0.78 cm cell size (dx), respectively.

The Governing Equations and Boundary Conditions

The finite difference method has been employed in the solution of the three dimensional, time-dependent conservation equations of mass, momentum, energy and species.

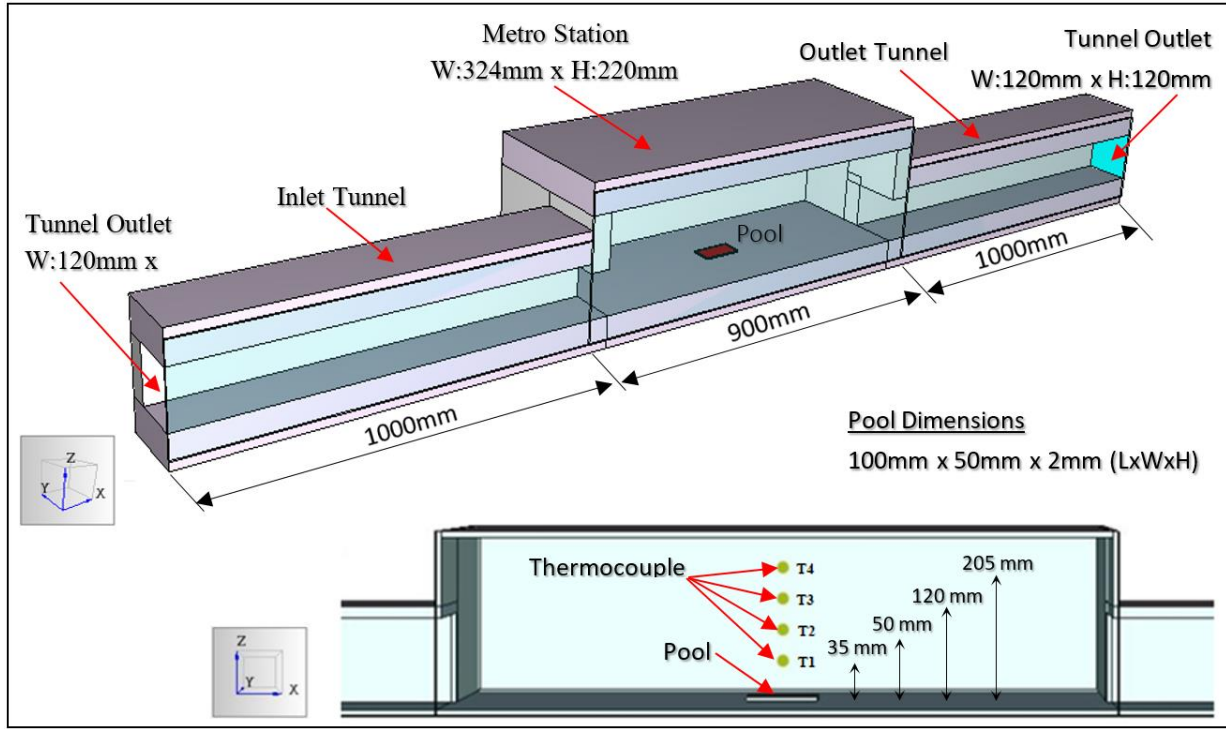


Figure 2. Computational model of the metro station

Thermal distribution and air flow are simulated by solving conservation equations. The filtering operation is applied to the three-dimensional time-dependent Navier–Stokes equations in order to remove the small turbulent scales of the total flow field and to obtain the filtered conservation equations to conduct large-eddy simulations (Aybay, 2010). The Favre-filtered conservation equations can be written as follows:

Conservation of mass:

$$\frac{\partial \bar{\rho}}{\partial t} + \frac{\partial \bar{\rho} \tilde{u}_j}{\partial x_j} = 0 \quad (2)$$

Conservation of momentum:

$$\frac{\partial \bar{\rho} \tilde{u}_i}{\partial t} + \frac{\partial}{\partial x_j} (\bar{\rho} \tilde{u}_i \tilde{u}_j) = -\frac{\partial \bar{p}}{\partial x_i} - \frac{\partial \bar{\tau}_{ij}}{\partial x_j} - \frac{\partial \tau_{ij}^{sgs}}{\partial x_j} + \bar{\rho} g_i + \bar{f}_{d,i} + \bar{m}_b''' \tilde{u}_{b,i} \quad (3)$$

Conservation of energy:

$$\frac{\partial (\bar{\rho} \tilde{h})}{\partial t} + \frac{\partial (\bar{\rho} \tilde{u}_j \tilde{h})}{\partial x_j} = \frac{D\bar{p}}{Dt} - \frac{\partial q_j^r}{\partial x_j} + \frac{\partial}{\partial x_j} (k_c \frac{\partial \bar{\tau}}{\partial x_j}) + \frac{\partial}{\partial x_j} \sum_l (\bar{\rho} D_l \tilde{h}_l \frac{\partial \tilde{Y}_l}{\partial x_j}) \quad (4)$$

Conservation of species:

$$\frac{\partial (\bar{\rho} \tilde{Y}_l)}{\partial t} + \frac{\partial (\bar{\rho} \tilde{u}_j \tilde{Y}_l)}{\partial x_j} = -\frac{\partial}{\partial x_j} (\overline{\rho u_j Y_l} - \bar{\rho} \tilde{u}_j \tilde{Y}_l) + \frac{\partial}{\partial x_j} (\bar{\rho} D_l \frac{\partial \tilde{Y}_l}{\partial x_j}) + \bar{w}_l \quad (5)$$

where k_c is the thermal conductivity, $\bar{\rho}$ is the filtered density, q^r is the radiative heat flux, D_l is the material diffusivity, \tilde{Y}_l is Favre-filtered mass species concentration, \tilde{h} is the Favre-filtered enthalpy, \tilde{u} is the Favre-filtered velocity, \bar{w}_l is the Favre-filtered species source term and Dp/Dt is the material derivative. The Favre-filtered quantities are denoted by $\tilde{\phi} = \overline{\rho \phi} / \bar{\rho}$.

FDS major features in its default operation were used for simulations in the present study (McGrattan et al., 2021a). This major features are large-eddy simulation (LES), low Mach number flow, explicit, second-order discretization, kinetic-energy-conserving numerics, lumped species method, deardoff eddy viscosity subgrid scale closure, constant turbulent Schmidt and Prandtl numbers, simple immersed boundary method for treatment of flow obstructions, eddy dissipation concept (fast chemistry) for single-step reaction between fuel and oxidizer, gray gas radiation with finite volume solution to the radiation transport equation and the rest of simulation parameters and boundary conditions are given in Table 1. In Table 1, U represents the overall heat transfer coefficient calculated based on local regulation for thermal insulation requirements for buildings (TS 825, 2013).

Table 1. Simulation parameters and boundary conditions

Surface Boundary Conditions	Wall: U=1.228 W/m ² K, u=v=w=0
	Ceiling: U=1.033 W/m ² K, u=v=w=0
	Floor: U=0.954 W/m ² K, u=v=w=0
	Glass: U=5.700 W/m ² K, u=v=w=0
Tunnel Outlets Boundary Conditions	$\frac{\partial P}{\partial x} = 0$, $\frac{\partial T}{\partial x} = 0$, $\frac{\partial u}{\partial x} = \frac{\partial v}{\partial x} = \frac{\partial w}{\partial x} = 0$
Environment Temperature	21°C
Grid	Structured, uniform, staggered grid
Soot Yield	0.037 kg/kg
CO Yield	0.01 kg/kg
Fuel	Heptane (C ₇ H ₁₆)
Fuel Volume	10cc
Pool Dimension	0.1 m x 0.05 m x 0.004 m (LxWxH)
HRR	1.89 kW

Turbulence Model

Turbulence model means the closure for sub-grid scales flux terms in LES. In order to close both the SGS momentum and scalar flux terms, the gradient diffusion is the turbulence model used in FDS. There are two turbulent transport coefficients: turbulent viscosity and the turbulent diffusivity. Turbulent viscosity is a mixing ratio that allows predicting the net effective mixing between species and fluids at sub-grid scales that cannot be resolved. The mesh size determines the smallest eddy scale that the software can resolve. To estimate the net effective mixing in each smaller cells, turbulent viscosity μ_{LES} is determined and multiplied by the velocity gradient of the fluid surrounding the cell. In order to obtain the turbulent diffusivity the constant Schmidt number and Prandtl number are used. In the present study the turbulent viscosity μ_{LES} and turbulent kinetic energy k_{sgs} are obtained based on the Deardorff model, which are given as follows (McGrattan et al., 2021a):

$$\mu_{LES} = \rho C_V \Delta \sqrt{k_{sgs}} \quad (6)$$

$$k_{sgs} = \frac{1}{2} ((\bar{u} - \hat{u})^2 + (\bar{v} - \hat{v})^2 + (\bar{w} - \hat{w})^2) \quad (7)$$

\hat{u} , \hat{v} , and \hat{w} are weighted average of u , v , and w over the adjacent cells, respectively.

Combustion Model

FDS uses mixing-controlled, infinitely fast combustion model. The turbulence-chemistry interaction is handled

with partially-stirred batch reactor model which is implemented in each computational cell where only the mixed composition can react. Here concentration is computed for each species and mixing degree. Reactant species are converted to product species at a rate determined by a characteristic mixing time, τ_{mix} expressed as follows (McGrattan et al., 2021a):

$$\tau_{mix} = \max(\tau_{chem}, \min(\tau_d, \tau_u, \tau_g, \tau_{flame})) \quad (8)$$

Physical processes associated with sub-grid scale (SGS) advections, molecular diffusion, and the buoyant acceleration are involved in Eq. (8).

Chemical time scale, τ_{chem} , is given as

$$\tau_{chem} \sim D_F / (S_L)^2 \quad (9)$$

Molecular diffusion time scale, τ_d , is

$$\tau_d = \frac{\Delta^2}{D_F} \quad (10)$$

Turbulent advection mixing time scale, τ_u , is expressed as

$$\tau_u = \frac{c_u \Delta}{\sqrt{(2/3)k_{sgs}}} \quad (11)$$

Buoyant acceleration mixing time scale, τ_g , is

$$\tau_g = \sqrt{2\Delta/g} \quad (12)$$

where SL is the flame spread, DF is the diffusivity of the fuel, Δ is the LES filter width, Cu is the time scale constant, g is the acceleration of gravity (9.81 m/s²), and τ_{flame} is the acceleration controlled mixing time scale for highly turbulent flames which is neglected since grid spacings stay within a quarter of the minimum flame dimension according to Heskestad correlation given below (McDermott et al., 2011).

$$\frac{L_f}{D} = 3.7(Q^*)^{2/5} - 1.02 \quad (13)$$

$$Q^* = \frac{\dot{Q}_c}{\rho_{\infty} c_p T_{\infty} \sqrt{g D} D^2} \quad (14)$$

where L_f is the flame height, D is the effective diameter of the base of the plume, Q^* is the fire Froude number, and \dot{Q}_c is the global heat release of the plume. Ambient values for temperature, specific heat, and density are taken to be $T_{\infty}=293$ K, $C_p=1.01$ kJ/kg·K and $\rho_{\infty}=1.20$ kg/m³, respectively.

Grid Sensitivity Analysis

The studied cell sizes and the total number of cells are given in Table-2. Mesh number 3 ($D^*/dx = 10$) has been selected which produces favorable results at a moderate computational cost.

Figure 3 shows the comparison of the predicted temperature variation 5 cm above the fire source with respect to time using four different grid resolutions, i.e., the coarse grid with cell size of 1.5 cm, the medium grid with cell size of 1.0 cm, the fine grid with cell size of 0.75 cm, and the extra-fine grid with cell size of 0.6 cm. The predictions with the coarse grid were found to have the largest discrepancies with the other grid resolutions. The results obtained with the fine grid, as employed in the present study, were found to be reasonably close to the predictions with the medium and extra-fine grid results. Therefore, the fine grid was chosen for the present study.

Table 2. Mesh descriptions

Mesh No	Cell Size [cm]	Number of Cell			
		Inlet Tunnel	Metro Station	Outlet Tunnel	Total
1	1.50	9648	23424	9648	42720
2	1.00	32400	79488	32400	144288
3	0.75	76608	188928	76608	342144
4	0.60	150300	367200	150300	667800

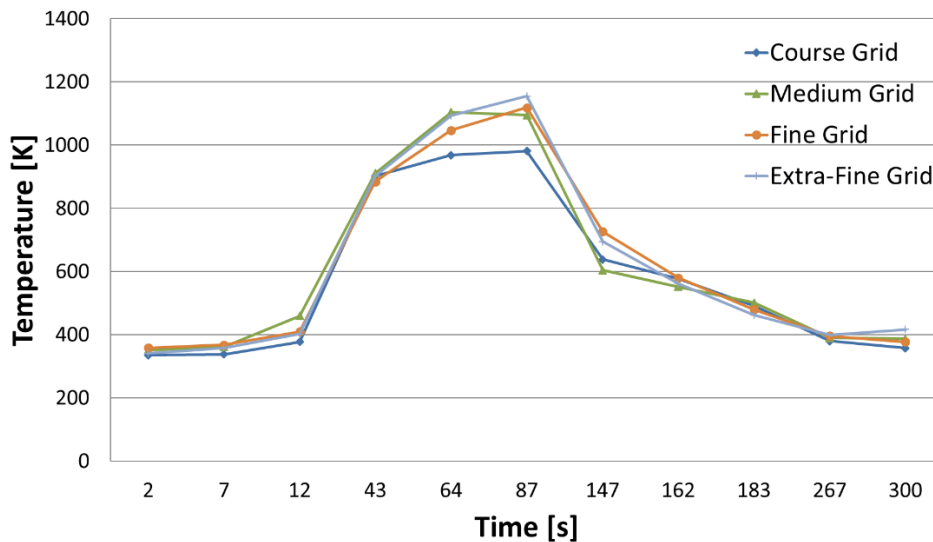


Figure 3. Grid sensitivity analysis

DESIGN FIRE CURVE

Performance-based design with numerical simulation is one of the engineering approach to reduce the loss of life and property due to fire. Validated user defined inputs such as turbulence parameters, radiation parameters, and

fire development curve should be used in order to obtain reliable fire simulation results. The fire curve is generally expressed as the variation of temperature or heat release rate (HRR) over time. The main phases are defined as growth, fully developed and decay shown in Fig. 4.

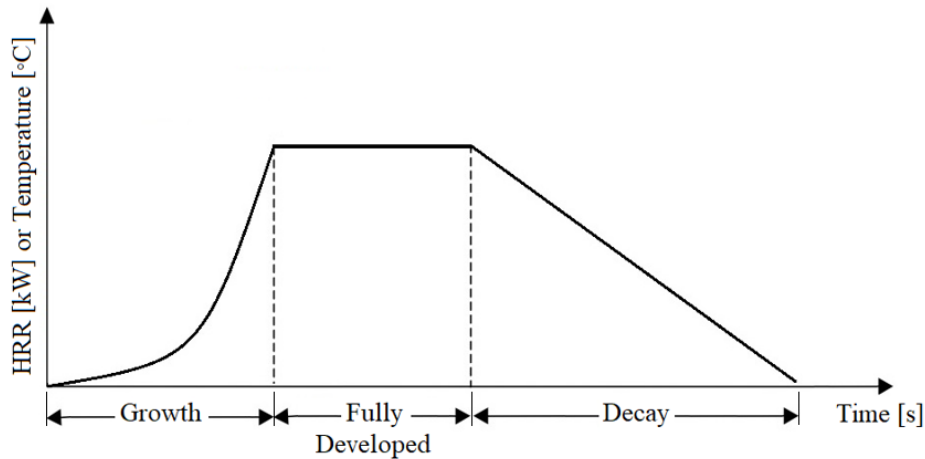


Figure 4. Typical schematic fire design curve

Table 3. Design fire curves used in the study

Case Number	Fire Development		
	Growth	Fully Developed	Decay
1	t^2 (NFPA 204, 2015)	Linear	t^2 (NFPA 204, 2015)
2	\tanh (McGrattan et al., 2021c)	Linear	t^2 (NFPA 204, 2015)
3	Eurocode 1 (BS EN 1991-1-2, 2002)	Linear	t^2 (NFPA 204, 2015)
4	Exponential (Ingason, 2009)		
5	Quadratic (Ingason et al, 2015)	Linear	Exponential (Ingason, 2009)

Fire growth is composed of the processes of ignition, flame spread, and burning rate (Quintiere, 1997). Fully developed phase starts when the growth phase has reached its maximum and continues up to combustible materials become run out. The final and usually the longest phase of fire named decay is characterized a significant decrease in fuel or oxygen, putting an end to the fire. Design fire curves can be linear, quadratic or exponential (Baek et al., 2017).

The design fire curve should be able to reflect the characteristics of the overall fire. Besides that, in particular, it is important to predict the behavior of the

growth phase to ensure fire safety. Based on this information, depending on the type of fire, the activation temperature of fire protection equipment such as heat detectors and sprinklers can be decided. Fire development is also important to foreseen evacuation times in metro stations and time required for the fire brigade to arrive at the scene, respond to the fire. In this study, several types of design fire curves in the literature (BS ISO-TR 13387-2 1999), (Ingason, 2009), (NFPA 204, 2015), (BS EN 1991-1-2, 2002) were used in numerical analysis to obtain the closest results to the experimental data. Design fire curves used in the study are tabulated and given on the Table 3.

t^2 fire curve

The heat release rate (HRR) in the fire growth phase is commonly expressed as follows. \dot{Q} is the HRR (kW), t is the time after ignition (s), and α is the fire growth rate (kW/s²).

$$\dot{Q} = \alpha \cdot t^2 \quad (15)$$

tanh fire curve

If the characteristic ramp-up time of the heat release rate per unit area which is defined as TAU_Q in FDS is greater than zero then the ramp up can be defined as tanh ($1/\tau$) at the software (McGrattan et al., 2021c). Hyperbolic tangent is a hyperbolic function that is the ratio of sinh to cosh. It was observed that the growth phase of the fire curve obtained from the experimental results is similar to the tanh curve development.

It is assumed that the fire starts to decay when 80% of the fuel has been consumed as per International Fire Engineering Guidelines (2005) and Staffansson (2010).

In this study, the α_g , α_d , t_g and t_d values used in the numerical analysis of the t^2 and tanh curves were calculated with the help of experimental results given in Fig. 5.

Eurocode 1 fire curve

Eurocode 1 hydrocarbon curve (BS EN 1991-1-2, 2002) was used at the growth phase of the Case 3 as indicated on Table 3. The curve of the growth phase was created by finding the temperature values for each second for 65 seconds. The development of the Hydrocarbon (HC) fire temperature curve is described by the following equation (BS EN 1991-1-2, 2002).

$$T = 20 + 1080(1 - 0.325e^{-0.167t} - 0.675e^{-2.5t}) \quad (16)$$

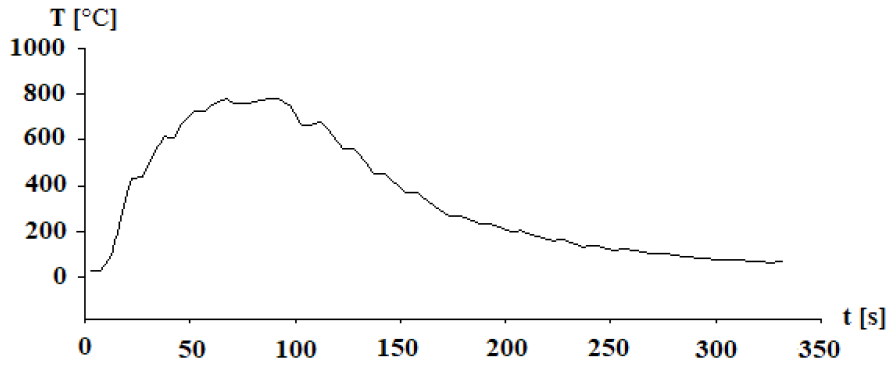


Figure 5. 10cc n-heptane pool fire temperature-time graph measured from T₂ point (Berberoğlu, 2008).

Exponential fire curve

Ingason (2009) suggested a single exponential function for fire design, instead of evaluating the fire development in three separate time phases. Ingason's (2009) fire design is based on Numajiri and Furukawa's works (1998) and it is only applicable to fuel-controlled fires with a small or negligible constant maximum heat release rate period. \dot{Q}_{max} is the maximum HRR (kW), E_{tot} is the total calorific value (kJ), and n is the retard index. With the help of these parameters, the time to total fire duration t_d (s), and the time to reach maximum HRR, t_{max} (s), were calculated. Other parameters r and k are calculated based on \dot{Q}_{max} and E_{tot} (Ingason, 2009). The time dependent HRR ($\dot{Q}(t)$) can be calculated with the following equation:

$$\dot{Q}(t) = \dot{Q}_{max} \cdot n \cdot r \cdot (1 - e^{-k \cdot t})^{n-1} \cdot e^{-k \cdot t} \quad (17)$$

where k shows the time width and is calculated as follows:

$$k = \frac{\dot{Q}_{max}}{E_{tot}} \cdot r \quad (18)$$

In Eq. (17) r and n represent the amplitude and retard index, respectively. The amplitude could be obtained as follows:

$$r = (1 - \frac{1}{n})^{1-n} \quad (19)$$

$$n \approx 0.74294e^{(2.9\dot{Q}_{max}t_{max}/E_{tot})} \quad (20)$$

t_{max} and t_d are calculated by the following equations:

$$t_{max} = \frac{\ln(n)}{k} \quad (21)$$

$$t_d = \frac{1}{k} \ln\left(\frac{1}{1-\beta_d^{(1/n)}}\right) \quad (22)$$

where

$$\beta_d = E_{tot,t_d}/E_{tot} \quad (23)$$

and E_{tot,t_d} is integrated energy at time t_d .

Quadratic fire curve

A time-dependent design fire curve for various road tunnel fires with a quadratic growth from zero to time t_{max} was proposed by Ingason (Ingason et al., 2015). The design curve includes quadratic growth, constant maximum HRR value to the time to decay t_D and an exponential decrease from the maximum HRR value to zero. Time dependent HRR, time to reach maximum HRR t_{max} (s) and time to start of decay period t_D (s) can be calculated with the following equations (Ingason et al., 2015).

$$\begin{aligned} \dot{Q}(t) &= \alpha_{g,q} \cdot t^2 \quad (t \leq t_{max}), \quad \dot{Q}(t) = \alpha_{g,q} \cdot t_{max}^2 \quad (t_{max} < t < t_D), \\ \dot{Q}(t) &= \dot{Q}_{max} e^{-\alpha_{D,q}(t-t_D)} \quad (t \geq t_D) \end{aligned} \quad (24)$$

$$t_{max} = \sqrt{\frac{\dot{Q}_{max}}{\alpha_{g,q}}} \quad (25)$$

$$t_D = \frac{E_{tot}}{\dot{Q}_{max}} + \frac{2}{3} t_{max} - \frac{1}{\alpha_{D,q}} \quad (26)$$

Since the maximum HRR is very low ($Q_{max}=1.89$ kW), the time to decay obtained as negative value from the Eq. (22). Therefore, the quadratic curve was not included in the comparison study.

RESULTS AND DISCUSSION

Numerical simulations were performed with the Fire Dynamics Simulator (FDS v6.7.5) for an n-heptane pool fire in a 1:100 scaled metro station model based on the experimental study of Berberoğlu (2008) to evaluate the prediction performance of quadratic, exponential, linear, t^2 and combination of design fire curves. In addition, it was aimed to perform numerical analysis and determine the most appropriate parameters and fire curves for predicting small scale pool fires without using experimental data.

Design fire curves implemented in the FDS code are shown in Fig. 6. The t^2 , tanh and exponential curves have been dimensionalized by using instantaneous HRR over peak HRR, and for Eurocode curve by using instantaneous temperature over maximum temperature. The values of the fire growth rate α for growth and decay phases of the fire curve have been taken from experimental data. It was observed that Eurocode and tanh curves were more compatible with the curve obtained from the experimental results.

Detailed results obtained for different fire development curves have been presented in this part of the study. First of all, the numerical results have been validated with experimental results. Fig. 7 shows the time-temperature curves obtained for mentioned fire designs and experimental result. The data have been obtained 5 cm above the pool.

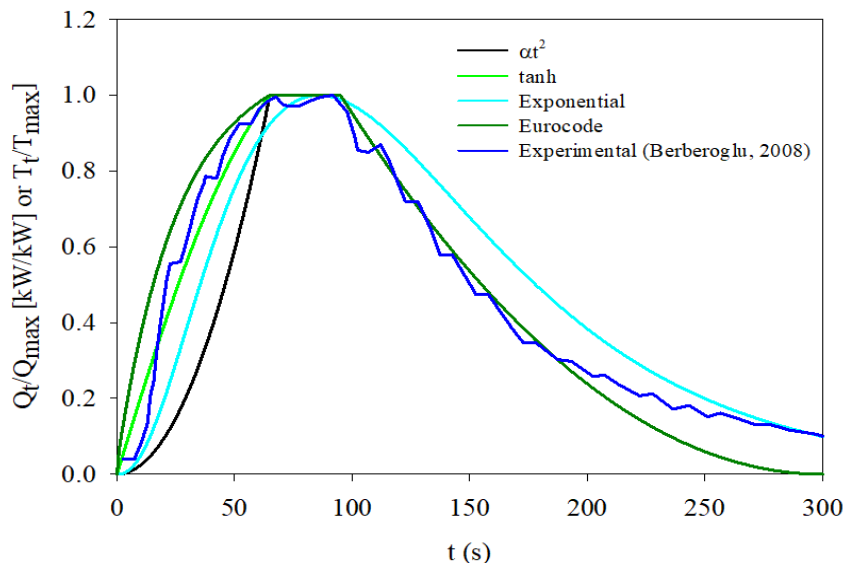


Figure 6. Design fire curves

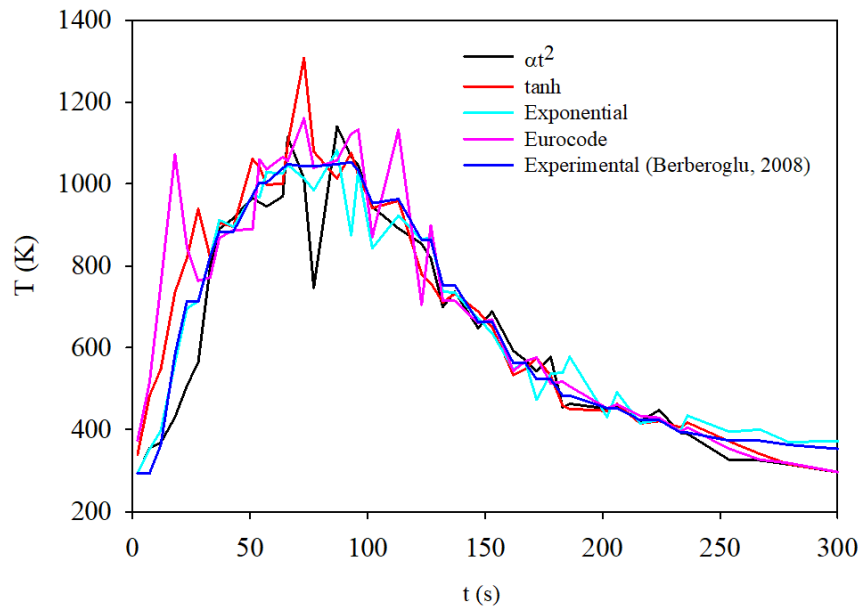


Figure 7. Time-temperature curves for numerical and experimental results

The predictions with αt^2 , tanh and exponential design curves are reasonably good agreement with each other and with the experimental data. Accordingly, it has been observed that the most suitable fire design curve was obtained as the exponential design curve which showed an average difference of 4.59% with the experimental results. It has been seen that the t^2 and tanh curves have acceptable differences of 6.92% and 9.02%, respectively, and the Eurocode HC is less suitable than the other curves with a difference of 12.17%. It is also stated in the literature that the exponential curve gives good results in pool fires with a short or negligible fully developed phase (Numajiri and Furukawa, 1998, Ingason, 2009, Ingason et al, 2015).

The experimental and numerical analysis results obtained from T1, T3 and T4 thermocouple positions given in Fig. 2 are compared in Fig. 8. The numerical data obtained using the exponential fire development curve were found to be in agreement with the test results. Since the T1 thermocouple is just above the fire and the graph reflects the instantaneous data, oscillation was observed in the numerical results. In the experimental study, it is seen that the oscillation is low because the measurements were taken at longer intervals.

The time – HRR curves obtained using different design curves are given in Fig. 9. Accordingly, it is understood that all results are compatible with each other. However, as it is observed in Fig. 9, it is seen that the Eurocode

curve and Exponential curve are of higher order than the other curves in the development and decay phase, respectively.

Temperature distributions along the station at the level of $z=205$ mm and $z=120$ mm above the floor are obtained from numerical analysis and given in Fig. 10. It is seen that the temperature distribution is higher on the upper plane and reaches up to 720 K. Also it is observed that minimum temperature on the occupied zone is around 480 K which is higher than the tenability temperature.

The temperature distribution images obtained along the plane passing through the center of the station at $t=80$ s (peak HRR) by using different fire design curves are given in Fig. 11 below.

It is observed in Fig. 11 that different temperature distributions are obtained especially in the ceiling region of the station by using different fire design curves. It is also observed that high temperature values are more distributed along the ceiling compared with the exponential case. In addition, it is seen that Eurocode 1 curve releases more heat than other curves in the period up to t_{max} . Hence, it is understood that the fire design selection is important to obtain accurate temperature distribution. This is attributed to fire design curve (Fig. 6) which reaches higher temperatures sooner compared with the other curves.

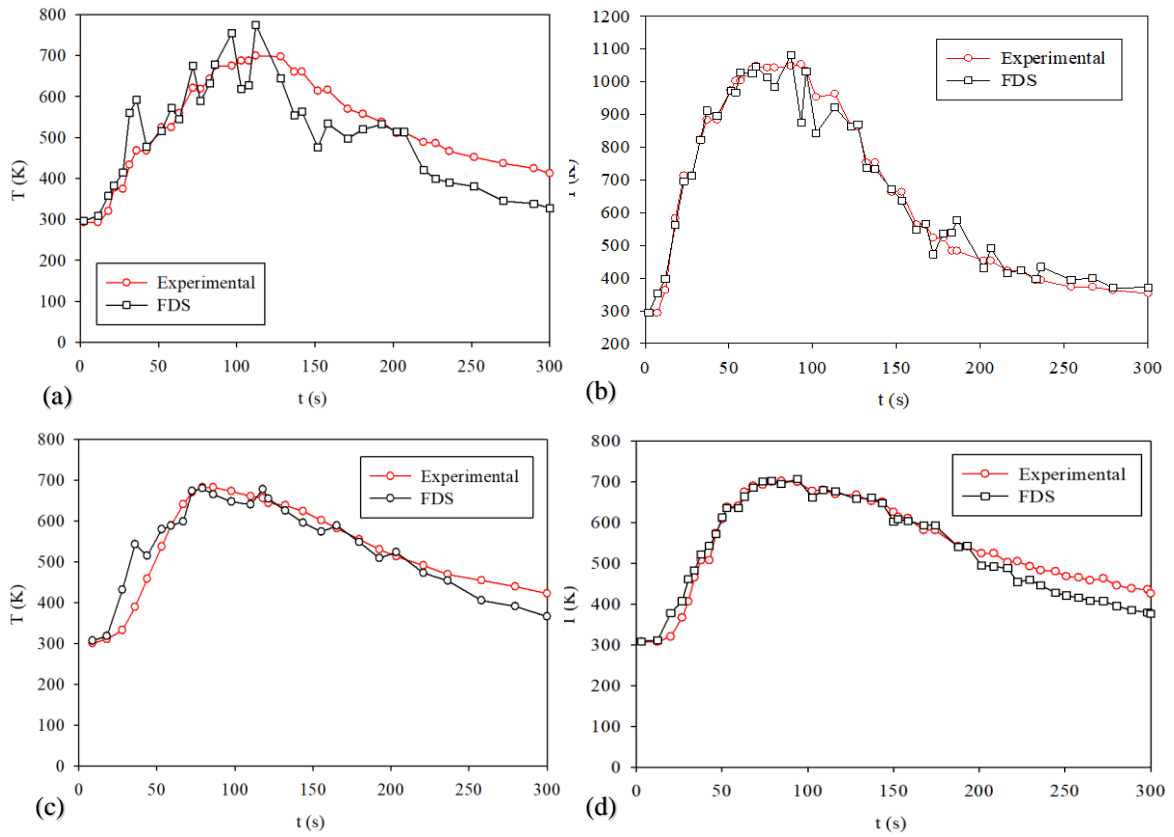


Figure 8. Time-temperature curves for (a) T1, (b) T2, (c) T3, and (d) T4 thermocouple

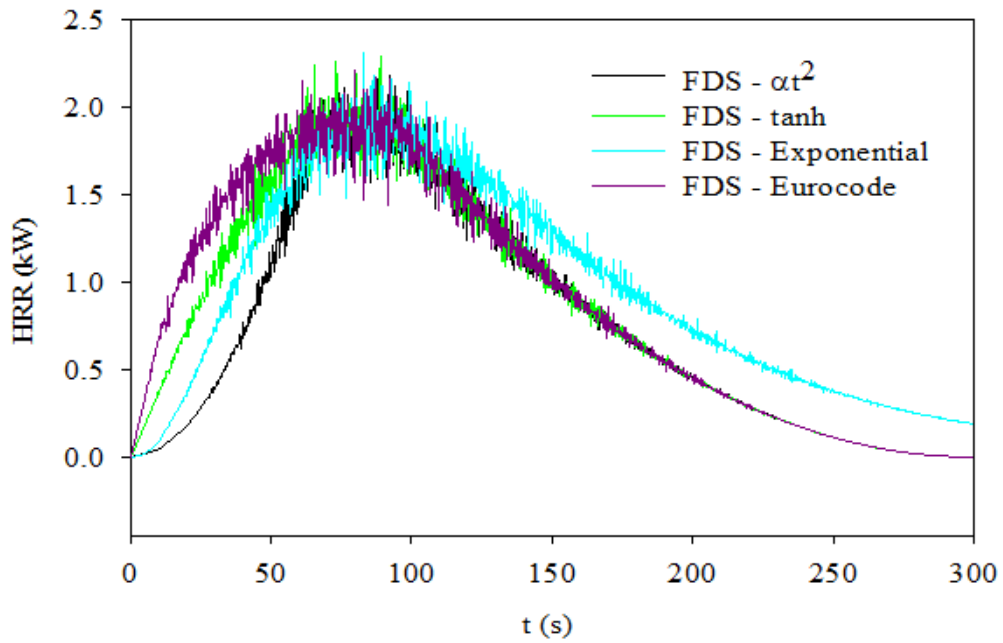


Figure 9. Time-HRR curves for different numerical results

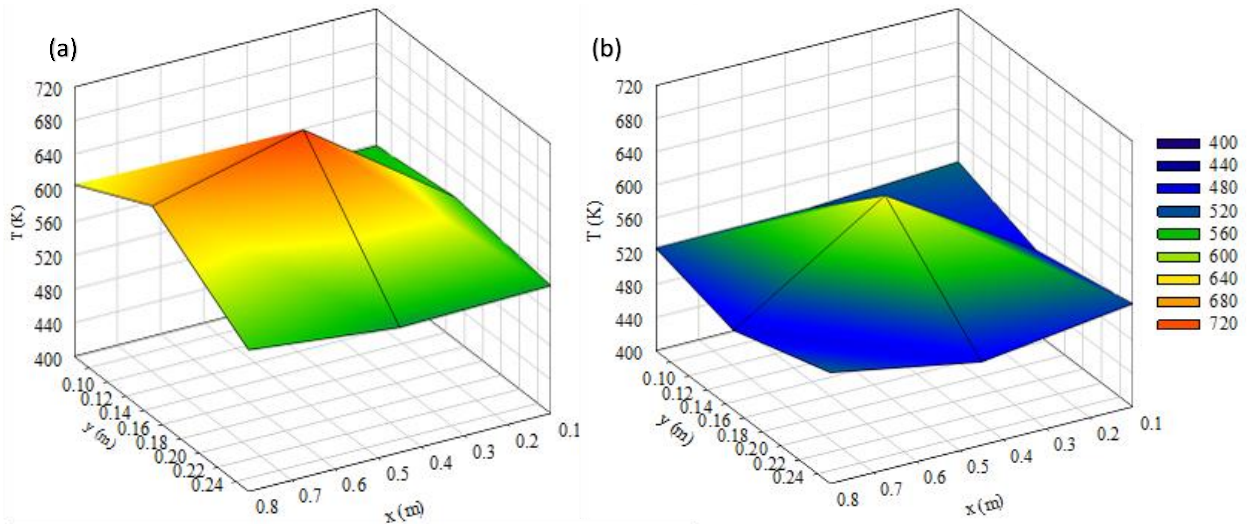


Figure 10. Temperature distributions at the level of $z=205$ mm (a) and $z=120$ mm (b) along the station

The soot distributions obtained along the same plane for different time steps by using exponential design curve are given in Fig. 12.

As can be seen from Fig. 12, it is understood that the soot level in the station rises at the 60th second when the combustion comes to peak heat release rate and the soot remains at the same level for 2 minutes, then it is exhausted from the tunnel outlets over time.

The carbon monoxide (CO) content obtained along the same plane for different time steps by using exponential design curve are given in Fig. 13.

According to NFPA 130 (2020) the maximum carbon monoxide exposure should not be more than 1706 ppm for sensitive populations up to four minutes. As can be seen in Fig. 13 the amount of CO at 240 seconds (4th minute) is found to be around 120 ppm and below the value specified in the standard.

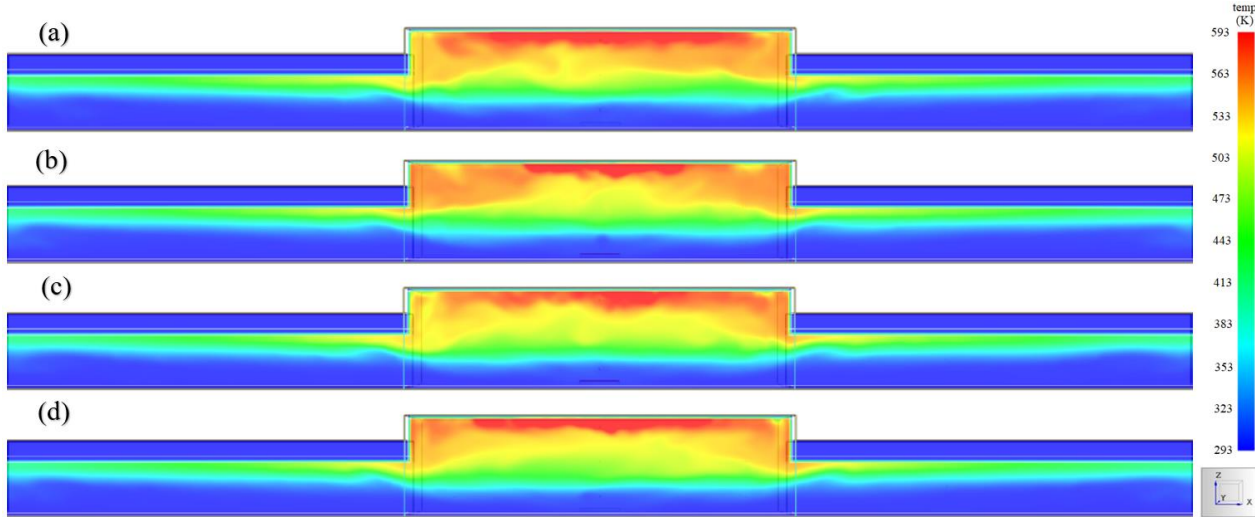


Figure 11. The temperature distribution along the station at the center of the station for (a) αt^2 , (b) tanh, (c) exponential, and (d) Eurocode 1 fire curves

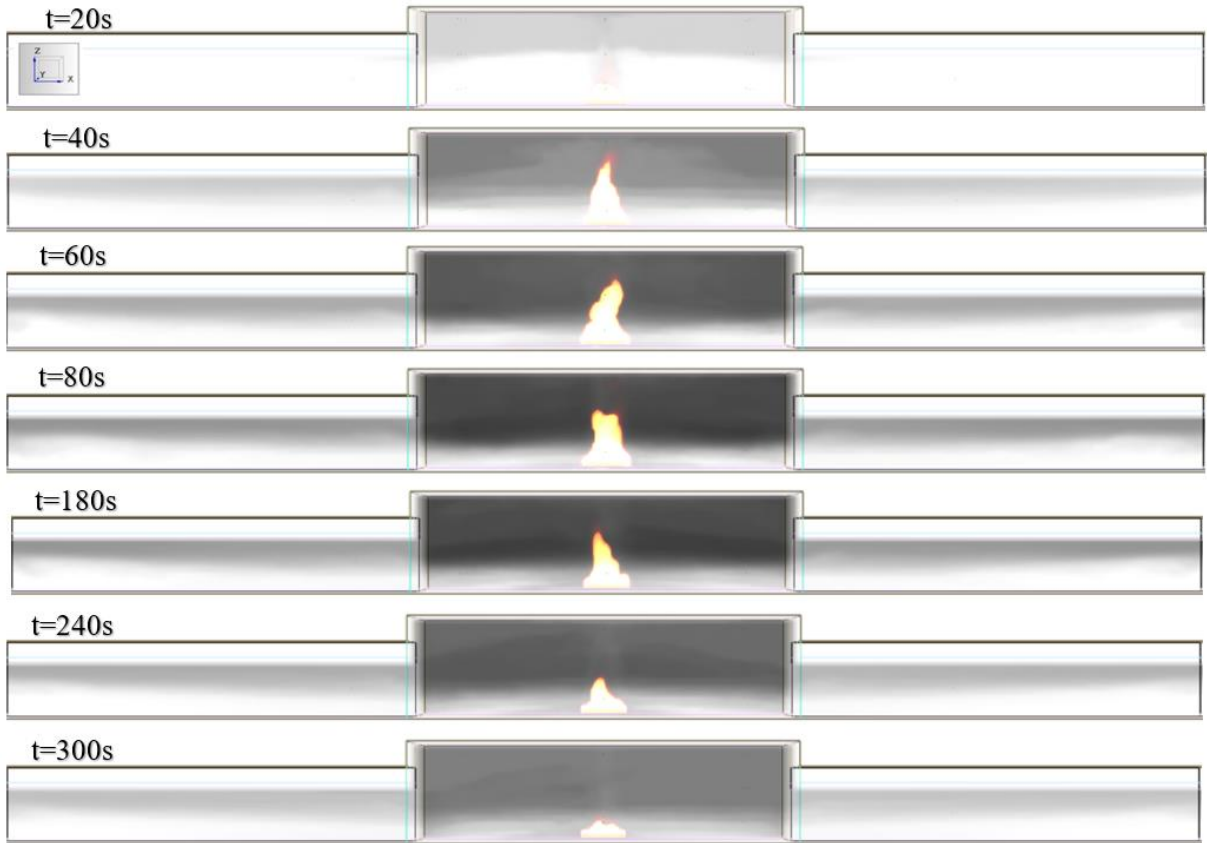


Figure 12. The soot distribution along the station during fire

The visibility obtained along the same plane for different time steps by using exponential design curve is given in Fig. 14. According to NFPA 130 (2020), in places where emergency lighting and exit indicators should be discernible at 30 m, and the visibility of doors and walls should be at least 10 m in order not to hinder evacuation.

If the visibility is below these values, loss of vision due to smoke could make the occupants lose their sense of direction and thus cause heavier losses. As can be seen in Fig. 14 the visibility is under 10 m after 60 seconds. For this reason, it is understood that a forced ventilation system should be installed in the metro stations.

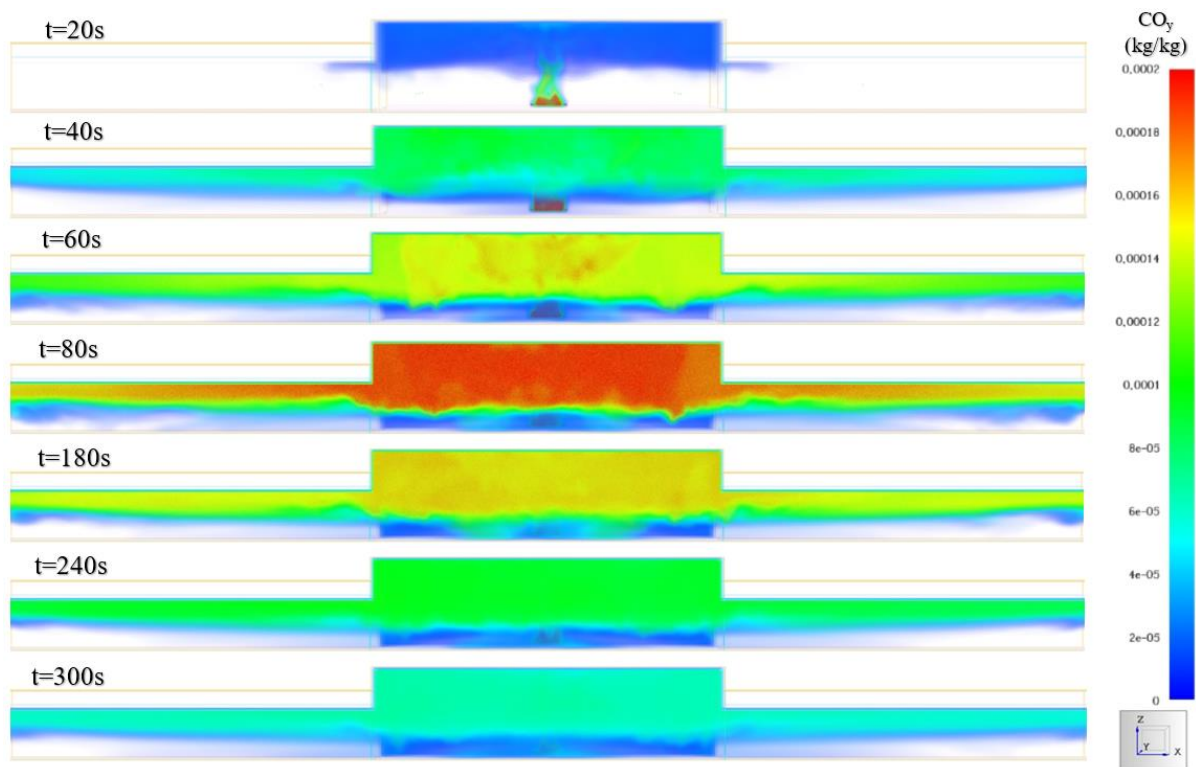


Figure 13. The CO content obtained along the station during fire

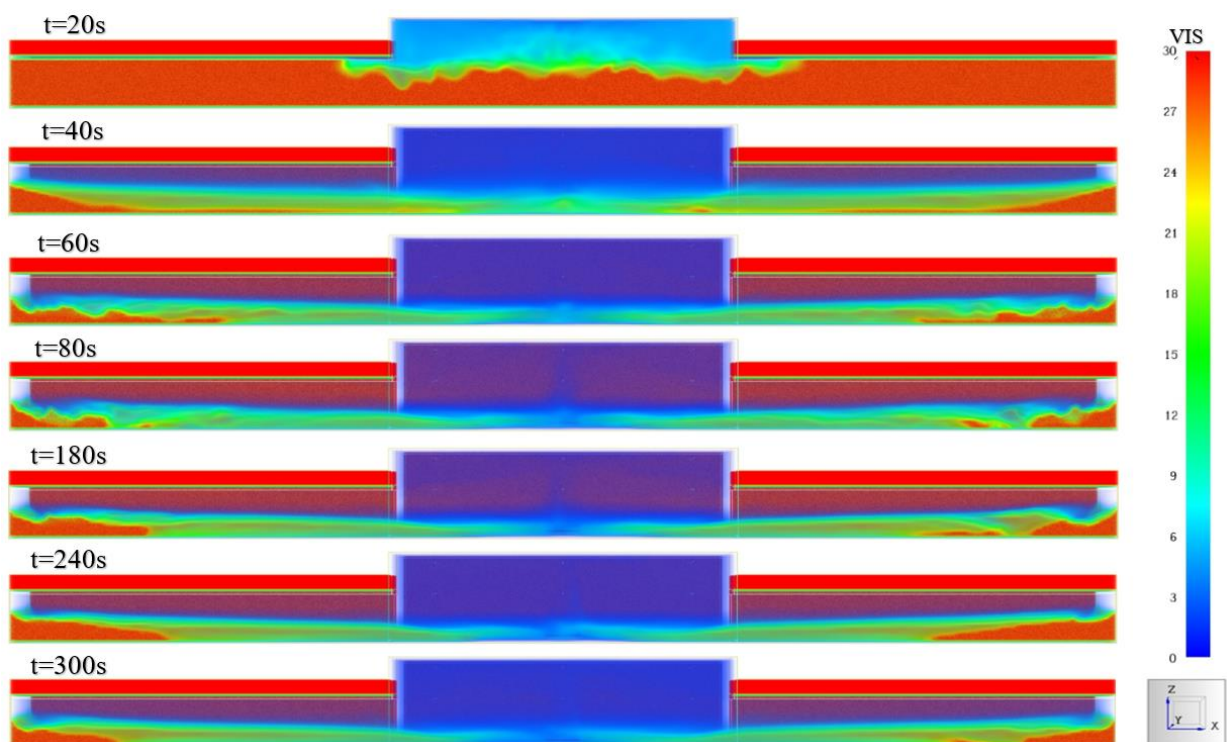


Figure 14. Visibility along the station during fire

CONCLUSIONS

In this study, experimental and numerical simulations are performed for an n-heptane pool fire in a 1:100 scaled metro station model to evaluate the prediction performance of quadratic, exponential, linear, t^2 and combination of the design fire curves. In addition, it is aimed to perform numerical analysis and determine the most appropriate parameters and fire curves for predicting small scale pool fires without using experimental data. The most important conclusions depicted from the findings are presented below:

- The numerical results obtained using FDS are validated with experimental data and good agreement is observed for all design fire curves between 4.59% to 9.02%, except Eurocode HC one which is less suitable than the other curves with a difference of 12.17%.
- It is observed that the exponential design fire curve predicted more similarly to the fire growth phase with about 1.2% mean difference measured in the experiment and duration of fire with about 4.49% mean difference better than the design fire curves proposed by other studies.
- Results showed that the visibility is under 10 m after 60 seconds. For this reason, it is understood that a forced ventilation system should be installed in the metro stations.
- It is observed that the carbon monoxide content obtained as 120 ppm, which is far below the tenability limit of 1706 ppm that affect human health in the standards.
- It is seen that the HRR obtained via Eurocode and exponential curves is of higher order than the other curves in the development and decay phase, respectively. It was observed that there was an average difference of 8.4% between the HRR values obtained with the Eurocode and tanh fire development curves.
- Regardless of the experimental results, it is seen that the temperature distribution results obtained from the numerical study using exponential fire design curve and the radiation / turbulence parameters obtained from the literature are found to have an average of 5% difference with the experimental results. Therefore, it can be said that in small scale hydrocarbon pool fires, fire design can be done using exponential design curve.

- Further numerical and experimental works are needed in the future to have in sight of pool fires for different type of fuels and sizes to validate fire design curves.

ACKNOWLEDGEMENTS

The authors of this article declare that the materials and methods used in this study do not require ethical committee permission and/or legal-special permission.

REFERENCES

- Australian Government, State and Territories of Australia, *International Fire Engineering Guidelines*, 2005.
- Aybay, O., 2010, *Time-Conservative Finite-Volume Method with Large-Eddy Simulation for Computational Aeroacoustics*, Ph.D. Thesis, Durham University, Durham, UK.
- Baek, B., Oh, C. B., Lee, E. J., 2017, Nam, D. G., Application Study of Design Fire Curves for Liquid Pool Fires in a Compartment, *Fire Sci. Eng.*, 31, 4, 43-51.
- Baek, B., Oh, C. B., Lee, C. Y., 2018, Evaluation of Modified Design Fire Curves for Liquid Pool Fires Using the FDS and CFAST, *Fire Sci. Eng.*, 32, 2, 7-16.
- Berberoğlu, M. İ., 2008, *Fire Modelling and Simulation for Subway Stations*, M.Sc. Thesis, Gazi University Institute of Science and Technology, Ankara, Turkey.
- Blinov, V. I. and Khudiakov, G.N., 1957, The Burning of Liquid Pools, *Doklady Akademi Nauk SSSR*, 113, 1094.
- Bordbar, H., Hostikka, S., 2019, Numerical Solution of LBL Spectral Radiation of a N-Heptane Pool Fire, *Proceedings of the 9th International Symposium on Radiative Transfer*, RAD-19.
- BS EN 1991-1-2 Eurocode 1: Actions on Structures - Part 1-2: General Actions - Actions on Structures Exposed To Fire, 2002.
- BS ISO-TR 13387-2 Fire Safety Engineering - Part 2: Design Fire Scenarios and Design Fires, 1999.
- Ciani, F., Capobellin, M., 2018, Fire Growth Rate Strategies in FDS, *3rd European Symposium on Fire Safety Science*.

- Dobashi, R., Okura, T., Nagaoka, R., Hayashi, Y., Mog, T., 2016, Experimental Study on Flame Height and Radiant Heat of Fire Whirls, *Fire Technol.* 52, 1069–1080.
- Drysdale, D., 2011, *An Introduction to Fire Dynamics*, A John Wiley & Sons, University of Edinburgh, Scotland, UK.
- Hall, A. R., 1973, Pool Burning: A Review, In *Oxidation and Combustion Reviews*, Volume 6 (ed. C.F.H. Tipper), 169–225, Elsevier, Amsterdam.
- Hietaniemi, J., Hostikka S., and Vaari J., 2004, *FDS Simulation of Fire Spread – Comparison of Model Results with Experimental Data*, VTT Working Papers 4, VTT Building and Transport, Espoo, Finland.
- Hottel, H. C., 1959, Review: Certain Laws Governing The Diffusive Burning Of Liquids by Blinov and Khudiakov (1957) (Dokl. Akad. Nauk SSSR, 113, 1096). *Fire Research Abstracts and Reviews*, 1, 41–43.
- Ingason, H., Li, Y. Z., Lönnemark, A., 2015, *Tunnel Fire Dynamics*, Springer, New York.
- Ingason, H., 2009, Design Fire Curves for Tunnels, *Fire Safety Journal*, 44, 259–265.
- Kang, Q., Lu S., Chen, B., 2010, *Experimental Study on Burning Rate of Small Scale Heptane Pool Fires*, *Chinese Science Bulletin*, 55, 10, 973–979.
- Khan, M., Tewarson, A., and Chaos, M., 2015, *Combustion Characteristics of Materials and Generation of Fire Products*, SFPE Handbook of Fire Protection Engineering, 5th ed. Springer, New York.
- McDermott, R., McGrattan K., and Floyd, J., 2011, A Simple Reaction Time Scale for Under-Resolved Fire Dynamics. In *Fire Safety Science – Proceedings of the 10th International Symposium*, 809– 820, University of Maryland, College Park, Maryland, USA.
- McGrattan, K., Hostikka, S., McDermott, R., Floyd, J., and Vanella M., 2021a, *NIST Special Publication 1018-1 Sixth Edition Fire Dynamics Simulator Technical Reference Guide Volume 1: Mathematical Model*.
- McGrattan, K., Hostikka, S., McDermott, R., Floyd, J., and Vanella M., 2021b, *NIST Special Publication 1018-3 Sixth Edition, Fire Dynamics Simulator, Technical Reference Guide VTT Technical Research Centre of Finland, Volume 3: Validation*.
- McGrattan, K., Hostikka, S., McDermott, R., Floyd, J., and Vanella M., 2021c, *NIST Special Publication 1019 Sixth Edition, Fire Dynamics Simulator User's Guide*.
- NFPA (National Fire Protection Association) 204 - *Standard for Smoke and Heat Venting*, 2015.
- NFPA (National Fire Protection Association) 130 - *Standard for Fixed Guideway Transit and Passenger Rail Systems*, 2020.
- Numajiri, F., Furukawa, K., 1998, Short Communication: Mathematical Expression Of Heat Release Rate Curve and Proposal of ‘Burning Index’, *Fire Mater*, 22, 39–42.
- NUREG -1824, *Verification and Validation of Selected Fire Models for Nuclear Power Plant Applications*, U.S. Nuclear Regulatory Commission, 2007.
- Quintiere, J. G., 1997, *Fire Growth: An Overview*, Fire Technology First Quarter, Department of Fire Protection Engineering, University of Maryland, College Park, USA.
- Staffansson, L., 2010, *Selecting Design Fires. Department of Fire Safety Engineering and Systems Safety*, Lund University, Sweden.
- Sudheer, S., 2013, *Characterization of Open Pool Fires and Study of Heat Transfer in Bodies Engulfed in Pool Fires*, Ph.D. Thesis, Indian Institute of Technology, Bombay, India.
- Tewarson, A., 1986, *Prediction of Fire Properties of Materials Part 1: Aliphatic and Aromatic Hydrocarbons and Related Polymers*, Technical Report NBS-GCR-86-521, National Institute of Standards and Technology, Gaithersburg, MD, USA.
- TS 825 Thermal insulation requirements for buildings, TSE Turkish Standard, 2013.
- Xin, Y., Gore J. P., McGrattan K.B., Rehm R.G., and Baum H.R., 2002, Large Eddy Simulation of Buoyant Turbulent Pool Fires, In *Twenty-Ninth Symposium (International) on Combustion*, 259–266. Combustion Institute, Pittsburgh, Pennsylvania.

Xin, Y., 2005a, Baroclinic Effects on Fire Flow Field, *In Proceedings of the Fourth Joint Meeting of the U.S. Sections of the Combustion Institute*, Combustion Institute, Pittsburgh, Pennsylvania, USA.

Xin, Y., Gore J. P., McGrattan K. B., Rehm R. G., and Baum H. R., 2005b, Fire Dynamics Simulation of A Turbulent Buoyant flame Using A Mixture-Fraction-Based Combustion Model, *Combustion and Flame*, 141, 329–335.

Xin, Y., and Gore, J. P., 2005c, Two-Dimensional Soot Distributions in Buoyant Turbulent Fires, *In Thirtieth Symposium (International) on Combustion*, Combustion Institute, Pittsburgh, Pennsylvania, USA.

Yao, W., Yin, J., Hu X., Wang, J., Zhang, H., 2013, Numerical Modeling of Liquid -Heptane Pool Fires Based On Heat Feedback Equilibrium, *Procedia Engineering*, 62, 377-388.

Yin, J., Yao, W., Liua, Q., Wua N., Zhou Z., Wuc Y., Zhang H., 2013, Experimental Study of N-Heptane Pool Fire Behaviors under Dynamic Pressures in an Altitude Chamber, *Procedia Engineering*, 52, 548-556.



FAST AND PREDICTIVE HEAT PIPE DESIGN AND ANALYSIS TOOLBOX: H-PAT

Samet SAYGAN^{a*}, Yigit AKKUS^{a**}, Zafer DURSUNKAYA^{b***} and Barbaros ÇETİN^{c****}

^aASELSAN Inc., 06200 Yenimahalle, Ankara, Turkey

^bDepartment of Mechanical Engineering, Middle East Technical University, 06800 Çankaya, Ankara, Turkey

^cMechanical Engineering Department, I.D. Bilkent University, 06800 Çankaya, Ankara, Turkey

*ssaygan@aselsan.com.tr, ORCID: 0000-0002-8392-6292

**yakkus@aselsan.com.tr, ORCID: 0000-0001-8978-3934

***refaz@metu.edu.tr, ORCID: 0000-0003-3711-0361

****barbaros.cetin@bilkent.edu.tr, ORCID: 0000-0001-9824-4000

(Geliş Tarihi: 28.12.2021, Kabul Tarihi: 12.04.2022)

Abstract: For the assessment of the thermal performance of heat pipes, a wide range of modeling is available in the literature, ranging from simple capillary limit analyses to comprehensive 3D models. While simplistic models may result in less accurate predictions of heat transfer and operating temperatures, comprehensive models may be computationally expensive. In this study, a universal computational framework is developed for a fast but sufficiently accurate modeling of traditional heat pipes, and an analysis tool based on this framework, named Heat Pipe Analysis Toolbox, in short H-PAT is presented. As a diagnostic tool, H-PAT can predict the fluid flow and heat transfer from a heat pipe under varying heat inputs up to the onset of dryout. During the initial estimation of phase change rates, the solutions of particular thin film phase change models are avoided by specifying an appropriate pattern for the mass flow rate of the liquid along the heat pipe rather than using finite element/volume based methods for the computational domain. With the help of a modular structure, H-PAT can simulate heat pipes with different wick structures as long as an expression for the average liquid velocity and corresponding pressure drop can be introduced. H-PAT is also capable of analyzing heat pipes with variable cross-sections, favorable/unfavorable gravity conditions and utilizes temperature dependent thermo-physical properties at evaporator, condenser and adiabatic regions together with heat input sensitive vapor pressure. In addition, H-PAT performs the computation very fast which also makes it a perfect design tool for researchers and design engineers in the field of thermal management.

Keywords: Heat pipe modeling, flat-grooved heat pipes, phase-change modeling, H-PAT

HIZLI VE ÖNGÖRÜLÜ ISI BORUSU TASARIM VE ANALİZ ARACI: H-PAT

Özet: Isı borularının termal performansının değerlendirilmesi için, literatürde basit kılcal limit analizlerinden kapsamlı 3D modellere kadar geniş bir modelleme yelpazesi mevcuttur. Basit modeller, ısı transferi ve çalışma sıcaklıklarının daha düşük doğrulukla tahmin ederken, kapsamlı modeller hesaplama açısından yük getirmektedir. Bu çalışmada, geleneksel ısı borularının hızlı fakat yeterince doğru bir şekilde modellenmesi için evrensel bir hesaplama yöntemi geliştirilmiş ve bu yöntemeye dayalı olarak Isı Borusu Analizi Araç Aracı, kısaca H-PAT olarak adlandırılan bir analiz aracı sunulmuştur. Bir tanı aracı olarak H-PAT, kuruma başlangıcına kadar değişen ısı girdileri altında bir ısı borusundan sıvı akışını ve ısı transferini tahmin edebilir. Faz değişim hızlarının ilk tahmini sırasında, hesaplama alanı için sonlu eleman/hacim tabanlı yöntemler kullanmak yerine, ısı borusu boyunca sıvının kütle akış hızı için uygun bir model belirlenerek belirli ince film faz değişim modellerinin çözümlerinden kaçınılır. Modüler bir yapının yardımıyla, H-PAT, ortalama sıvı hızı ve buna karşılık gelen basınç düşüşü için bir formülasyon sunulabildiği sürece farklı fitil yapılarına sahip ısı borularını simüle edebilir. H-PAT ayrıca değişken kesitli ısı borularını, yerçekiminin pozitif/negatif yönde etki ettiği koşullarını da analiz etme yeteneğine sahiptir ve ısı girdisine duyarlı buhar basıncı ile evaporatör, kondenser ve adyabatik bölgelerde sıcaklığa bağlı termo-fiziksel özellikleri kullanır. Buna ek olarak, H-PAT hesaplamayı çok hızlı gerçekleştirir ve bu da onu termal yönetim alanındaki araştırmacılar ve tasarım mühendisleri için mükemmel bir tasarım aracı haline getirir.

Anahtar Kelimeler: Isı borusu modellemesi, düz oluklu ısı borusu, faz değişimi modellenmesi, H-PAT.

NOMENCLATURE

Symbols

g	gravitational acceleration [m/s ²]
$\mathbb{G}(z)$	geometric function
h	height [m]
h_{fg}	latent heat of evaporation [J/kg]
k	thermal conductivity [W/m·K]
L	length [m]
M	molar mass of liquid [kg/mol]
\dot{m}	mass flow rate [kg/s]
\mathbf{n}	unit vector in normal direction
P	pressure [Pa]
\dot{q}	heat transfer rate [W]
\mathcal{R}	meniscus radius of curvature [m]
R	thermal resistance [K/W]
R_u	universal gas constant [J/mol·K]
T	temperature [K]
U	velocity [m/s]
V	volume [m ³]
w	width [m]

Greek Symbols

$\hat{\sigma}$	accommodation coefficient
δ	liquid film thickness [m]
ε	convergence criterion
θ	contact angle [rad]
ρ	density [kg/m ³]
μ	dynamic viscosity [Pa·s]
ν	kinematic viscosity [m ² /s]
σ	surface tension [N/m]
Δ	delta

Subscripts

a	adiabatic
ax	axial
b	base
c	condenser
$cond$	conduction
e	evaporation
f	fin
ft	fin top
g	groove
gf	groove film
l	liquid
m	mean
$p.c.$	phase change
s	solid
tf	thin film
tot	total
v	vapor

INTRODUCTION

Thermal management of electronics has always been an essential part of device design to secure operation without any thermal damage or performance degradation. Today, this is of utmost importance for high density electronics since the peak power density of modern chip technology is limited by the heat spreading ability of the thermal architecture. The key factor in the removal of hot

spots in high heat flux electronics is the minimization of thermal resistance of the path whereby the waste heat is conveyed to the heat sink. When the heat is transported through a solid media, thermal resistance is dictated by its thermal conductivity, a material property with a modest upper limit. This barrier, on the other hand, can be overcome by heat spreaders utilizing the liquid-vapor phase change mechanism to transport the energy. As the most prevalent, heat pipes have been serving thermal engineers for more than half a century (Grover *et al.*, 1964) in both terrestrial and space applications (Faghri, 1995; Reay *et al.*, 2013), in most cases without an alternative.

Heat pipe is a sealed container, in which liquid and vapor phases of a pure substance, the working fluid, continuously circulate to sustain the phase change heat transfer. Various types of heat pipes based on the routes of the phases exist, such as traditional heat pipes (cross flow of the phases along the same axis), loop heat pipes (different paths for the two phases) and pulsating heat pipes (conjugate flow of the phases along the same direction). Heat pipes can be manufactured in various geometrical shapes (Reay *et al.*, 2013) and their size can range from nanometers to meters (Hoa *et al.*, 2003; Peterson *et al.*, 1993; Akkus *et al.*, 2019). Regardless of their type, shape or size, all heat pipes share the same working principle: passive transport of the working fluid triggered by continuous phase change.

Capillary structures positioned at the inner wall of a heat pipe (called the wick) are responsible for the transportation of the liquid from the condenser to the evaporator. Whilst wick structures are generally made of porous material or parallel grooves, some heat pipes with sharp-angled corners (generally called micro heat pipes) utilize the inner corners as liquid arteries without a need for an additional wick structure. Since the amount of energy transferred via phase change is proportional to the amount of liquid transport, the ultimate objective is to maximize mass transfer through the wick, yet this is restricted by the capillary limit. A proper estimation of the capillary limit requires writing a balance between the surface, body and pressure forces for flow modeling, which is not straightforward due the complexity of solving the inherently non-linear flow equations. Introducing several simplifying assumptions is inevitable in order to obtain a solution to the flow.

In the case of a porous wick, a common approach in the literature (Vafai and Wang, 1992; Aghvami and Faghri, 2011; Ferrandi *et al.*, 2013; Kolliyil *et al.*, 2020) is to apply Darcy's law, which, however, neglects the boundary, inertial and variable porosity effects (Vafai, 1984). As a result, several modifications were suggested for Darcy's law in the literature. Following the analysis reported in (Vafai and Tien, 1981), non-Darcian transport of liquid was considered in (Zhu and Vafai, 1996; Zhu and Vafai, 1999) by incorporating the boundary and inertial effects. Inclusion of gravity as a body force into the Darcy's equation was also attempted (Zhu and Vafai, 1996; Anand *et al.*, 2008).

Due to the ease of controllable manufacturing and developing associated numerical and analytical solutions, grooved and micro heat pipes have been widely studied in the literature (Babin *et al.*, 1990; Kim *et al.*, 2008; Do *et al.*, 2008; Alijani *et al.*, 2018; Alijani *et al.*, 2019). In the case of flow in open channels, gradually changing flow area does not lead to a sudden acceleration or deceleration of the liquid enabling the omission of inertial and boundary effects. This results in a force balance between the Laplace pressure originating from the curvature change of liquid-vapor interface, viscous losses and gravity, which is in general, more effective in grooved heat pipes compared to the ones with a porous wick (Reay *et al.*, 2013; Atay *et al.*, 2019). Counter flow of vapor and liquid results in viscous losses due to shear stresses between liquid-wall, vapor-wall and liquid-vapor at the interface. While the amount of mass transported through the adiabatic region remains nearly constant, the main change is along the evaporator and condenser regions; consequently, additional models (Akkus and Dursunkaya, 2016; Akdag *et al.*, 2020) to account for phase change rates along the evaporator and condenser sections should be employed. When all of these effects are considered, the solution approach is to numerically solve the mass and momentum balance equations in both domains together with the Young-Laplace equation (Do *et al.*, 2008; Lefèvre *et al.*, 2008; Odabasi, 2014). One basic simplification is to estimate the variation of phase change rates along the evaporator and the condenser. Linear variation of the phase change was assumed (Anand *et al.*, 2008; Kim *et al.*, 2003; Chen *et al.*, 2009; Desai *et al.*, 2019; Singh, 2020) and confirmed (Aghvami and Faghri, 2011; Odabasi, 2014) in previous studies. Similarly, the assumption of uniform heat flux in these regions also eliminated the need for phase change models (Lips *et al.*, 2011). On the other hand, the most common assumption in flow modeling is the decoupling of phase change and axial liquid flow by assuming the liquid flow between the mid-planes of the condenser and the evaporator (Faghri, 1995; Reay *et al.*, 2013; Jiang *et al.*, 2014; Ömür *et al.*, 2018). However, this approach may lead to substantial errors in the modeling of heat pipes with short or no adiabatic sections.

Despite the presupposition of the phase change mass transfer variation, the flow problem still remains complex due to the alteration of both liquid and vapor pressures, which are coupled via the Young-Laplace equation throughout the flow domain. Momentum balance in both domains with the Young-Laplace equation form a set of ordinary differential equations, which was solved by numerical methods (such as Runge-Kutta) in previous studies (Anand *et al.*, 2008; Kim *et al.*, 2003). An analytical solution, on the other hand, is viable when the vapor pressure variation is not taken into consideration in the Young-Laplace equation. In this case, liquid pressure distribution can be obtained by integrating the momentum equation and the Young-Laplace equation can be employed to calculate the distribution of the interfacial curvature. In fact, capillary limit analyses in well-known textbooks (Faghri, 1995; Reay *et al.*, 2013;

Jiang *et al.*, 2014; Peterson, 1994) also rely on the assumption of a constant vapor pressure, which can be the saturation pressure at the average working temperature of the heat pipe. However, these analyses still accounted for the vapor pressure loss by employing correlations for the vapor pressure drop (Reay *et al.*, 2013; Chi, 1976; Faghri, 1989). In certain cases such as short adiabatic region or low Reynolds number, the omission of liquid-vapor shear (Lefèvre *et al.*, 2008) and vapor pressure loss (Suman *et al.*, 2005) were also suggested, which further simplifies the problem and aids in finding analytical solutions.

Even after the aforementioned simplifications, finding analytical solutions to the momentum equation of the liquid is still challenging due to the presence of free surface boundaries such as menisci attached to groove edges in grooved heat pipes or those in the corner regions of micro heat pipes. Therefore, suitable correlations have been employed to relate the pressure gradient with an average flow velocity or mass flow rate. The crudest approach is to utilize Darcy's law, derived for a circular groove with a suitable effective flow diameter (Reay *et al.*, 2013). A better approach is to employ a cross-section specific permeability in terms of a non-dimensional parameter, the Poiseuille number, which can be viewed as a friction factor and is commonly expressed by Shah and London correlation (Faghri, 1995). However, a correction is necessary to include the effect of liquid-vapor interaction at the interfacial boundary (Kim *et al.*, 2003). Schneider and DeVos, 1980 suggested a modification to the Poiseuille number to account for the interfacial shear, and many subsequent studies (Anand *et al.*, 2008; Do *et al.*, 2003; Ömür *et al.*, 2018; Khrustalev *et al.*, 1995) adopted this approach to calculate the viscous losses at liquid-wall and liquid-vapor boundaries. Instead of utilizing shear stress correlations, direct analytical solution of momentum equation for vapor and/or liquid phases was also suggested by solving Poisson's equation or assuming parabolic velocity distribution in the literature (Zhu and Vafai, 1999; Chen *et al.*, 2009).

Modeling the fluid flow, thereby estimating the capillary limit is crucial, but not adequate for the assessment of the overall performance of a heat pipe due to several reasons. First of all, some portion of the heat load is inevitably transferred by the conduction in the axial direction through the container walls. The ratio of the heat transfer rate via phase change to the conduction heat transfer, which can be viewed as an effectiveness parameter (Akkus *et al.*, 2019; Alijani *et al.*, 2018), should be high to ensure the proper functioning of the heat pipe. Therefore, axial conduction should be incorporated in the modeling. Moreover, depending on the heat input, the amount of liquid and vapor changes considerably along the heat pipe. The accumulation of the liquid in the condenser, referred to as liquid block/pool or flooded region (Ki *et al.*, 2003; Do *et al.*, 2008; Alijani *et al.*, 2019; Chen *et al.*, 2009; Desai *et al.*, 2019), affects not only the effective flow length but also the thermal resistance along both longitudinal and vertical directions

(Do *et al.*, 2008). Furthermore, the axial distribution of temperature directly affects the thermal properties of the fluid along the heat pipe. Thus, the effective thermal resistance of a heat pipe may change across varying heat inputs (Li *et al.*, 2015; Khalili and Shafii, 2016). As a result, thermal modeling is inherently coupled to the flow modeling, and they should be solved simultaneously, which requires an iterative solution approach. In the literature, in addition to the studies considering phase change as the sole energy transport mechanism (Babin *et al.*, 1990; Chen *et al.*, 2009; Singh, 2020; Suman *et al.*, 2005; Khrustalev and Faghri, 1995; Khrustalev and Faghri, 1994; Longtin *et al.*, 1994; Rullière *et al.*, 2007), uni-directional (Do *et al.*, 2008; Hung and Tio, 2010; Hung and Tio, 2012; Chang and Hung, 2014; Tio and Hung, 2015; Jafari *et al.*, 2020) and multidirectional (Kim *et al.*, 2003; Lefèvre *et al.*, 2008; Desai *et al.*, 2019; Lips *et al.*, 2011; Catton and Yao, 2016) thermal resistance networks were implemented to model the heat transfer in a heat pipe.

In summary, a massive body of literature exists for heat pipe modeling from simple capillary limit analyses (Faghri, 1995; Reay *et al.*, 2013; Peterson, 1994) to the comprehensive 3D models (Do *et al.*, 2008; Lefèvre *et al.*, 2008). While simplistic models may fail to capture the flow domain properly, thereby result in inaccurate predictions for the heat transfer; comprehensive models are computationally expensive demanding long computation times. The objective of the current study is to draw a universal computational framework for a fast but sufficiently accurate modeling of traditional heat pipes and to develop an associated analysis tool named Heat Pipe Analysis Toolbox, in short H-PAT, which is also available as a MATLAB Toolbox for academic use. H-PAT is capable of diagnosing the operation of a heat pipe working under varying heat inputs up to the onset of dryout. It targets to find an accurate liquid distribution along the wick (including liquid pool if present) based on the available analytical solutions and/or correlations for the liquid flow, then establishing the corresponding 3D thermal resistance network, which is composed of evaporator, condenser and adiabatic region resistances. During the initial estimation of phase change rates, the solutions of particular thin film phase change models are avoided by specifying an appropriate pattern for the mass flow rate of the liquid along the heat pipe rather than using finite element method for the computational domain. Modular structure of H-PAT enables handling heat pipes with different wick structures as long as an expression can be introduced for the average liquid velocity. H-PAT is also able to analyze heat pipes with varying cross-sections, favorable/unfavorable gravity conditions and utilizes temperature dependent thermo-physical properties at the evaporator, condenser and adiabatic regions together with heat input sensitive vapor pressure, which makes the tool distinctive.

The paper is organized as follows: in Section 2, computational scheme and modeling strategies in flow and thermal models of H-PAT are introduced. In Section 3, H-PAT is validated with benchmark simulations for

rectangular grooves with both constant and variable cross-sections along the heat pipe. Concluding remarks are provided in Section 4.

MODELING FRAMEWORK

Heat pipe modeling requires solving the fluid flow and heat transfer. While the former basically determines the overall mass flow rate and the amount of phase change heat transfer thereof, the latter is linked to the overall temperature distribution along the heat pipe. In fact, these two are strongly coupled due to the conjugate heat and mass transfer, especially when the phase change mechanism is considered. Moreover, temperature dependence of thermo-physical properties affects the results to a certain extent. Thus, the fluid flow and heat transfer should be simultaneously considered in modeling, which can be accomplished by implementing an iterative solution approach. In this section, first, the details of flow model and thermal model are provided, then the iterative solution procedure is presented.

Flow Model

Flow model considers only the liquid flow based on the assumption of negligible shear stress associated with the liquid-vapor interaction. The model adopts an analytical approach for the solution of the liquid flow. A relation between mass flow rate of the liquid and the pressure variation along the heat pipe should be defined to find the pressure distribution. Therefore, a geometrical function, $\mathbb{G}(z)$, which depends on the type and geometry of the wick structure, can be defined. Liquid flow along the heat pipe axis is sustained by the pressure gradient in the same direction. If the analytical solution of the liquid velocity is available over the cross-sectional flow area, then the pressure gradient term appears in the solution. Mass flow rate can be calculated by integrating the velocity distribution and mass flow rate along the heat pipe axis, and expressed as the product of the pressure gradient and the resultant function following the integration as:

$$\dot{m}_l(z) = \int (\rho \mathbf{u}) \cdot \mathbf{n} dA = \mathbb{G}(z) \left(\frac{dp}{dz} + f_b \right) \quad (2.1)$$

where ρ and f_b are the liquid density and the constant associated with a body force, respectively. The equation for pressure distribution in the liquid is obtained by integrating the prediction for mass flow rate variation along the heat pipe as:

$$p(z) = \int \left(\frac{\dot{m}_l}{\mathbb{G}(z)} - f_b \right) dz, \quad 0 \leq z \leq L^{eff} \quad (2.2)$$

where L^{eff} is the effective axial flow length of the liquid. Boundary conditions for the liquid pressure required for the integration in Eq. (2.2) are directly linked to the assumptions on the operation of the heat pipe. A proper operation should be free from the occurrence of dryout in the evaporator. The onset of dryout can be determined

based on the angle at the triple line, where three phases (solid walls of the wick and liquid and vapor phases of the working fluid) meet. This angle can decrease up to the *contact angle*, θ_{ca} , a characteristic property of a liquid in contact with a certain solid surface. Further stretching of the liquid beyond the contact angle may result in sudden occurrence of dryout (Nilson *et al.*, 2006). Therefore, the pressure value at the evaporator end of the heat pipe ($z = 0$) is calculated based on the contact angle using Young-Laplace relation (Eq. 2.3a). At the opposite side of the heat pipe, pressure gradient vanishes at the point where the axial liquid flow ceases ($z = L^{eff}$). This point is the physical end boundary of the heat pipe if there is no pool region at the condenser, whereas, when the pool region is present, the point corresponds to the starting point of the flooded region since there is no considerable axial flow along the liquid pool. In accordance with these discussions, the boundary conditions can be summarized as:

$$p(z = 0) - p_v = -\sigma \left(\frac{1}{\mathcal{R}_1} + \frac{1}{\mathcal{R}_2} \right) \quad (2.3a)$$

$$\left(\frac{dp}{dz} \right)_{z=L^{eff}} = 0 \quad (2.3b)$$

where p_v and σ are vapor pressure and surface tension, respectively. \mathcal{R}_1 and \mathcal{R}_2 are radii of curvature of the free surface in principal directions. The mass flow rate of the liquid, \dot{m}_l , along the heat pipe can be approximated to change linearly in evaporator and condenser regions considering the predictions of prior works (Odabasi, 2014; Chen *et al.*, 2009; Rullière *et al.*, 2007; Hung and Tio, 2012; Elnaggar *et al.*, 2012; Huang and Chen, 2017), while the axial liquid flow rate remains approximately constant in the adiabatic region due to negligible phase change. To this effect, \dot{m}_l can be expressed as a linear function of the axial coordinate, z , in the evaporator and condenser. However, this approach is not accurate due to presence of axial conduction in the solid, and in general, will not yield smooth transitions between the evaporator/condenser regions in the adiabatic zone. By the inclusion of axial conduction in the analysis and solving the axial domain with fine increments resolves this handicap. Therefore, the liquid domain is divided into a number of slices in each region accordingly. Inside each slice, the mass flow rate of liquid is approximated as a linear function of z , *i. e.* $\dot{m}_{l,i} = d_{0,i} + d_{1,i}z_i$, where subscript i designates the corresponding slice. The implementation of multiple slices in the numerical modeling introduces additional boundaries in between, where flow continuity serves as the boundary condition for each slice as follows:

$$\left(\frac{dp}{dz} \right)_i = \frac{\dot{m}_i}{\mathbb{G}(z_i)} \quad (2.3c)$$

where \dot{m}_i is the flow rate at the intersection of the slices. At the first iterative step, its value is assigned based on initially estimation of the distribution of total liquid flow

along the heat pipe. In the following iterations, the predictions of the previous iteration are employed.

The flow model is valid for different types of wick structures or geometries. Each wick structure yields a specific geometrical function $\mathbb{G}(z)$. Two versatile wick structures are grooved and sintered wicks. While the former is primarily investigated in the current study, the extension of the current modeling for the latter is provided in Appendix B by summarizing the corresponding equations. Regardless of the geometry, the capillary pressure associated with the varying topology of the free surface drives the liquid flow, whereas viscous forces due to the friction of the liquid with the walls oppose it. Consequently, the force balance is established between viscous and pressure forces similar to Poiseuille flow in channels and the linear momentum equation in the axial direction becomes Poisson's equation. To enable the utilization of an available solution to this equation, open channel (groove) flow is treated as the half-domain flow in rectangular duct of width w and height $2h$. Then, the separation of variables is used to solve Poisson's equation with homogeneous Dirichlet boundary conditions. Finally, the mean velocity, U_m , is determined by integrating the velocity distribution over the cross-section as:

$$U_m = \frac{16}{(wh)^2} \frac{\Delta P}{\mu L^{eff}} \sum_{m=1}^{\infty} \sum_{n=1}^{\infty} \frac{1}{(\beta_m^2 + \lambda_n^2) \beta_m^2 \lambda_n^2} \quad (2.4)$$

where μ is the dynamic viscosity of the liquid, $\lambda_n = (2n - 1)\pi/w$ and $\beta_m = (2m - 1)\pi/2h$. The convergence of the series in Eq. 2.4 is fast; therefore, the leading term gives a sufficiently accurate approximation. Mass flow rate inside the groove can be determined by multiplying the mean velocity with density and half cross-sectional area of the rectangular duct. This approach induces a restricted deviation when meniscus is near at, *i. e.* the edge angle between meniscus and wall, θ , is around 90° , because of the slight deformation of the meniscus with respect to the total cross-sectional area of the liquid. However, the meniscus deformation becomes non-negligible near the evaporator end of the heat pipe; therefore, a correction factor, $\Gamma(\theta)$, based on the ratio of deformation area to total cross-sectional area is applied in the calculation of mass flow rate. Finally, the geometrical function, $\mathbb{G}(z)$, for the rectangular groove is obtained as:

$$\mathbb{G}(z) = \Gamma \frac{256}{v\pi^6} \frac{w^3(z)h^3(z)}{[w^2(z) + 4h^2(z)]} \quad (2.5)$$

where v is the kinematic viscosity of the liquid. The width and height of the groove are written as a function of z , which enables the calculation of pressure variation in both constant and variable cross-sections in the rectangular grooved heat pipes. The extension of the flow model for sintered wicks is provided in Appendix B.

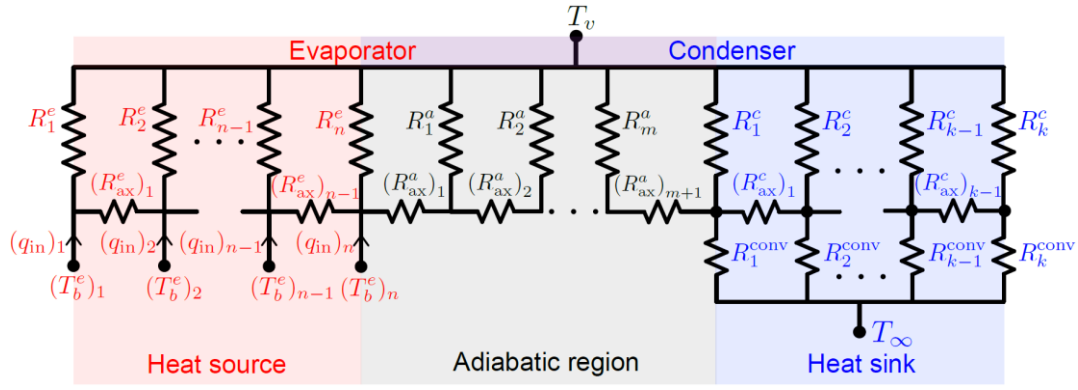


Figure 1. Schematic representation of the thermal resistance model. Heat source and heat sink indicate the outside surface of the heat pipe, where the heat load is applied and removed, respectively. Adiabatic region is the zone exposed to the exterior with no heat input or output. The evaporator and condenser stand for the internal zones, where evaporation and condensation takes place, respectively. T_v and T_∞ are the internal vapor and external coolant temperatures, respectively. There are n , m , and k numbers of slices for the heat source, adiabatic, and heat sink regions, respectively

Thermal Model

The thermal model establishes a thermal resistance network to simulate the heat transfer through a heat pipe. Similar to the approach adopted in the flow model, the thermal model divides regions of the heat pipe into slices as shown in Fig. 1. The model determines the direction of the phase change in a slice by comparing the slice (wall) and vapor temperatures. If the superheat ($T_w - T_v$) is positive, evaporation takes place and the slice is a part of the evaporator; otherwise, it belongs to the condenser. This modeling strategy is applicable for all wick types. The axial heat conduction is accounted for by including the pertinent thermal resistances (R_{ax}) along the axial direction. The transverse heat transfer is modeled inserting the thermal resistances, which are specific to the evaporator (R_e) and condenser (R_c) regions. In what follows, the derivation of region specific thermal resistances is performed for the wick structure with rectangular grooves, as an example. The extension of the thermal model for sintered wicks is provided in Appendix B.

Figure 2 shows the transverse thermal resistance network on an arbitrary cross-section in the evaporator. The network is established between the base temperature (T_b^e) and the vapor temperature (T_v). It includes resistances due to heat conduction in both solid and liquid, and the phase change on the liquid-vapor interface. Since a considerable amount of evaporation originates from a micro-scale thin film region near the contact line (Akkus *et al.* 2017), the resolution of the solution should be increased in this region. Accordingly, the interfacial heat transfer is handled in two regions: (i) thin film region (the resistance associated with this region is R_{tf}^e) and (ii) intrinsic meniscus region (the resistance associated with this region is R_{gf}^e). In the actual case, 2D heat transfer takes place throughout the cross-section. The current approach, on the other hand, considers a 1D transfer of heat in two parallel routes by ignoring the 2-dimensionality of the problem. This is a reasonable approach considering the thickness of the liquid films in these regions. Thin film and meniscus regions are divided into p – and q – slices. The details of these regions are illustrated in Fig. 2B. The circuit representation of transverse thermal resistances in the evaporator together with the definition of each thermal resistance are

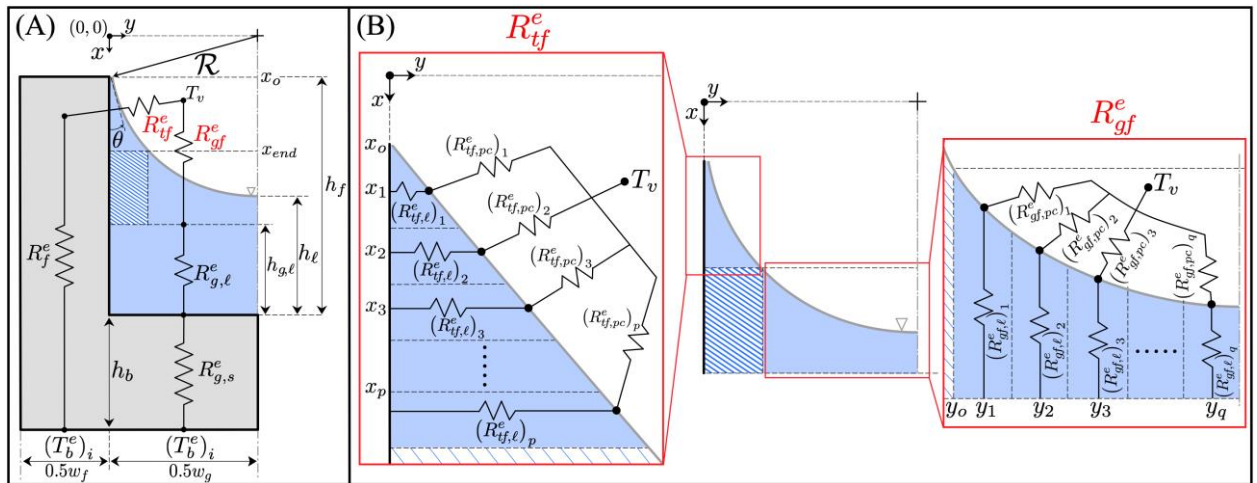


Figure 2. (A) Outline of transverse thermal resistance network in the evaporator. (B) Detailed view of thermal resistance network in thin film and intrinsic meniscus regions

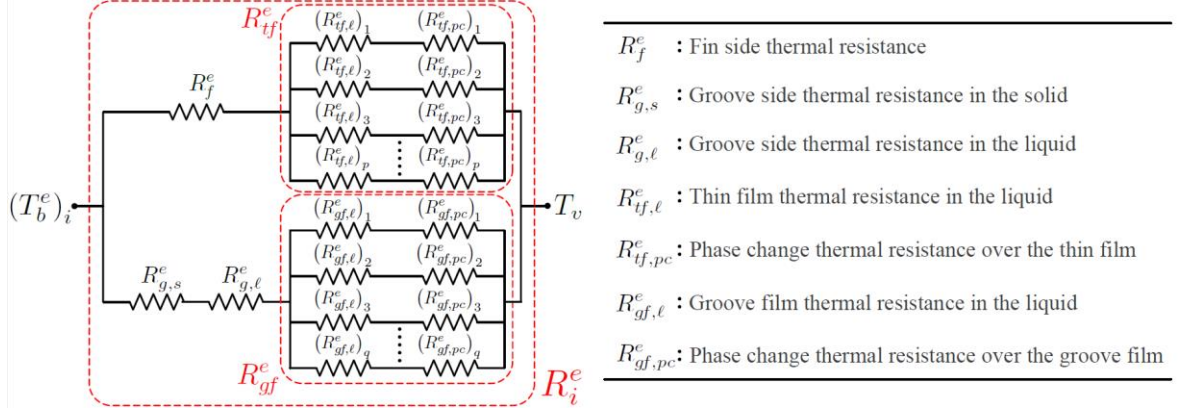


Figure 3. Circuit representation and the list of transverse thermal resistances in the evaporator

presented in Fig. 3. Formulations of these thermal resistances are provided in Appendix A.1.

Figure 4 shows the transverse thermal resistance network on an arbitrary cross-section in the condenser. Structure of the network is similar to that in the evaporator, but the thin film region expands on the fin top, where the majority of the condensation occurs (Akdag *et al.* 2019). This region is resolved by a denser thermal resistance network, whose details are illustrated in Fig. 4B. While the shape of the interface is defined as a circular meniscus in the evaporator, the film profile (on the fin top) in the condenser is determined based on a 4th order polynomial (Do *et al.* 2008). The circuit representation of transverse thermal resistances in the condenser together with the definition of each thermal resistance are presented in Fig. 5. Formulations of these thermal resistances are provided in Appendix A.1.

The phase change process at the liquid-vapor interface induces a pertinent thermal resistance. This resistance depends on the rate of the phase change and the interfacial temperature difference. Relations derived from the kinetic theory of gases have been widely utilized in the estimation of phase change rates. Among them Schrage relation (Schrage, 1953) has been widely used because of its ability to successfully predict the rates during non-equilibrium phase change processes (Akkus *et al.* 2021). When the interfacial temperature difference is small, the approximate Schrage relation reduces to a popular form (Sujanani and Wayner Jr., 1991) that depends on the interfacial temperature and pressure jumps:

$$\dot{m}_{pc}'' = a(T_{lv} - T_v) + b(p_v - p_l) \quad (2.6)$$

where

$$a = \frac{2\hat{\sigma}}{2 - \hat{\sigma}} \left(\frac{M}{2\pi R_u T_{lv}} \right)^{1/2} \left(\frac{M p_v h_{fg}}{R_u T_v T_{lv}} \right) \quad (2.7a)$$

$$b = \frac{2\hat{\sigma}}{2 - \hat{\sigma}} \left(\frac{M}{2\pi R_u T_{lv}} \right)^{1/2} \left(\frac{p_v V_l}{R_u T_{lv}} \right) \quad (2.7b)$$

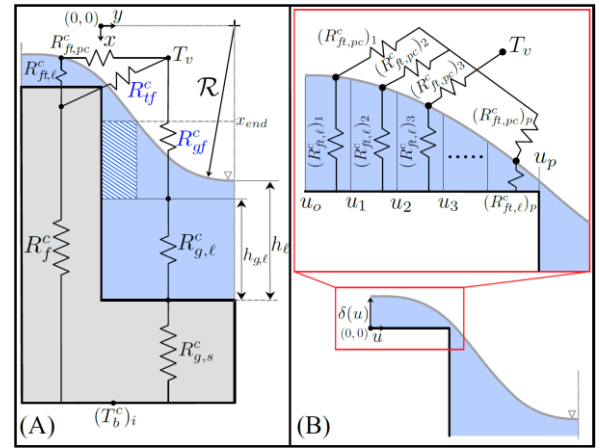


Figure 4. (A) Outline of transverse thermal resistance network in the condenser. (B) Detailed thermal resistance network in thin film (on the fin top) and intrinsic meniscus regions.

where R_u , M , and $\hat{\sigma}$ are universal gas constant, molar mass, and accommodation coefficient (taken as unity), respectively. Moreover, h_{fg} and V_l are latent heat of vaporization and molar volume of the fluid, respectively; and including those, all the fluid properties are evaluated at the vapor temperature in both thermal and fluid models. The pressure jump term in Eqn. (2.6) becomes effective when the variation of curvature and/or the effect of disjoining pressure are included. In the scope of this work, a detailed modeling of evaporating contact line is not performed, therefore the effect of pressure jump term is not accounted for. By negating this term, the interfacial phase change resistance can be written as follows:

$$(R_{*,pc}^*)_i = \frac{1}{a h_{fg} s_i L_i} \quad (2.8)$$

where s_i and L_i are the arc length of the interface and axial length of the slice, respectively. While the superscript (*) stands for the evaporator or condenser, the subscript (...), pc denotes the location of the phase changing interface in the corresponding cross-section.

It should be noted that, unlike other capillary limit analysis in the literature which utilize simpler models, the multidimensional nature of HPAT necessitates the

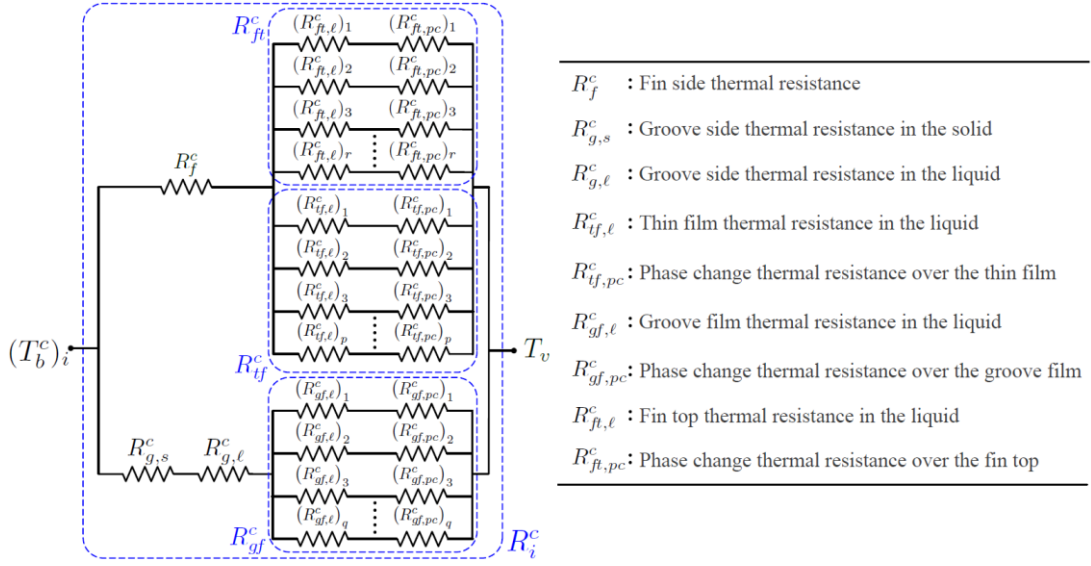


Figure 5. Circuit representation and the list of transverse thermal resistances in the condenser.

presence of several thermal resistances in the thermal network for a more realistic simulation of the inherently complex thermal phenomena. Several parameters, including the axial location, affect the magnitude of the resistances; and dominant paths of heat flow along the wick axis may change due to the changing magnitude of thermal resistances. Depending on the groove dimensions and edge angles, at a particular location, thin-film region thermal resistance may be at a minimum, creating a favorable path for heat flow, particularly on the evaporator side. Similarly, depending on the groove width, groove height and the thermal conductivity of the solid, the fin side and groove side thermal resistances in the solid may be negligible compared to other resistances in the thermal circuit. The fast computation ability of HPAT enables the inclusion of the entire network of resistances in the analysis, the relative significance of which can only be identified at a post processing step.

Solution Procedure

The iterative solution procedure is presented in Fig. 6. The lengths of the heat source length (L_e), adiabatic region (L_a) and heat sink (L_c), the details of the wick structure, the cooling condition at the heat sink (R^{conv} and T_∞) or alternatively a constant outer wall (base) temperature (T_b^c) and total heat input from the heat source (q_{tot}) are input parameters for the numerical model. For a given geometry and heat input, the phase change heat transfer (q_{pc}) and vapor temperature (T_v) are initially estimated. First, the flow model is utilized to determine the effective flow length (L^{eff}) and edge angle variation along the heat pipe ($\theta(z)$) (i.e. $\mathcal{R}(z)$). The resolution of the flow solution is determined by adjusting the number of slices in the axial direction, which can be set independently in each region. Second, the thermal model is utilized to determine q_{pc} , T_v , and the temperature distribution along the heat pipe. Similar to the flow model, the resolution is determined by adjusting the

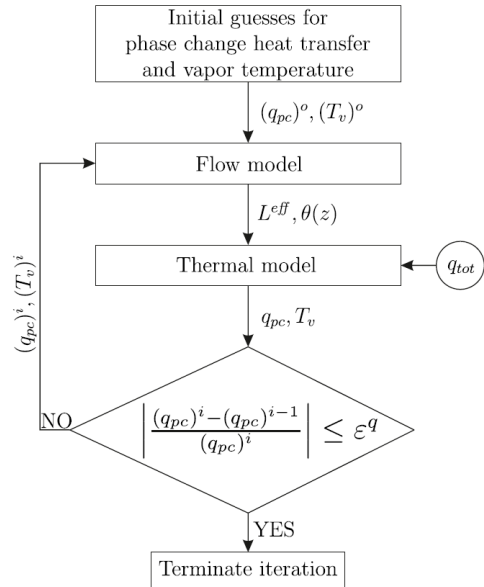


Figure 6. Solution algorithm

number of slices in the axial direction (see Fig. 1). Moreover, the frequency of slices utilized in resolving the phase change process on the liquid films is adjusted to ensure grid independence (see Fig. 2B and Fig. 4B). Finally, the calculated q_{pc} is compared against the estimates at the beginning of the loop. If the convergence criterion on q_{pc} is satisfied, the computation is terminated. Otherwise, q_{pc} and T_v are updated. Solution procedure is repeated until the convergence criterion is satisfied.

In the algorithm laid out in Fig. 6 the vapor temperature is needed for the calculation of the thermo-physical properties and phase change resistances, and during the iterations it is back calculated upon the solution of the thermal resistance circuit. This is a distinctive feature of

RESULT AND DISCUSSION

Validation of the Flow Model

The flow model basically determines the variation of the meniscus shape. The performance of the present flow model can be evaluated by comparing its predictions with the previous experimental measurements. To this effect, two past works, which utilized rectangular grooved wicks with constant (Lefèvre *et al.*, 2008) and varying (Lefèvre *et al.*, 2010) cross-sections along the groove axis, are selected for the validation of the flow model. Both studies reported the variation of the radius of curvature of the meniscus along the groove axis measured by confocal microscopy. The details of the heat pipe configurations utilized in Refs. (Lefèvre *et al.*, 2008) and (Lefèvre *et al.*, 2010) are provided in Table 1 (please see Fig. 12 for the geometric parameters).

Former study (with constant cross-section) (Lefèvre *et al.*, 2008) was conducted for three different heat fluxes: 0.5 W/cm^2 , 0.7 W/cm^2 and 0.9 W/cm^2 . In addition to the measurement of meniscus curvature, a comprehensive 3D numerical model was also developed in (Lefèvre *et al.*, 2008) by solving the mass and momentum equations in both liquid and vapor domains together with Young-Laplace equation and a multi-directional thermal resistance network. Using the same geometry and conditions (see Table 1), the experiments are simulated by H-PAT. In order to match the vapor (working) temperature kept constant at the experiments, the cooling conditions at the heat sink are adjusted in H-PAT similar to the practice adopted in the experiments. The experimental and numerical findings of (Lefèvre *et al.*, 2008) are compared with the predictions of H-PAT in Fig. 7. Results show that the radius of curvature estimates of H-PAT along the heat pipe are in excellent agreement with the experiments. The predictions of comprehensive numerical model developed in (Lefèvre *et al.*, 2008) deviate with increasing heat loads, whereas H-PAT matches the experiments for all heat loads applied.

H-PAT has the ability to simulate wicks with variable flow area by defining the variation of wick dimensions as a function of the axial direction (see Eq. 2.5). In order to assess its computational performance on the rectangular grooves with variable cross-section area, H-PAT is utilized to simulate a pertinent previous experiment (Lefèvre *et al.*, 2010), where the groove width varied linearly (see Fig. 8A), *i.e.* $w(z) = w_1 + w_2(z)$. The constants w_1 and w_2 are calculated as $1.1 \times 10^{-4} \text{ [m]}$ and 2.43×10^{-2} , respectively, for the groove geometry in (Lefèvre *et al.*, 2010).

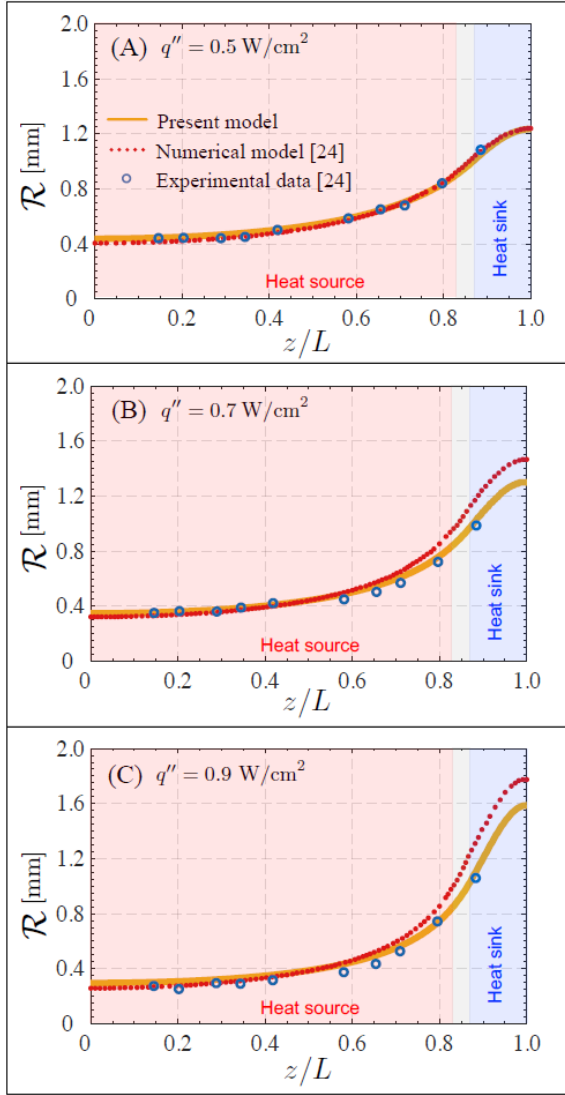


Figure 7. Radius of curvature variation along the heat pipe for heat loads (A) $q'' = 0.5 \text{ W/cm}^2$, (B) $q'' = 0.7 \text{ W/cm}^2$ and (C) $q'' = 0.9 \text{ W/cm}^2$. Blue dots and red dotted lines indicate the experimental and numerical results of Lefèvre *et al.* (2008), respectively. Yellow lines show the predictions of H-PAT.

the current solution algorithm, since other models solving the differential equation form of the energy balance need to use the vapor temperature as a boundary condition, hence requiring the convergence of the vapor temperature for the convergence of the combined heat transfer/fluid flow/phase change/interface shape problem. In the current approach, the necessity of using the vapor temperature as a boundary condition is avoided, which results in a faster solution of the iterative process. This is why the convergence of the solution is checked based on the convergence of phase change heat fluxes, q_{pc} , rather than the vapor temperature, T_v .

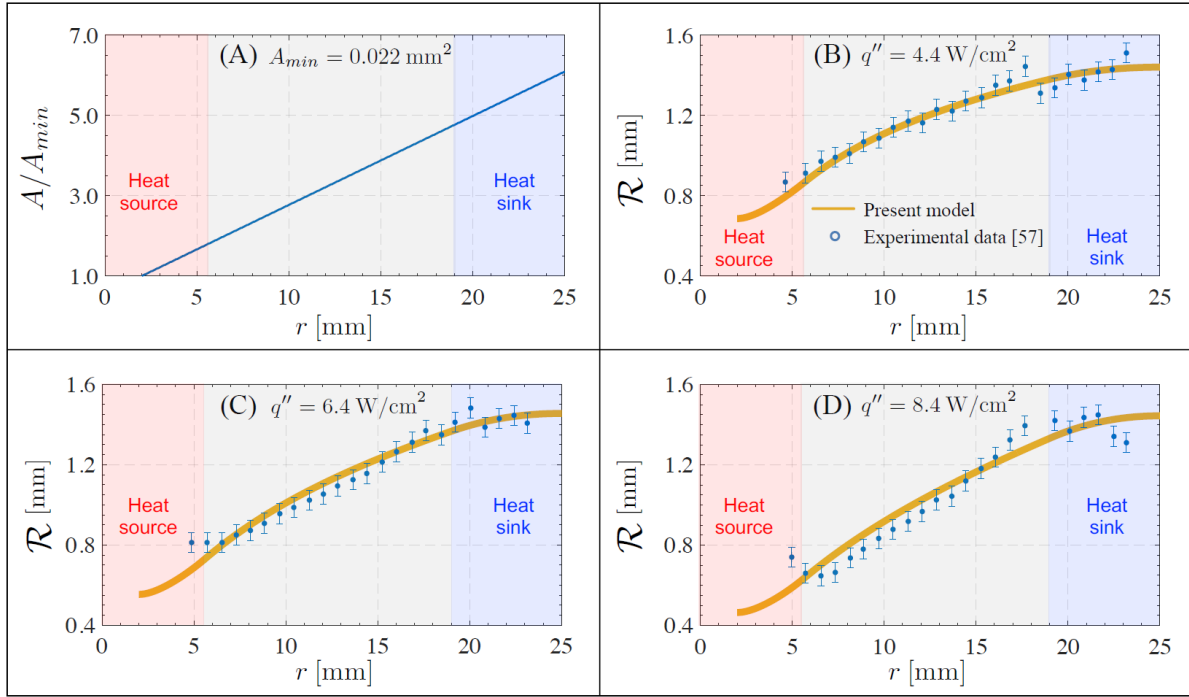


Figure 8. (A) Variation of cross-sectional groove area and radius of curvature along the flow axis for the heat loads: (B) $q'' = 4.4 \text{ W/cm}^2$, (C) $q'' = 6.4 \text{ W/cm}^2$ and (D) $q'' = 8.4 \text{ W/cm}^2$. Blue dots are experimental results of Lefèvre *et al.* (2010). Yellow lines are the predictions of H-PAT.

Although five different heat loads were applied, the radius of curvature variation along the heat pipe was significant only for the highest three heat loads (4.4 W/cm^2 , 6.4 W/cm^2 and 8.4 W/cm^2). Vapor temperature was kept constant at 30°C for all heat exes. The experimental measurements of the radius of curvature in (Lefèvre *et al.*, 2010) are compared against the predictions of H-PAT in Figs. 8B-D. The results show that for the majority of the experimental results, the predictions of H-PAT match the experiments within the uncertainty of measurements, the match being particularly good in the adiabatic region. Small deviations near the evaporator end can be attributed to the transition of the wick geometry from a grooved to a pillar structure at the evaporator in the experiment. To the best of authors' knowledge, the numerical validation of the experiments in (Lefèvre *et al.*, 2010) is performed for the first time owing to the capability of H-PAT in handling wicks with varying cross-sectional flow area.

Validation of Thermal Model

The output of the thermal model is the temperature distribution along the heat pipe which can be used to determine the effective thermal resistance (or effective thermal conductivity) of a heat pipe subjected to a certain heat load. As a first attempt for the validation of thermal model, H-PAT is exercised to simulate the experiments conducted on the heat pipes with rectangular grooves in (Hopkins *et al.*, 1999), where the experiments were conducted for 15 different heat loads between 3.0 and 127 W, and the effective thermal resistances were reported for each case.

Likewise, utilizing the same geometry and conditions (see Table 1), H-PAT calculates the effective thermal

resistance by dividing the temperature difference between the two ends to the total heat input. As shown in Fig. 9, there is an excellent match between the predictions of the current model and the experimental results in (Hopkins *et al.*, 1999) across a wide range of heat loads. Hopkins *et al.*, (1999) attributed their decreasing thermal resistances with heat loads to the thinning liquid film at the evaporator. In essence, the liquid distribution is adjusted along the entire groove such that the liquid film may become thicker or form a liquid pool near the condenser end, while it becomes thinner at the evaporator. H-PAT is able to catch these variations, and accordingly, it is successful in capturing the converging pattern of resistance with heat loads up to the onset of dryout.

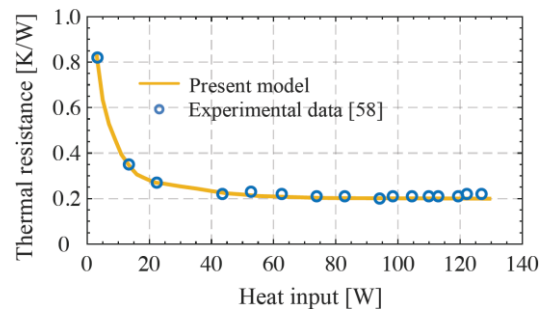


Figure 9. Variation of thermal resistance with heat load. Blue circles are the experimental results of Hopkins *et al.* (1999). Yellow line shows the predictions of H-PAT.

As a second attempt, the performance of H-PAT is assessed by conducting a benchmark experiment on a plate heat pipe setup constructed for the current study. The experimental heat pipe assembly consists of five parts, namely main frame, grooved base plate, transparent top cover, heat source, and heat sink (see Fig. 10). In the experimental setup Edward RV3 two stage rotary vane pumps, Agilent 34972A data acquisition/data logger switch unit, Thermo/Neslab digital refrigerated bath circulator ($\pm 0.01^\circ\text{C}$), Omega T-type thermocouple ($\pm 0.5^\circ\text{C}$) were used. This modular structure enables testing wicks with different geometries and materials by simply changing the grooved base plate, which was aluminum for this particular experiment set. T-type thermocouples were placed inside the holes machined at the bottom of the groove frame. Transparent top cover is manufactured from acrylic to enable a clear visualization of the groove frame. Sealing between the main and top frames as well as that with the main and grooved base plate were secured by vacuum grade o-rings. Moreover, the heat sources and heat sinks with different sizes/geometries can be interchangeably utilized in this setup. At the beginning of the experiment, the heat pipe was filled with the working fluid, IPA. Then, the heat pipe was operated under the heat load of 2.1 W/cm^2 until steady state was reached. Following this, an incremental amount of IPA was aspirated from the heat pipe and testing was commenced. This procedure was repeated until no IPA remains in the heat pipe. The temperature data was recorded throughout the entire test. The point with minimum temperature difference was obtained from these experiments was accepted as the optimum working point of the heat pipe. The parameters and working conditions, the experiment is also simulated by H-PAT for the operating condition corresponding to the optimum point. Predictions of H-PAT are compared with experimental wall temperature measurements for

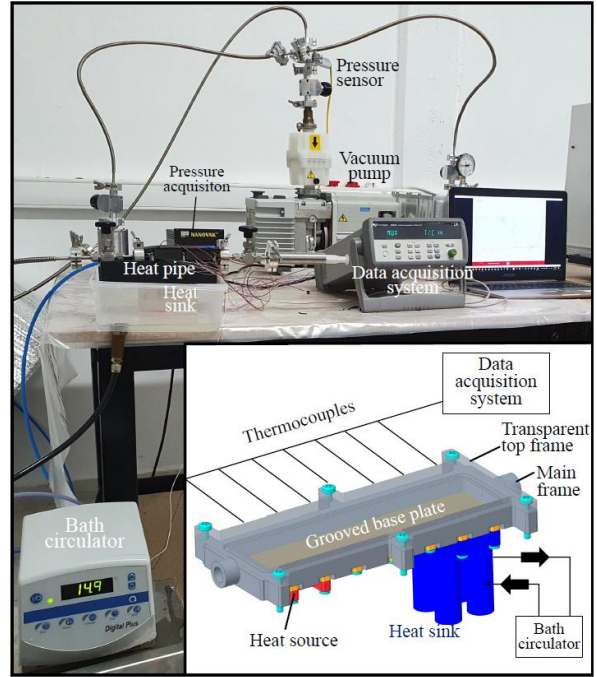


Figure 10. Experimental setup

both heat pipes in Fig. 11. As shown, the thermal model successfully captures the temperature variation along both heat pipes. Slightly overestimated temperatures near the heat source of the heat pipe with smaller grooves might be attributed to parasitic experiments were conducted for two different heat pipes (geometries given in Table 1). Utilizing the same geometrical heat loss to the ambient, although insulation was applied in every experiments. As shown in Fig. 11, H-PAT is able to provide vapor temperature, which can be viewed as the working temperature of the heat pipe. Intersection of

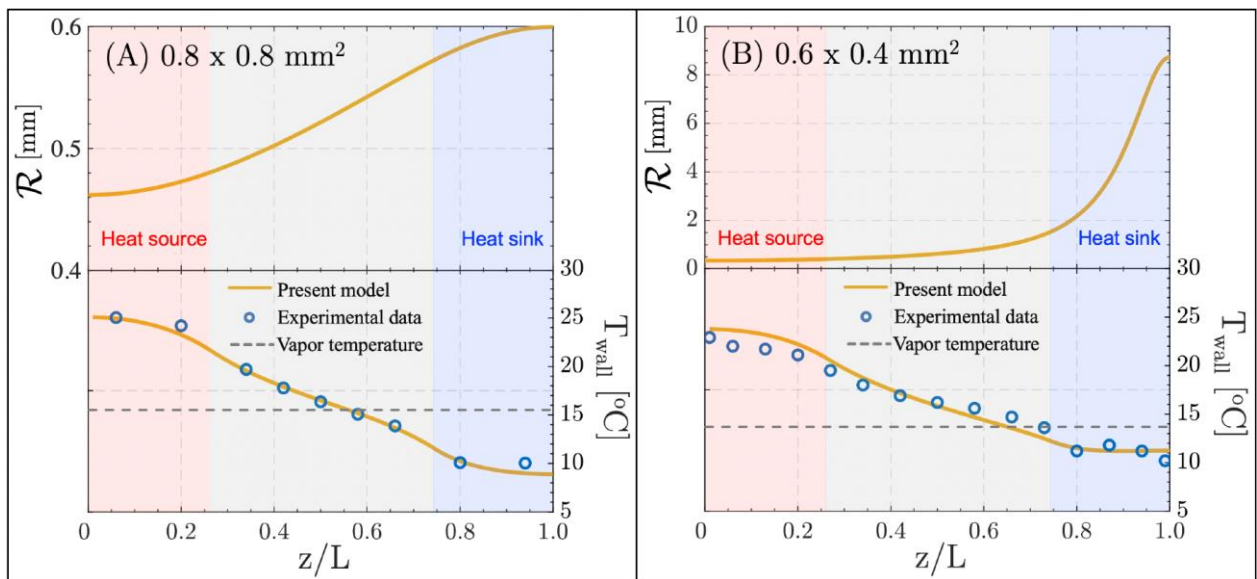


Figure 11. Variation of wall temperature along the heat pipe. Blue circles are experimental results and experimental uncertainty is smaller than the size of the circles. Yellow solid and gray dashed lines shows the wall temperature and vapor temperature predictions of H-PAT, respectively.

vapor temperature and wall temperature marks the point of transition between evaporator and condenser sections.

As demonstrated by preceding validations, H-PAT is highly successful in simulating the operation of a heat pipe working for different heat loads. Moreover, the simulation time is fast (in the order of seconds) owing to its unique solution approach that accounts for the all geometric variations in both wick structure and liquid film profile in the construction of thermal model, but avoids the solution of particular thin film phase change models by specifying and iterating the axial mass flow rate in the flow model, which eliminates the need for solving a multi-dimensional flow problem. This approach enables the prediction of the amount of overall heat transfer via phase change together with vapor temperature. Considering its accuracy along with fast computation, H-PAT positions itself not only as a diagnostic tool, but also as a design tool that can be confidently utilized by thermal design engineers in iterative design processes.

CONCLUDING REMARKS AND OUTLOOK

Heat Pipe Analysis Toolbox, in short H-PAT, is a fast diagnosis and design toolbox for the simulation of heat pipes. H-PAT can predict the fluid flow and heat transfer in a heat pipe under varying heat inputs up to the onset of dryout. In other words, H-PAT captures the capillary limit of the heat pipe, whereas sonic, entrainment, and viscous (vapor pressure) limits are not taken into consideration in the current version, which does not include vapor zone in its solution domain. In addition, boiling heat transfer is not covered by H-PAT based on the assumption of bubble-free evaporation throughout the evaporator. Adaptable structure of H-PAT allows the simulation of heat pipes with different wick structures. A heat pipe responds to heat input changes by simply varying the liquid distribution along the wick. H-PAT is able to capture these variations including the rarely considered pool region in the condenser. Reliability of H-PAT is proved with benchmark simulations for rectangular grooves with both constant and variable cross-section along the heat pipe. The latter remarks a distinctive feature reflecting the potential of H-PAT in the assessment of heat pipes having wicks with varying topology.

Because of its high accuracy and fast computation together with a user friendly interface, H-PAT is a candidate for frequent use by researchers and design engineers in the field of thermal management, and available via MathWorks File Exchange. Although its accuracy and fast computation, H-PAT has some restrictions. First and fore-most, it requires the analytical solutions and/or correlations for the liquid flow along the wick, which may not be available for unconventional complex geometries. Moreover, skipping the solution of detailed thin film phase change models may prevent obtaining the precise variation of the liquid film at a cross-section due to the absence of near wall effects such as dispersion and structural components of disjoining

pressure (Akdag *et al.*, 2020; Setchi *et al.*, 2019). In addition, in its current form, H-PAT does not solve the vapor flow, thereby neglecting the associated viscous losses, and assumes uniform vapor properties along the heat pipe. Despite its negligible role in the benchmark studies considered in this work, resolving vapor flow may be crucial in certain heat pipe applications, especially in the case of thin heat pipes with small vapor spacing. Finally, operation with partial dryout is not considered in the current version of H-PAT. In the light of these our future research efforts will focus on adding the following features to H-PAT: the inclusion of vapor flow and porous wick structures, and simulation in the presence of partial dryout.

ACKNOWLEDGEMENTS

S.S. acknowledges the support provided by Scientific and Technological Research Council of Turkey (TÜBİTAK) through Science Fellowships and Grant Programmes (BİDEB 2211). B.Ç. would like to acknowledge the funding from the Turkish Academy of Sciences through Outstanding Young Scientist Program (TÜBA-GEBİP) and The Science Academy, Turkey through Distinguished Young Scientist Award (BAGEP).

DECLARATIONS OF INTEREST

None.

APPENDIX A. Formulation of Thermal Resistances in Grooved Wicks

Formulations of thermal resistances utilized in the both evaporator and the condenser are listed below. Note that the superscript (*) in the following equations is replaced with “e” for the evaporator and “c” for the condenser.

$$R_f^* = \frac{h_b + h_g - 0.5(x_{end} - x_0)}{k_s(0.5w_f)L_i} \quad (A.1)$$

$$R_{g,s}^* = \frac{h_b}{k_s(0.5w_g)L_i} \quad (A.2)$$

$$R_{g,l}^* = \frac{h_{g,l}}{k_l(0.5w_g)L_i} \quad (A.3)$$

$$(R_{t,f,l}^*)_n = \frac{\bar{\delta}_n}{k_l(x_n - x_{n-1})L_i} \quad (A.4)$$

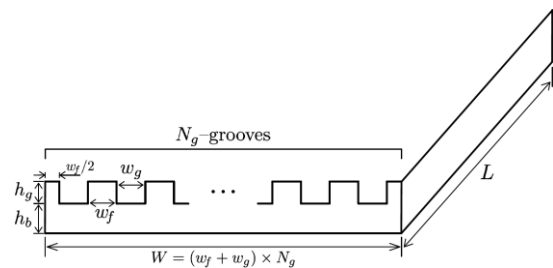


Figure 12. Grooved heat pipe

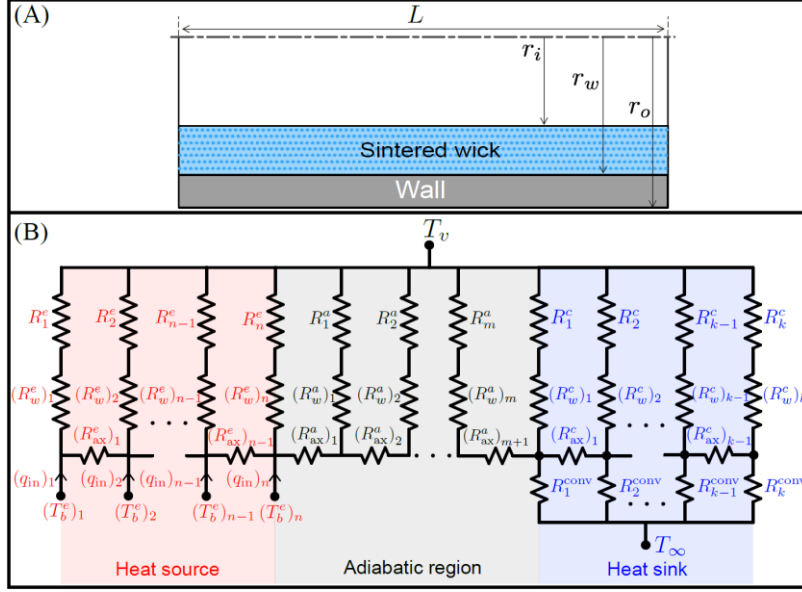


Figure 13. Cylindrical sintered wick heat pipe

$$(R_{tf,pc}^*)_n = \frac{1}{ah_{fg}(s_n - s_{n-1})L_i} \quad (\text{A.5})$$

$$(R_{gf,l}^*)_n = \frac{\bar{\delta}_{g,n}}{k_l(y_n - y_{n-1})L_i} \quad (\text{A.6})$$

$$(R_{gf,pc}^*)_n = \frac{1}{ah_{fg}(s_{g,n} - s_{g,n-1})L_i} \quad (\text{A.7})$$

where h_{fg} is the latent heat of vaporization, k_s , k_l , and k_w are the thermal conductivity of the wall material, working liquid, and wick structure, respectively. All the geometric parameters are shown in Fig. 12. In addition to these resistances, the fin top resistances due to condensation of the liquid at the condenser occur and formulated as:

$$(R_{ft,l}^c)_n = \frac{\bar{\delta}_n}{k_l(u_n - u_{n-1})L_i} \quad (\text{A.8})$$

$$(R_{ft,pc}^*)_n = \frac{1}{ah_{fg}(s_{ft,n} - s_{ft,n-1})L_i} \quad (\text{A.9})$$

Finally, overall resistances for evaporating and condensing cross-sections are:

$$R^e = \left[\frac{1}{R_{fb}^e + R_f^e + R_{tf}^e} + \frac{1}{R_{gb}^e + R_{g,l}^e + R_{gf}^e} \right]^{-1} \quad (\text{A.10})$$

$$R^c = \left[\frac{1}{R_{fb}^c + R_f^c + (1/R_{tf}^c + 1/R_{ft}^c)} + \frac{1}{R_{gb}^c + R_{g,l}^c + R_{gf}^c} \right]^{-1} \quad (\text{A.11})$$

APPENDIX B. Extension of the Model for Sintered Wicks

In this section, the extension of the fluid flow and thermal models are given for cylindrical heat pipes with sintered wicks. A relation between mass flow rate of the liquid and the pressure variation along the heat pipe for sintered wicks can be written using Darcy equation:

$$U_m = \frac{\kappa \Delta P}{\mu_l L^{eff}} \quad (\text{B.1})$$

$$A_{wick} = \pi(r_w^2 - r_i^2) \quad (\text{B.2})$$

where κ is the permeability, and the r_i and r_w are the corresponding radius values shown in Fig. 13A. The pressure distribution equation for the liquid can be obtained by combining mass flow rate prediction along the heat pipe with the mass flow rate equation as follows:

$$p(z) = \int \left(\frac{\dot{m}_l}{\mathbb{G}(z)} - f_b \right) dz, \quad 0 \leq z \leq L^{eff} \quad (\text{B.3})$$

where

$$\mathbb{G}(z) = \frac{\nu_l}{\kappa \pi A_{wick}} \quad (\text{B.4})$$

where ν_l kinematic viscosity of the liquid. It should be noted that geometric function, \mathbb{G} , is not the function of axial distance due to the assumption of constant flow area. Formulations of the resistances forming the thermal resistance network are shown in Fig. 13B as follows:

$$(R_w^*)_i = \frac{\ln(r_o/r_w)}{2\pi k_s L_i} \quad (\text{B.5})$$

$$R_i^* = \frac{\ln(r_w/r_i)}{2\pi k_{eff} L_i} \quad (\text{B.6})$$

$$(R_{ax}^*)_i = \frac{L_i}{\pi[k_s(r_o^2 - r_w^2) + k_{eff}(r_w^2 - r_i^2)]} \quad (\text{B.7})$$

where effective thermal conductivity of the porous wick structure can be defined as:

$$k_{eff} = k_w \frac{[2 + (k_l/k_w) - 2\varepsilon(1 - k_l/k_w)]}{[2 + (k_l/k_w) + \varepsilon(1 - k_l/k_w)]} \quad (\text{B.8})$$

where ε is the porosity of the wick, k_s , k_l , and k_w are the thermal conductivity of the wall material, working liquid, and wick structure, respectively.

REFERENCES

- Aghvami M. and Faghri A., 2011, Analysis of flat heat pipes with various heating and cooling configurations. *Appl. Therm. Eng.*, 31(14-15):2645-2655.
- Akdag O., Akkus Y., and Dursunkaya Z., 2019, The effect of disjoining pressure on the shape of condensing films in a fin-groove corner. *Int. J. Therm. Sci.*, 142:357-365.
- Akdag O., Akkus Y., and Dursunkaya Z., 2020, On the effect of structural forces on a condensing film profile near a fin-groove corner. *Int. Commun. Heat Mass*, 116:104686.
- Akkus Y. and Dursunkaya Z., 2016, A new approach to thin film evaporation modeling. *Int. J. Heat Mass Tran.*, 101:742-748.
- Akkus Y., Gurer A. T., and Bellur K., 2021, Drifting mass accommodation coefficients: *in situ* measurements from a steady state molecular dynamics setup. *Nanosc. Microsc. Therm.*, 25(1):25-45.
- Akkus Y., Nguyen C. T., Celebi A. T., and Beskok A., 2019, A first look at the performance of nano-grooved heat pipes. *Int. J. Heat Mass Tran.*, 132:280-287.
- Akkus Y., Tarman H. I., Çetin B., and Dursunkaya Z., 2017, Two-dimensional computational modeling of thin film evaporation. *Int. J. Therm. Sci.*, 121:237-248.
- Alijani H., Cetin B., Akkus Y., and Dursunkaya Z., 2018, Effect of design and operating parameters on the thermal performance of flat grooved heat pipes. *Appl. Therm. Eng.*, 132:174-187.
- Alijani H., Cetin B., Akkus Y., and Dursunkaya Z., 2019, Experimental thermal performance characterization of flat grooved heat pipes. *Heat Transfer Eng.*, 40(9-10):784-793.
- Anand A. R., Vedamurthy A. J., Chikkala S. R., Kumar S., Kumar D., and Gupta P. P., 2008, Analytical and experimental investigations on axially grooved aluminum-ethane heat pipe. *Heat Transfer Eng.*, 29(4):410-416.
- Atay A., Sariaslan B., Kuşcu Y. F., Saygan S., Akkus Y., Gürer A. T., Çetin B., and Dursunkaya Z., 2019, Performance assessment of commercial heat pipes with sintered and grooved wicks under natural convection. *J. Therm. Sci. Tech.*, 39(2):101-110.
- Babin B. R., Peterson G. P., and Wu D., 1990, Steady-state modeling and testing of a micro heat pipe. *J. Heat Transf.*, 112:595-601.
- Catton I. and Yao Q., 2016, A designer fluid for aluminum phase change devices, Volume III Performance enhancement in copper heat pipes. *Technical report, University of California, Los Angeles, United States.*
- Chang F. L. and Hung Y. M., 2014, The coupled effects of working fluid and solid wall on thermal performance of micro heat pipes. *Int. J. Heat Mass Tran.*, 73:76-87.
- Chen Y., Zhang C., Shi M., Wu J., and Peterson G. P., 2009, Study on flow and heat transfer characteristics of heat pipe with axial “ω”-shaped microgrooves. *Int. J. Heat Mass Tran.*, 52(3-4):636-643.
- Chi S. W., 1976, Heat Pipe Theory and Practice: A Sourcebook. *McGraw-Hill-Hemisphere Series in Fluids and Thermal Engineering. Hemisphere Publishing Corporation.*
- Desai A. N., Singh V. K., and Patel R. N., 2019, Effect of geometrical parameters on the thermal performance of ammonia-based trapezoidal-shaped axial grooved heat pipe. *J. Heat Transf.*, 141(12).
- Do K. H., Kim S. J., and Garimella S. V., 2008, A mathematical model for analyzing the thermal characteristics of a flat micro heat pipe with a grooved wick. *Int. J. Heat Mass Tran.*, 51(19-20):4637-4650.
- Elnaggar M. H. A., Abdullah M. Z., and Mujeebu M. A., 2012, Characterization of working fluid in vertically mounted finned u-shape twin heat pipe for electronic cooling. *Energy Convers. Manage.*, 62:31-39.
- Faghri A., 1989, Performance characteristics of a concentric annular heat pipe: Part 2-vapor flow analysis. *J. Heat Transf.*, 111(4).
- Faghri A., 1995, Heat Pipe Science and Technology. *Global Digital Press.*

- Ferrandi C., Iorizzo F., Mameli M., Zinna S., and Marengo M., 2013, Lumped parameter model of sintered heat pipe: Transient numerical analysis and validation. *Appl. Therm. Eng.*, 50(1):1280-1290.
- Grover G. M., Cotter T. P., and Erickson G. F., 1964, Structures of very high thermal conductance. *J. Appl. Phys.*, 35(6):1990-1991.
- Hoa C., Demolder B., and Alexandre A., 2003, Roadmap for developing heat pipes for Alcatel space's satellites. *Appl. Therm. Eng.*, 23(9):1099-1108.
- Hopkins R., Faghri A., and Khurstalev D., 1999, Flat miniature heat pipes with micro capillary grooves. *J. Heat Transf.*, 121(1):102-109.
- Huang Y. and Chen Q., 2017, A numerical model for transient simulation of porous wicked heat pipes by lattice boltzmann method. *Int. J. Heat Mass Tran.*, 105:270-278.
- Hung Y. M. and Tio K. K., 2010, Analysis of microheat pipes with axial conduction in the solid wall. *J. Heat Transf.*, 132(7).
- Hung Y. M. and Tio K. K., 2012, Thermal analysis of optimally designed inclined micro heat pipes with axial solid wall conduction. *Int. Commun. Heat Mass*, 39(8):1146-1153.
- Jafari D., Wits W. W., and Geurts B. J., 2020, Phase change heat transfer characteristics of an additively manufactured wick for heat pipe applications. *Appl. Therm. Eng.*, 168:114890.
- Jiang L., Ling J., Jiang L., Tang Y., Li Y., Zhou W., and Gao J., 2014, Thermal performance of a novel porous crack composite wick heat pipe. *Energ. Convers. Manage.*, 81:10-18.
- Khalili M. and Shafii M. B., 2016, Experimental and numerical investigation of the thermal performance of a novel sintered-wick heat pipe. *Appl. Therm. Eng.*, 94:59-75.
- Khurstalev D. and Faghri A., 1994, Thermal analysis of a micro heat pipe. *J. Heat Transf.*, 116(1):189-198.
- Khurstalev D. and Faghri A., 1995, Thermal characteristics of conventional and flat miniature axially grooved heat pipes. *J. Heat Transf.*, 117(4):1048-1054.
- Kim S. J., Seo J. K., and Do K. H., 2003, Analytical and experimental investigation on the operational characteristics and the thermal optimization of a miniature heat pipe with a grooved wick structure. *Int. J. Heat Mass Tran.*, 46(11):2051-2063.
- Kolliyil J., Yarramsetty N., and Balaji C., 2020, Numerical modeling of a wicked heat pipe using lumped parameter network incorporating the Marangoni effect. *Heat Transfer Eng.*, :1-15.
- Lefèvre F., Rullière R., Lips S., and Bonjour J., 2010, Confocal microscopy for capillary film measurements in a flat plate heat pipe. *J. Heat Transf.*, 132(3).
- Lefèvre F., Rullière R., Pandraud G., and Lallemand M., 2008, Prediction of the temperature field in flat plate heat pipes with micro-grooves—experimental validation. *Int. J. Heat Mass Tran.*, 51(15-16):4083-4094.
- Li Y., He J., He H., Yan Y., Zeng Z., and Li B., 2015, Investigation of ultra-thin flattened heat pipes with sintered wick structure. *Appl. Therm. Eng.*, 86:106-118.
- Lips S., Lefèvre F., and Bonjour J., 2011, Physical mechanisms involved in grooved flat heat pipes: experimental and numerical analyses. *Int. J. Therm. Sci.*, 50(7):1243-1252.
- Longtin J. P., Badran B., and Gerner F. M., 1994, A one-dimensional model of a micro heat pipe during steady-state operation. *J. Heat Transf.*, 116:709-715.
- Nilson R. H., Tchikanda S. W., Griffiths S. K., and Martinez M. J., 2006, Steady evaporating flow in rectangular microchannels. *Int. J. Heat Mass Tran.*, 49:1603-1618.
- Odabaşı G., 2014, Modeling of multidimensional heat transfer in a rectangular grooved heat pipe. Ph.D. Thesis, Middle East Technical University.
- Ömür C., Uygur A. B., Horuz İ., Işık H. G., Ayan S., and Konar M., 2018, Incorporation of manufacturing constraints into an algorithm for the determination of maximum heat transport capacity of extruded axially grooved heat pipes. *Int. J. Therm. Sci.*, 123:181-190.
- Peterson G. P., 1994, An Introduction to Heat Pipes: Modeling, Testing, and Applications. Wiley.
- Peterson G. P., Duncan A. B., and Weichold M. H., 1993, Experimental investigation of micro heat pipes fabricated in silicon wafers. *J. Heat Transf.*, 115(3):751-756.
- Reay D., McGlen R., and Kew P., 2013, Heat Pipes: Theory, Design and Applications. *Butterworth-Heinemann*.
- Rullière R., Lefèvre F., and Lallemand M., 2007, Prediction of the maximum heat transfer capability of two-phase heat spreaders—experimental validation. *Int. J. Heat Mass Tran.*, 50(7-8):1255-1262.
- Schneider G. E. and DeVos R., 1980, Non-dimensional analysis for the heat transport capability of axially grooved heat pipes including liquid/vapor interaction. *In AIAA*, page 214.
- Schrage R.W., 1953, A Theoretical Study of Interphase Mass Transfer. *Columbia University Press, New York*.

- Setchi A., Chen Y., Yu J., and Wang H., 2019, Structural effects in partially-wetting thin evaporating liquid films near the contact line. *Int. J. Heat Mass Tran.*, 132:420-430.
- Singh M., 2020, Capillarity enhancement of micro heat pipes using grooves with variable apex angle. *Int. J. Therm. Sci.*, 150:106239.
- Sujanani M. and Wayner P.C., 1991, Microcomputer-enhanced optical investigation of transport processes with phase change in near-equilibrium thin liquid films. *J. Colloid Interf. Sci.*, 2:472-488.
- Suman B., De S., and DasGupta S., 2005, A model of the capillary limit of a micro heat pipe and prediction of the dry-out length. *Int. J. Heat Fluid Fl.*, 26(3):495-505.
- Tio K. K. and Hung Y. M., 2015, Analysis of overloaded micro heat pipes: Effects of solid thermal conductivity. *Int. J. Heat Mass Tran.*, 81:737-749.
- Vafai K., 1984, Convective flow and heat transfer in variable-porosity media. *J. Fluid Mech.*, 147:233-259.
- Vafai K. and Tien C. L., 1981, Boundary and inertia effects on flow and heat transfer in porous media. *Int. J. Heat Mass Tran.*, 24(2):195-203.
- Vafai K. and Wang W., 1992 Analysis of flow and heat transfer characteristics of an asymmetrical flat plate heat pipe. *Int. J. Heat Mass Tran.*, 35(9):2087-2099.
- Zhu N. and Vafai K., 1999, Analysis of cylindrical heat pipes incorporating the effects of liquid-vapor coupling and non-darcian transport-a closed form solution. *Int. J. Heat Mass Tran.*, 42(18):3405-3418.
- Zhu N. and Vafai K., 1996, The effects of liquid-vapor coupling and non-Darcian transport on asymmetrical disk-shaped heat pipes. *Int. J. Heat Mass Tran.*, 39(10):2095-2113.

ISI BİLİMİ VE TEKNİĞİ DERGİSİ İÇİN MAKALE HAZIRLAMA ESASLARI

Isı Bilimi ve Tekniği Dergisi'nde, ısı bilimi alanındaki özgün teorik ve deneysel çalışmaların sonuçlarının sunulduğu makaleler ve yeterli sayıda makaleyi tarayarak hazırlanmış olan literatür özeti makaleler yayınlanmaktadır. Makaleler, Türkçe veya İngilizce olarak kabul edilmektedir. Makaleler ilk sunumda serbest formatta hazırlanabilir. Ancak yayın için kabul edilmiş olan makaleler dergimizin basım formatına tam uygun olarak yazarlar tarafından hazırlanmalıdır. Aşağıda, ilk sunuş ve basıma hazır formatta makale hazırlamak için uyulması gereken esaslar detaylı olarak açıklanmıştır.

İLK SUNUŞ FORMATI

İlk sunuşta, makale A4 boyutundaki kağıda tek sütun düzeninde, 1.5 satır aralıklı ve sayfa kenarlarından 25'er mm boşluk bırakılarak yazılmalıdır. Yazı boyutu 11 punto olmalı ve **Times New Roman** karakter kullanılmalıdır. Şekiller, tablolar ve fotoğraflar makale içinde **olmaları gereken yerlere** yerleştirilmelidir. Makale, elektronik olarak editörün e-posta adresine gönderilmelidir.

BASIMA HAZIR MAKALE FORMATI

Hakem değerlendirmelerinden sonra, yayın için kabul edilmiş olan makaleler, dergimizin basım formatına tam uygun olarak yazarlar tarafından hazırlanmalıdır. Makaleler yazarların hazırladığı haliyle basıldığı için, yazarların makalelerini basım için hazır formatta hazırlarken burada belirtilen esasları titizlikle takip etmeleri çok önemlidir. Aşağıda, basıma hazır formatta makale hazırlamak için uyulması gereken esaslar detaylı olarak açıklanmıştır.

Genel Esaslar

Makaleler genel olarak şu başlıklar altında düzenlenmelidir: Makale başlığı (title), yazar(lar)ın ad(lar)ı, yazar(lar)ın adres(ler)i, özet (abstract), anahtar kelimeler (keywords), semboller, giriş, materyal ve metod, araştırma sonuçları, tartışma ve sonuçlar, teşekkür, kaynaklar, yazarların fotoğrafları ve kısa özgeçmişleri ve ekler. Yazılar bilgisayarda tek satır aralıklı olarak, 10 punto Times New Roman karakteri kullanılarak Microsoft Office Word ile iki sütun düzeninde yazılmalıdır. Sayfalar, üst kenardan 25 mm, sol kenardan 23 mm, sağ ve alt kenarlardan 20 mm boşluk bırakılarak düzenlenmelidir. İki sütun arasındaki boşluk 7 mm olmalıdır. Paragraf başları, sütunun sol kenarına yaslanmalı ve paragraflar arasında bir satır boşluk olmalıdır.

Birinci seviye başlıklar büyük harflerle kalın olarak, ikinci seviye başlıklar bold ve kelimelerin ilk harfleri büyük harf olarak ve üçüncü seviye başlıklar sadece ilk harfi büyük olarak yazılır. Bütün başlıklar sütunun sol kenarı ile aynı hizadan başlamalıdır ve takip eden paragrafla başlık arasında bir satır boşluk olmalıdır. Şekiller, tablolar, fotoğraflar v.b. metin içinde ilk atıf

yapılan yerden hemen sonra uygun şekilde yerleştirilmelidir. İlk ana bölüm başlığı, Özetten (Abstract'tan) sonra iki satır boşluk bırakılarak birinci sütuna yazılır.

Başlık, Yazarların Adresi, Özet, Abstract ve Anahtar Kelimeler

Yazılar Türkçe veya İngilizce olarak hazırlanabilir. Her iki durumda da makale özeti, başlığı ve anahtar kelimeler her iki dilde de yazılmalıdır. Eğer makale Türkçe olarak kaleme alınmışsa, Türkçe başlık ve özet önce, İngilizce başlık ve Özet (Abstract) sonra yazılır. Eğer makale İngilizce olarak kaleme alınmışsa önce İngilizce başlık ve özet (abstract) sonra Türkçe başlık ve özet yazılır. Başlık, sayfanın üst kenarından 50 mm aşağıdan başlar ve kalın olarak 12 punto büyüklüğünde, büyük harflerle bütün sayfayı ortalayacak şekilde yazılır. Yazar(lar)ın adı, adresi ve elektronik posta adresi başlıktan sonra bir satır boşluk bırakılarak yazılmalıdır. Yazarların adı küçük, soyadı büyük harflerle yazılmalı ve bold olmalıdır. Yazarların adresinden sonra üç satır boşluk bırakılarak, Özet ve Abstract 10 punto büyüklüğünde bütün sayfa genişliğinde yazılır. Özet ve Abstracttan sonra anahtar kelimeler (Keywords) yazılır.

Birimler

Yazılarda SI birim sistemi kullanılmalıdır.

Denklemler

Denklemler, 10 punto karakter boyutu ile bir sütuna (8 cm) sığacak şekilde düzenlenmelidir. Veriliş sırasına göre yazı alanının sağ kenarına yaslanacak şekilde parantez içinde numaralanmalıdır. Metin içinde, denklemlere '**Eş. (numara)**' şeklinde atıfta bulunulmalıdır.

Şekiller

Şekiller 8 cm (bir sütun) veya 16 cm (iki sütun) genişliğinde olmalıdır ve makale içerisinde olmaları gereken yerlere bilgisayar ortamında sütunu (veya bütün sayfa genişliğini) ortalayacak şekilde yerleştirilmelidir. Şekil numaraları (sıra ile) ve isimleri şekil **altına, 9 punto büyüklüğünde** yazılmalıdır.

Tablolar

Tablolar 8 cm (bir sütun) veya 16 cm (iki sütun) genişliğinde olmalıdır. Makale içerisinde olmaları gereken yerlere bilgisayar ortamında sütunu (veya bütün sayfa genişliğini) ortalayacak şekilde yerleştirilmelidir. Tablo numaraları (sıra ile) ve isimleri tablo **üstüne, 9 punto büyüklüğünde** yazılmalıdır.

Fotograflar

Fotograflar, siyah/beyaz ve 8 cm (bir sütun) veya 16 cm (iki sütun) genişliğinde olmalıdır. Fotograflar digitize edilerek, makale içinde bulunmaları gereken yerlere bilgisayar ortamında sütunu (veya bütün sayfa genişliğini) ortalayacak şekilde yerleştirilmelidir ve şekil gibi numaralandırılmalı ve adlandırılmalıdır.

Yazar(lar)ın Fotoğraf ve Kısa Özgeçmişleri

Yazarların fotoğrafları digitize edilerek, makalenin en sonuna özgeçmişleri ile birlikte uygun bir şekilde yerleştirilmelidir.

SEMBOLLER

Makale içinde kullanılan bütün semboller alfabetik sırada Özetten sonra liste halinde tek sütun düzeninde yazılmalıdır. Boyutlu büyüklükler birimleri ile birlikte ve boyutsuz sayılar (Re, Nu, vb.) tanımları ile birlikte verilmelidir.

KAYNAKLAR

Kaynaklar metin sonunda, ilk yazarın soyadına göre alfabetik sırada listelenmelidir. Kaynaklara, yazı içinde, yazar(lar)ın soyad(lar)ı ve yayın yılı belirtilerek atıfta

bulunulmalıdır. Bir ve iki yazarlı kaynaklara, her iki yazarın soyadları ve yayın yılı belirtilerek (Bejan, 1988; Türkoğlu ve Farouk, 1993), ikiden çok yazarlı kaynaklara ise birinci yazarın soyadı ve "vd." eki ve yayın yılı ile atıfta bulunulmalıdır (Ataer vd, 1995). Aşağıda makale, kitap ve bildirilerin kaynaklar listesine yazım formatı için örnekler verilmiştir.

Ataer Ö. E., Ileri A. and Göğüş, Y. A., 1995, Transient Behaviour of Finned-Tube Cross-Flow Heat Exchangers, *Int. J. Refrigeration*, 18, 153-160.

Bejan A., 1998, *Advanced Engineering Thermodynamics* (First Ed.), Wiley, New York.

Türkoğlu H. and Farouk B., 1993, Modeling of Interfacial Transport Processes in a Direct-Contact Condenser for Metal Recovery, *Proc. of 73rd Steel Making Conference*, Detroit, 571-578.

Türkoğlu H., 1990, *Transport Processes in Gas-Injected Liquid Baths*, Ph.D. Thesis, Drexel University, Philadelphia, PA, USA.

İnternet, 2004, Türkiye İstatistik Kurumu, *Atıksu İstatistikleri*, <http://www.tuik.gov.tr/HaberBulteni>.

DIĞER HUSUSLAR

Hakem değerlendirmesinden sonra kabul edilen makaleler, yukarıda açıklandığı şekilde dizilerek basıma hazırlandıktan sonra, bir elektronik kopyası editöre gönderilmelidir. Makalenin basıma hazır kopyası ile birlikte, "Telif Hakkı Devri Formu" da doldurularak gönderilmelidir. Telif Hakkı Devri Formu'na ve bu yazım klavuzuna www.tibt.org.tr adresinden ulaşılabilir.



TÜRK ISI BİLİMİ VE TEKNİĞİ DERNEĞİ
ÜYELİK BAŞVURU FORMU

FOTOĞRAFINIZ

A. Adınız Soyadınız :
Ünvanınız :
Doğum yeri : : Doğum tarihi: / / 19 T.C. Kimlik No:
İş Adresiniz :
Ev adresiniz :
Telefonunuz : İş Ev Cep
E-posta :

B. *Derneğe Asil üye Fahri üye olmak istiyorum.

1. Sizi tanıyan dernek üyesi (Üyelik için) :

2. Mezun olduğunuz
Yüksek Okullar Yıl Branşınız Ünvanınız

3. İlgilendiğiniz konular :

2015 yılı aidatı olarak toplam 25 YTL (Yirmibeş Milyon TL) derneğin

İş Bankası Maltepe Şubesi Hesap No: 42120867567
IBAN: TR08 0006 4000 0014 2120 8675 67

hesabına yatırılmıştır.

Tarih :

İmza :

* Asil üye olmak için beş yıllık deneyim gereklidir.
Fahri üyelik için yüksekokul mezunu olma şartı yoktur.

Türk Isı Bilimi ve Tekniđi Derneđi
Gazi Üniversitesi
Mühendislik Fakültesi
Makina Mühendisliđi Bölümü
06570 Maltepe/ ANKARA

İÇİNDEKİLER / CONTENTS

Dik kanal içerisindeki taşınım ile ısı transferinin yarı silindirik akış engelleri kullanılarak iyileştirilmesinin sayısal olarak incelenmesi	1
<i>Numerical investigation of enhancing mixed convection heat transfer by using semi-cylindrical obstacles in a vertical channel</i> Sedat ÖZDEMİR, Mustafa KILIÇ, Tamer ÇALIŞIR ve Şenol BAŞKAYA	
The determination of the heat extraction ratio in the solar pond	17
<i>Güneş havuzlarında ısı çekme oranının belirlenmesi</i> Hacı SOĞUKPINAR and İsmail BOZKURT	
Modüler Helyum reaktörünün kaza durumunun zamana bağlı ısı akış analizi	25
<i>Transient thermal hydraulic analysis of modular Helium reactor under accident condition</i> Ömür AKBAYIR	
Numerical analysis of microwave cancer therapy using single and double slot antennas for breast and liver tissues	37
<i>Meme ve karaciğer dokularında tek ve çift yuvalı anten kullanılarak yapılan mikrodalga kanser tedavisinin nümerik analizi</i> Aykut EREN, Zeynep AYTAÇ, Oğuz TURGUT and Burak TİĞLİ	
Determination of indoor design temperature, thermal characteristics and insulation thickness under hot climate conditions	49
<i>Sıcak iklim şartları altında iç dizayn sıcaklığı, termal özellikler ve yalıtım kalınlığının belirlenmesi</i> Meral ÖZEL	
Analysis and optimization of activated carbon coated heat sinks	65
<i>Aktif karbon kaplamalı soğutucuların analiz ve optimizasyonu</i> Alperen GÜNAY	
Experimental investigation of the effects of water adding into the intake air on the engine performance and exhaust emissions in a spark-ignition engine	75
<i>Bir benzin motorunda emme havasına su eklenmesinin motor performansına ve egzoz emisyonlarına etkilerinin deneysel olarak incelenmesi</i> Derya SOYSAL, Zehra ŞAHİN and Orhan DURGUN	
An accelerated nodal discontinuous Galerkin method for thermal convection on unstructured meshes: Formulation and validation	91
<i>Isı Taşınımı için yapısal olmayan ağlarda bir hızlandırılmış süreksiz Galerkin metodu: Formülasyonu ve doğrulaması</i> Ali KARAKUS	
Exergy analysis of Graphene-based nanofluids in a compact heat exchanger	101
<i>Kompakt bir ısı değiştiricisinde Grafen bazlı nano akışkanların ekserji analizi</i> Ferhat KILINÇ and Cihan Zeki UYGUN	
Implementation, verification and assessment of vortex capturing capabilities of k-kL turbulence model	113
<i>k-kL türbülans modelinin uygulaması, doğrulaması ve girdap yakalama yeteneklerinin değerlendirilmesi</i> Erdem DİKBAŞ and Özgür Uğraş BARAN	
Design fire curve selection of small scale pool fires in a scaled metro station	123
<i>Ölçeklendirilmiş bir metro istasyonunda küçük ölçekli sıvı havuz yangınlarının yangın tasarım eğrisi seçimi</i> Umut Barış YILMAZ, Oğuz TURGUT, Nuri YÜCEL and Muhammed İlter BERBEROĞLU	
Fast and predictive heat pipe design and analysis toolbox: H-PAT	141
<i>Hızlı ve öngörülü ısı borusu tasarım ve analiz aracı: H-PAT</i> Samet SAYGAN, Yiğit AKKUŞ, Zafer DURSUNKAYA and Barbaros ÇETİN	